DISSERTATION

A MULTIMETHOD SIMULATION PARADIGM FOR INVESTIGATING COMPLEX CELLULAR RESPONSES IN BIOLOGICAL SYSTEMS OF AGING AND DISEASE

Submitted by

Timothy Edward Hoffman

Department of Environmental and Radiological Health Sciences

In partial fulfillment of the requirements

For the Degree of Doctor of Philosophy

Colorado State University

Fort Collins, Colorado

Summer 2019

Doctoral Committee:

Advisor: William H. Hanneman
Co-Advisor: Marie E. Legare

Lyle E. Wallis
Julie A. Moreno

ABSTRACT

A MULTIMETHOD SIMULATION PARADIGM FOR INVESTIGATING COMPLEX CELLULAR RESPONSES IN BIOLOGICAL SYSTEMS OF AGING AND DISEASE

Classical studies in toxicology and disease research have relied on the use of high-dose experiments and often lacked quantitative and comprehensive components essential to understanding biological queries. These shortcomings in the research community have been the result of modern methodological limitations, however, more robust and expansive experimental and computational methods are emerging. In this dissertation, I present a novel multimethod computational simulation paradigm that adds value to new and existing studies of toxicological and pathological endeavors. First, I established the use of this approach for pharmacokinetic and pharmacodynamic applications, with published examples in regulatory toxicology and contemporary dose-response nuances. Following establishing the success of this approach in toxicology, I then applied this methodology to degenerative aging, as it has been arduous with conventional techniques to understand the various mechanisms that determine cellular aging. The foundational simulation created for general cellular aging was then expanded in the context of tauopathies and Alzheimer's disease to better quantify and understand the pathways involved in this age-dependent disorder. The final results presented here improve experimental translatability, robustness and descriptiveness in order to better understand age-related diseases. More broadly, this dissertation ultimately minimizes quantitative deficits in toxicological and pharmacological research.

DEDICATION

This work is dedicated to all those who have challenged and inspired me over the years. To my parents Steph and Jeff for giving me every opportunity I have ever had in my life. To my sister Ellen and my dear friend Lauren for lending their ears and helping hands when I needed them most. To my better half Luke for seeing these successes within me when I could not see them for myself. To my committee and all my mentors for teaching me the supreme values of diligence, repetition, humility, and failure. Most sincerely, to “H” for showing me what it means to make a truly great difference in this world.

TABLE OF CONTENTS

LIST OF TABLES

LIST OF FIGURES

LIST OF EQUATION APPENDICIES AND BOXES

CHAPTER 1: INTRODUCTIONS AND METHODOLOGICAL PERSPECTIVES

1.1 An enhanced scientific method and biological testing paradigm

The inner workings of cell and molecular biology have slowly been uncovered over the past century through the tried-and-true scientific method: hypothesis generation, laborious experimentation, and keen observation. Due to the amazing complexity of infinitesimal biological systems, toxicological mechanisms of disease have been difficult to pinpoint with precision in this classic process and have become even more elusive in the wake of diminished funding. To improve this process, a more extensive and meaningful interpretation of quantitative data must be conducted, which is possible through the understanding of circuit-based systems biology and the employment of innovative *in silico* simulation technologies. This chapter opens the debate for a spectrum of computational cellular dynamic modeling techniques as indispensable tools for accelerating the production of important physiological and toxicological research.

As the knowledge of cellular systems becomes more correct and thus more complex, the need for accurate and easily understood experimental models becomes increasingly paramount. This is primarily because biological scientists are, by nature, wired to increase their knowledge-span and discover the elusive causal agent or earliest trigger in any given physiological process. For over a century, research in cell biology has uncovered a vast array of important processes within the fields of applied pharmacology, toxicology and general pathology, but many initiating steps and propagating processes of the relevant cellular mechanisms remain unknown. Such is

the case with natural biological functions that lead to age-related cellular damage [1, 2] and carcinogenesis [3, 4], as well as with many toxicological responses that require better etiological and mechanistic explanations [5, 6]. The drive to fully comprehend these complex relationships has not weakened, so what methodological obstacles have made this research so difficult for so long?

Traditionally, biologists and toxicologists have been obliged to make broad strokes in their experiments—using epidemiological studies, high-dose *in vivo* models, histological techniques and purely qualitative macromolecule measurements—to draw relatively loose conclusions about absolute mechanistic pathways underlying homeostatic conditions and toxicological disease states [7]. Even well-researched mechanisms lack some predictive capability in their experimental models [8], as they are often unable to address extensively connected cellular pathways and quantitative dynamic variables, such as the ever-changing variable of time. Other notable observations among these types of studies include their likelihood of inaccuracy [9] and very low rate of reproducibility, which have been thoroughly discussed with concern in several major press releases [10–12]. It is speculated that such experiments, especially those involving oncological pursuits, can only be replicated 10–25% of the time [10], likely due to a poor understanding of molecular targets and predictive biomarkers [12].

Many studies about diseases and toxicities have innately lacked a genuine biological basis in their experimental designs—with regard to intrinsic cellular function and xenobiotic-induced dose-response relationships. These specific advances in molecular biology have been stunted by a stagnant understanding of complex cellular circuitry and a severe deficit of a universal “quantitative language” by which to address

mechanistic metrics [13]. This dilemma has been gradually remedied by the advent of systems biology, a precise quantitative science that deals with whole biological systems, i.e. the network of finite processes involved in particular physiological states and pathological outcomes. This relatively young field of computational systems biology is now burgeoning, and has initiated several radical reports on the state of the necessary experimentation paradigm [14–18]. Most notably, the National Research Council issued “a blueprint for change” in 2007 [17] to reevaluate how toxicity testing should be conducted, focusing on the necessary inclusion of high-throughput *in vitro* assays, omics technologies, quantitative structure-activity relationships, and, especially, computational modeling efforts. This report was followed by a battery of commentary articles [7, 19–21] and was lauded by the scientific community for its useful innovations. From these ideas spawned the creation of powerful predictive biological models [22–24] that employ high-throughput technologies and systemic quantitative analyses, and the number of biological researchers employing mathematical models continues to rise [25].

The promise of this shift in the scientific community lies within synthetic biological simulations, which interpret a massive collection of quantitative data and have extraordinary power in their predictive capacity. Historically, computational simulations have been underutilized in biological research due to poorly communicated methodology and a limited technical capacity within classic modeling software [26]. Discussed here are the valuable advancements made in quantitative systems biology and a novel function of simulation technology. Together these may promote the use of computational biological modeling to ultimately accelerate the generation of important physiological and toxicological research.

1.2 A quantitative language for cellular biology

In 2002, Yuri Lazebnik wrote about his perspective of traditional experiments in biology [13]. To do so, he applied the molecular biologist's reductionist approaches to a problem with a known solution: reverse-engineering a broken transistor radio. He described how biologists would dissect such a device and qualitatively assess each piece (e.g., by color, size, shape, part-deficient "phenotypes"), thus inciting more confusion about the entire system and not achieving the original goal of fixing the radio. Engineers, however, are equipped to tackle these problems because 1) they are formally trained to recognize and appropriately render the connections within complete circuits and 2) there is a commonality among the specific parameters that accompany such systems. These concepts, Lazebnik and many others argue [13, 27, 28], are directly applicable to molecular biology, where signal transduction pathways and cellular response mechanisms can be understood as mathematical circuits. With this mindset, it is easier to predict how all the intricate workings of a cell interact with one another in a physiological system and to understand how they do so in a very calculable way.

Lazebnik's thought experiment exemplifies why there must be more structural commonalities driving quantitative biological experimentation and modeling techniques. To begin, biologists must elucidate the crucial connections within a biological system and the time-dependent biochemical reactions that occur within each individual segment at play. In other words, to comprehend the full cellular mechanism of interest, it must be broken down into its measurable parts and subsequently reconstructed to make apt predictions about physiological effects.

This reconstruction phase requires a bit of targeted data-mining to determine the battery of active pathways within a cellular system, through the discovery of critical proteins and transcription factors (i.e. via proteomic technologies) as well as the array of functional transcripts expressed or repressed in a given response (i.e. via transcriptomic technologies). With these data on key proteins and genes, tissue-specific biological circuits can be accurately proposed and continually refined with more specific laboratory assays to establish all the significant connections within a working model [29, 30]. Technological advances are even starting to allow for single-cell analysis of transcriptomic landscapes for researchers to more precisely define mechanistic machinery at the cellular level [31]. From a practical standpoint, drug discovery and product safety are becoming more heavily reliant on transcriptomics and computational reconstruction to break out of the reductionist "targephilic" mindset and to provide more meaningful multi-pathway assessments for relevant compounds [16, 32, 33]. Such omics-driven systemic approaches have also identified biological networks useful for studying developmental cardiac pathologies [34], neurodevelopmental and neurodegenerative disorders [35], hepatic metabolism in the pathogenesis of type 2 diabetes mellitus [36], and cellular senescence and concomitant tissue aging [37].

Once a cellular network has been closely reconstructed to create the framework of a biological model, the distinct reactions and events it consists of should be quantitatively evaluated. The two most important factors that define any molecular event in cell biology are *stimulus magnitude* and *time*, and network connections should be evaluated within these dynamic contexts.

In toxicology, these variables define *chemical dose* and *response duration*, and purely endogenous processes can be viewed all the same (e.g. time-dependent responses elicited by varying hormone levels). These variables are used as inputs for a physiological system to produce dose-response and time-course curves. Such resulting datasets provide the basic quantitative knowledge by which to observe cellular mechanisms, and these curves are unsurprisingly far from linear [28]. They are the product of complex dynamic systems comprised of varying network motifs, whose structural mathematics have been successfully derived by select few computational biologists [28, 38–44]. With great distinction, James Ferrell Jr. devotes his career to creating and understanding the complex equations that explain specific cellular behaviors such as biochemical steady-states and irreversibility in cell signaling [40], Michaelian enzyme kinetics and cooperative binding [41], oscillatory behavior in signaling cascades [42], and ultrasensitivity born out of either positive feedback or negative cooperativity [43, 44]. The composite of these network motifs often results in ultrasensitive or switch-like functional responses in cell biology. This is certainly true for Ferrell's initial investigation of phosphorylation-induced oocyte maturation [45], and this also holds true for classic toxicological mechanisms involving the hepatic aryl hydrocarbon receptor, which have been thoroughly probed and analyzed at the single-cell level [46, 47].

It is crucial for life scientists to study biological networks by, at the very least, acknowledging the appropriate mechanistic motifs and appreciating the mathematical efforts that can closely define them. The next leap in biological and toxicological research is to use segmented quantitative data of individual reactions in a universally

systematic format that can help explain or predict the behavior of larger systems. Systematic interpretations will always be limited as cellular systems appear to approach infinite biological connections, but as models are more well designed and eloquently assumed, their predictive capacity will reach a very close estimate of the real world.

1.3 Innovative approaches in biological modeling

Several prolific scientists speculate that, with the right tools in place, computational systems biology will not only accelerate the production of meaningful research, but will eventually become an indispensable component, a requisite, of formal biologist training [7, 13, 15, 48]. It is therefore a top priority to find the best tools to do so, i.e., the best simulation modeling interface at which to study such systems.

Systems biologists begin with mental models—abstractions of the real cellular world. Mental models are innately used to define perceptions of reality and they allow smoother navigation through the learning process [49]. Mental models of living systems, assembled based on previous data, have classically been challenged and substantiated at the bench through a laborious (and sometimes unfruitful) experimentation process. To learn more about a given research project and to design more thoughtful experiments going forward, quantitative data must be more carefully analyzed in the context of a working mental model. Biological simulation work offers the best initial method for visualizing and interrogating these models, as simulations allow for real experimentation of ideas in a virtually risk-free environment (Fig. 1.1). Reagents are spared, animal use is reduced, and most importantly, valuable time is not squandered.

Biological *in silico* modeling not only integrates more thought into the experimentation process, but it also welcomes more unique ideas to be tested in a virtual world. When predicting the quantitative circuitry of cells, perhaps it would be wise to draw on how other non-biological systems behave over time—in order to hypothesize about non-intuitive mathematical relationships seen in cell biology and toxicology. This idea is best described by the esteemed Frans Johansson, and what he has coined *The Medici Effect* [50]. Johansson states in his text that "[n]ew discoveries, world-changing discoveries, will come from the intersections of disciplines, not from within them." The intersection of computational simulations and systems biology allows scientists to draw on concepts from any mathematical discipline—be it fluid dynamics, behavioral economics, or quantum mechanics—and employ them in biological models to make bizarre and potentially groundbreaking predictions. Lazebnik made an excellent connection between signal transduction networks and the electrical circuits that allow radios to function; it is likely that other unique intersectional mental models will follow suit. After establishing the best mental model of a biological query, it must then be simulated appropriately. The two most useful formats in simulation software are agent-based models and system dynamics models.

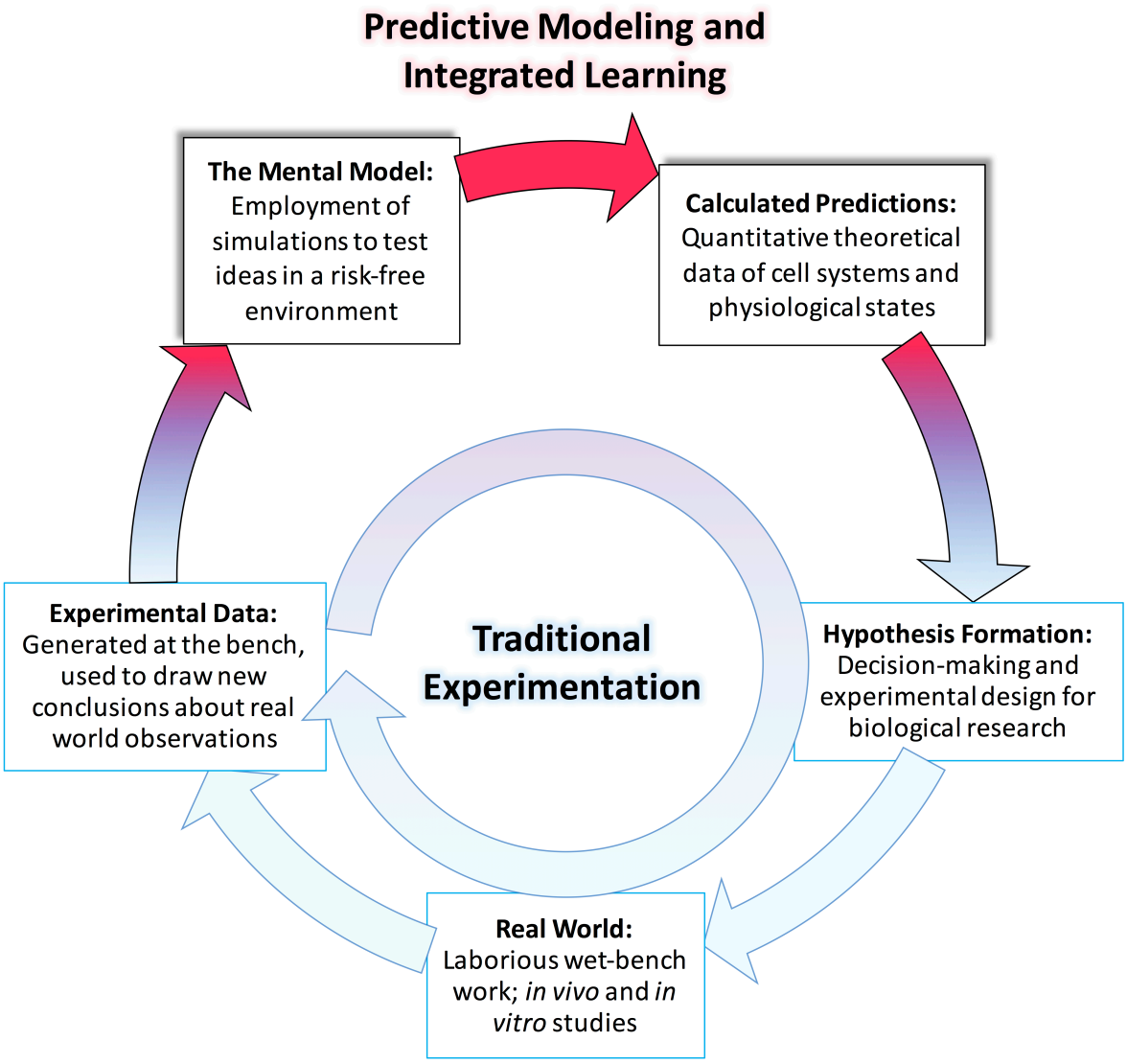

FIGURE 1.1

The scientific method and traditional loop of learning for both traditional practices and newly developed analytical practices with the use of computational modeling.

Agent-based (AB) models are valuable tools for simulating the behavior of concrete biological entities (e.g. proteins, organelles, cells, tissues, organisms) that have seemingly autonomous or rule-obeying behavior [51]. Agents interact and influence one another through discrete events, causing compelling non-linear mathematical patterns to emerge that cannot be explicitly programmed into a simulation [53]. Additionally, AB models are designed to incorporate stochasticity in systemic models, where genetic, environmental or intrinsic factors can be governed by a degree of expected randomness [54]. AB paradigms have been used to successfully model a number of biological processes [51, 52], and most recently to simulate the time-dependent lipid raft changes in neuronal tissue as it relates to the progression of Alzheimer's disease [55].

System dynamics (SD) models are more formal representations of biological structures, employing stocks, flow rates and differential equations to simulate the behavior of continuously changing entities [56]. These formats are largely useful for logically connecting such equations to determine the chemical concentrations within a given space, as well as determining the magnitude and direction of feedback loops. SD models and similar structures have largely been applied for physiologically-based pharmacokinetic modeling [57], however, this particular computational tool has more recently been explored for studying the kinetic parameters of cellular networks, which has been substantiated by a productive case study of chemotaxis of *Escherichia coli* [58].

Some relationships in molecular biology are best represented by AB models (e.g. seemingly autonomous mitochondrial behavior and organelle phenotyping), whereas

others are easily understood at the SD interface (e.g. estimations of cytosolic protein concentration). It is not only possible but highly favorable for these continuous- and discrete-event approaches to coexist within a biological model in order to reach the most appropriate representation of a complex lifeform [59]. For instance, cells, often represented by active agents, are filled with macromolecules and chemical concentrations that are constantly changing, which are easily defined in a SD space.

AB–SD hybrid models for system sciences have been proposed for over a decade [60], yet this approach is just now garnering significant attention for systems biology [61, 62]. As an extensive case study, Krinner et al. (2013) designed a multimethod computational framework to emulate a human population of hematopoietic stem cells and the corresponding maturation into granulocytes that ensues [63]. For this model, the stem cells are each individually modeled as agents, where they have a probabilistic propensity to either differentiate or maintain their pluripotency. The behavior of these hematopoietic stem cell agents is controlled by the dynamic availability of growth factors, other cell counts, and chemotherapeutic agents, which are all represented by ordinary differential equations within SD compartments. Another example of this modeling approach is the more recent use of hybrid simulations to define the chemotactic pathogen-detecting behavior of alveolar macrophages in response to a fungal infection [64]. In this study, single cells are represented as rule-obeying agents that live and operate within a continuously changing space that consists of dynamic alveolar epithelial chemokine secretions. These are only a couple of the innovative studies that have set the standard for hybrid models in computational systems biology.

Multimethod simulations and hybrid models are now being explored among the scientific community, though very few software packages offer this capability in a functional way. AnyLogic (The AnyLogic Company; Chicago, IL) offers a new intuitive interface that allows for this multimethod approach, and although its use has not yet been fully realized for biologics, its agent-based capabilities *have* been experimented with for a preliminary simulation of antibody production [65]. It is likely that more software packages will begin to emulate this multimethod capability.

Experimentation for biological sciences has made a powerful progression towards the use and full integration of computational methods. To augment this movement, cellular and molecular networks must be more easily communicated, understood and rendered, which is possible at the interface of intuitive multimethod simulations. Fusing such techniques as AB and SD modeling while employing an array of mathematical concepts is therefore the hallmark of the approach highlighted here. These innovative methods in systems biology may very well provide more inclusive and well-calculated *in silico* models, and thus more effective hypothesis generation and meaningful results in predictive biology and toxicology.

CHAPTER 2: CASE STUDIES OF SIMULATION APPLICATIONS IN BIOLOGY

2.1 Multispecies internal exposure modeling of dietary compounds

To assess the effectiveness of our simulation approach on pharmacokinetic predictability, we conducted such an analysis on a relevant toxicological issue involving benzoic acid, which is presented here. *To view the peer-reviewed research article that accompanies this section, see: Hoffman and Hanneman (2017) Physiologically-based pharmacokinetic analysis of benzoic acid in rats, guinea pigs and humans: Implications for dietary exposures and interspecies uncertainty. Computational Toxicology.* ***3****, 19–32.*

2.1.1 The benzoic acid story and why pharmacokinetics matter

Benzoic acid (BA) and benzoate salts have been used as direct food and beverage additives for decades. These compounds effectively prevent microbial growth, as benzoates exert a high toxicological specificity toward bacteria and other food contaminants [66] while maintaining a remarkably high safety margin for humans and other mammalian species. Toxicological data for BA and related available experimental information date back as far as the 1940s, ‘50s and ‘60s [67]. In the majority of these existing studies, liberal dosing of BA or sodium benzoate elicited no toxicological responses or any stark physiological changes in rodent models. In a handful of chronic feeding studies from this era that have concrete dosing values, little to no toxicological responses were observed, where growth impairments had been assessed as a possible adverse outcome at exceptionally high doses [68–70]. In these developmental rodent models, the no observable adverse effect level (NOAEL) has been determined to be the

highest doses used in these studies, which fall within the range of 550–2195 mg/kg(bw)/day. Regulatory agencies have also placed special emphasis on a multi-generational reproductive toxicity study that showed no offspring defects after up to ~500 mg/kg(bw)/day of oral BA administration [70]. This study has been regarded as having the pivotal datasets that govern the current worldwide regulations on benzoates as food additives, where the maximum acceptable daily intake (ADI) for humans has been conservatively set at 5 mg/kg(bw)/day [71] by extrapolating down from the highest tested dose in rodents (the NOAEL of 500 mg/kg(bw)/day) by the standard uncertainty factor (of 100×).

As these preservatives have been undergoing constant reevaluation, many intake assessments and estimates have been recently produced [72–76]. A portion of these exposure studies, especially those in eastern Asia, have found that the largest probable estimations (i.e. those within the 95th percentile) were still substantially lower than the 5 mg/kg(bw)/day ADI. Among the most heavily benzoate-exposed populations in Taiwan, the highest daily dose was determined to be 3.1 mg/kg(bw)/day, or 62% of the ADI [72]. A similar study done in Hong Kong found that estimated benzoate exposure due to pre-packaged beverages was 0.97 mg/kg(bw)/day, or 19.4% of the ADI [73]. In contrast, there are a number of conservative assumptions made in the European Food Safety Authority (EFSA) 2016 opinion on benzoates that when compounded result in unrealistic estimated daily intake of benzoates [74]. Such compounded dietary estimates exceed the ADI, especially among European populations. In French populations, the highest average daily benzoate dose, based on consumption occurrence data, was calculated to be 0.79 mg/kg(bw)/day, with 2% of individuals

estimated to have exceeded the ADI [75]. In a study of Flemish populations, the upper bound estimated intake was about 5.9 mg/kg(bw)day [76], however, as the authors point out, this is based upon the assumption that all the products contain the maximum allowable benzoate concentrations. Among a population in Denmark, the median values for average BA consumption all fell below the current ADI, yet the maximum high-end intake estimate did exceed the limit [77].

The Joint Expert Committee on Food Additives (JECFA) and the EFSA have both reported on these recent intake estimates [71, 74], drawing special attention to the purported 95th percentile value of 7 mg/kg(bw)/day in adolescents and the purported 97.5th percentile value of 10.9 mg/kg(bw)/day in toddlers. The concerns associated with these high-end ADI-exceeding exposure estimates relate to the aforementioned developmental studies [68–70]; however, the current dietary levels still fall 100× below the doses required to elicit any significant response in rats. These estimations have led to calls to action for either (a) readjusting the maximum limit used in food and beverage products, or (b) reevaluating the safety database and thus the current ADI. With respect to the latter, one major area of uncertainty in defining and regulating intake limits is interspecies pharmacokinetic variability.

Following oral intake, BA is rapidly absorbed into the blood stream, metabolized into hippuric acid (HA), and readily excreted in many different mammalian species [78]. The distribution and elimination of BA in a physiological setting is primarily governed by metabolic processes, which are virtually all localized to the liver [79], and more specifically, to the mitochondrial matrix of hepatocytes [80]. The pharmacokinetic profile of BA, along with the primary metabolite HA, appears to be relatively conserved among

mammalian species, as the same principle events have been observed in rats, mice, guinea pigs, pigs, monkeys, and humans. However, interspecies variations up until this point have only been assessed qualitatively, bearing no weight in the risk assessment process and causing regulatory agencies to rely on default uncertainty values.

We have thoroughly and quantitatively analyzed the pharmacokinetic database for benzoate preservatives to reach a more accurate measure of the interspecies internal exposure extrapolation. To do so, we have conducted a computational simulation study, employing physiologically-based pharmacokinetic (PBPK) models for BA, HA, and a variety of precursor compound exposures as they relate to estimated and assumed dietary exposures. It is important to note that the EFSA has determined that the ADME (i.e. absorption, distribution, metabolism, excretion) profile of BA is virtually the same as that of sodium or potassium benzoate [74], allowing full read-across for our models which are all based on biochemical characteristics of BA. These models and simulated dosing schemes have allowed us to reach a more accurate margin of exposure (MOE) ratio when considering pivotal toxicological rodent data for determining human safety.

2.1.2 Pharmacokinetic simulation methods

Study design and simulation approach

For this study, PBPK models were fully developed for three different mammalian species in order to assess pharmacokinetic differences from systemic exposures. To do so, similar modeling frameworks with established tissues that have been previously validated were implemented in Berkeley Madonna software (version 8.3.18; University

of California, Berkeley, CA) and translated to a system dynamics format in AnyLogic multimethod simulation software (version 7.3.5; The AnyLogic Company, Chicago, IL). This adapted modeling interface provided (a) better visual development and formatting of the multi-species paradigm, (b) high-throughput parameter calibration tools, (c) useful graphing and data-capture tools for parameter variation experiments, and (d) computational discrete-event tools for complex dietary exposure scenarios, as discussed in subsequent sections of this paper. Simulation constructs are available upon request.

Multi-species PBPK development and parameterization

The models described herein were based upon important organs that have been previously compartmentalized (i.e. blood pool, liver, brain, adipose tissue, and gonads) with quantifiable properties, and remaining tissues have been categorized as either highly-perfused or poorly-perfused tissue conglomerates as described previously [81, 82]. The models are also based upon the flow rates of blood to and from each of these compartments, the chemical-specific partitioning within each tissue, the oral absorption rate of the compounds, and chemical-specific metabolic and urinary elimination rates. These concepts are all (a) visualized in Fig. 2.1, taking into account the full model schematics specifically for BA and HA, and (b) mathematically constructed and elucidated by the differential equations listed below (Equation List A). Additional inputs for precursor compounds, benzyl acetate, benzyl alcohol and benzaldehyde, are schematically visualized in Fig. 2.1 as one aggregate input; however, their more

complex bioavailable time-dependent inputs are described mathematically in the equation list below (Equation List B).

Equation List A: Differential equations governing BA and HA PBPK models

Non-Liver Tissue "X" BA conc. over time (mg/L/hr; gonadal tissue as example):

$$\frac{d[BA]_X}{dt} = \left[\frac{(QX*Q*[BA]_{blood} - QX*Q*[BA]_X/KX_{BA})}{BW*FXV}\right] \quad (A.1)$$

$$\frac{d[BA]_{gonads}}{dt} = \left[\frac{(QG*Q*[BA]_{blood} - QG*Q*[BA]_{gonads}/KG_{BA})}{BW*FGV}\right] \quad (A.2)$$

Liver BA concentration over time (mg/L/hr):

$$\frac{d[BA]_{liver}}{dt} =$$

$$\left[\frac{DoseInput*KAb*BW^{0.25} + (QL*Q*[BA]_{blood}) - (QL*Q*[BA]_{liver}/KL_{BA}) - BW^{0.75}*Vmax\left(\frac{[BA]_{liver}}{[BA]_{liver}+Km}\right)}{BW*FLV}\right] \quad (A.3)$$

Plasma BA concentration over time (mg/L/hr):

$$\frac{d[BA]_{blood}}{dt} = \left[\frac{\left(\sum_0^i\{QX*Q*[BA]_X/KX_{BA}\}_i - \sum_0^i\{QX*Q*[BA]_{blood}\}_i\right) - BW*KELB*[BA]_{blood}}{BW*FBLV}\right] \quad (A.4)$$

Non-Liver Tissue "X" HA conc. over time (mg/L/hr; gonadal tissue as example):

$$\frac{d[HA]_X}{dt} = \left[\frac{(QX*Q*[HA]_{blood} - QX*Q*[HA]_X/KX_{HA})}{BW*FXV}\right] \quad (A.5)$$

$$\frac{d[HA]_{gonads}}{dt} = \left[\frac{(QG*Q*[HA]_{blood} - QG*Q*[HA]_{gonads}/KG_{HA})}{BW*FGV}\right] \quad (A.6)$$

Liver HA concentration over time (mg/L/hr):

$$\frac{d[HA]_{liver}}{dt} = \left[\frac{BW^{0.75}*Vmax\left(\frac{[BA]_{liver}}{[BA]_{liver}+Km}\right)*1.63 + (QL*Q*[HA]_{blood}) - (QL*Q*[HA]_{liver}/KL_{HA})}{BW*FLV}\right] \quad (A.7)$$

Plasma HA concentration over time (mg/L/hr):

$$\frac{d[HA]_{blood}}{dt} = \left[\frac{(\sum_0^i\{QX*Q*[HA]_X/KX_{HA}\}_i - \sum_0^i\{QX*Q*[HA]_{blood}\}_i) - BW*KELH*[HA]_{blood}}{BW*FBLV}\right] \quad \text{(A.8)}$$

Urinary capture of BA and HA (mg/hr):

$$\frac{d[BA]_{urine}}{dt} = BW*KELB*[BA]_{blood} \quad \text{(A.9)}$$

$$\frac{d[HA]_{urine}}{dt} = BW*KELH*[HA]_{blood} \quad \text{(A.10)}$$

Equation List B: Equations and parameters governing precursor PBPK models

Liver BAc concentration over time (mg/L/hr):

$$\frac{d[BAc]_{liver}}{dt} =$$

$$\left[\frac{\left(DoseInput*KAbAc*BW^{0.25} + (QL*Q*[BAc]_{blood}) - (QL*Q*[BAc]_{liver}) - \left(BW^{0.75}*Vmax1*\frac{[BAc]_{liver}}{Km1+[BAc]_{liver}}\right)\right)}{BW*FLV}\right] \quad \text{(B.1)}$$

Plasma BAc concentration over time (mg/L/hr):

$$\frac{d[BAc]_{blood}}{dt} =$$

$$\left[\frac{\left((QL*Q*[BAc]_{liver}) + \left((1-\text{FLV})*Q*[BAc]_{body}\right) - (QL*Q*[BAc]_{blood}) - \left((1-\text{FLV})*Q*[BAc]_{blood}\right)\right)}{BW*FBLV}\right] \quad \text{(B.2)}$$

Body remainder BAc concentration over time (mg/L/hr):

$$\frac{d[BAc]_{body}}{dt} = \left[\frac{\left((1-\text{FLV})*Q*[BAc]_{blood}\right) - \left((1-\text{FLV})*Q*[BAc]_{body}\right)}{BW*(1-FLV-FBLV)}\right] \quad \text{(B.3)}$$

Liver BAlc concentration over time (mg/L/hr):

$$\frac{d[BAlc]_{liver}}{dt} = \left[\begin{array}{l}\left(X_{BAcBAlc}*BW^{0.75}*Vmax1*\frac{[BAc]_{liver}}{Km1+[BAc]_{liver}}\right) + DoseInput*KAbAlc*BW^{0.25} + \\ \frac{(QL*Q*[BAlc]_{blood}) - (QL*Q*[BAlc]_{liver}) - \left(BW^{0.75}*Vmax2*\frac{[BAlc]_{liver}}{Km2+[BAlc]_{liver}}\right)}{BW*FLV}\end{array}\right] \quad \text{(B.4)}$$

Plasma BAlc concentration over time (mg/L/hr):

$$\frac{d[BAlc]_{blood}}{dt} = \left[\frac{\begin{pmatrix}(QL*Q*[BAlc]_{liver})+\left((1-\mathrm{FLV})*Q*[BAlc]_{body}\right)-(QL*Q*[BAlc]_{blood})\\ -\left((1-\mathrm{FLV})*Q*\,[BAlc]_{blood}\right)-(BW*KELAlc*[BAlc]_{blood})\end{pmatrix}}{BW*FBLV}\right] \quad \text{(B.5)}$$

Body remainder BAlc concentration over time (mg/L/hr):

$$\frac{d[BAlc]_{body}}{dt} = \left[\frac{\left(\left((1-\mathrm{FLV})*Q*\,[BAlc]_{blood}\right)-\left((1-\mathrm{FLV})*Q*[BAlc]_{body}\right)\right)}{BW*(1-FLV-FBLV)}\right] \quad \text{(B.6)}$$

Liver BAld concentration over time (mg/L/hr):

$$\frac{d[BAld]_{liver}}{dt} = \left[\frac{\left(\begin{pmatrix}\left(X_{BAlcBAld}*BW^{0.75}*Vmax2*\frac{[BAlc]_{liver}}{Km2+[BAlc]_{liver}}\right)+\\ \left(QL*Q*[BAld]_{blood}\right)\\ -(QL*Q*[BAld]_{liver})\end{pmatrix}-\left(BW^{0.75}*Vmax3*\frac{[BAld]_{liver}}{Km3+[BAld]_{liver}}\right)\right)}{BW*FLV}\right] \quad \text{(B.7)}$$

Plasma BAld concentration over time (mg/L/hr):

$$\frac{d[BAld]_{blood}}{dt} = \left[\frac{\begin{pmatrix}(QL*Q*[BAld]_{liver})+\left((1-\mathrm{FLV})*Q*[BAld]_{body}\right)-(QL*Q*[BAld]_{blood})\\ -\left((1-\mathrm{FLV})*Q*\,[BAld]_{blood}\right)-BW*KELBMA*[BAld]_{blood}\end{pmatrix}}{BW*FBLV}\right] \quad \text{(B.8)}$$

Body remainder BAld concentration over time (mg/L/hr):

$$\frac{d[BAld]_{body}}{dt} = \left[\frac{\left(\left((1-\mathrm{FLV})*Q*\,[BAld]_{blood}\right)-\left((1-\mathrm{FLV})*Q*[BAld]_{body}\right)\right)}{BW*(1-FLV-FBLV)}\right] \quad \text{(B.9)}$$

Urinary capture of BAlc and benzylmercapturic acid (BMA) (mg/hr):

$$\frac{d[BAlc]_{urine}}{dt} = BW * KELAlc * [BAlc]_{blood} \quad \text{(B.10)}$$

$$\frac{d[BMA]_{urine}}{dt} = X_{BAldBMA} * BW * KELBMA * [BAld]_{blood} \quad \text{(B.11)}$$

Modified liver BA concentration over time including new input (mg/L/hr):

$$\frac{d[BA]_{liver}}{dt} = \left[\frac{\begin{matrix} DoseInput*KAb*BW^{0.25}+(QL*Q*KL_{BA}*[BA]_{blood})-(QL*Q*[BA]_{liver}) \\ -BW^{0.75}*Vmax\left(\frac{[BA]_{liver}}{[BA]_{liver}+Km}\right)+\left(X_{BAldBA}*BW^{0.75}*Vmax3*\frac{[BAld]_{liver}}{Km3+[BAld]_{liver}}\right) \end{matrix}}{BW*FLV}\right] \quad \text{(B.12)}$$

Precursor segment parameters:

$BAc\ to\ BAlc\ conversion,\ X_{BAcBAlc} = 0.72\frac{mg\ of\ BAlc}{mg\ of\ BAc}$

$BAlc\ to\ BAld\ conversion,\ X_{BAlcBAld} = 0.98\frac{mg\ of\ BAld}{mg\ of\ BAlc}$

$BAld\ to\ BA\ conversion,\ X_{BAldBA} = 1.15\frac{mg\ of\ BA}{mg\ of\ BAld}$

$BAld\ to\ BMA\ conversion,\ X_{BAldBMA} = 2.39\frac{mg\ of\ BMA}{mg\ of\ BAld}$

$Vmax\ (BAc\ to\ BAlc),\ Vmax1 = 198.0\frac{mg}{hr*kg_{BW}^{0.75}}$

$Km\ (BAc\ to\ BAlc), Km1 = 15\frac{mg}{L}$

$Vmax\ (BAlc\ to\ BAld),\ Vmax2 = 198.0\frac{mg}{hr*kg_{BW}^{0.75}}$

$Km\ (BAlc\ to\ BAld), Km2 = 10\frac{mg}{L}$

$Vmax\ (BAld\ to\ BA),\ Vmax3 = 141.4\frac{mg}{hr*kg_{BW}^{0.75}}$

$Km\ (BAld\ to\ BA), Km3 = 15\frac{mg}{L}$

$BAc\ oral\ absorption\ constant,\ KAbAc = \frac{0.707}{kg_{BW}^{0.25}*hr}$

$BAlc\ oral\ absorption\ constant,\ KAbAlc = \frac{0.141}{kg_{BW}^{0.25}*hr}$

$BAlc\ urinary\ elimination\ constant,\ KELAlc = \frac{0.02\ L}{kg_{BW}*hr}$

$BMA\ urinary\ elimination\ constant,\ KELBMA = \frac{0.80\ L}{kg_{BW}*hr}$

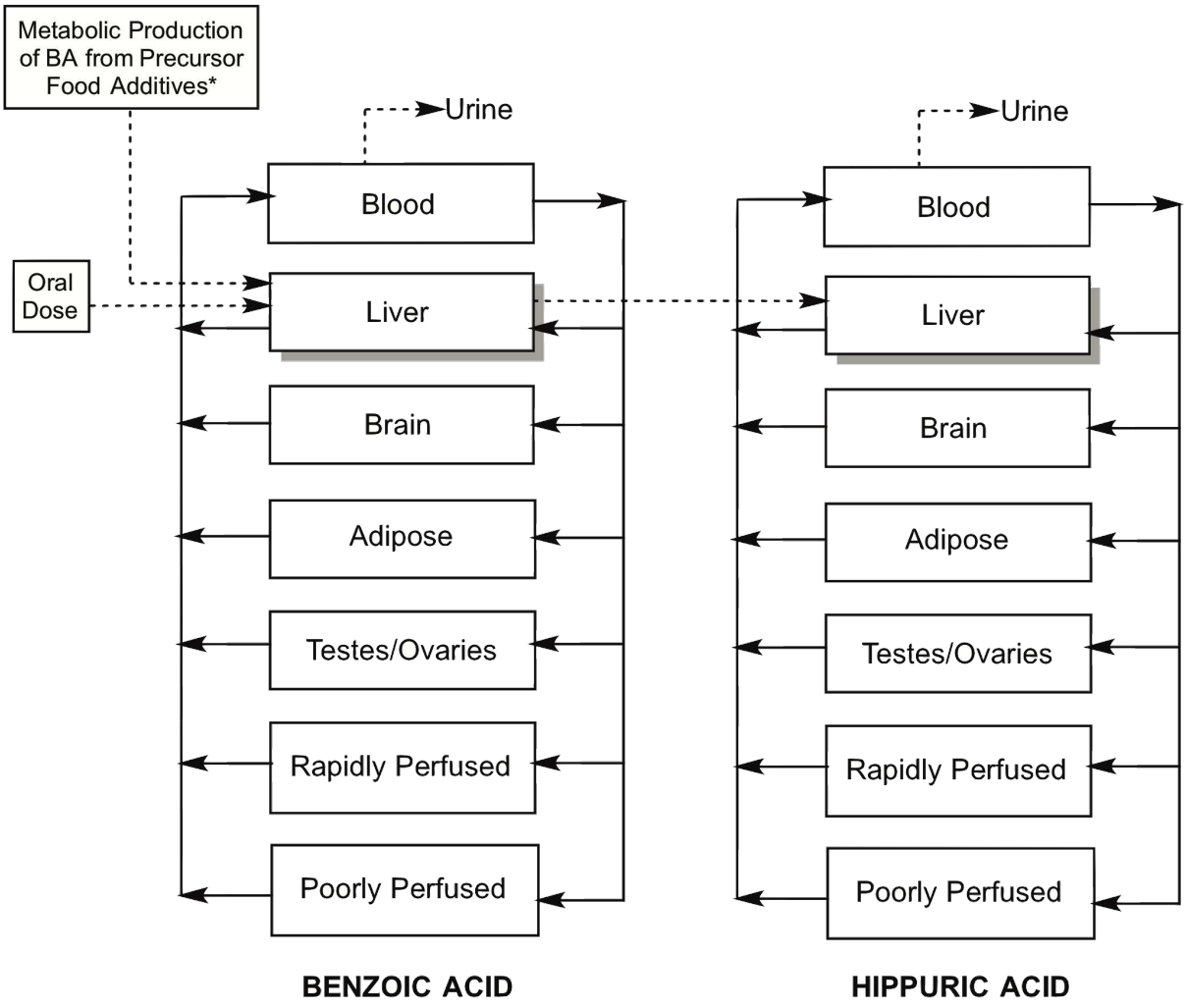

FIGURE 2.1

Schematic of the PBPK models for benzoic acid and its primary metabolite hippuric acid. Dashed lines represent dosing inputs, metabolic processes or urinary excretion. Additional dietary exposures were used to determine metabolism-dependent benzoic acid equivalency in diet and are represented here by a single input pathway; however, the determination of such inputs is based on simpler PBPK inputs, as discussed and listed later on in Equation List B.

Model parameters have been categorically organized and tabulated for rats, guinea pigs, and humans (Table 2.1), where the only assumed and fixed parameter is body weight (*BW*). Rat weight in this model is assumed to be 0.25 kg, guinea pig weight is assumed to be 0.50 kg, and human weight is assumed to be 60 kg. Organization of parameters pertain to weight-dependent compartment volumes (*FXV*), chemical- and tissue-specific partition coefficients (*KX*), weight-dependent cardiac outputs (*Q*), tissue-specific blood flows as a fraction of total cardiac output (*QX*), first-order absorption and elimination constants (*KAb*, *KELB*, *KELH*), and Michaelian metabolic parameters for the critical enzymatic conjugation of BA to form HA (*VMAX*, *KM*). Generally, BA tissue concentration follows the most basic equation construct seen in the beginning of Equation List A (Eq. A.1) and displayed here:

$$\frac{d[BA]_X}{dt} = \left[\frac{\left(QX * Q * [BA]_{blood} - \frac{QX * Q * [BA]_X}{KX_{BA}}\right)}{BW * FXV}\right]$$

where *X* denotes the tissue or compartment of interest. In Table 2.1 and in Appendices A and B, liver parameters are denoted with the use of *L*, brain with *BR*, adipose tissue with *A*, highly-perfused with *HP*, poorly-perfused with *PP*, gonads with *G*, and blood with *BL*. BA concentration in the liver has additional differential components pertaining to oral absorption and metabolic elimination, as seen in Eq. A.4.

TABLE 2.1

Table 2.1. Parameters of the PBPK model as they are seen within each species of interest.

Physiological Parameters	**Symbol**	**Rat Value**	**Guinea Pig Value**	**Human Value**
Body weight (kg)	*BW*	0.25	0.50	60
Tissue Volumes (fraction of BW)				
Fraction of liver volume	*FLV*	0.034[a]	0.038[d]	0.026[a]
Fraction of adipose volume	*FAV*	0.07[a]	0.014[d]	0.21[a]
Fraction of HP tissue volume	*FHPV*	(0.25 – *FBRV* – *FLV*)[c]	0.054[d]	(0.25 – *FBRV* – *FLV*)[c]
Fraction of PP tissue volume	*FPPV*	1 – *Sum of other values*	1 – *Sum of other values*	1 – *Sum of other values*
Fraction of gonadal volume	*FGV*	0.0063[c]	0.0063[f]	0.00048[b]
Fraction of brain volume	*FBRV*	0.006[a]	0.0044[e]	0.02[a]
Fraction of blood volume	*FBLV*	0.074[a]	0.054[d]	0.079[a]
Chemical- and Tissue-Specific Partition Coefficients				
Octanol-water partition coefficient for BA	*KowBA*	74.13	74.13	74.13
Octanol-water partition coefficient for HA	*KowHA*	2.04	2.04	2.04
Liver to blood partition coefficient (BA/HA)	*KL*	0.925[g] / 0.604[g]	0.925[f] / 0.604[f]	0.915[g] / 0.608[g]
Adipose to blood partition coefficient (BA/HA)	*KA*	0.984[g] / 0.650[g]	0.984[f] / 0.650[f]	0.981[g] / 0.683[g]
HP tissue to blood partition coefficient (BA/HA)	*KHP*	0.500[k] / 0.650[g]	0.300[k] / 0.650[f]	0.187[k] / 0.655[g]
PP tissue to blood partition coefficient (BA/HA)	*KPP*	0.300[k] / 0.760[g]	0.150[k] / 0.760[f]	0.095[k] / 0.763[g]
Gonad to blood partition coefficient (BA/HA)	*KG*	0.877[g] / 0.578[g]	0.877[f] / 0.578[f]	0.862[g] / 0.582[g]
Brain to blood partition coefficient (BA/HA)	*KBR*	1[g] / 1[g]	1[f] / 1[f]	1[g] / 1[g]
Tissue Blood Flows (fraction of Q)				
Cardiac output (L hr^{-1})	*Q*	6.7[c]	8.82[e]	322.8[c]
Fraction of liver blood flow	*QL*	0.174[c]	0.18[d]	0.25[c]
Fraction of adipose blood flow	*QA*	0.07[c]	0.007[d]	0.05[c]
Fraction of highly perfused blood flow	*QHP*	1 – *Sum of other values*	1 – *Sum of other values*	1 – *Sum of other values*
Fraction of poorly perfused blood flow	*QPP*	0.19[c]	0.26[d]	0.19[c]
Fraction of gonadal blood flow	*QG*	0.0005[c]	0.0005[f]	0.0012[c]
Fraction of brain blood flow	*QBR*	0.02[c]	0.019[e]	0.114[c]
Absorption, Clearance and Metabolic Parameters				
Maximum velocity, BA to HA (mg hr^{-1} $kg_{BW}^{-0.75}$)	*Vmax*	57.24[h]	8.45[i]	59.14[j]
Michaelian constant for BA to HA (mg L^{-1})	*Km*	29.04[h]	54.99[i]	2.5[j]
BA urinary excretion constant (L hr^{-1} kg_{BW}^{-1})	*KELB*	0.004[k]	0.0001[k]	0.0000833[k]
HA urinary excretion constant (L hr^{-1} kg_{BW}^{-1})	*KELH*	2.548[k]	0.1114[k]	1[k]
Oral absorption constant (hr^{-1} $kg_{BW}^{-0.25}$)	*KAb*	0.898[k]	0.898[f]	0.898[k]

[a] Brown *et al*. [83]. [b] ICRP [84]. [c] Campbell *et al*. [81]. [d] Sweeney *et al*. [85]. [e] Langenberg *et al*. [86]. [f] Set equal to rat parameter. [g] Calculated using data and algorithms derived by Haddad *et al*. [87] and Schmitt [88]. [h] Adapted from metabolic data from Gregus *et al*. [92]. [i] Adapted from metabolic data generated by Macpherson *et al*. [91]. [j] Adapted from metabolic data generated by Kubota and Ishizaki [89]. [k] Calibrated to fit experimental data. HP, Highly perfused. PP, Poorly perfused.

Parameter sources, calculations and optimizations

Sources for each of the physiological and biochemical parameters are identified in Table 2.1, consisting of previously reported values in the literature, calculated estimates, or simulation-based parameter optimizations. Fractional tissue volumes for each species have been gathered from previous studies [81, 83–86] and were implemented in the analysis described here.

Chemical- and tissue-specific partition coefficients have been estimated using the octanol-water partition coefficient and physicochemical properties for each chemical, along with lipid composition data and algorithms derived by Haddad and colleagues [87] and Schmitt [88]. These calculations yielded a tissue-to-blood partitioning value, which was then converted to a fractional value (i.e. percentage of chemical transiently retained) for the differential equations that represent blood flow from tissue.

For the parameters of interest that determine absorption rates, metabolic rates, and urinary elimination rates, the most functional and usable pharmacokinetic datasets available have been taken into account to produce robust and biologically-sound model components. Such experimental datasets include quantitative plasma concentrations and excreted dose values of BA and HA in each species. Human metabolic constants were all systematically optimized to quantitatively match the pharmacokinetic profile reported by Kubota and Ishizaki [89] at 3 different oral dosing schemes (40, 80, or 160 mg/kg(bw) single oral dose); the resulting excretion percentage fell well within the same order when compared to radiolabeled human data [90]. Hairless guinea pig metabolic constants were all systematically optimized to quantitatively match the pharmacokinetic profile reported by Macpherson *et al*. [91] using a dermal exposure condition previously

determined by a single rate equation; these values quantitatively fell well within the same range when compared to the unscaled experimental liver homogenate and slice data of the same study. Rat metabolic constants were all systematically optimized to quantitatively match the pharmacokinetic profile reported by Gregus *et al*. [92] at an intravenous exposure scenario (122 mg/kg(bw)); the resulting excretion percentage fell well within the same order when compared to radiolabeled data in rats [93]. The resulting model performances of each species after optimizations were validated by urinary elimination data collected from Bridges *et al*. [78]. Each calibration experiment within the simulation software consisted of 50,000 iterations to determine the set of values that produce the best possible fit of the experimental data, determined by the objective of the lowest collective difference.

To determine the relevant PBPK parameters for the benzoate precursor segment of the model, optimization experiments were also performed and were validated by measured internal exposure values of the same scenarios [94, 95]. Each precursor compound was represented by a 3-compartment model (i.e. blood, liver, and body remainder) and were stoichiometrically connected in the appropriate sequence by hepatic metabolism flow rates. The parameters that have been systematically optimized via the AnyLogic calibration tool (50,000 iterations) and selected for precursor pharmacokinetics have been directly inserted into Appendix B, as they are simpler yet analogous to the differential structures implemented in the full BA and HA models.

Repeated dosing schemes and dietary exposure scenarios

To evaluate a realistic, albeit liberal, range of dietary exposure scenarios, the model was designed to include not only BA intake, but precursor intake as well (Fig. 2.1). This included the intake of benzyl acetate and benzyl alcohol, as each of these are fairly common flavoring agents and food additives that are regulated by the same intake limit as BA. In addition, benzaldehyde was implemented here as an intermediate metabolite, as it is also approved for use as a food additive. However, due to the extremely low internal exposures predicted for benzaldehyde, it was not implemented here as a substantial, direct source of dietary BA exposure. To use the model for dietary intake assumptions and internal BA exposure estimates, seven different dosing schemes have been implemented over a 15-hour daily intake period, consisting of different additive combinations and amounts that meet or exceed the set ADI values. Specific precursor intake estimates were not readily available, and therefore the simulation schemes assumed values both below and above the ADI for these compounds. The combinations that comprise these different schemes are displayed in Table 2.2.

TABLE 2.2

Table 2.2. Combination dosing schemes employed in the simulated dietary exposure assessment.

Treatment group	5 mg/kg/day BA[†]	5 mg/kg/day BA[‡]	10 mg/kg/day BA[‡]	15 mg/kg/day BA[‡]	3 mg/kg/day BAc[§]	3 mg/kg/day BAlc[§]	10 mg/kg/day BAc[§]	10 mg/kg/day BAlc[§]
Diet (1)	X				X			
Diet (2)	X				X	X		
Diet (3)	X	X						
Diet (4)	X		X					
Diet (5)	X		X		X	X		
Diet (6)	X		X				X	X
Diet (7)	X			X			X	X

[†] Administered continuously (150 fractional exposures) over a 15-hour intake period.

[‡] Administered in 10 fractional exposures over a 15-hour intake period.

[§] Administered in 6 fractional exposures over a 15-hour intake period.

BAc, benzyl acetate. BAlc, benzyl alcohol.

Sensitivity analysis

To determine the quantitative significance of certain parameters within each of the species models, a general sensitivity strategy was used as described previously [96, 97]. Each parameter was individually changed by 1%, and the resulting model outputs, also referred to as response variables, were assessed. This was done for all static parameters within the model, and the change in several response variables (e.g. chemical-specific plasma concentrations, urinary excretion rates) were measured after

steady-state values were reached for 5 mg/kg(bw)/day continuous dosing. Sensitivity coefficients for each scenario were calculated as follows:

$$SC = \left(\frac{\partial O_i}{\partial P_j}\right) \times \left(\frac{P_j}{O_i}\right) = \left(\frac{\partial O_i}{O_i}\right) \times 100$$

where *SC* represents the normalized sensitivity coefficient, O_i is the model output value, P_j is the value of the parameter of interest, and ∂ represents the partial derivative of either the parameter value or measured PBPK output. When |SC| ≥ 1.0000, i.e. when the proportional change in the response variable is greater than the proportional change in the parameter, the parameter is deemed sensitive over the respective output.

2.1.3 Pharmacokinetic results

Model performance and initial species comparisons

The PBPK models were curated and optimized to produce predictions that closely followed experimental data for all species surveyed. For humans, datasets were collected consisting of BA and HA plasma concentrations after single oral BA doses of 40, 80, and 160 mg/kg(bw) [89]. The resulting predictions and experimental points are overlaid in Fig. 2.2 for a 12-hour period. The model constructs were optimized to produce the lowest objective difference from the average data points of the experimental results after a 160 mg/kg(bw) dosing scheme. While the human PBPK model slightly over-predicted the early BA concentrations in plasma following the highest dose (160 mg/kg(bw)), the values fell well within the corresponding experimental uncertainty. Predictive time-course plasma concentrations of BA and HA for the alternative schemes (40 and 80 mg/kg(bw) doses) were produced post-

optimization and matched experimental data well. A PBPK model was tailored for guinea pigs as well, as existing experimental data were captured over a 24-hour period after dermal exposure to BA in hairless guinea pigs [91]. The guinea pig model predicted plasma BA and HA concentrations that matched experimental data after a 40 $\mu g/cm^2$ (0.0256 mg total dose) skin-patch exposure to BA (Fig. 2.3). A PBPK model was also designed for rats and was validated by experimental data after 1 mmol/kg(bw) intravenous injection of sodium benzoate, equivalent to 122 mg/kg(bw) of BA [92]. Predictive time-course data of BA and HA plasma concentrations were captured over a 4-hour period and were compared to experimental data points (Fig. 2.4). Simulation data produced a very low cumulative difference objective compared to experimental data points, which displayed very low uncertainty.

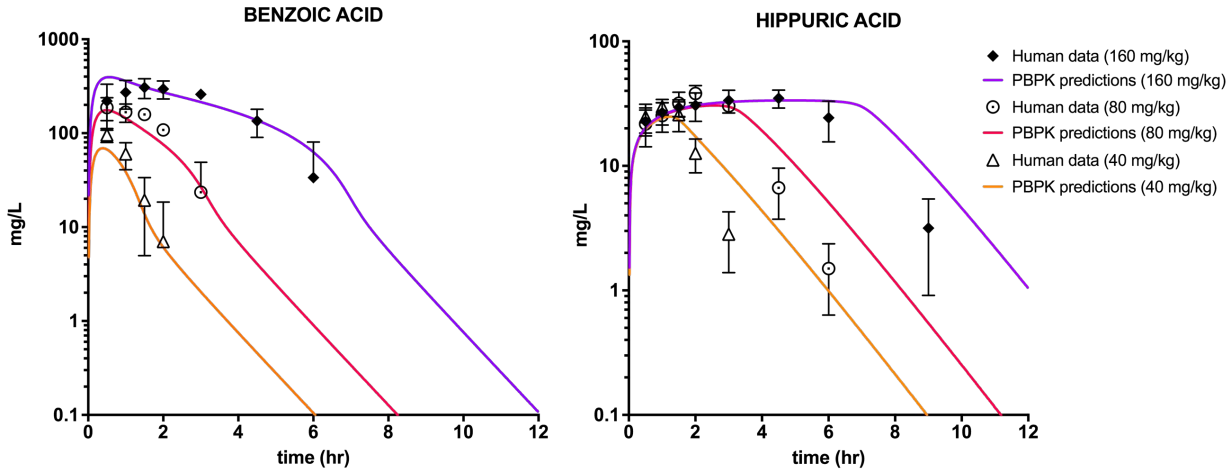

FIGURE 2.2

Simulation data closely matched experimental data for oral dosing of benzoic acid in humans. PBPK models were employed to assess plasma concentrations of benzoic acid (left panel) and hippuric acid (right panel) after single oral doses of BA: 40, 80, and 160 mg/kg(bw). Experimental data for the same metrics were collected and converted from Kubota and Ishizaki (n = 6) [89].

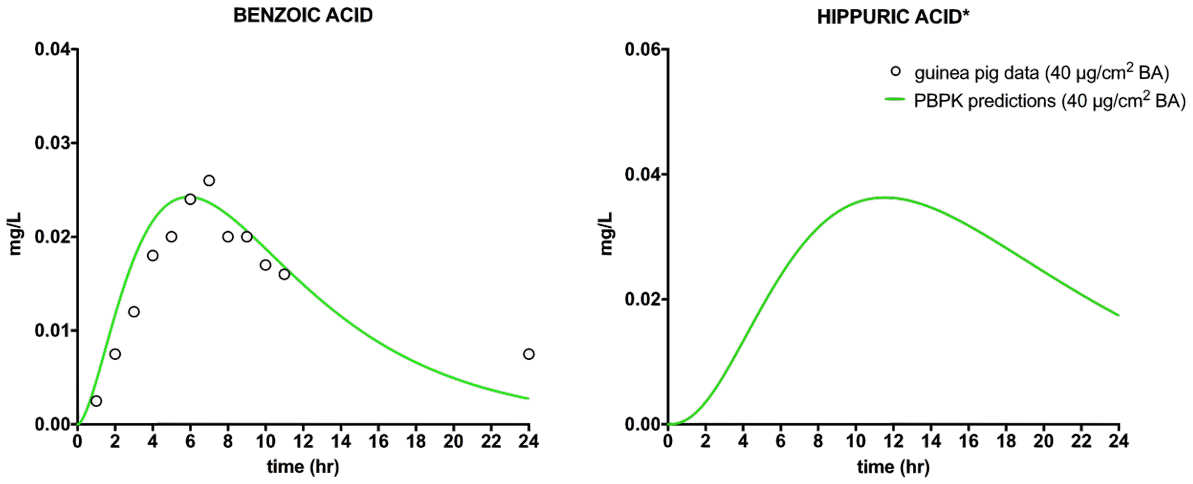

FIGURE 2.3

Simulation data closely matched experimental data for dermal exposure to benzoic acid in guinea pigs. PBPK models were employed to assess plasma concentrations of benzoic acid (left panel) and hippuric acid (right panel) after a 40 µg/cm^2 skin-patch exposure to benzoic acid. Dermal absorption kinetics used here were adapted from the mathematical descriptions elucidated by Macpherson *et al*. [91], and experimental data for benzoic acid plasma concentration were collected and converted from the same study. *Experimental time-course data for hippuric acid plasma concentration were not available from the guinea pig studies.

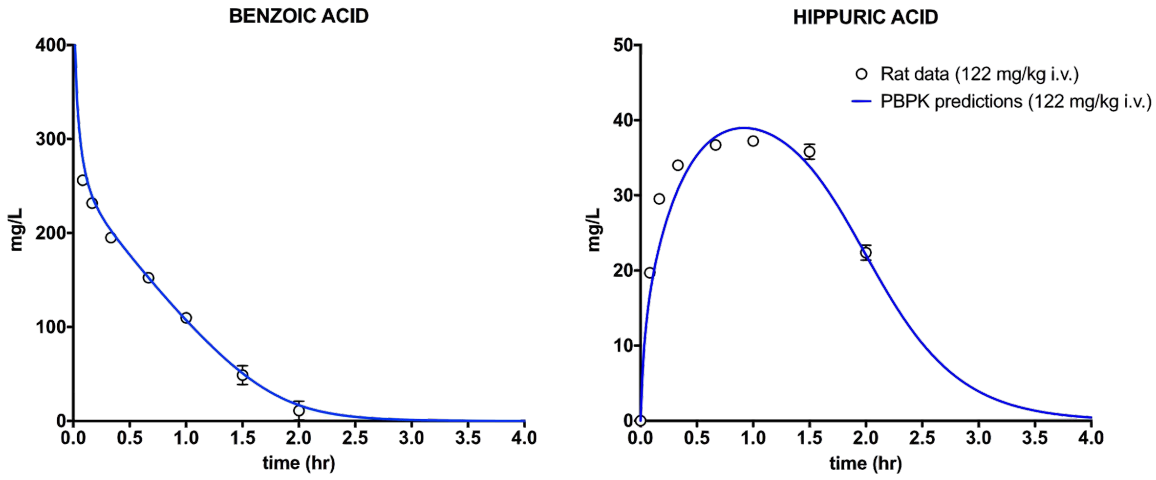

FIGURE 2.4

Simulation data closely matched experimental data for intravenous dosing of benzoic acid in rats. PBPK models were employed to assess plasma concentrations of benzoic acid (left panel) and hippuric acid (right panel) after a single 122 mg/kg(bw) i.v. dose of benzoic acid. Experimental data for the same metrics were collected and converted from Gregus *et al*. (n = 5–8) [92].

After optimizing and validating all species-specific PBPK models, they were used to assess excretion rates over a 24-hour period after a single oral BA dose of 5 mg/kg(bw) (Fig. 2.5A). As an initial comparison, human and rat excretion profiles presented significant similarities, whereas the guinea pig rates of excretion were markedly slower. As guinea pigs show the same metabolite profile [78], this slower elimination can most likely be ascribed to a lower glycine conjugation capacity. Experimental data generated by Bridges *et al*. [78] were collected, displaying real proportional urinary excretion of BA doses after 24 hours; these data were compared to PBPK model predictions (Fig. 2.5B). Humans and rats were both capable of excreting the entire dose administered, based on their respective recovery percentages in urine after the elapsed time; these results were mirrored by the predictive data generated by the PBPK models. Guinea pigs showed, on average, much slower excretion experimentally, albeit with large variations, and the dose excreted *in silico* was marginally over-predictive but still within the margin of uncertainty.

The PBPK models were used to produce absorption and elimination curves of BA and HA after a single oral dose of 5 mg/kg(bw) in each species (Fig. 2.6A). In accordance with excretion comparisons, humans shared an internal exposure profile more similar to rats than guinea pigs. As another measure of total internal dose, area under the curve (AUC) values were calculated from plasma BA concentrations after a variety of single oral BA bolus doses, 0–20 mg/kg(bw), in both the human and rat models (Fig. 2.6B). These AUC values were strikingly similar across both species, with the lower oral dose scenarios resulting in slightly larger total doses in rats; an opposite but marginal relationship was seen with the higher single oral doses. These

comparisons relate large single oral bolus doses, which are unrealistic for dietary exposure, eliciting the more applicable analysis of fractional daily doses discussed in subsequent sections of this paper.

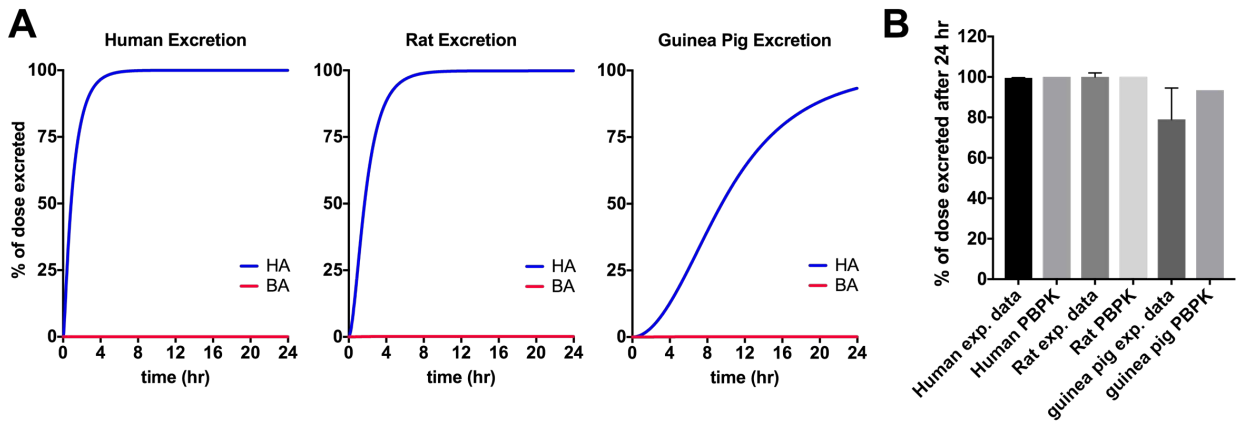

FIGURE 2.5

Assessment of urinary excretion rates following single oral doses of BA in the simulation. **(A)** Time-course comparisons following a single oral bolus of 5 mg/kg(bw) BA in humans, rats, and guinea pigs. **(B)** Experimental and simulation data pertaining to the amount of a single oral dose recovered in urine 24 hr after administration. In both the *in vivo* and *in silico* experiments, humans received 1 mg/kg(bw) BA, rats received 50 mg/kg(bw) BA, and guinea pigs received 49 mg/kg(bw) BA. Experimental data were collected from Bridges *et al*. [78].

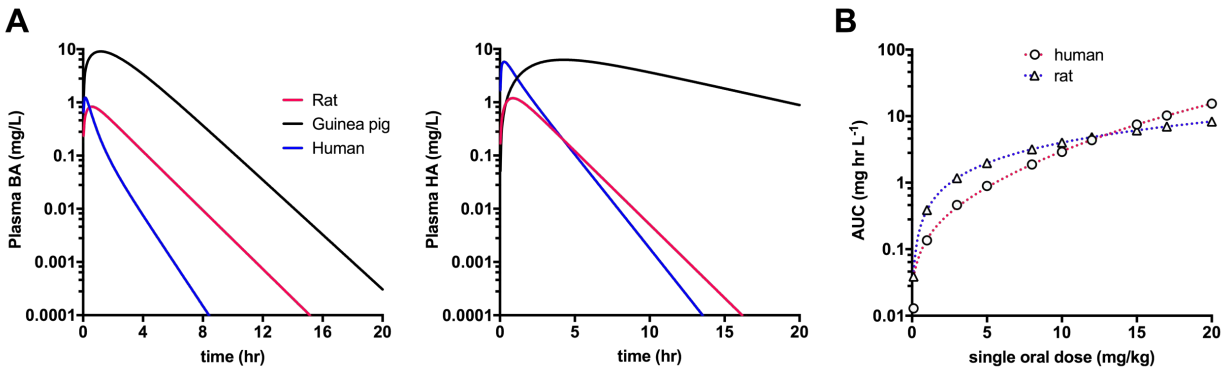

FIGURE 2.6

Use of the PBPK models to perform internal exposure comparisons after a single oral dose in rats, guinea pigs and humans. **(A)** Time-course plasma BA (left panel) and HA (right panel) concentration comparisons after a single oral dose of 5 mg/kg(bw) BA in rats, guinea pigs and humans. **(B)** Resulting plasma AUC values of BA for both rats and humans with increasing single oral doses.

Sensitivity analysis results

A sensitivity analysis was conducted to identify which parameters heavily influenced the specific functional outputs and overall integrity of the model. To do so, each parameter was altered by 1% and the observable changes that occurred were quantified within a slew of model endpoints. These resulting coefficients, using the finite-difference algorithm described previously, were normalized with respect to the original parameter and output values, and those that affected at least one response variable are displayed in Table 2.3. A parameter was determined to have sensitive control over a particular model output if the absolute value of the normalized coefficient was ≥ 1.0000. As expected, BA plasma concentration and urinary excretion rate of BA were the most affected variables from this analysis, controlled primarily by the hepatic metabolic parameters and the corresponding liver partition coefficient that regulates the hepatic concentration of the compound. HA plasma concentration was determined to be most sensitively controlled by the simulation's urinary excretion rate constant. This finding is biologically sound, as the hallmark of this metabolite is its high capacity for renal elimination.

TABLE 2.3

Table 2.3. Normalized sensitivity coefficients (SC) for plasma concentrations and urinary excretion rates under steady-state exposure conditions after continuous oral dose of 5 mg/kg(bw)/day (parameter is sensitive if |SC| ≥ 1). Parameters that elicited significant changes to specific response variables are bolded. Parameters that elicited no detectable variable change in the sensitivity analysis are not shown.

Parameter	**Response variable**							
	Human				**Rat**			
	Plasma concentration		**Urinary excretion rate**		**Plasma concentration**		**Urinary excretion rate**	
	BA	**HA**	**BA**	**HA**	**BA**	**HA**	**BA**	**HA**
Vmax	**-1.0316**	-0.0020	**-1.0459**	0.0031	**-1.0153**	0.0005	**-1.0811**	0.0000
Km	**1.0058**	0.0019	**1.0005**	0.0000	**1.0013**	-0.0005	0.9266	0.0000
KELB	0.0000	0.0000	**1.0005**	0.0000	-0.0023	-0.0014	0.9266	0.0000
KELH	0.0000	**-1.0160**	0.0000	0.0061	0.0000	**-1.0114**	0.0000	0.0000
KAb	-0.0211	-0.0061	0.0000	0.0061	-0.0031	-0.0005	0.0000	0.0000
KL_{BA}	**-1.0293**	0.0000	**-1.0005**	0.0000	**-1.0106**	0.0014	**-1.0039**	0.0000
KA_{BA}	0.0000	0.0000	0.0000	0.0000	0.0008	0.0000	0.0000	0.0000
KHP_{BA}	0.0023	0.0000	0.0000	0.0000	0.0016	0.0000	0.0000	0.0000
KPP_{BA}	0.0000	0.0000	0.0000	0.0000	0.0008	0.0000	0.0000	0.0000
KBR_{BA}	0.0023	0.0000	0.0000	0.0000	0.0000	0.0000	0.0000	0.0000
KL_{HA}	0.0000	0.0004	0.0000	0.0000	0.0000	0.0000	0.0000	0.0000
KHP_{HA}	0.0000	0.0002	0.0000	0.0000	0.0000	0.0005	0.0000	0.0000
KBR_{HA}	0.0000	0.0002	0.0000	0.0000	0.0000	0.0000	0.0000	0.0000

Use of the models to predict biologically relevant internal exposures in rats and humans

To assess internal exposures of BA after relevant exposure scenarios, the rat and human PBPK models were employed in conjunction with repeated and continuous BA dosing schemes. Initial repeated scenarios consisted of 1, 5, 10, 50, and 100 mg/kg(bw)/day (relevant across the ADI range and up to two orders of magnitude similar to the point of departure) and the full daily doses were administered fractionally over a 12-hour exposure period. These time-course data were generated from dose variation experiments within the simulation software and are displayed in Fig. 2.7. Due to relatively faster absorption and elimination rates in humans (top panels), BA and HA did not tend to accumulate internally when compared to rats (bottom panels). Continuous doses were assessed as well for the same daily dosing schemes, assuming smaller intake events and a larger number of fractional exposures occurring over a 15-hour dietary exposure period, surveyed over 3 days (Fig. 2.8). These highly fractional continuous exposure analyses were presumptive in nature, as they do not reflect realistic dietary regimens that would not allow for such maintained accumulation, and they were instead purely employed as a means to determine internal steady-state BA concentrations among rats and humans. Such steady state internal exposures were markedly lower in humans (top panels) than in rats (bottom panels) for all continuous daily doses tested. These steady-state values are enumerated in Table 2.4, and give rise to margin of exposure (MOE) ratios, identifying the multipliers required to extrapolate from rat to human steady-state values. Steady-state BA plasma concentration ranges were 0.0257–2.8002 mg/L and 0.0084–1.2209 mg/L for rats and humans, respectively. MOE ratio values ranged from 0.3268 to 0.4360 across the wide

variety of continuous dosing schemes tested. As these multipliers all fall below a 1:1 ratio, it is clear from a steady-state perspective that BA is cleared more quickly in humans than in rats, and is thus less bioavailable.

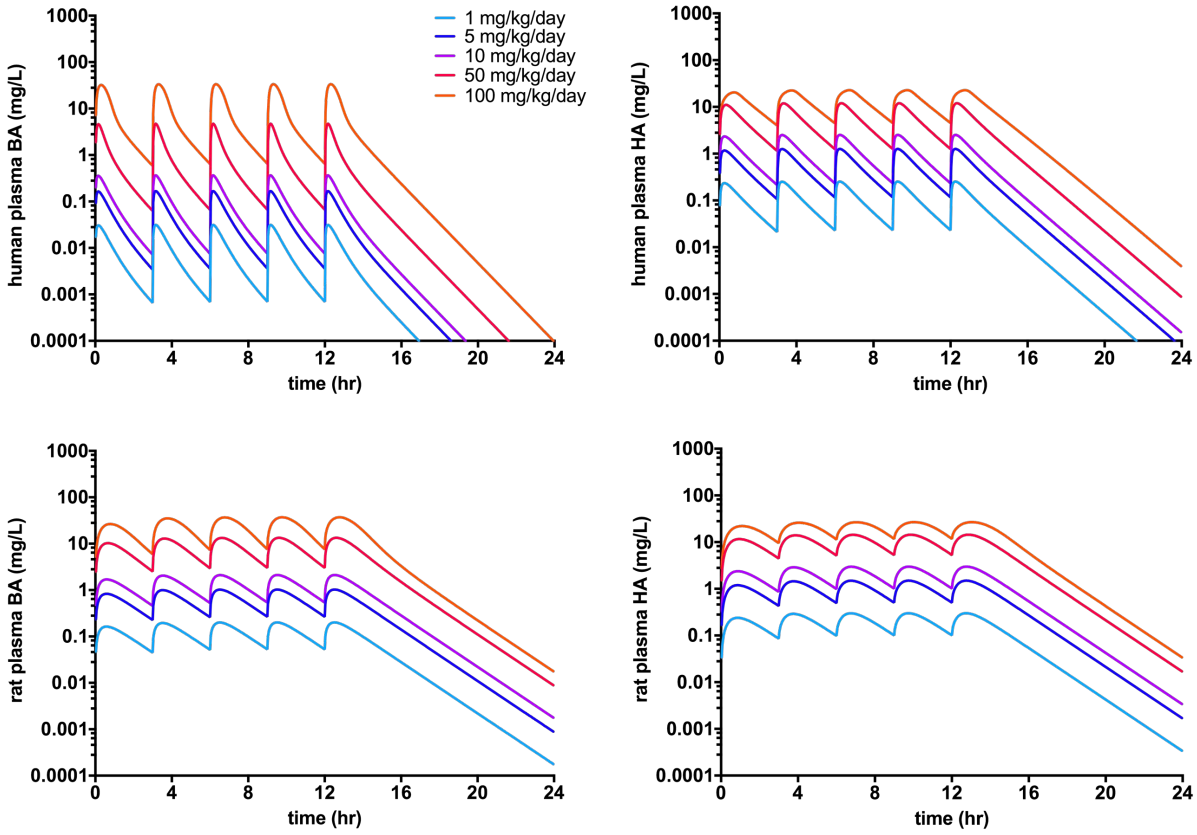

FIGURE 2.7

Full oral doses were split into 5 fractional exposures over a liberal 12-hour exposure period during each day in the simulation. Dosing regimens were 1, 5, 10, 50, and 100 mg/kg(bw)/day, which were assessed for 24 hr in both rats (bottom panels) and humans (top panels). Both plasma BA concentrations (left panels) and plasma HA concentrations (right panels) were captured and assessed for each regimen in each species.

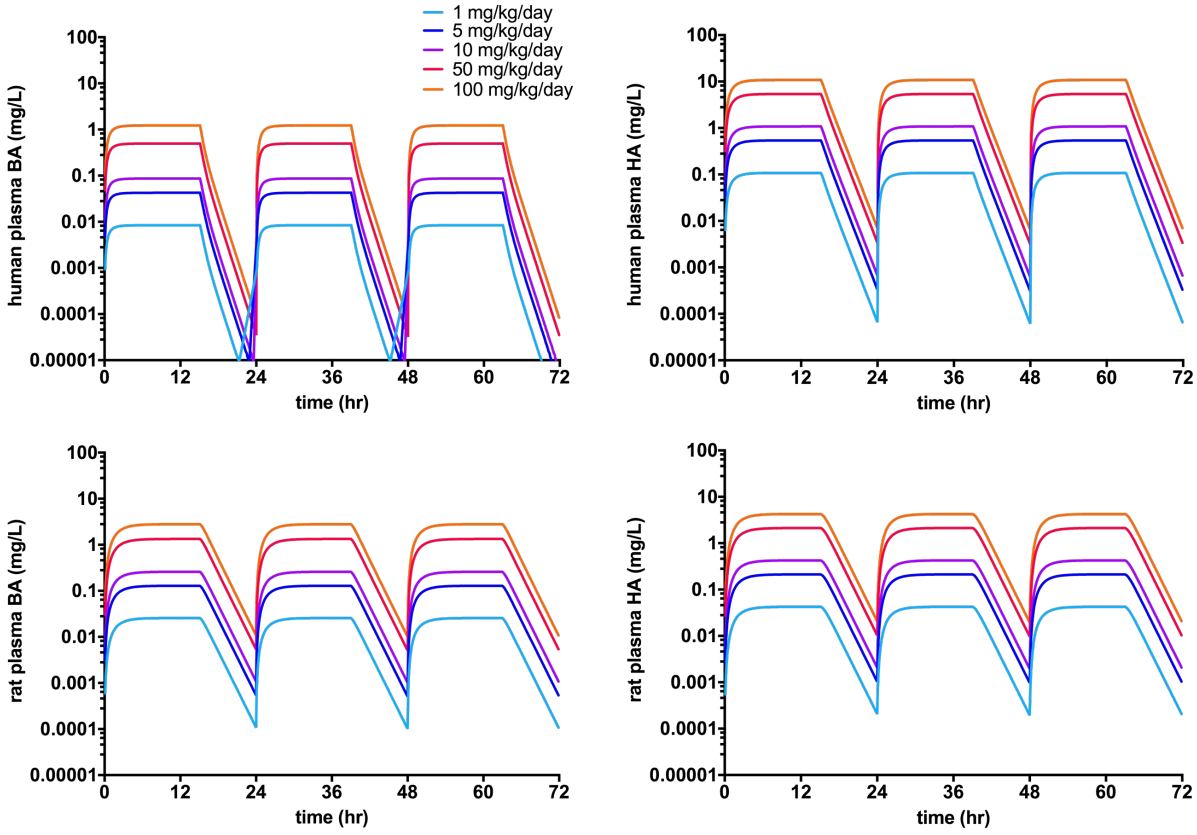

FIGURE 2.8

Fractional exposures of the daily BA dose were administered orally every 0.1 hr over a liberal 15-hour dietary intake period during each day in the simulation. Dosing regimens were 1, 5, 10, 50, and 100 mg/kg(bw)/day, which were assessed for 3 days in both rats (bottom panels) and humans (top panels). Both plasma BA concentrations (left panels) and plasma HA concentrations (right panels) were captured and assessed for each regimen in each species.

TABLE 2.4

Table 2.4. Steady-state plasma concentrations of BA and HA after simulated continuous oral exposures of BA.

Simulated continuous dietary BA exposure	Rat BA steady-state plasma conc. (mg/L)	Human BA steady-state plasma conc. (mg/L)	Margin of exposure (MOE) ratio[†]
1 mg/kg(bw)/day	0.0257	0.0084	0.3268
5 mg/kg(bw)/day (Current ADI)	0.1288	0.0426	0.3307
10 mg/kg(bw)/day	0.2591	0.0866	0.3342
50 mg/kg(bw)/day	1.3380	0.4962	0.3709
100 mg/kg(bw)/day (⅕ POD)	2.8002	1.2209	0.4360

[†] MOE ratio calculated: predicted human internal dose metric ÷ predicted rat internal dose metric. All values calculated were less than 1, which correlate with lesser internal steady-state exposures in humans.
ADI = acceptable daily intake
POD = point of departure

Dietary intake assumptions for BA and precursor compounds as they relate to internal exposures across rats and humans

Several other food additive compounds amount to BA bioequivalencies due to metabolic processes and thus contribute to the aggregate exposure of BA that humans see in their diet. Such compounds were integrated into the PBPK analysis to view their aggregate effects on interspecies variation. Of these compounds, benzyl acetate, benzyl alcohol and benzaldehyde are some of the most widely used flavoring agents and formulation additives [98]. These additives are all precursors of BA, and are quickly metabolized predominately by liver enzymes after oral exposure. Benzyl acetate is quickly hydrolyzed to produce acetic acid and benzyl alcohol, which is then mainly acted on by alcohol dehydrogenases to produce benzaldehyde. Benzaldehyde is then oxidized further to yield BA (Fig. 2.9). These compounds have similar safety profiles as BA, with benzyl acetate presenting a NOAEL of 550–840 mg/kg(bw)/day [99], benzyl alcohol presenting a NOAEL of 143–500 mg/kg(bw)/day [67], and benzaldehyde presenting a NOAEL of 400–600 mg/kg(bw)/day [100–102]. Because of their similar safety profiles, all of these precursor compounds are governed by the same conservative ADI value of 0–5 mg/kg(bw)/day, which was taken into account in our analysis.

In the development of precursor PBPK inputs, data were collected regarding internal BA concentrations following a single 500 mg/kg(bw) oral dose of benzyl acetate [94]. These data were used to design and optimize the precursor segments of the rat and human models, and the resulting simulation-generated predictions were successful in matching the experimental data (Fig. 2.10A). The precursor PBPK segments were

further validated by urinary excretion analysis, where urinary metabolite data were assessed *in silico* and compared to previous experimental rat data [95] (Fig. 2.10B). Both simulation data and experimental data show that the oral dose administered, 500 mg/kg(bw), was predominately recovered as HA, with small amounts of benzylmercapturic acid as well as trace amounts of benzyl alcohol present.

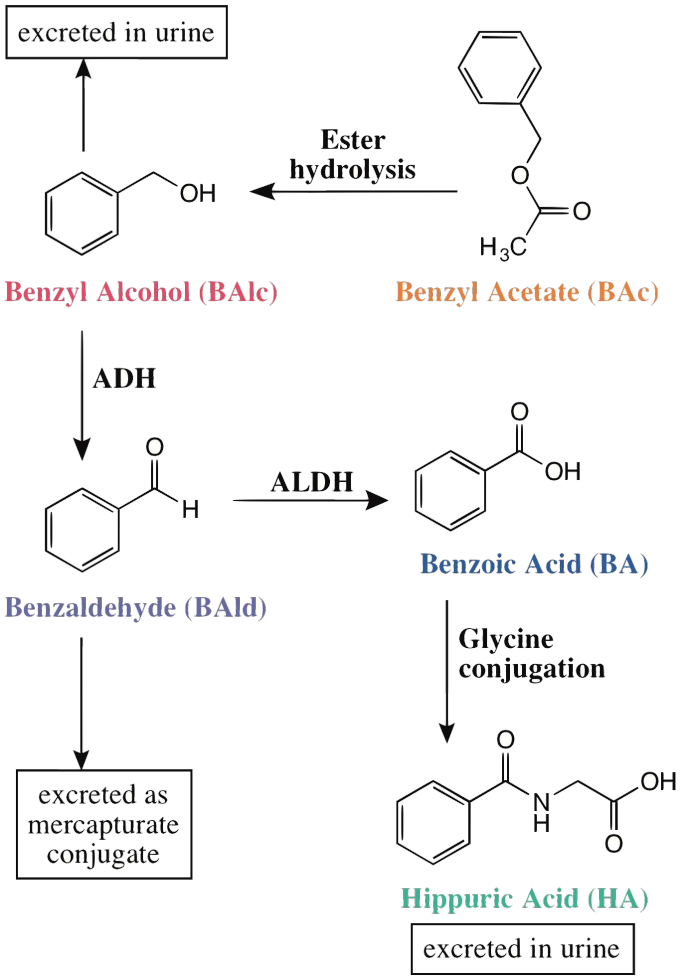

FIGURE 2.9

Metabolism and elimination scheme for benzoic acid and a variety of its precursor compounds used as flavoring agents and food additives. ADH, alcohol dehydrogenase. ALDH, aldehyde dehydrogenase.

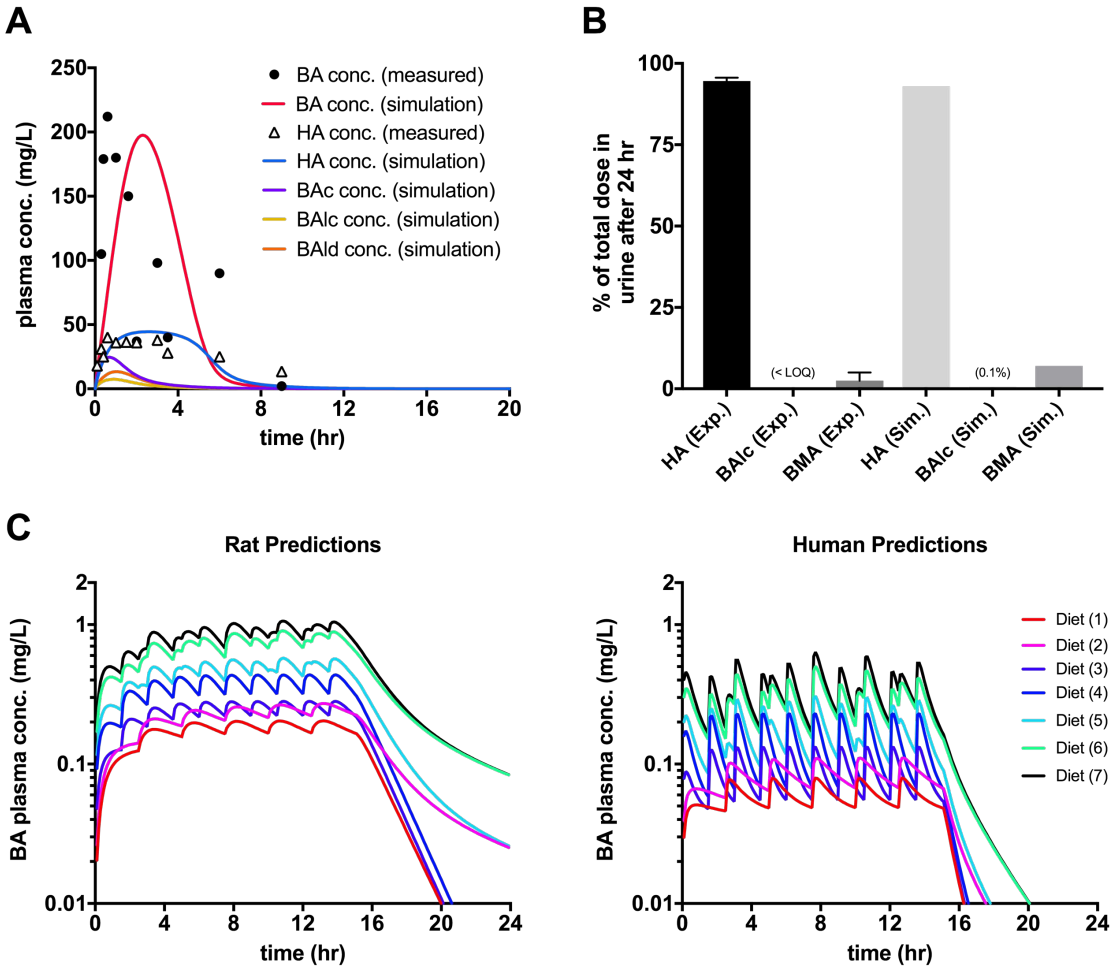

FIGURE 2.10

Internal exposure to BA following various dietary regimens of BA, benzyl acetate (BAc), and benzyl alcohol (BAlc). **(A)** Model prediction of plasma concentrations of BA, HA, BAc, BAlc and benzaldehyde (BAld) following a dose of 500 mg/kg(bw) BAc in rats. Experimental data from the same scenario have been collected from Yuan *et al*. [94] and overlaid to view model performance. Each experimental data point was captured from a different animal in the previous study. **(B)** Urinary metabolites were assessed, *in vivo* [95] and *in silico*, 24 hr after administering a single oral dose of 500 mg/kg(bw) BAc in rats. BMA, benzylmercapturic acid. LOQ, limit of quantification. **(C)** Dietary dosing schemes were assessed in order to determine internal BA exposures in both rats (left) and humans (right). The seven dietary regimens are listed in Table 2.2.

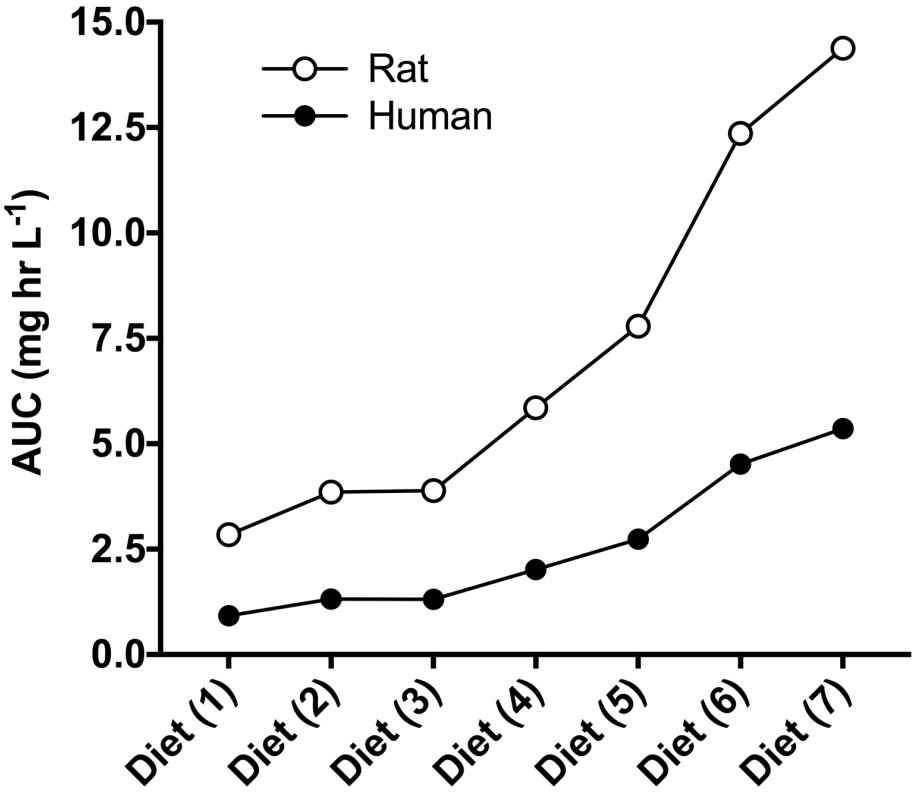

FIGURE 2.11

Plasma BA-based AUC comparisons between rats and humans for different aggregate dietary exposure schemes (1–7), as described in the text. AUC values have been determined from plasma concentrations over the 24-hr periods of exposure, shown in Fig. 2.10C.

After validation of both the primary BA PBPK model and the extended precursor segments, rat and human simulation experiments were performed for a variety of complex repeated dosing schemes. Seven different daily dosing schemes were implemented, as discussed in detail previously, and the results of these analyses over a 24-hour period are displayed in Fig. 2.10C. As with the previous steady-state internal exposure analyses, internal exposures generated here were more greatly retained in rats (left panel) than in humans (right panel). These complex pharmacokinetic curves could not be resolved to a steady-state value due to their sporadic nature, and thus AUC values have been calculated for each of the dietary exposure schemes and are presented in Fig. 2.11. The AUC-based human:rat MOE ratios were calculated to be, in succession for all theoretical diets, 0.325, 0.342, 0.336, 0.345, 0.351, 0.365, and 0.373, indicating much lower relevant exposures in humans.

2.1.4. Discussions and conclusions of pharmacokinetic modeling insights

Discussions of new pharmacokinetic data and impacts on regulatory toxicology

In the development of toxicological risk assessments for environmental contaminants, pharmaceuticals, food additives or other consumer products, a general approach is applied where a point of departure (POD) is determined as the dosage value for safety to be based upon. This value is either (a) the experimental dose value determined to the lowest dose value reported to elicit an adverse response (i.e. the LOAEL value), or (b) the highest possible value reported to elicit no adverse effect at all (i.e. the NOAEL value). This pivotal NOAEL-based POD, often ascertained through relevant experiments in rodent models, is divided by a default 100× factor to conservatively account for uncertainties associated with interspecies extrapolation and

human variability. The World Health Organization (WHO) has characterized the initial subdivisions of this default factor as intraspecies (10×) and interspecies (10×) uncertainty [103]. The standard interspecies uncertainty factor accounts for both pharmacokinetic variations (4×) and toxicodynamics variations (2.5×). All of these factors, combined to form the default 100× uncertainty factor, have been applied to a 500 mg/kg(bw)/day POD for oral BA exposure [71], resulting in a health-based guidance value for the group of benzoic acid, its salts and precursor compounds of 5 mg/kg(bw)/day, assuming full read-across.

A few recent studies using extremely conservative assumptions estimated that certain subpopulations may exceed the allowable ADI for BA [75–77]. In view of these studies, an investigation into the appropriateness of the default uncertainty values used in establishing safety for BA and related compounds is warranted. As a component of this uncertainty reevaluation, we have closely examined the pharmacokinetic landscape of BA and related compounds to reach a more accurate extrapolation factor of total internal doses. At first glance, the BA pharmacokinetic profile of humans was more similar to rats than guinea pigs (Fig. 2.5, Fig. 2.6). This is an important finding considering that all pivotal toxicological experiments with BA and sodium benzoate were performed in rats [68–70], and therefore this comparison is much more valuable in determining interspecies differences with respect to ingredient safety. Upon further interrogation of human and rat pharmacokinetic profiles, the model-generated internal exposures to BA (after repeated, continuous or complex aggregate dietary assumptions) were significantly below the internal exposures seen in rats at the assumed intake estimate dose ranges (Fig. 2.7, Fig. 2.8, Fig. 2.10C). The ranges

analyzed went as low as 1 mg/kg(bw)/day, to dietary mixtures amassing 20 mg/kg(bw)/day BA and 20 mg/kg(bw)/day benzoate precursors, to 100 mg/kg(bw)/day of repeated or continuous administration of BA. Among all analyses in this study, the highest multiplier found to estimate human internal doses from measured rat values was 0.436 (Table 2.4), implicating that humans require at least double the oral dose in rats to see the same magnitude of internal exposure. This higher metabolic clearance seen in humans is likely attributed to higher enzymatic activity, which may be heavily dependent on slight yet significant species differences in hepatic glycine N-acyltransferase expression [104] or on glycine co-factor availability [105].

From these data some conclusions can be drawn with respect to readjusting the level of pharmacokinetic interspecies uncertainty, as researchers have similarly noted in the past for other compounds [106, 107]. As BA is internally distributed in lower quantities in humans than in rats due to significant metabolic and excretion differences, the interspecies 4× uncertainty factor for pharmacokinetic differences can either become a fractional value or can be reduced to 1×. In keeping with the conservative nature of risk assessments, these data support the removal of the interspecies pharmacokinetic uncertainty factor, leaving only factors for toxicodynamic interspecies uncertainty (2.5×) and intraspecies uncertainty (10×).

Reevaluation of default uncertainty factors has been addressed in the past, and others have made recommendations to provide more accurate measures in making regulatory decisions [108]. In particular, pharmacokinetic uncertainties have been refined in the past for specific environmental contaminants and consumer chemicals. The pharmacokinetic landscape of adicarb, a carbamate pesticide, has been

extensively analyzed in the past to view interspecies differences [106]. As a result, researchers found that rats internalized far less adicarb and therefore the factors that govern regulations needed to be far more stringent, concluding that the 4× factor should be replaced with one on the order of 17× or more. This reevaluation approach has been applied to the use of 2-phenoxyethanol and phenoxyacetic acid as well [107], where the researchers generated proportional MOE values that suggest far less exposure in humans, concluding that the 4× factor be eliminated to approach a more accurate extrapolation value from rats to humans.

Pharmacokinetic conclusions

In conclusion, the multimethod simulation approach was extremely successful in predicting pharmacokinetic outcomes for a very relevant issue in regulatory toxicology. The analyses provided here, as seen with other chemical-specific studies, provide support for refinement of default uncertainty factors to reach a more accurate, realistic and adequately protective toxicological health-based guidance value in promoting consumer safety. These analyses were done for relevant dosing schemes that span and exceed the range of intake estimates using liberal dietary assumptions. In addition, the final result of eliminating the pharmacokinetic interspecies uncertainty factor remains adequately conservative, as these data suggest that this factor could even be fractional to generate a more accurate extrapolation. This study adds to the growing body of literature that supports an improvement to the uncertainty paradigm, shifting from an over-reliance on default values to empirically-based PBPK-refined value. Refinement of uncertainty factors is appropriate when supported by data and affords a more targeted risk management approach relative to consumer safety.

2.2 Modeling ultrasensitivity nuances in transcription factor activation

To assess the effectiveness of our multimethod simulation approach on pharmacodynamic quantifications, we conducted a study of an important toxicological and pharmacological query involving the classical aryl hydrocarbon receptor, which is presented here. To view the peer-reviewed research article that accompanies this section, see: *Hoffman et al. (2018) Ultrasensitivity dynamics of diverse aryl hydrocarbon receptor modulators in a hepatoma cell line. Archives of Toxicology.*

2.2.1 The aryl hydrocarbon receptor and its dynamic activation nuances

The aryl hydrocarbon receptor (AhR) is a nuclear receptor known classically for its dioxin-dependent activation and subsequent toxicological effects [109]. The triggered activation of AhR requires the intracellular presence of a high-affinity ligand, many signaling events that allow for its translocation into the nucleus, and additional protein complexes that enable binding to DNA for a wide transcriptional response of mainly drug-metabolizing enzyme genes [110]. Classically-identified ligands for this receptor include a variety of polycyclic aromatic hydrocarbons (PAHs) such as: 2,3,7,8-tetrochlorodibenzo-*p*-dioxin (TCDD) and other members of the dioxin family [109]; 3,3′,4,4′,5-pentachlorobiphenyl (PCB-126) and other polychlorinated biphenyls (PCBs) [111]; and large nonpolar pyrene derivatives such as benzo[a]pyrene (BaP) [112]. The AhR-mediated responses elicited by these ligands are all deleterious in nature and primarily result in immunotoxicity, skin lesions known as chloracne, hepatotoxicity, and various forms of tumor promotion [113, 114].

While early studies focusing on the AhR all provide strong evidence of its toxicological responses, recent studies have reoriented our understanding of this complex receptor and solidified it as a potential therapeutic target in modulating the progression of several inflammatory diseases and cancers [115–118]. As one potential benefit, it has been shown that sustained activation of the AhR by TCDD can suppress the adaptive immune response and reduce *Leishmania major* burdens in mice [119]. While this parasitic resistance is a therapeutic outcome of TCDD exposure, classical toxicological data suggest that exposure to this compound will result in many unintended health hazards and render it unsuitable as a treatment for any infection or disease.

In light of these data, current research has turned to the activation of AhR using more natural endogenous and exogenous ligands. Indole-3-carbinol (13C) is one such exogenous ligand identified in cruciferous vegetables that allows for potent AhR activation upon consumption [120]. This receptor activation is mediated through direct binding as well as through binding of I3C's major metabolite 3,3′-diindolylmethane (DIM) [120–122]. These compounds fall within a class of substituted indoles that predominately originate from dietary sources and all variably activate the AhR [123]. It is known that I3C and related indoles can reduce oxidative stress in cell culture models [124] in addition to regulating carbohydrate metabolism in mouse models [125]. AhR activation by such ligands is critical for preventing the metabolic and genetic dysfunction seen in mammalian metabolic syndrome [126]. As perhaps the most impactful pharmacological aspect of these indole compounds, their activation of the AhR regulates intestinal immune cells and drives a powerfully therapeutic anti-inflammatory

response in the rodent gut [127]. Mice treated with I3C displayed a significant increase in beneficial intraepithelial lymphocytes and a drastic reduction in intestinal inflammation and damage [128]. Several laboratories have further elucidated additional gastrointestinal benefits, showing I3C- and DIM-mediated prevention of intestinal carcinogenesis in mice [129, 130]. These studies have revealed a compelling AhR-based reason to advocate for liberal cruciferous vegetable intake and functional nutrition [131, 132]. Investigators have also identified an endogenously-sourced indole ligand that potently activates the human AhR: 2-(1′H-indole-3′-carbonyl)-thiazole-4-carboxylic acid methyl ester (ITE) [133, 134]. Much like the other indole ligands, ITE has been shown to upregulate specific regulatory T-cells and reduce the intestinal inflammation that drives mammalian colitis in an AhR-dependent manner [135, 136].

Non-classical ligands lacking an indole moiety can also trigger AhR activity [137]. Cannabidiol, derived as a primary cannabinoid constituent from the *Cannabis* plant genus, can potently induce CYP1A1 through AhR-mediated signaling [138]. Natural phenolic compounds such as curcumin have identified AhR activity [139], and many plant-derived tetraterpenoids such as apocarotenal, canthaxanthin and astaxanthin have been identified as AhR agonists as well mainly by their CYP1A1 and CYP1A2 induction [140, 141]. These compounds, while less understood for their AhR modulation than the aforementioned indole compounds, may also provide insight into the differential effects of consumption-based AhR activation.

The AhR is activated by a structurally-diverse spectrum of compounds [137, 142]. The variable response profile of the AhR has been thoroughly reviewed [113; 143], where any given AhR-mediated physiological outcome is highly dependent upon

the ligand that stimulates it. Other receptors have different signaling profiles and thus dichotomous physiological outcomes for a spectrum of agonists as well, which has been extensively documented as “biased agonism” [144]; examples of such receptors are the opioid receptors [145], serotonin 5-HT_{2A} receptor [146], glucagon-like-peptide-1 receptor [147], and the glucocorticoid receptor [148].

While differences in AhR-mediated transcriptional responses have been well-documented between different cell types [149], there are no documented differences in immediate expressional changes within the same cell type by different ligand types [150]. While gene expression profile changes appear to be the similar for AhR ligands, physiological outcomes between TCDD and ITE are vastly different in biological systems like the placenta [151]. Ligand-intrinsic and dose-dependent differences in AhR activity have also been well documented for the fate of differentiating $CD4^+$ T-cells, where different amounts of different AhR ligands will facilitate the production of different sets and quantities of lymphocytic markers [152].

It is assumed that there are a variety of complex factors that allow for different ligands to activate the same receptor and produce dichotomous responses. Such factors may include different direct binding domains on the intracellular receptor, dynamic activation nuances (e.g. via direct binding or indirect phosphorylation events), alterations in metabolic activity, pharmacokinetics of a given ligand, and different intrinsic affinities for the receptor and resulting activation durations. Additionally, receptors and signaling proteins are sometimes rapidly stimulated within a narrow stimulus window, giving rise to ultrasensitive or “switch-like” behavior [45], and indeed we have previously demonstrated that the AhR is activated by the classical ligand PCB-

126 in a variably ultrasensitive manner [46, 47, 153]. Ultrasensitivity dynamics have been unpacked extensively at the molecular level, and the mathematics explaining this phenomenon have been keenly approximated for computational modeling studies [41]. Ultrasensitive response motifs manifest as a result of a variety of molecular processes including cooperative binding, dimerization sequences, and multistep signaling processes [154]. For the AhR, the protein modification and translocation that occurs after ligand binding appears to form the basis of this switch-like activation; however, the rapid activity of this bound complex is highly ligand-dependent.

Because of these observations and in light of recent non-classical ligand experimentation, we hypothesized that the ligand-specific disparity between AhR-mediated responses can be in part explained by the nuances in each ligand's ability to directly bind and ultrasensitively activate this nuclear receptor. To define these nuances, we offer here an experimental approach that integrates a high-throughput single-cell *in vitro* assay and a robust mathematical simulation method to understand the graded and switch-like dynamics of this nuclear receptor activation, and predict the impact of specific exogenous stimuli on this molecular target. The AhR modulators used in this study consist of three classical aryl hydrocarbon ligands and three non-traditional exogenous ligands, displayed in Fig. 2.12.

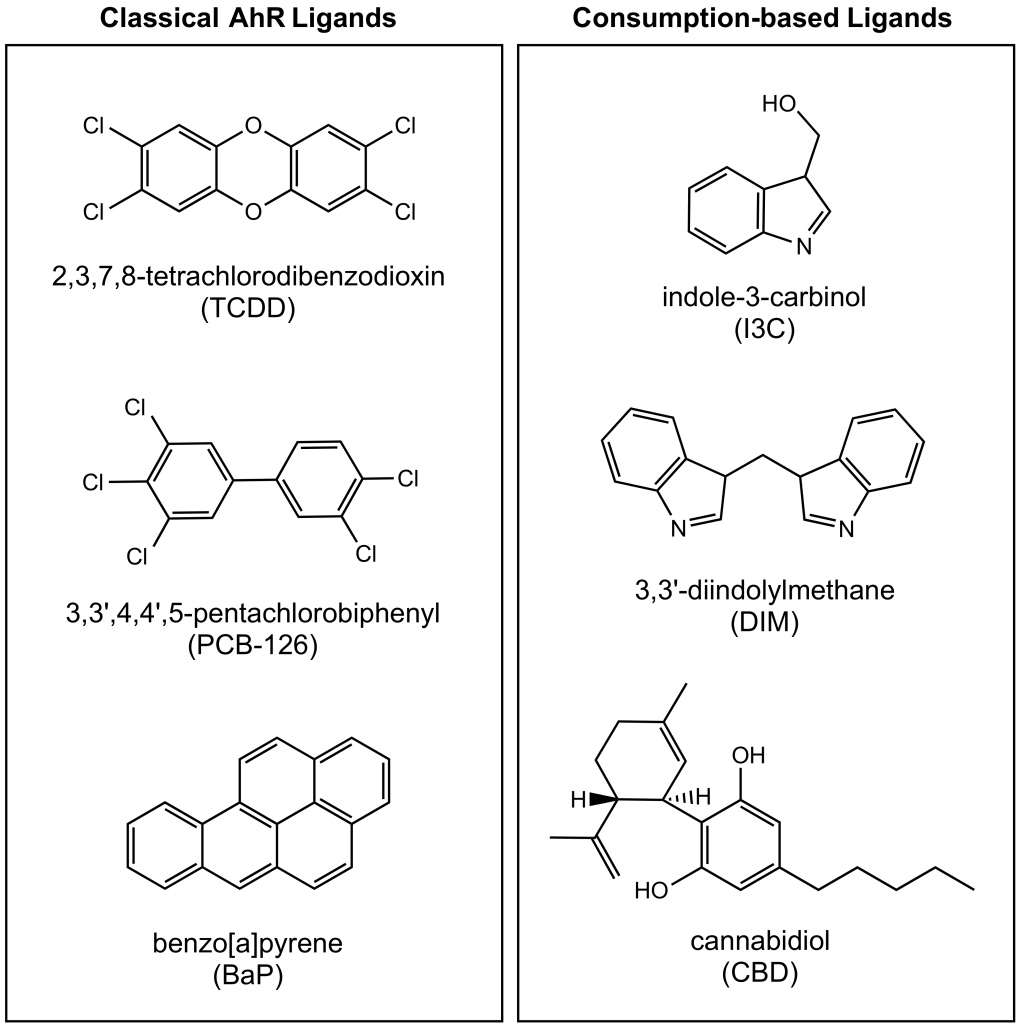

FIGURE 2.12

The chemical structures of the six compounds used in this study that act differentially to modulate AhR activity.

2.2.2 Materials and methods

Chemicals and Reagents

TCDD (≥98% pure) was purchased from Cambridge Isotopes (Andover, MA, USA). PCB-126 (≥99% pure) was obtained from Accustandard (New Haven, CT, USA) and confirmed by GCMS to be pure and free of other congeners. BaP (≥96% pure), I3C (≥96% pure), and DIM (≥98% pure) were purchased from Sigma-Aldrich (St. Louis, MO, USA). CBD (≥99% pure) was purchased from Cerilliant Corporation (Round Rock, TX, USA). For treatments, all compounds were diluted in sterile-filtered DMSO; treatments and vehicle groups contained less than or equal to 0.1% v/v DMSO. Geneticin (G418) used for selective media was obtained from Thermo Fisher Scientific (Waltham, MA, USA).

Cell Culture Model and Flow Cytometry

H1G1.1C3-GFP cells, the generous gift of Dr. Michael Denison at University of California Davis, were used as an AhR reporter line as described previously [155]. Briefly, this is a stably transfected mouse hepatoma (Hepa1c1c7) cell line with an enhanced green fluorescent protein (EGFP) reporter gene linked to the aryl hydrocarbon response element, referred to here as the xenobiotic response element (XRE). Cells were maintained in αMEM containing 10% fetal bovine serum in a humidified environment of 5% CO_2 at 37 °C. Because it was observed by Nagy et al. [155] that these cells require constant selective pressure in order for the EGFP gene to be strongly expressed, cells were placed in selective media (αMEM containing 10%

fetal bovine serum and 968 mg/L G418) 48 hr prior to treatments. Cells were plated into 24-well plates and allowed 24 hr to adhere, where they were subsequently treated for 24 hr with varying doses of each of the 6 treatment compounds. Cells were treated with TCDD (7-point scheme, 10^{-1}–10^{5} pM), PCB-126 (9-point scheme, 10^{-1}–10^{7} pM), BaP (8-point scheme, 10^{-1}–10^{6} pM), I3C (7-point scheme, 10^{3}–10^{9} pM), DIM (6-point scheme, 10^{3}–10^{8} pM), or CBD (6-point scheme, 10^{3}–10^{8} pM). After each treatment duration, cells were trypsinized (0.025% trypsin/EDTA) and resuspended in media at 10^{6} cells/mL for flow cytometric analyses. Cells suspensions were read by a Beckman Coulter CyAn^{ADP} flow cytometer equipped with a 488 nm laser for excitation and FITC channel (530/30 bandpass filter) for EGFP intensity readouts. FCS files were captured for each treatment group using a Summit Software System (v4.3; Cytomation, Fort Collins, CO, USA), and files were further analyzed using FlowJo Software (v10.5.0; FlowJo LLC, Ashland, OR, USA) for mean fluorescence intensity (MFI) values and bifurcation-gated cell percentages. All samples were run in biological triplicate.

Computational Simulation

The simulation approach employed herein utilizes the AnyLogic multimethod simulation software (v8.0; The AnyLogic Company, Chicago, IL, USA), integrating agent-based, discrete-event and system-dynamics modeling techniques. Primarily, the simulation interface was built with a population of hepatocyte agents (cell number adjustable), each with an intrinsic equation network defining AhR activation. This equation network uses the tissue-level exposure of each compound of interest (assumed first-order diffusion and first-order elimination) within a standard Hill equation

that defines a cell's AhR response fraction. The mathematics and equation sets defining biological responses used here have been previously documented [41]. The main components of this equation are the Hill coefficient and threshold (EC_{50}) value (as seen in Fig. 2.13A), both of which have been systematically optimized to fit to previous experimental datasets. Validations and corrections of these simulation optimizations were further performed using our own experimental data. The hill coefficient is optimized based on histogram readouts generated by the flow cytometer as well as MFI values that define activation levels; as cells are activated experimentally, their response shape, and thus Hill coefficient, remain the same within a cellular population for each given ligand. For the threshold value, however, cellular variance exists as some cells will respond to different amounts of ligands; because of this, the threshold is defined as a distribution for each cellular population respective to each specific ligand. Upon simulation startup, each cell is instructed by the program to pull threshold values from a theoretical distribution. Optimization experiments performed within the simulation for these value distributions all consist of 50,000 randomly sampled iterations each consisting of 1,000-cell populations to reach the most appropriate values and ranges. Each treatment scenario was further analyzed by Monte Carlo analyses of 100 sampling iterations each to elucidate the level of variance in the stochastic simulation data. All other details on simulation builds are elaborated on in the results section and files used may be openly accessed via the AnyLogic Cloud online platform. Representative 1,000 pM TCDD simulation experiment can be run directly in web browser at: https://tinyurl.com/y9yzt8dd. Files (.alp format) can be downloaded from this same site.

Data Visualization and Further Mathematical Analyses

Graphical representations and non-linear curve analyses of data were produced using both AnyLogic simulation software and GraphPad Prism (v7.0; GraphPad Software Inc.; La Jolla, CA, USA). One-phase decay analyses were conducted to further characterize Weibull-based threshold distributions and elucidate median values. Simulated fluorescence histograms were fitted accordingly using either a smoothed fourth order polynomial analysis or Gaussian analysis for biphasic (highly ultrasensitive) or monophasic (graded) plots, respectively. Sigmoidal (variable slope; four parameter) analyses and concomitant EC_{50} value generation were conducted for all dose-response curves.

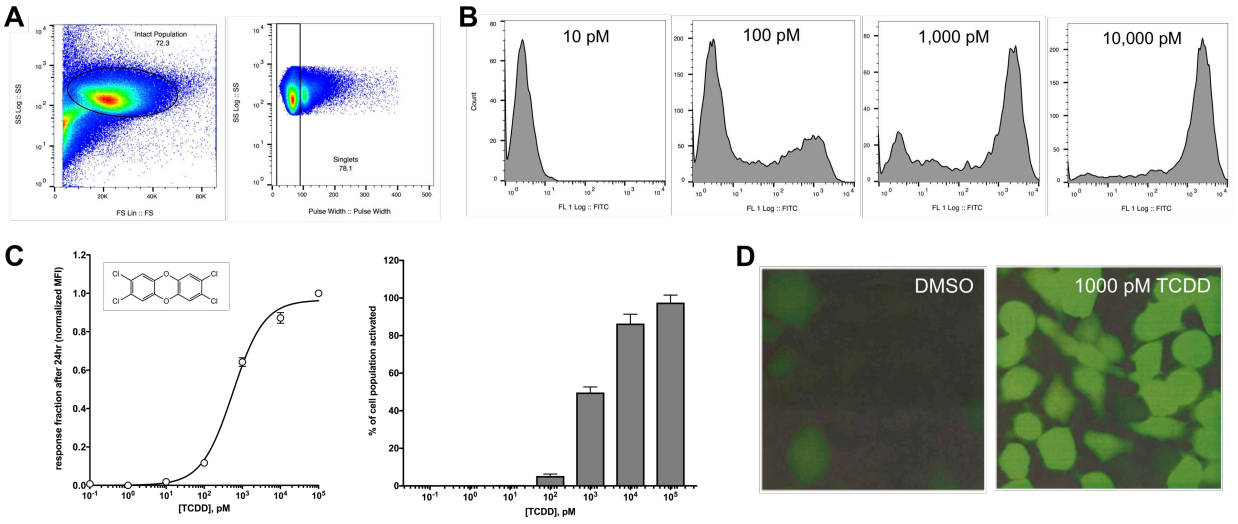

FIGURE 2.13

Optimized AhR activation assay using the XRE-EGFP coupled hepatoma cell line. **(A)** Gating scheme for each sample that was used to select hepatoma cell populations for analysis. Intact cells were first separated from debris and noise based on appropriate size (FS, forward scatter) and granularity (SS, side scatter); single cell events were then separated from doublet events. **(B)** Dose-dependent variation in EGFP-based fluorescence intensity (captured via FITC channel) seen in cell populations after 24 hr of different TCDD exposures (10^1–10^4 pM). **(C)** 7-point dose-response analysis (10^{-1}–10^5 pM TCDD) for response fraction and activated cell counts, measured as corrected mean fluorescence intensity (MFI) and bifurcated $FITC^+$ cells, respectively. **(D)** Fluorescence imaging of the transfected hepatoma cells exposed to either DMSO vehicle or 1,000 pM TCDD, as seen in the original documentation of these cells by Nagy et al. [155].

2.2.3 Pharmacodynamic results

Single-cell AhR Activation Assay

The flow cytometric assay used here has been optimized by our laboratory and is suitable for investigating ultrasensitivity dynamics for functional activation of the AhR. This assay directly measures the level of AhR-dependent protein product (EGFP) in individual H1G1.1C3-GFP cells. Collecting these single cell and population-based metrics were critical for use in the subsequent simulation approach. We first identified the hepatocyte population of interest gathered by the cytometer by gating for appropriate size and complexity seen in the cells (measured as forward and side scatter) as well as by gating out false doublet or triplet events as clumped cells can sometimes make their way through the point of observation (Fig. 2.13A). Each treatment group's cell population was excited by the 488 nm laser and their level of EGFP-based fluorescence was observed, which for increasing TCDD treatments, showed mainly two distinct states: inactive or fully active. This is defined by the bimodal distributions in the fluorescence intensity histograms shown (Fig. 2.13B). These mean fluorescence intensity (MFI) data were quantified at the population level and plotted against the varying doses of TCDD used, resulting in a steep sigmoidal curve (Fig. 2.13C, left panel). MFI values were corrected for autofluorescence and normalized. A bifurcation gating scheme was also employed to divide the percent of cells that exist within the inactive state (FITC-) or the fully active state (FITC+), seen in Fig. 2.13C (right panel). A visual representation of this TCDD-dependent switch-like response in H1G1.1C3-GFP cells was previously gathered by Nagy et al. [155], where the cells were treated with DMSO vehicle or 10^3 pM TCDD (Fig. 2.13D).

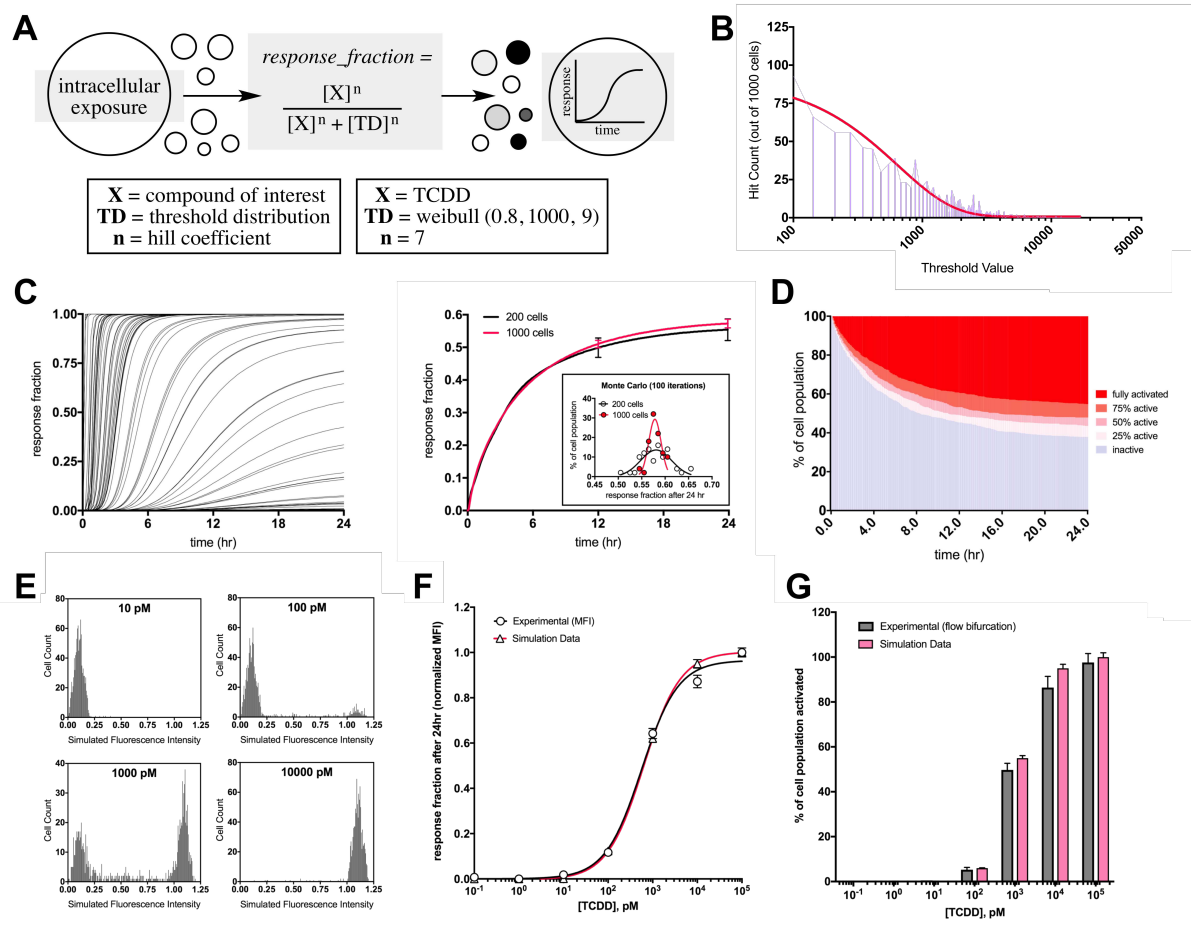

FIGURE 2.14

The computational constructs and simulation results for the TCDD-mediated AhR response in immortalized hepatocytes. **(A)** Simplified schematic of the simulation interface and primary mathematics. Circles represent cellular agents in the simulation, where each is designed to respond probabilistically based on their threshold magnitude pulled from an identified distribution. The identified vales and ranges that correspond to TCDD are enumerated. **(B)** Simulation-generated threshold distribution for TCDD, sampled from 1,000 cellular agents. **(C)** Single-cell (left panel, 100 sampled curves from runtime) and compounded population (right panel) simulation results following 1,000 pM TCDD. Population results were iterated 100 times each in a Monte Carlo analysis; resulting Gaussian curves are seen in the subplot for 200 and 1,000 cell agents. **(D)** Levels of activation within the simulation following 1,000 pM TCDD. Cells were phenotyped based on their response fraction values. **(E)** Dose-dependent variation in simulated fluorescence intensity seen in cell populations after 24 hr of different TCDD exposures (10^1–10^4 pM). **(F)** Experimental and simulated dose-response analyses overlaid for response fraction (10^{-1}–10^5 pM TCDD) and **(G)** activated cell counts (10^{-1}–10^5 pM TCDD).

Ultrasensitivity Dynamics Elucidated via Computational Simulation

We designed a simulation for this study that is consistent with the behavior of individual cells as they respond to AhR modulators, in either slowly graded or highly ultrasensitive manners. The foundational construct of our simulation is an agent-based approach where “cell agents” exist as a population and each contain a stochastic equation-based response network that is dependent upon intracellular exposure inputs (Fig. 2.14A). TCDD was the prototypical compound used for the initial simulation build, and its ligand-specific Hill coefficient of 7 and threshold distribution (also displayed in Fig. 2.14A) were systematically optimized and defined by simulation experiments. The graphical representation of the threshold distribution elicited by TCDD is displayed in Fig. 2.14B. After a simulation run at 10^3 pM TCDD exposure, the responses of 100 sampled cells were collected and overlaid, displaying the stochastic nature of the simulation interface (Fig. 2.14C, left panel); these datasets were then compounded to reveal the population-based response (Fig. 2.14C, right panel). The population-based response was collected for experiments containing 200 or 1,000 cell agents where the datasets change only marginally, showing that these are enough agents in the simulation to display the compounded effects of the distribution metrics. Variance of the programmed stochasticity was further quantified by Monte Carlo analysis (100 iterations per group), and the results are displayed as Gaussian distribution subplots (Fig. 2.14C, right panel). Cells were then phenotyped based on their response fraction values (inactive, 25%, 50%, 75%, and ≥90% or fully active), and cell percentages dominated either the inactive or fully active states in response to 10^3 pM TCDD (Fig. 2.14D), correlating appropriately to our experimental data. After the 24 hr runtime in the

simulation, histograms of response fractions for different TCDD doses were collected (Fig. 2.14E), paralleling the experimental histograms seen in Fig. 2.13B. As final analyses in the simulation design, dose-response curves were generated for all TCDD doses after 24 hr of exposure. Response fractions and activated cell percentages were recorded and overlaid on top of experimental data, shown in Fig. 2.14F and Fig. 2.14G, respectively. The similarity between the experimental and simulation datasets highlights the validity of this approach for studying the ligand-dependent AhR response.

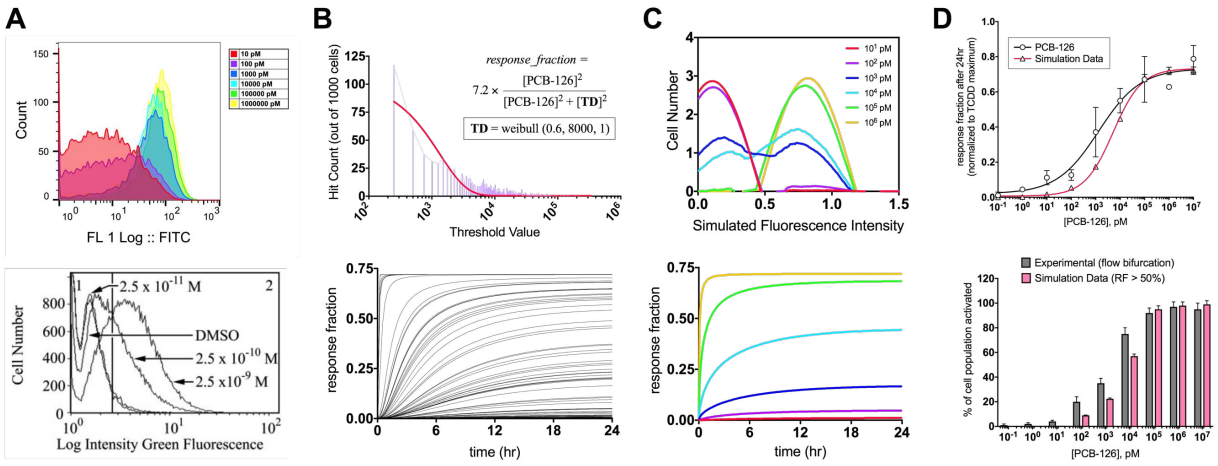

FIGURE 2.15

Quantitative analysis of AhR activation by PCB-126. **(A)** Dose-dependent variation in EGFP-based fluorescence intensity (captured via FITC channel) seen in cell populations after 24 hr of different PCB-126 exposures (10^1–10^6 pM). The lower panel displays historical flow cytometric histogram data from Broccardo et al. [47], of PCB-126-mediated AhR activation following 24 hr of treatment using CYP1A1 antibodies. **(B)** Hepatocyte population characteristics with respect to PCB-126-mediated AhR response. The optimized threshold distribution with mathematical setup is displayed (top panel), and single cell simulation results are overlaid for 100 sampled cells following 1,000 pM PCB-126 (bottom panel). **(C)** For varying doses of PCB-126 (10^1–10^6 pM), response fraction histograms are overlaid (top panel), and time-course evaluations for the same doses are overlaid (bottom panel). **(D)** Comparison of PCB-126 dose-response simulation data to experimental flow data (10^{-1}–10^6 pM); response fraction (top panel) and cell percentages (bottom panel) were evaluated.

Dose-Response and Simulation Analyses Performed for Each Test Compound

Following the preliminary TCDD optimization and analysis, the flow cytometric and simulation analyses were performed for all classical and consumption based ligands. PCB-126 was exposed to the hepatoma cells at a range of 10^{-1}–10^{7} pM. Experimental histograms of fluorescence intensity after 24 hr of PCB-126 treatment are displayed in Fig. 2.15A, showing the switch from inactive to fully active states. Current flow cytometric data (top panel) and historical data from our laboratory (published as Broccardo et al. [47]; bottom panel) are shown for PCB-126 in both the mutated and traditional Hepa1c1c7 cells respectively. Historical data was used to further confirm the actions of PCB-126 qualitatively, but optimized simulation data for this ligand were gathered using newly obtained flow cytometric data for consistency throughout this study. Simulation experiments revealed a Hill coefficient of 2 and a threshold distribution similar in nature and shape to that of TCDD, but different in magnitude (Fig. 2.15B, top panel); additionally, since all compounds were normalized to maximal induction TCDD data, it was found experimentally that PCB-126 hit a maximum response fraction of 0.72 which was included in the simulation makeup. Response fraction simulation data from 100 sampled cell agents after 10^{3} pM of PCB-126 were collected and overlaid to display individual stochastic activations (Fig. 2.15B, bottom panel). Simulated fluorescence intensity histograms were overlaid for relevant PCB-126 doses (Fig. 2.15C, top panel), and simulation-generated time-course compounded population results were overlaid for the same doses (Fig. 2.15C, bottom panel). Full dose-response curves were then generated for response fraction values (Fig. 2.15D, top panel) and activated cell percentages (Fig. 2.15D, bottom panel), overlaid on top of experimental flow cytometry

data. The full experimental and simulation analyses was performed for BaP as well (not shown for brevity), resulting in a Hill coefficient of 3, a threshold distribution median of 1231 pM, and experimental EC_{50} of 491.4 pM.

Consumption-based ligands all underwent the same experimental and simulation analyses, and the highlights of these results are displayed for I3C (Fig. 2.16A), DIM (Fig. 2.16B), and CBD (Fig. 2.16C). Shown for each of these ligands are (i) the generated threshold distribution and equation framework employed in simulation experiments, (ii) the overlaid histograms of simulated fluorescence intensity for all relevant doses within the experimental curve, and (iii) the overlaid full dose-response curves generated experimentally and via simulation. Representative dose-response histograms generated via flow cytometry experiments are shown for each compound as well.

Comparative Analyses Between AhR Modulators

The experimental and simulation-generated response activation values were finally compared for all the classical AhR ligands and contemporary consumption-based ligands. The experimental EC_{50} and simulated threshold distribution medians were markedly higher for the consumption-based ligands than for the classical AhR ligands, whereas the simulated Hill coefficients revealed for each of the consumption-based ligands were markedly lower. When plotted as Hill coefficients against either threshold distribution medians or against experimental EC_{50} values, the resulting graph can be divided into quadrants defining the type of AhR modulation, and thus predicting regions with distinct physiological outcomes (Fig. 2.17A). These outcomes of differential AhR

activation are summarized in Fig. 2.17B, where small amounts of potent classical ligands are required to elicit highly ultrasensitive responses with a propensity for deleterious outcomes. In contrast, this summary diagram shows how much larger quantities of contemporary AhR-modulating ligands result in much less steepness in their activation curves, which may in part be responsible for their mild transcriptional conditioning and harmless or even therapeutic outcomes, with respect to AhR activity alone.

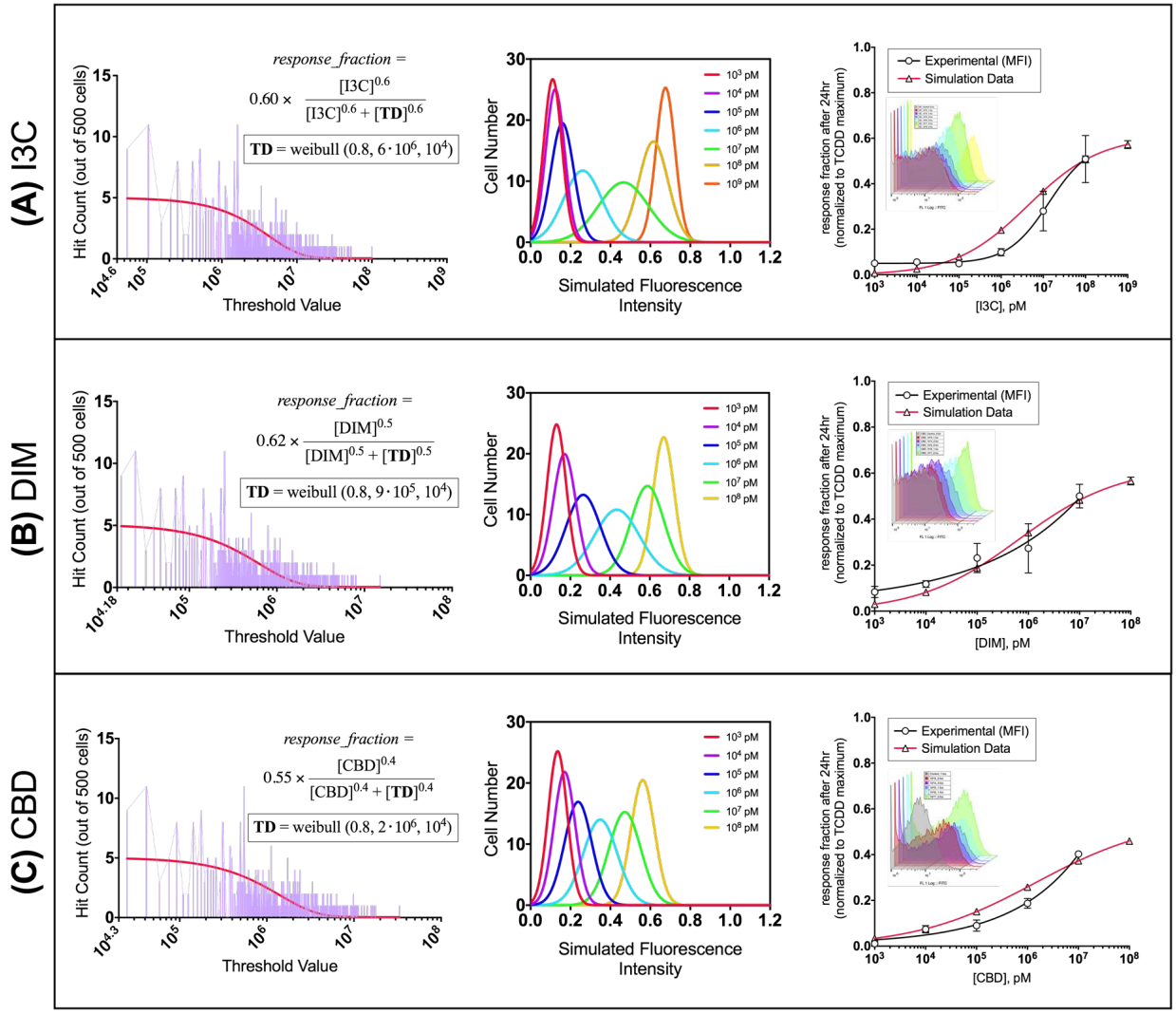

FIGURE 2.16

Analyses of consumption-based ligands. **(A)** I3C, **(B)** DIM, and **(C)** CBD computational analyses and experimental flow data. For each consumption-based ligand, the optimized threshold distribution with mathematical setup is displayed (left panels), simulated fluorescence histograms are overlaid for all dose points (middle panels), and comparative experimental-to-simulation dose-response plot is shown (right panels). Representative experimental histograms of measured fluorescence intensity for each compound are seen in the dose-response subplots.

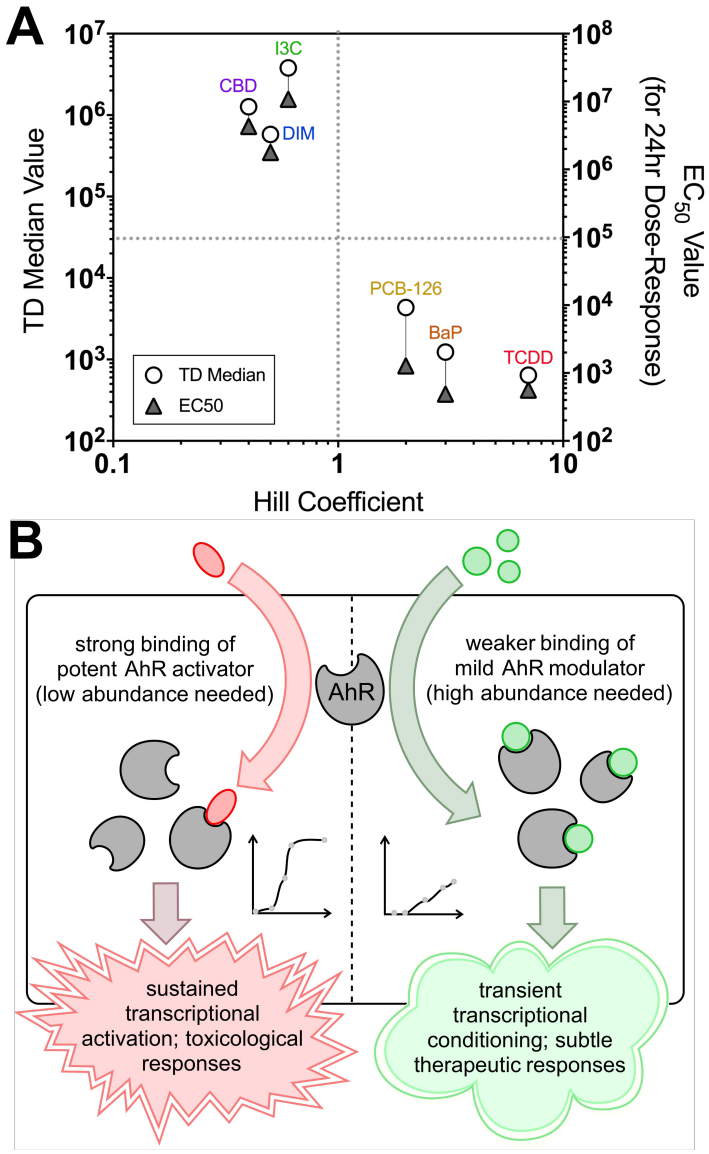

FIGURE 2.17

Final comparisons between all AhR modulators of interest. **(A)** Hill coefficient values plotted against respective threshold distribution medians (left axis) and experimentally-measured EC_{50} values (right axis). Classical/toxicological and contemporary/dietary/therapeutic ligands are clustered in different quadrants outlining graphical regions with differential physiological outcomes. **(B)** Conclusive disparity between different ligand-specific ultrasensitivity dynamics and how they correlate with cellular and physiological outcomes.

2.2.4 Discussions and conclusions of pharmacodynamic modeling insights

Discussions of new AhR activation data and insights for dietary therapies

This study is highly innovative because it greatly advances our understanding of how different AhR ligands can elicit drastically different and sometimes opposite physiological outcomes. While there are many theoretical components accounting for the disparity observed in the literature, our results view the kinetic and dynamic relationships that exist through an intricate quantitative lens. We have previously identified ultrasensitivity dynamics within AhR-mediated responses in liver cell lines and primary hepatocytes [46, 47, 153]. These previous analyses of the AhR response have utilized population-based mathematics that have been derived for these types of substrate-dependent curves and phosphorylation systems [41]. Due to the advancement of adaptable agent-based simulation technology, our current study now reveals specific nuances to quantifying each individual cell that mounts the response and to further characterizing different types of ligands as AhR modulators.

While we have generated an appropriate quantitative model for cell distribution-based Hill dynamics relative to the AhR, different ultrasensitivity mathematics born out of either positive feedback [40] or negative cooperativity [44] are yet to be fully understood for this particular receptor. Our study indicates that potent prototypical ligands like TCDD allow for a more bistable system with reinforced signal transduction and long-lasting effects. Alternative ligands like DIM or CBD may result in weaker cooperativity at the nuclear dimerization point and thus more graded and short-lived responses, as it is possible to produce AhR dimers with quantifiably lower affinities for DNA binding [156, 157].

The nuances in activating this receptor are also purportedly attributed to differing recruitment biomolecules in the cytosol giving rise to varying levels of receptor translocation and transcriptional activity. In specific cases with ligands like omeprazole, receptor activation is completely dependent upon particular AhR protein residues and co-activating kinases, whereas traditional toxicological ligands like TCDD elicit no such dependency [158]. Investigators have also noted distinct differences in the binding fingerprints of TCDD versus ITE and other indole-based ligands toward murine AhR residues [159], finding that particular moieties within contemporary ligands are best for targeting the AhR with less stable molecular confirmations for therapy. These limiting factors in AhR activation overall show reduced transcriptional magnitudes and shortened activity durations [158]. Such factors may be at play with many contemporary consumption-based ligands such as those observed in the current study. As a critical observation, when the endogenous indole ITE is compared to TCDD exposure in mouse lung fibroblasts, immediate expressional changes are seemingly analogous [150]. Looking at these data from acute exposures and considering the limiting factors for low affinity ligands, it appears that the AhR response disparity is fully observed in a more subacute or even chronic fashion when probed with subtler levels of ultrasensitivity.

In contrast to the intestinal and hepatic differences noted for varying AhR ligand types [142], different AhR ligands causing similar physiological responses have also been observed for very specific tissues like the placenta. Following treatment with TCDD or ITE, a modulation in the angiogenic response of the placenta is seen due to differential AhR roles between placental endothelial cells [160, 161]. While TCDD and ITE both appear to have suppressive angiogenic responses in the placenta, it has also

been reported that the expressional changes and final vascular remodeling elicited by both are vastly different [151]. These observations lead to the speculation that AhR modulators of any kind may have a more hypervariable physiological response within tissues that are highly estrogen-responsive, as there is much signaling crosstalk and shared ligands between the AhR and estrogen receptor (ER) family [162]. While the AhR may be an emerging therapeutic target for alleviating the progression of intestinal diseases and inflammatory responses, it appears that there are estrogen-dependent caveats to stimulating this pathway. Known AhR modulators TCDD and ITE can potentially harm a growing fetus via stunting placental growth [160, 161]. DIM has been shown to allow for the proliferation of breast cancer cells [163]. Because of these reports, future work into therapeutic AhR modulators should carefully take into account direct and indirect estrogenic potential to eliminate any unintended effects.

Throughout this study and future experimental analyses, it is important to consider experimental dosing schemes and their relevancies to environmental and dietary exposures. Because many studies for AhR ligands are performed *in vitro* and *in vivo*, exposure assessments and physiologically-based pharmacokinetic analyses are required to understand the correlation between the two. For the toxicological ligands addressed in this study, the dose ranges applied are identified intracellular ranges that are known to activate the AhR and were once environmentally relevant, but measured internal blood doses for average and at risk populations have since declined far below their activation thresholds following years of remediation for TCDD [164, 165] and most PCB congeners [166]. Interestingly, lung perfusate doses up to 10^4 pM BaP can still be reached and maintained for cigarette smokers [167]. Internal doses for contemporary

consumption-based ligands are user-dependent, and investigators must rely on established PBPK studies for internal exposure estimation. Following 100 mg/kg I3C prodrug oral dosing in mice, $>10^6$ pM serum ranges can be reached for several hours [168]. Following 250 mg/kg crystalline DIM oral dosing in mice, $>10^7$ pM serum ranges can be reached for several hours [169]. Following 10 mg/kg CBD oral dosing in rats, $>10^5$ pM serum ranges can be reached for several hours [170]. While these pharmacokinetic dosing schemes may be relatively high for human supplements (e.g. 10 mg/kg CBD in an average human would be a 600 mg CBD oral dose), the internal doses reached are all relevant to the activation ranges elucidated.

AhR activation by the appropriate amount of a particular ligand can elicit therapeutic responses, as it has been seen for carbohydrate metabolism in mice [125], gastric cancer reduction [129, 130], and alleviated intestinal inflammation [128]. The current study greatly aids in the understanding of why a potent AhR ligand can result in hepatic oxidative stress and hepatocellular carcinoma while a weak activator like I3C can result in enhanced hepatic and metabolic processes. The growing body of literature on therapeutic effects, however, warrants more differential ultrasensitivity quantification for other cell types such as intestinal lymphocytes and endothelial cells.

Conclusions

In conclusion, we have provided a novel integrated experimental simulation approach that allows us to understand and visualize the dynamics of the AhR response for a variety of classical toxicological ligands as well as consumption-based constituents. Using these newly developed tools, we have been able to quantify

important constants respective to each ligand that affords us the opportunity to draw a correlation to the phenotypic AhR-dependent response each ligand will mount. This analysis along with future studies will greatly aid in quantifying and targeting ligand-specific AhR responses as a therapeutic modality.

CHAPTER 3: NETWORK SYSTEMS IN CELLULAR AGING

3.1 Leveraging the simulation techniques in fundamental biology

After establishing the scientific value of multimethod computational simulation for biological queries, we began to employ this methodology toward larger more vexing questions: What molecular events cause complex organisms to age? What drives the degenerative aging process and facilities cellular dysfunction? How does the aging process contribute to disease? This chapter opens the discussion for how we may theoretically address these questions. To view the peer-reviewed research article that accompanies this section, see: *Hoffman et al. (2018) Mitochondrial avatars for quantitative aging research. Aging (Albany NY).*

3.1.1 Seeking molecular determinants of the aging process

As the search for determinants of degenerative aging continues, research efforts are becoming more focused on molecular targets and pathways that converge on the mitochondrion. The genesis of mitochondrial aging research stems from the original free radical theory of aging, where reactive oxygen species produced spontaneously within each cell's mitochondria go on to damage the cell in a deleterious feedback loop [171]. This classical theory, albeit rooted in fine physicochemical logic, neglects to include the profoundly robust interconnectivity of living systems, and in doing so, assumes that cells are not built with some level of resilience against this spontaneous oxidative damage.

It is now well understood that cells have many defense mechanisms in place to respond to oxidative damage, especially that of the age-dependent mitochondrial variety

[2], but the slew of pathways involved in producing and mitigating damage continues to become more abundant and more highly connected as we reveal more experimental information. One such connection at the forefront of aging research is the relationship between broad spectrum mitochondrial stress and the activation of the mitochondrial unfolded protein response, a story about the complex maintenance of mitochondrial integrity and cellular proteostasis [2]. Intertwined further into these cellular networks are the activities of sirtuins, a type of deacetylases with a multitude of beneficial functions that preserve mitochondrial efficiency and curb age-dependent oxidative signaling [172].

While it is difficult to identify all the relevant mechanistic details that account for mitochondrial aging, investigators are beginning to approach a realistic comprehensive understanding of the fundamental circuitry at play. The difficulty in this work then rises exponentially as we attempt to quantify the individual cellular circuit components under a variety of environmental conditions and over relevant lengths of time. The purpose in doing so is to quantitatively evaluate these connections and to see their net response when compounded (Fig. 3.1). In this process, a legitimate set of numbers with useful units will surface, and if correct computational methods are employed, you will reveal a focal point that the system depends upon: a node of interest or even a particular set of connections.

In this perspective, we emphasize that the degenerative aging response is not a consequence of a single concrete cellular pathway, but is a phenomenon driven by multifarious events in concert. This can be interpreted at the computational simulation interface as the specific magnitude of selected mitochondrion-oriented interactions, often represented by sets of differential equations or discrete numerical events. While

simulation techniques robustly complement experimental data and offer us the most hope for interpreting this biogerontological system, scientists continue to search for (i) the most appropriate and insightful computational formats, and (ii) the key cellular network connections and molecular convergences that truly matter [173]. A prime example of this ambitious undertaking is a recent study carried out by Tam *et al*. [174] that presents a unique computational approach to understanding a relevant link explaining age-associated damage and dysfunction: the accumulation of faulty mitochondrial contents as a result of organelle fusion-fission dynamics. These computational biochemists successfully constructed a chemical master equation framework to quantitatively demonstrate how mitochondrial dynamics may influence the clonal expansion of aberrant mitochondrial DNA, while implementing expected cellular stochasticity. This study highlights not only how age-dependent damage can occur by simulating a substantial set of mitochondrial processes; it also draws attention to the most significant processes that dictate a cell's age-dependent outcome.

There is no doubt that it is immensely valuable to quantitate the net effects of molecular pathways to determine age-dependent behavior of a cell; however, the usefulness of this approach is amplified further when it is applied to populations of cells in order to determine the response of whole tissues. The chapter following this one describes a similar expansive hierarchical computational landscape we created, (i) by drawing upon many previous computational models of mitochondrial aging [173, 174] and (ii) by building new integrated simulation constructs for significant pathway-driven concepts as they have been identified in the model organism *Caenorhabditis elegans* [2, 172]. What our group illuminated was a large-scale simulation approach capable of

teasing out significant relationships and network motifs responsible for producing purely age-driven degenerative phenotypes. Such relationships notably include positive and negative feedback loops, ultrasensitive or switch-like transcriptional responses, and linearity between molecular determinants of aging and pathological cellular phenotypes. More applicably for all biologists (computational or empirical), we discovered that this intuitive simulation construct is capable of making apt predictions in the context of the genetic targets involved. Important genes implicated within this network include *skn-1*, *daf-16*, and *sod-2*, all exceptionally important for controlling the redox state of cells and the integrity of mitochondrial populations.

Many labs continually contribute to the growing body of literature on computational systems biology for mitochondrial aging research. These studies mark the progression toward more simulation-based methods in the field. Although these studies exist at all conceptual scales and levels of abstraction, they all uniquely provide a degree of fruitful quantitative insight, no matter how small [175]. Our group and others have demonstrated the impact of simulation studies for mitochondrial dysfunction on degenerative aging [173, 174], drawing upon oxidative signaling as a focal point. As simulations continue to build on one another and expand in their capabilities, we may very well approach a computational tool that the field can consider a realistic representation of mitochondria to unravel the mysteries of biological aging.

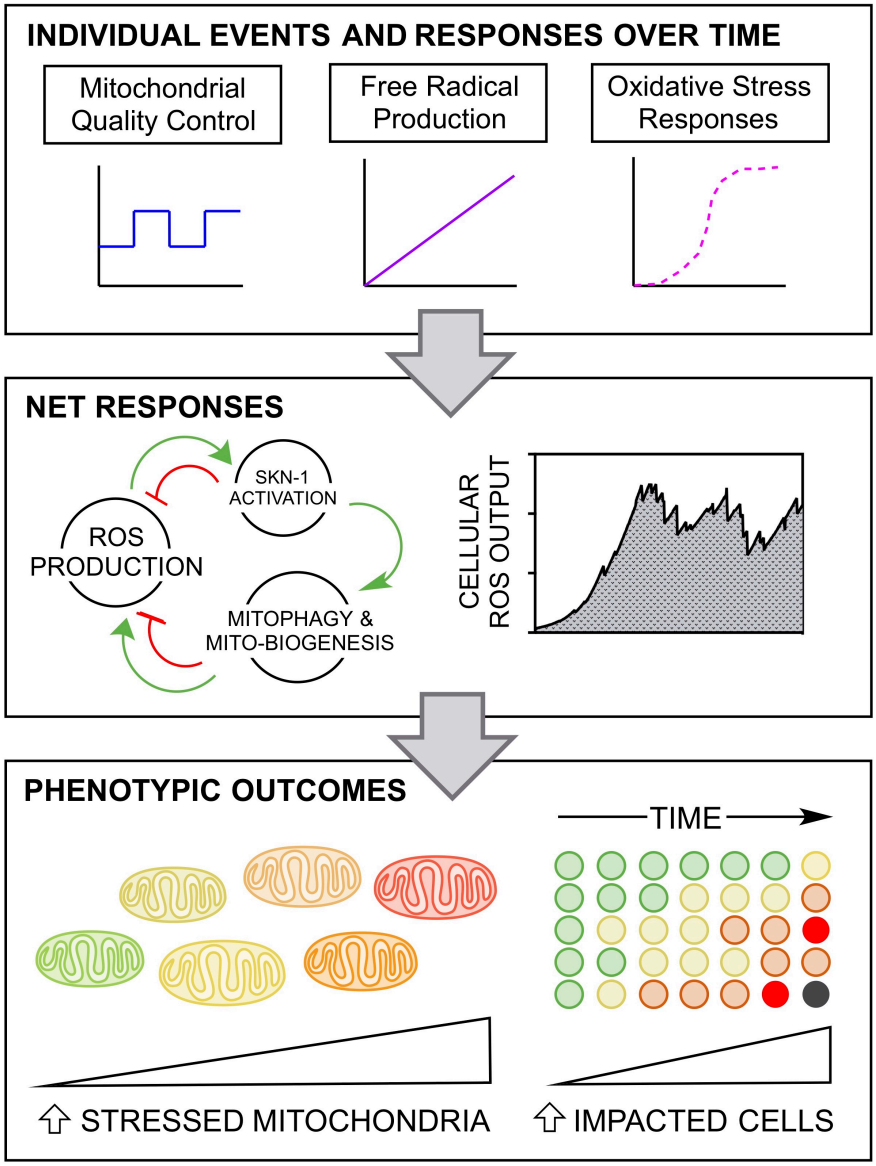

FIGURE 3.1

Quantitative responses compounded to produce the net effects of aging. The experimental simulation paradigm defined in this perspective describes a computational landscape that quantifies individual cellular responses (top panel), makes use of them in large multifaceted circuits to calculate net responses over time (middle panel), and ultimately determines the phenotypic viability outcomes for both mitochondrial and cell populations.

CHAPTER 4. MODELING MITOCHONDRIAL DYSFUNCTION IN AGING

4.1 Designing an appropriate multimethod simulation approach

In order to comprehensively assess the significant and non-intuitive observations seen in mitochondrial aging, we have conducted a study using a novel simulation network approach, which is presented in this chapter. The results reported herein provide new insights into molecular determinants of aging as well as cytoprotective strategies that may improve neurological or muscular healthspan. To view the peer-reviewed research article that accompanies this section, see: *Hoffman et al. (2017) A multimethod computational simulation approach for investigating mitochondrial dynamics and dysfunction in degenerative aging. Aging Cell.*

4.1.1 Introduction of mitochondrial aging

Loss of mitochondrial function is one of the most well-established characteristics of aging cells. Because of this, many researchers speculate that the decline in mitochondrial function is not only a complex consequence of biological aging, but may provide the earliest trigger in time-dependent cellular senescence and degeneration [2, 176]. The first viable theory explaining this relationship is the mitochondrial free radical theory of aging (MFRTA), which suggests that increasing levels of mitochondrial reactive oxygen species (mtROS) produced by cellular respiration and the electron transport chain (ETC) are responsible for age-dependent damage, especially toward copies of mitochondrial DNA (mtDNA) [171, 177]. According to this theory, when mtDNA and matrix proteins exist in an oxidatively damaged state, ETC function may be reduced

and proteostasis may be lost, resulting in a deleterious cyclic propagation of mtROS generation and a decrease in cellular respiratory function. The MFRTA has been adapted and strengthened over the years to address many of the complexities and nuances associated with mitochondrial dysfunction in aging cells [178, 179]. For example, more recent findings suggest that the accumulation of loss-of-function mutations are not entirely mtROS-dependent [180, 181] and have demonstrated that minimal increases in endogenous mtROS may be fairly benign or, controversially, cytoprotective in nature [182, 183]. These contrasting data warrant further investigation of this theory as a pertinent and highly multifaceted system in aging organisms.

One additional dimension that adds much value to the MFRTA involves the general response pathway by which the mitochondrion adapts to stress: the mitochondrial unfolded protein response (UPR^{mt}). This response is conserved across an array of species, and presumably all eukaryotes, and may largely account for the interplay that dulls the downstream oxidative effects of mitochondrial damage during aging [184]. The UPR^{mt} is activated directly or indirectly by a variety of stress signals originating from the ETC and the intramitochondrial environment [185–187]. This activated response has been extensively studied within the nematode *Caenorhabditis elegans*, where the UPR^{mt} is mediated by nuclear import of an important protein known as activating transcription factor associated with stress-1 (ATFS-1) [187]. This transcription factor is regulated in such a way that allows the cell to globally monitor mitochondrial stress and damage, and it effectively produces a widely protective transcriptional response when present in the nucleus. Among the several hundred transcripts upregulated by nuclear ATFS-1 accumulation include those encoding for

important mitochondrial proteins necessary for antioxidant defense and proteostasis, e.g. *sod-2/3*, *hsp-60*, *hsp-70*, *ymel-1*, *timm-23* [187, 188]. Additionally, this response negatively regulates the nuclear and mitochondrial expression of oxidative phosphorylation (OXPHOS) subunits to avoid the accumulation of superfluous proteins when mitochondria are already experiencing severe metabolic stress [189]. All of these functional changes promote mitochondrial health, which may in turn allow cells to live longer at a heightened state of performance.

Though widely beneficial for proteostasis and respiratory maintenance within cells, the UPR^{mt} has also been noted as a process that can sustain damage within the mitochondrial genome [190]. It has been suggested that the UPR^{mt} can be overprotective by sustaining the numbers of both functional and severely defective mitochondria within a given cell, though the mechanism by which this occurs is far from clear. The activation of this stress response may allow for high respiratory function for the majority of a lifespan, but once enough mtDNA copies hold deletions or mutations within their sequences, it is possible that the balance may shift toward a deleterious cellular mechanism caused in part by sustained UPR^{mt} activation. This complete relationship has yet to be fully investigated.

Mitochondrial autophagy, or mitophagy, is another process that appears to play a critical role in biological aging. Poor regulation of this process allows for the accumulation of aberrant mitochondrial content, which has been postulated as a driving force for deleterious senescence states, particularly for age-associated neurodegenerative diseases such as dementia, Alzheimer's disease (AD), and Parkinson's disease (PD) [191, 192]. Drastic manipulation of mitochondrial biogenesis

and mitophagy flux in *C. elegans* stress models has been shown to cause decreases in ATP production, increased oxidative burdens, and ultimately shortened lifespans [193], demonstrating how important it is for these processes to be tightly regulated to allow for healthy aging. These regulatory dynamics are also well conserved across a variety of animal species.

The causal role of dysfunctional mitochondrial dynamics in the process of biological aging remains fairly nebulous. Each of the aforementioned mitochondrial processes have been hypothesized as important factors that determine the rate and results of biological aging, yet it has been rather difficult to investigate all of these processes simultaneously and to quantitate their ultimate effects when compounded. Computational models have been able to provide an additional means to investigate such complex systems and have gained a great deal of interest specifically for the field of biogerontology [173]. The aim of using such an approach is to not only gain insights about the molecular determinants of tissue aging but to also gain quantitative insights about how such determinants can be targeted therapeutically.

Here we emphasize that the degenerative aging response is not a result of a single concrete cellular pathway, but is dependent upon specific magnitudes of multiple key mitochondrial pathways that allow for cellular senescence states and pathological phenotypes. To illuminate these theories in a more nuanced manner, we took an approach that highlights existing data and integrates them into a systemic computational modeling approach. Our theoretical model addresses vital cellular components and time-dependent macromolecule quantities that account for biological aging within the model organism *C. elegans*—including bioenergetic functions of the

mitochondrion, fundamental observations of the MFRTA, known elements of the UPR^{mt}, and mitophagy-dependent quality control processes (Fig. 4.1A). This framework was modeled using multimethod simulation software, allowing us to employ system-dynamics elements (e.g. stocks and flows) as well as agent-based functions (i.e. those that define discrete events, stochasticity, and seemingly autonomous cellular behavior). Additionally, our *in silico* approach included a hierarchical modeling scheme to control mitochondrial-level dynamics within a population of energetically-demanding cells, allowing us to generate predictive and probabilistic data at the single-cell level (Fig. 4.1B). This theoretical model aims to provide a better understanding of all the significant cellular components that may account for mitochondrial function and dysfunction in biological aging with a quantitative backing that may aid in making experimental predictions for age-related diseases, toxicological endpoints, and potential pharmacological or dietary anti-aging therapies.

4.1.2 Experimental procedures in the complete simulation design

Hierarchical cell simulation design and agent-based modeling

In order to simulate intramitochondrial system dynamics and global cellular reactions, we formulated our model using AnyLogic® multimethod simulation software (The AnyLogic Company; Chicago, IL), which allowed us to develop a hierarchical agent-based simulation scheme. This allowed us to simulate a population of cell agents, with each individual cell agent containing its own population of mitochondrion agents (Fig. 4.1B). Each agent contained discrete event statements and system-dynamics reaction networks, both of which were programmed to deal with natural biological

stochasticity. As a critical agent-based element employed in our model, cells harboring a high percentage of faulty mitochondria were forced into a compromised state via a discrete event. These types of events can be activated once a particular condition is met, and in this case, the event was triggered once enough mitochondria were severely damaged and defective. As this percentage trigger is presumably different for each cell, we incorporated a stochastic transition statement that allowed each cell to pull from a triangular probability:

```
Condition: (Defective_Mitochondria/TotalMitoCount) > triangular
                                                (0.6,0.65,0.8)
```

The range is denoted by the outer bounds and the most probable value is denoted by the middle value of 65%. Similar agent-based principles were utilized for mitochondrial stress-state transitions and all agent-based methods are unpacked in the subsequent method subsections.

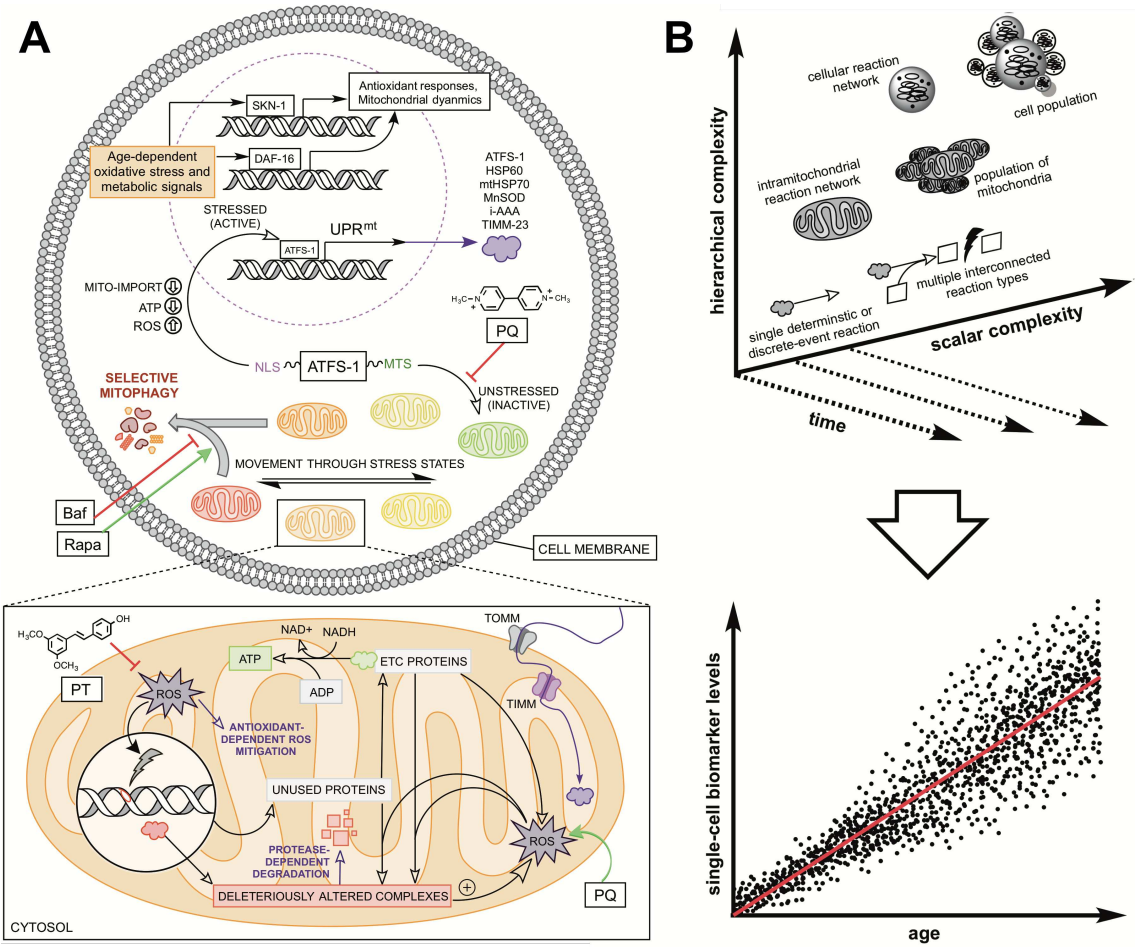

FIGURE 4.1

The integrated aging mechanism of interest and computational simulation approach. **(A)** Respiratory machinery produces both ATP and superoxide, which elicits different types of intramitochondrial damage (noted above as changes in mitochondrial stress states) and activation of various cellular stress response pathways. Such pathways focused on here are the UPR^{mt}, dictated by nuclear accumulation of transcription factor ATFS-1, mitochondrial biogenesis and selective mitophagy, and activation of transcription factors DAF-16 and SKN-1. This integrated mechanism was also virtually probed by pharmacological agents that either modulate mitophagy, oxidative metabolism, or antioxidant defenses. Rapamycin induces mitophagy, bafilomycin hinders mitophagy, paraquat causes additional superoxide production and can activate the UPR^{mt}, and pterostilbene directly and indirectly boosts cellular antioxidant capacity. UPR^{mt}, mitochondrial unfolded protein response; NLS, nuclear localization signal; MTS, mitochondria targeting sequence; Rapa, rapamycin; Baf, bafilomycin; PQ, paraquat; PT, pterostilbene. **(B)** The simulation approach has been characterized as having two dimensions of complexity integrated over time: hierarchical or leveled complexity, and scalar complexity (i.e. magnitude of segments). These constructs were employed to produce large scale predictive datasets over time on the single-cell level (denoted by black dots) which were distilled down into tissue-level averages (denoted by red line).

Deterministic modeling components

Many biological events have been proposed as crucial elements in regulating cellular and organismal lifespan. We manually selected and organized several such elements from the literature and implemented them in complement to our agent-based work as a deterministic modeling framework, i.e., an intricate web of molecule-dependent ODEs. Such elements included (1) mitochondrial reaction networks that govern oxidative metabolism, proteostasis, and genomic alterations, and (2) global cellular reaction networks pertaining to ATFS-1 movement in the cell, protein synthesis, and mitochondrial import. The majority of these curated reactions are detailed in (Fig. 4.1A), and all of the equations and corresponding parameters used are organized and tabulated in the subsequent subsections.

Sensitivity analysis

To determine the quantitative significance of certain parameters and functions within the system, a similar global sensitivity strategy was used that has been described previously [174]. Briefly, each parameter was individually reduced by 5%, and the resulting model outputs, referred to in the text as response variables, were assessed. This was done for all static parameters within the model, and the changes in several response variables (e.g. ROS output) were measured at particular time points determined for young age, midlife, and old age. Sensitivity coefficients for each scenario were calculated:

$$SC = \left(\frac{\partial O_i}{\partial P_j}\right) \times \left(\frac{P_j}{O_i}\right) = \left(\frac{\partial O_i}{O_i}\right) \times 20$$

where *SC* represents the normalized sensitivity coefficient, O_i is the model output value, P_j is the value of the parameter of interest, and ∂ represents the partial derivative of either the parameter value or model output. When |SC| ≥ 1.0000, i.e. when the proportional change in the response variable is greater than the proportional change in the parameter, the parameter is deemed to have significant sensitive control over the respective output at the specified age.

Statistical analysis

Statistical significance was determined by using GraphPad Prism 7.0 software, and *P* values were calculated by a one-way analysis of variance (ANOVA). Significance was considered to be a *P* value of 0.05.

General model units and organism-specific cellular organization parameters

The model is designed to survey a population of 65 neuron-like cells, each with its own population of functioning mitochondria. This cell number was chosen to produce a large enough population to observe without exceeding the limitations of the simulation software, as the methodology is computationally very intensive. The mitochondrial count within each cell varies between 5–35 organelles as determined by literature-based calculations (Table 4.1; Box 4.1). Since the cells will attempt to emulate the energy demand of neurons or myocytes within *C. elegans*, we chose a mean mitochondrial count of 15 with a Poisson distribution to introduce truer cellular stochasticity.

Mitochondrion-level system-dynamics and discrete-event computational methods

The intramitochondrial equation networks are displayed in Box 4.2, mitochondrial agent-based methods are displayed in Box 4.3, and all corresponding mitochondrial parameters are displayed in Table 4.2. Corresponding schematics in of the mitochondrial simulation build are displayed for the ODE-based network (Fig. 4.2A) and the agent state chart (Fig. 4.2B).

TABLE 4.1

Table 4.1. Cellular and anatomical parameters of interest for 3-day-old C. elegans (N2); ranged/averaged literature values.

Parameter	Symbol	Value Range	Units	Source
Average body volume	*Bv*	$3.5\ 10^{-9}$	L/worm	[194]
Average body density (young adult)	*Bd*	1081 ± 3	mg/L	[195]
mtDNA per mitochondria	*MmtDNA*	2 – 10 (rat)	mtDNA-count/mito	[196]
Average mtDNA per worm	*WmtDNA*	250,000 – 320,000	mtDNA-count/worm	[182]
Estimated mtDNA copies per cell	*CmtDNA*	45 – 70	mtDNA-count/cell	[197]
Mitochondria range per worm	*wMito*	25,000 – 160,000	mito-count/worm	calculated
Mitochondrial range per cell	*cMito*	5 – 35	mito-count/cell	calculated
Average ATP per worm	*wATP*	30 – 40	pmol/worm	[182]
Cellular ATP concentration	*cATP*	2.86 – 8.57	mM	calculated

EQUATION BOX 4.1

Box 4.1: Equations pertaining to the estimation of nematode-specific cellular parameters.

Mitochondria range per worm: $$wMito = \frac{WmtDNA}{MmtDNA}$$

Mitochondria range per cell: $$cMito = \frac{CmtDNA}{MmtDNA}$$

ATP concentration range: $$cATP = \frac{wATP}{Bv}$$

Average protein mass per worm: $$WormPMass = Bd * Bv * 18\% \left(\frac{protein}{total\ mass}\right) = 0.681 \pm 0.002\ \frac{\mu g_{protein}}{worm}$$

TABLE 4.2

Table 4.2. Parameters of interest for the proposed intramitochondrial biochemical system.

Parameter	Symbol	Value / Range	Units	Source
second-order rate constant for MnSOD-mediated superoxide transformation	*k1*	1.0×10^{-2}	$nM^{-1}\ min^{-1}$	[182]^{A,C}
average MnSOD conc. in mitochondria (WT)	$[MnSOD]_o$	$3.0 – 6.0 \times 10^{3}$	nM	[182,198]^{C}
aggregate first-order rate constant for other reactions yielding peroxide	*k2*	5.0	min^{-1}	[182]^{A,C}
aggregate first-order rate constant for reactions not yielding peroxide	*k3*	30.0	min^{-1}	[182]^{A,C}
zero-order superoxide generation rate	*v4*	$4.0 – 24.0 \times 10^{4}$	$nM\ min^{-1}$	[182,199]^{A,C}
constant for feedback inhibition by superoxide	*Ki*	7.8×10^{-2}	nM	[182]^{C}
first-order rate constant for peroxide disposition	*k5*	0.38	min^{-1}	[200]^{SS}
initial total concentration of functional ETC proteins	$oEP_{functional}$	100	%	fixed assumption
initial total concentration of faulty ETC proteins	oEP_{faulty}	1	%	fixed assumption
initial total concentration of unused ETC subunits	oEP_{usable}	100	%	fixed assumption

TABLE 4.2 (CONTINUED)

Table 4.2 (continued). Parameters of interest for the proposed intramitochondrial biochemical system.

Parameter	Symbol	Value / Range	Units	Source
pseudo zero-order ADP production rate	*v6*	15.8 – 21.0	mM min^{-1}	[201]^{SS,C}
pseudo first-order complete elimination rate constant for ATP	*k7*	1.87	min^{-1}	[201]^{C}
pseudo zero-order rate of total mitochondrial ETC subunit protein synthesis	*v8*	$9.0 – 36. \times 10^{-4}$	% min^{-1} $copy^{-1}$	[202]^{C}
second-order rate constant (with Kc) governing the protection/recovery of total mt-ETC proteins	*k9*	k10 (1/15)	min^{-1}	[203-205]^{A}
second-order rate constant (with Kros) for oxidation of usable ETC proteins	*k10*	0.1	min^{-1}	[206]^{A}
ROS-neutralizing component of the corresponding second-order rate constant for oxidative activity of $[O_2^{\cdot-}]$ and $[H_2O_2]$	*Kros*	0.094	nM^{-1}	[182, 200]^{O}
second-order rate constant (with Kc) for the elimination of usable proteins via ETC incorporation	*k11*	k14 (¼)	min^{-1}	[207]^{A}
second-order rate constant (with Kp) for the elimination of functional ETC complexes via protein turnover	*k12*	$3.5 – 10.5 \times 10^{-5}$	min^{-1}	[208]^{C}
protein-neutralizing component of the corresponding second-order rate constant for chaperone activity	*Kc*	0.001	$\%^{-1}$	[182]^{O}
protein-neutralizing component of the corresponding second-order rate constant for protease activity	*Kp*	0.094	$\%^{-1}$	[182]^{O}
pseudo zero-order rate of total faulty mitochondrial protein synthesis from damaged mtDNA	*v13*	$9.0 – 36.0 \times 10^{-4}$	% min^{-1} $copy^{-1}$	[202]^{C}
second-order degradation constant (with specific protease activity, Kp) for the elimination of deleteriously oxidized proteins	*k14*	1.7×10^{-2}	min^{-1}	[199]^{C}
rate variable governing oxidative damage to mtDNA	*damageRate*	0.070	events mM $week^{-1}$	[182, 181]^{O}
rate variable governing removal of ΔmtDNA	*destroyRate*	5.148	events $month^{-1}$	[182, 190]^{O}

SS Optimized in the simulation to achieve the reported unstressed physiological steady-state value, percentage or range.
O Individually optimized value, generated using AnyLogic calibration experiments to best fit/emulate reported curves.
A Quantitated assumption based on qualitative evidence.
C Units converted to adhere to model standards.

EQUATION BOX 4.2

Box 4.2: Equations and event statements pertaining to mitochondrion-level biochemical kinetics.

Differential equations governing the time-dependent amounts of key players (PQ_{ROS} represents a function of paraquat-induced increases in ROS production rate, and PT represents a function of pterostilbene-mediated ROS mitigation, as outlined in the last section; when unperturbed by either compound, functions PT and PQ_{ROS} = 1):

$$\frac{d[O_2^{\cdot-}]}{dt} = \boldsymbol{PQ_{ROS}} * \frac{v4}{\left(1 + \frac{[O_2^{\cdot-}]}{Ki}\right)} * \left(\frac{EP_{faulty}}{EP_{faulty} + EP_{functional}}\right) - (k1[MnSOD] + k2 + k3 * \boldsymbol{PT})[O_2^{\cdot-}]$$

$$\frac{d[H_2O_2]}{dt} = \left(\frac{1}{2}k1[MnSOD] + k2\right)[O_2^{\cdot-}] - k5[H_2O_2] * SKN1\_activity\ (GST)$$

$$\frac{d[EP_{usable}]}{dt} = v8(\boldsymbol{mtDNA})\left(1 - \left[\frac{[mATFS1]^n}{{K_b}^n + [mATFS1]^n}\right]\right) + k9[EP_{faulty}] * Kc([HSP60] + [HSP70]) - k10[EP_{usable}] * Kros[[O_2^{\cdot-}] + [H_2O_2]] - k11[EP_{usable}] * Kc([HSP60] + [HSP70])$$

$$\frac{d[EP_{functional}]}{dt} = k11[EP_{usable}] * Kc([HSP60] + [HSP70]) - k12[EP_{functional}] * Kp([mAAA] + [iAAA])$$

$$\frac{d[EP_{faulty}]}{dt} = v13(\Delta\boldsymbol{mtDNA})\left(1 - \left[\frac{[mATFS1]^n}{{K_b}^n + [mATFS1]^n}\right]\right) + k10[EP_{usable}] * Kros[[O_2^{\cdot-}] + [H_2O_2]] - k9[EP_{faulty}] * Kc([HSP60] + [HSP70]) - k14[EP_{faulty}] * Kp([mAAA] + [iAAA])$$

***Rate-dependent discrete events for changes in mtDNA copies:**

Damage to mitochondrial DNA is assessed here in totality. All perturbations (mainly point mutations and deletions) are regarded as a change in mitochondria DNA that will lead to dysfunctional protein synthesis and deleterious faulty protein aggregation. Copy numbers vary from mitochondrion to mitochondrion (2–10 copies), but it is assumed here that the mean copy number is 6, and the distribution falls rapidly in either direction. It is also assumed here that all mitochondria begin with ~15% perturbed mitochondrial DNA (~1 copy per mitochondrion), and that all subsequent DNA damage is both rate-dependent and ROS-dependent [181]. The damage rate is also not always the same for every mitochondrion, and therefore is represented by a stochastic ROS-dependent rate equation **(Eq. 1)** with a mean number of events per week and a corresponding exponential distribution for the initial trigger and recurrence time. Additionally, once mtDNA has been altered, it is apparent that the cell works to remove it when unstressed [182]; however, following the stressor-mediated nuclear activation of ATFS-1, ΔmtDNA is more easily sustained [190] **(Eq. 2)**.

$$(\mathbf{1}.)\ Mean\ number\ of\ mtDNA\ altering\ events\ per\ week = damageRate * ([O_2^{\cdot-}] + [H_2O_2])$$

$$(\mathbf{2}.)\ Mean\ number\ of\ \Delta mtDNA\ removal\ events\ per\ month = destroyRate * \left(1 - \left[\frac{[nATFS1]^n}{{K_b}^n + [nATFS1]^n}\right]\right)$$

***Dynamic expressions displayed in blue:**

Concentrations of proteases, chaperone proteins, ETC assembly factors, and superoxide dismutase are determined by total cellular concentrations following nuclear synthesis (as outlined in the cell-level system-dynamics methods). Additionally, the inhibitory factor governing the repression of mtDNA-mediated OXPHOS protein production is determined by the total mitochondrial concentration of ATFS-1 (all mitochondria presumably contain the same concentration at any given time due to the nature of the global response over a cell).

Box 4.2 (continued): Equations and event statements pertaining to mitochondrion-level biochemical kinetics.

Differential equations governing the time-dependent amounts of key substrates and variables involved in energy metabolism, condensed from simplified models of mitochondrial ATP production [209, 210] and expanded to include synthesis and breakdown of NAD^+ as well as NAD^+-dependent deacetylase (sirtuin) activity [188, 211–213]. The mathematics employed here were developed using some logistical expressions, converted parameters and relative substrate abundances from Saa and Siqueira [210], however, our current model breaks free from previous constructs that assume constant total adenine and adenosine nucleotide availabilities. The current adaptations of the model relate to the age-dependent OXPHOS complex integrity as well as dynamically changing nicotinamide/adenine nucleotide and ADP substrate availabilities. Expressions were best translated to be used in our system dynamics interface, with the critical flux rates outlined below:

$$\frac{d[NucleotidePool]}{dt} = 5.0\frac{mM}{min} - 20.0\frac{mM}{min}\left(\frac{[NucleotidePool]}{[NucleotidePool] + 50\ mM}\right) + \frac{0.5}{min}[NMN + AMN] - 0.0075[NucleotidePool]$$

$$\frac{d[NAD^+]}{dt} = 20.0\frac{mM}{min}\left(\frac{[NucleotidePool]}{[NucleotidePool] + 50\ mM}\right) - \frac{3.0}{min}[NAD^+] + \left[K_{NADH} * [NADH] * \left(\frac{EP_{functional}}{EP_{functional} + EP_{faulty}}\right)\right] - \left\{6.2\frac{mM}{min}\left(\frac{[NAD^+]}{[NAD^+] + K_{NAD+}}\right)\right\}$$

$$\frac{d[NADH]}{dt} = \frac{3.0}{min}[NAD^+] - \left[K_{NADH} * [NADH] * \left(\frac{EP_{functional}}{EP_{functional} + EP_{faulty}}\right)\right] - \frac{0.5}{min}[NADH]$$

$$\frac{d[NMN + AMN]}{dt} = \frac{2\ Mononucleotides}{1\ Dinucleotide}\left\{6.2\frac{mM}{min}\left(\frac{[NAD^+]}{[NAD^+] + K_{NAD+}}\right)\right\} - \left\{\left(\frac{0.5}{min} + \frac{2.0}{min}\right)[NMN + AMN]\right\}$$

$$\frac{d[\psi]}{dt} = \frac{8.6\ mV}{mM}\left[K_{NADH} * [NADH] * \left(\frac{EP_{functional}}{EP_{functional} + EP_{faulty}}\right)\right]$$

$$\frac{d[P_i]}{dt} \approx 0 \approx SS\ \ \therefore\ \ [P_i] = uniform(20, 25)\ mM$$

$$\frac{d[ADP]}{dt} = v6 - \frac{0.1}{min}[ADP] - \frac{3.2}{min}[ADP]\left(\frac{EP_{functional}}{EP_{functional}+EP_{faulty}}\right) * \left(\frac{[P_i]}{[P_i]+10\ mM}\right) * \frac{\psi^{2.5}}{\psi^{2.5}+K_\psi} + 2.0\frac{mM}{min} * \left(\frac{[ATP]}{[ATP]+6.0\ mM}\right)$$

$$\frac{d[ATP]}{dt} = \frac{3.2}{min}[ADP]\left(\frac{EP_{functional}}{EP_{functional}+EP_{faulty}}\right) * \left(\frac{[P_i]}{[P_i]+10\ mM}\right) * \frac{\psi^{2.5}}{\psi^{2.5}+K_\psi} - 2.0\frac{mM}{min} * \left(\frac{[ATP]}{[ATP]+6.0\ mM}\right) - k7[ATP]$$

$$K_{NADH} = \frac{7.0}{min}\ ;\ K_{NAD+} = 0.01\ mM\ ;\ K_\psi = 131\ mV$$

Oxygen consumption (J_O), as dictated by both OXPHOS activity and ROS production (pmol/min/worm):

$$\frac{d[J_O]}{dt} = \frac{3.5\ L * pmol}{worm * mmol}\left(\left[\frac{1}{4}K_{NADH} * [NADH] * \left(\frac{EP_{functional}}{EP_{functional}+EP_{faulty}}\right)\right] + \frac{1\ mM}{1000000\ nM}\left[PQ_{ROS} * \frac{v4}{\left(1+\frac{[O_2^{\cdot-}]}{Ki}\right)} * \left(\frac{EP_{faulty}}{EP_{functional}+EP_{faulty}}\right)\right]\right)$$

Sirtuin activity, as dictated by both NAD^+ breakdown and stilbenoid polyphenol exposure:

$$\frac{d[Sirtuin\_activity]}{dt} = PT * \left(\frac{[NAD^+]}{[NAD^+] + K_{NAD+}}\right)$$

EQUATION BOX 4.3

Box 4.3: Conditional and rate-dependent statements governing the rule-based categorization of mitochondrial stress, via the agent-based paradigm.

It is assumed that all mitochondria in the early stages of life are initially fully functioning and unstressed [187, 178]. As life progresses, the mitochondria undergo various levels of stress [178, 214], which have been roughly phenotyped and categorized for the purposes of the agent-based model. In our model, a mitochondrion can be **(A.)** functioning and optimal capacity (maximal ATP production), with little to no available stressors (ROS, accumulated proteins, damaged DNA), **(B.)** functioning below maximum capacity but still within the optimal range, in the presence of increased stressor concentrations, **(C.)** significantly stressed and malfunctioning with respect to energy production, or **(D.)** severely stressed with high amount of damaged genetic material, thus producing very little ATP and large amounts of superoxide. The transitions between these states are rate-dependent and governed by the corresponding stressors that account for these pathological micro-phenotypes [178, 214], as seen in the equations below. The constants involved in facilitating these stress and recovery transitions have been optimized (*StressConstant = 0.850 events* $\%EP_{faulty}^{-1}$ nM_{ROS}^{-1} hr^{-1}*; RecoveryConstant = 1.775 events* $\%EP_{faulty}$ nM_{ROS} hr^{-1}) so that the stress-state results relate closely to true biological stressor levels in WT *C. elegans* [182, 190]. Relative to these stress-states, the model accounts for mitochondrial autophagy (mitophagy), where the cell will recognize the existence of damaged mitochondria and effectively destroy such organelles in a rate-dependent manner following retrieval of such stress signals [174, 193]. The stress signals emitted from the mitochondria vary in magnitude from state to state, as defined by the model—where insignificantly-stressed mitochondria will weakly activate the mitophagic mechanisms, significantly stressed mitochondria will most effectively activate mitophagy, and severely stressed mitochondria will suffer from hypothesized UPR^{mt}-mediated overprotection and compromised stress signaling. Mitophagy here is assumed to be initiated by ineffective mitochondrial protein transport as well as SKN-1 or DAF-16 activation [193, 191, 215, 216, 217], and is therefore inversely correlated with these corresponding activities (outlined in the cell-level system-dynamics methods). Mitochondrial recycling/biogenesis is also a concomitant event that occurs within mitochondrial stress and quality control in the aging *C. elegans* [193], and it is here accounted for by (1.) the movement from high stress states to low stress states, and (2.) a timeout-triggered (every 1000-3000 min) agent-addition event. Such agent addition events occur more rapidly upon SKN-1 activation [193, 216], where biogenesis is increased by 7–20% at maximum activity.

Stochastic rates for movement of increasing stress states, based on protein accumulation:

$$\text{Transition 1}: Mean\ events\ per\ hour = StressConstant * [EP_{faulty}] * ([O_2{}^{\cdot -}] + [H_2O_2])$$

$$\text{Transition 2}: Mean\ events\ per\ hour = StressConstant * [EP_{faulty}] * ([O_2{}^{\cdot -}] + [H_2O_2])$$

$$\text{Transition 3}: Mean\ events\ per\ hour = StressConstant * [EP_{faulty}] * ([O_2{}^{\cdot -}] + [H_2O_2])$$

Stochastic rates for movement of decreasing stress states, based on recovery of mitochondrial quality:

$$\text{Transition 4}: Mean\ events\ per\ hour = RecoveryConstant * \frac{1}{[EP_{faulty}] * ([O_2{}^{\cdot -}] + [H_2O_2])}$$

$$\text{Transition 5}: Mean\ events\ per\ hour = RecoveryConstant * \frac{1}{[EP_{faulty}] * ([O_2{}^{\cdot -}] + [H_2O_2])}$$

$$\text{Transition 6}: Mean\ events\ per\ hour = RecoveryConstant * \frac{1}{[EP_{faulty}] * ([O_2{}^{\cdot -}] + [H_2O_2])}$$

Mito-transport-, SKN-1-, and DAF-16-dependent [215] rates of mitochondrial loss via mitophagy (Segments "R" and "B" represent xenobiotic-induced perturbations of mitophagy rate, outlined in the last section. When unperturbed, R = 1 and B = 1):

$$\text{Transition 7}: Mean\ events\ per\ day = 10\% \left(1 - \left(\frac{[TIMM23]}{[TIMM23] + Kt}\right)\right) * \mathbf{R} * \mathbf{B} * \text{DAF16\_activity} * \text{SKN1\_activity}$$

$$\text{Transition 8}: Mean\ events\ per\ day = 95\% \left(1 - \left(\frac{[TIMM23]}{[TIMM23] + Kt}\right)\right) * \mathbf{R} * \mathbf{B} * \text{DAF16\_activity} * \text{SKN1\_activity}$$

$$\text{Transition 9}: Mean\ events\ per\ day = 30\% \left(1 - \left(\frac{[TIMM23]}{[TIMM23] + Kt}\right)\right) * \mathbf{R} * \mathbf{B} * \text{DAF16\_activity} * \text{SKN1\_activity}$$

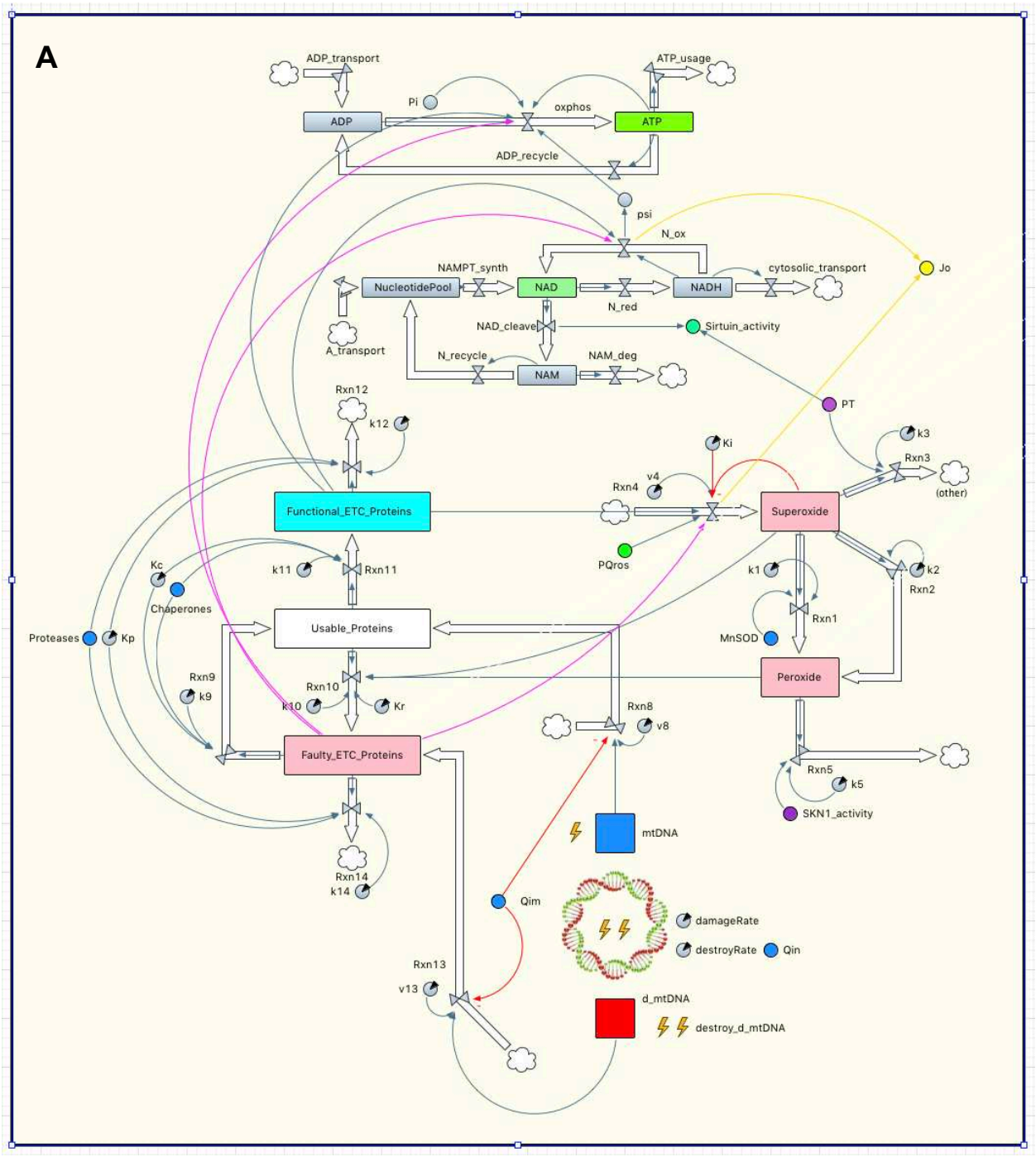

FIGURE 4.2A

Schematics of mitochondrion-level modeling dynamics: mitochondrion-level biochemical SD network in AnyLogic.

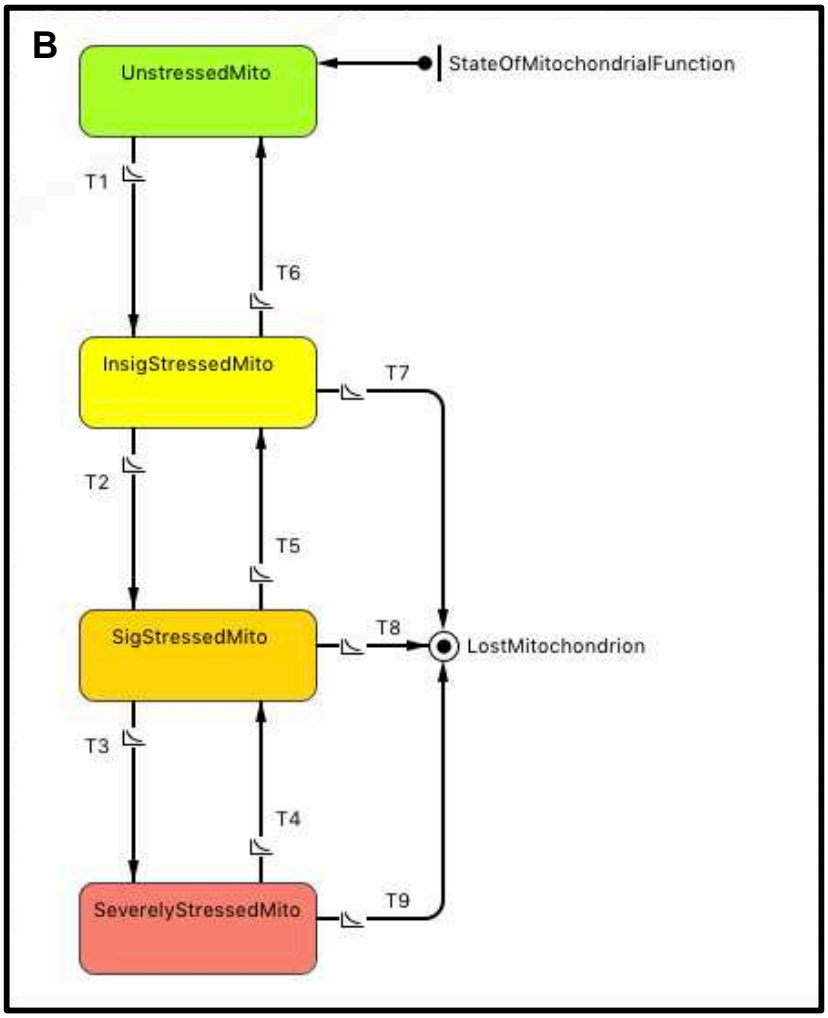

FIGURE 4.2B

Schematics of mitochondrion-level modeling dynamics: state-chart delineating the categorization of mitochondrial stress within the agent-based aging paradigm.

TABLE 4.3

Table 4.3. Parameters of interest for the proposed intracellular biochemical system.

Parameter	Symbol	Value Range	Units	Source
Zero-order production constant for ATFS-1	*v15*	8×10^{-2}	% min^{-1}	100%[SS]
Maximum UPR^{mt}-mediated production of ATFS-1	*v15max*	v15 (1.5)	% min^{-1}	[187,189][A]
Hill coefficient for graded UPR^{mt}-mediated response	*n*	1 – 2	unitless	[187][A]
ATFS-1 DNA-binding affinity constant	*Kb*	38.03	%	[182, 187][O]
Rate constant for mitochondrial import of ATFS-1	*Kmt*	95.01	min^{-1}	[187][O]
EC_{50} for ATP-dependent mitochondrial transport efficacy, presumably governed by Michaelian kinetics	*Ka*	11.95	mM	[182, 187][O]
Rate constant for nuclear import of ATFS-1	*Kni*	5.00	min^{-1}	[187][O]
Elimination constant for ATFS-1	*Ke15*	8.0×10^{-4}	min^{-1}	[208, 187][A]
Zero-order production constant for TIMM23	*Ko16*	1.4×10^{-3}	% min^{-1}	100%[SS]
Maximum UPR^{mt}-mediated production of TIMM23	*Kmax16*	Ko16 (0.7 – 1.5)	%	[187][A]
Elimination constant for TIMM23	*Ke16*	3.5×10^{-5}	min^{-1}	[208][C]
EC_{50} for TIMM23-dependent mitochondrial transport efficacy, presumably governed by Michaelian kinetics	*Kt*	34.843	%	[182, 218][O]
Zero-order production constant for HSP60	*Ko17*	1.9×10^{-2}	% min^{-1}	100%[SS]
Maximum UPR^{mt}-mediated production of HSP60	*Kmax17*	Ko17 (1.0)	%	[187,189][A]
Elimination constant for HSP60	*Ke17*	1.9×10^{-4}	min^{-1}	[208][C]
Zero-order production constant for HSP70	*Ko18*	1.9×10^{-2}	% min^{-1}	100%[SS]

TABLE 4.3 (CONTINUED)

Table 4.3 (continued). Parameters of interest for the proposed intracellular biochemical system.

Parameter	Symbol	Value Range	Units	Source
Maximum UPR^{mt}-mediated production of HSP70	*Kmax18*	Ko18 (1.7 – 3.0)	%	[187,189]^{A}
Elimination constant for HSP70	*Ke18*	1.9×10^{-4}	min^{-1}	[208]^{C}
Zero-order production constant for i-AAA	*Ko19*	2.6×10^{-2}	% min^{-1}	100%^{SS}
Maximum UPR^{mt}-mediated production of i-AAA	*Kmax19*	Ko19 (1.0)	%	[189]^{A}
Elimination constant for i-AAA	*Ke19*	2.6×10^{-4}	min^{-1}	[208]^{C}
Zero-order production constant for m-AAA	*Ko20*	2.6×10^{-2}	% min^{-1}	100%^{SS}
Maximum UPR^{mt}-mediated production of m-AAA	*Kmax20*	Ko20 (0)	%	[189]^{A}
Elimination constant for m-AAA	*Ke20*	2.6×10^{-4}	min^{-1}	[208]^{C}
Zero-order production constant for MnSOD	*Ko21*	3.0×10^{-6}	mM min^{-1}	[182,198]^{SS}
Maximum UPR^{mt}-mediated production of MnSOD (Indirect)	*Kmax21*	Ko21 (0.5 – 1.5)	mM min^{-1}	[188]^{A}
Elimination constant for MnSOD	*Ke21*	$6.0 – 12.0 \times 10^{-4}$	min^{-1}	[219]^{A}
Zero-order constant for glycolysis-mediated ATP production	*v22*	0 – 0.18	mM min^{-1}	[220]^{A}
Maximum UPR^{mt}-mediated production of glycolysis factors	*v22max*	v22 (0.5 – 3.0)	mM min^{-1}	[187,189,221]^{A}
Cytosolic ATP turnover	*k23*	2.1	min^{-1}	[201]^{C}

SS Optimized in the simulation to achieve the reported unstressed physiological steady-state value, percentage or range.
O Individually optimized value, generated using AnyLogic calibration experiments to best fit/emulate reported curves.
A Quantitated assumption based on qualitative evidence.
C Units converted to adhere to model standards.

EQUATION BOX 4.4

Box 4.4: Equations pertaining to cell-level biochemical kinetics.

Dynamics of ATFS-1 concentrations within the cytosolic, mitochondrial, and nuclear compartments (PQ_{UPRmt} is a function of paraquat exposure, outlined in the last section):

$$\frac{d[ATFS1]}{dt} = v_{15} + v15_{max}\left(\frac{[nATFS1]^n}{K_b{}^n + [nATFS1]^n}\right) - K_{mi}\left(\frac{[ATP]_{avg}}{[ATP]_{avg} + Ka}\right)\left(\frac{[TIMM23]}{[TIMM23] + Kt}\right)[ATFS1] - K_{ni}[ATFS1]$$

$$\frac{d[mATFS1]}{dt} = \boldsymbol{PQ_{UPRmt}} * K_{mi}\left(\frac{[ATP]_{avg}}{[ATP]_{avg} + Ka}\right)\left(\frac{[TIMM23]}{[TIMM23] + Kt}\right)[ATFS1] - K_{e15}[mATFS1]$$

$$\frac{d[nATFS1]}{dt} = K_{ni}[ATFS1] * (Sirtuin\_activity) - K_{e15}[nATFS1]$$

$$\frac{d[ATFS1\_activity]}{dt} = \left[\frac{[nATFS1]^n}{K_b{}^n + [nATFS1]^n}\right]$$

*where $[ATP]_{avg}$ represents the average ATP concentration surveyed over a population of mitochondria for a given cell.

Dynamics and normalized activity of DAF-16 and SKN-1 transcription factors, controlled by oxidative stress signaling (and to a degree sirtuin-mediated deacetylation), which leads to accumulation in the nuclear compartment:

$$\frac{d[nDAF\_16]}{dt} = K_{dni} * \left(\frac{[ROS]_{avg}}{[ROS]_{avg} + K_{dROSact}}\right) * (K_{dSIRact} * Sirtuin\_activity) - K_{de}[nDAF\_16]$$

$$K_{dni} = 1.0\frac{\%}{min} \quad \wedge \quad K_{de} = \frac{0.01}{min} \quad \wedge \quad K_{dROSact} = 100\ nM \quad \wedge \quad K_{dSIRact} = 75\%$$

$$\frac{d[DAF16\_activity]}{dt} = 1.0 + \left(\frac{[nDAF\_16]^2}{50\%^2 + [nDAF\_16]^2}\right)$$

$$\frac{d[nSKN\_1]}{dt} = K_{sni} * \left(\frac{[ROS]_{avg}}{[ROS]_{avg} + K_{sROSact}}\right) * (K_{sSIRact} * Sirtuin\_activity) - K_{se}[nSKN\_1]$$

$$K_{sni} = 1.0\frac{\%}{min} \quad \wedge \quad K_{se} = \frac{0.01}{min} \quad \wedge \quad K_{sROSact} = 75\ nM \quad \wedge \quad K_{sSIRact} = 25\%$$

$$\frac{d[SKN1\_activity]}{dt} = 1.0 + \left(\frac{[nSKN\_1]^2}{50\%^2 + [nSKN\_1]^2}\right)$$

*where $[ROS]_{avg}$ represents the average ROS concentration surveyed over a population of mitochondria for a given cell.

EQUATION BOX 4.4 (CONTINUED)

Box 4.4 (continued): Equations pertaining to cell-level biochemical kinetics.

Simplified differential equations for time-dependent protein synthesis and degradation of key mito-proteins controlled primarily by the UPR^{mt}:

$$\frac{d[TIMM23]}{dt} = K_{o16} + K_{max16}\left(\frac{[nATFS1]^n}{{K_b}^n + [nATFS1]^n}\right) - K_{e16}[TIM23]$$

$$\frac{d[HSP60]}{dt} = K_{o18} + \left(\frac{[TIMM23]}{[TIMM23] + Kt}\right)\left(K_{max18}\left(\frac{[nATFS1]^n}{{K_b}^n + [nATFS1]^n}\right)\right) - K_{e18}[HSP60]$$

$$\frac{d[HSP70]}{dt} = K_{o19} + \left(\frac{[TIMM23]}{[TIMM23] + Kt}\right)\left(K_{max19}\left(\frac{[nATFS1]^n}{{K_b}^n + [nATFS1]^n}\right)\right) - K_{e19}[HSP70]$$

$$\frac{d[iAAA]}{dt} = K_{o20} + \left(\frac{[TIMM23]}{[TIMM23] + Kt}\right)\left(K_{max20}\left(\frac{[nATFS1]^n}{{K_b}^n + [nATFS1]^n}\right)\right) - K_{e20}[iAAA]$$

$$\frac{d[mAAA]}{dt} = K_{o21} + \left(\frac{[TIMM23]}{[TIMM23] + Kt}\right)\left(K_{max21}\left(\frac{[nATFS1]^n}{{K_b}^n + [nATFS1]^n}\right)\right) - K_{e21}[mAAA]$$

$$\frac{d[MnSOD]}{dt} = K_{o22} + \left(\frac{[TIMM23]}{[TIMM23] + Kt}\right)\left(K_{max22}\left(\frac{[nATFS1]^n}{{K_b}^n + [nATFS1]^n}\right) * (DAF16\_activity)\right) - K_{e22}[MnSOD]$$

*DAF16_activity is coupled with MnSOD production as a known antioxidant response element for this transcription factor. All mitochondrial proteins are also reliant on the efficacy of their transport systems, as delineated by the mathematical expression that utilizes the translocase abundance.

Glycolysis-mediated ATP production, upregulated upon UPR^{mt} activation:

$$\frac{d[ATP]}{dt} = v24 + v24max\left(\frac{[nATFS1]^n}{{K_b}^n + [nATFS1]^n}\right) - k25[ATP]$$

EQUATION BOX 4.5

Box 4.5: Conditional and rate-dependent statements governing the rule-based categorization of cell integrity, dependent upon the mitochondrial agent population within each cell agent.

Respiratory capacity is reportedly lost when deleterious mtDNA mutations hit a threshold value between 60% and 90% [190, 174, 221]. It is assumed that this threshold value can be translated directly as general loss of mitochondrial function, which have been outlined by the conditional eustress and distress states of the model. This distribution of threshold values (triangular distribution used in the model: 60%-62.5%-75%) is used to govern the loss of cellular integrity and the increased probability in cell death. Recovery of such cells in the model is possible, if their mitochondria can restore enough function to return below the lowest possible threshold value of 60%. This strict assumption is made to uphold the standards of true biological systems, which face a great deal of difficulty restoring homeostasis when mitochondrial populations are largely compromised [222]. It has been reported that humans begin to lose brain volume around the age of 40, at a rate of 5% every decade, mainly due to spontaneous neuronal degeneration [223]. If we assume the average human life expectancy at birth is 70 years and if we assume these degradation checkpoints are similarly conserved among eukaryotes like *C. elegans* (average N2 lifespan @ 25 ^{O}C: 20 days [224]), then neuronal death will begin to occur within the nematode around day 11.5 at a rate of 5% every 2.8 days, with a more rapid decline immediately before death. That being said, it has been reported that *C. elegans* do not lose substantial neuronal integrity [225], yet vacuolated compromised neuronal cells and neurodegenerative responses have been observed in these organisms [226]. In light of these findings, the model was designed to primarily determine the dynamics of the age-compromised state for energetically-demanding cells, while attempting to shed light on potential tissue degeneration thereafter. Once mitochondrial conditions force the cell into a compromised state, they have a limited time to recover or they are destroyed. This rate is defined in the model by an exponential distribution that has been characterized meet expected physiological neuronal lifespan.

Stochastic Condition defining loss of general mitochondrial integrity:

$$\left(\frac{DefectiveMitochondria}{TotalMitoCount}\right) > \left(triangular(60\%, 62.5\%, 75\%)\right)$$

Static condition defining cell recovery based on restoration of general mitochondrial quality:

$$\left(\frac{DefectiveMitochondria}{TotalMitoCount}\right) < 60\%$$

Stochastic rate of cell death *subsequent* to loss of mitochondrial function:

$$Mean\ number\ of\ compromised\ cell\ death\ events\ per\ day = 8.25 \times 10^{-2}$$

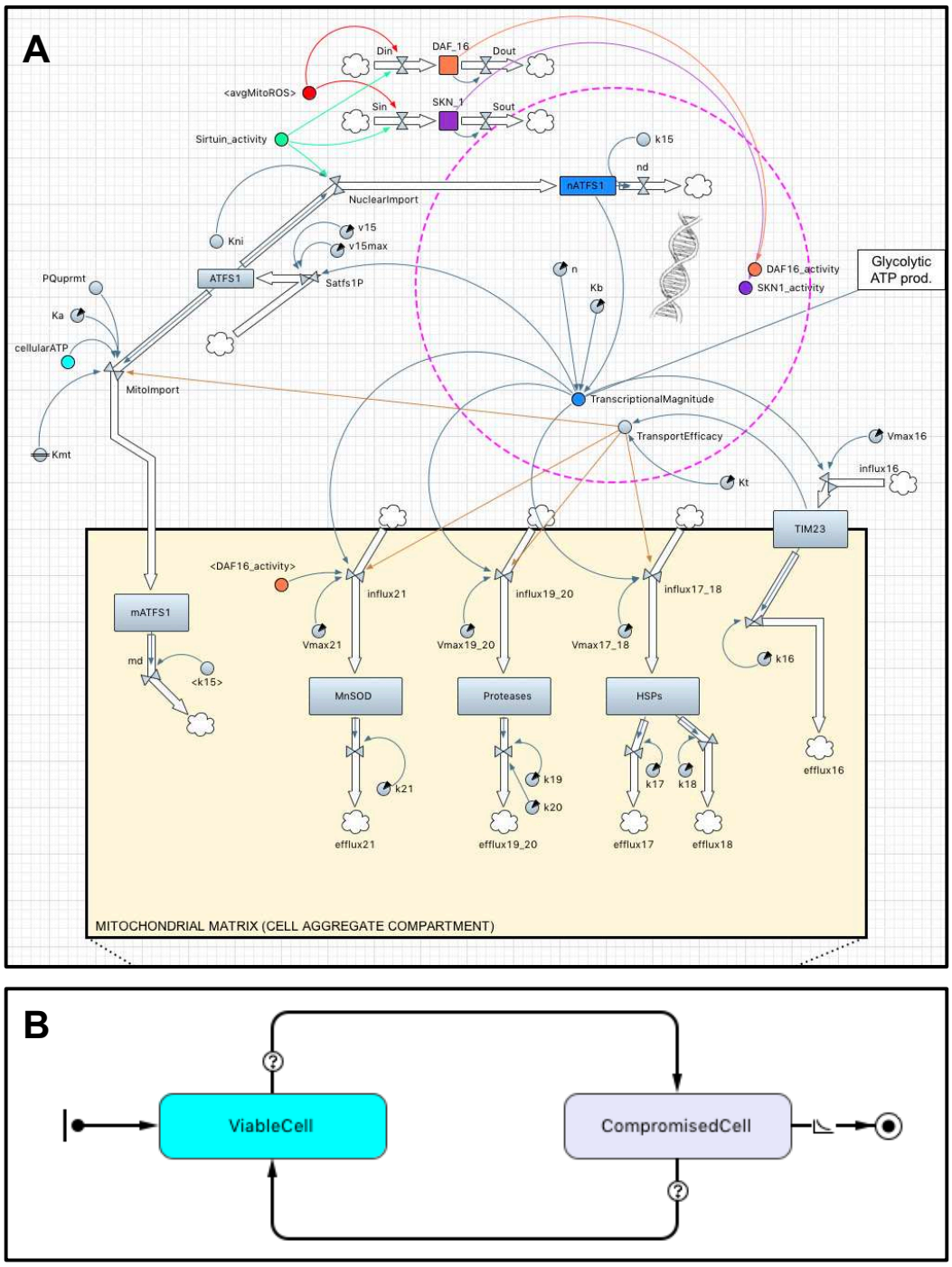

FIGURE 4.3

Schematics of cell-level modeling dynamics. **(A)** Cell-level biochemical SD network in AnyLogic. **(B)** State-chart for the conditional categorization of each cell's mitochondrial integrity.

Cell-level system-dynamics and discrete-event computational methods

The intracellular equation networks are displayed in Box 4.4, cellular agent-based methods are displayed in Box 4.5, and all corresponding parameters are displayed in Table 4.3. Schematics of the intracellular simulation build are displayed for the ODE-based network (Fig. 4.3A) and the agent state chart (Fig. 4.3B).

Computational methods for organism-level biomarker and endpoint capture

Equations used to capture agent counts and tissue concentrations of parameters of interest are displayed in Box 4.6.

EQUATION BOX 4.6

Box 4.6: Equations used to capture tissue concentrations of parameters of interest, where "i" is the current number of total mitochondria in the system and "n" is the current number of neurons. The system initially contains 65 neurons for simplicity.

$$Mitochondrial\ count\ at\ time\ t = i(t)$$

$$Initial\ cell\ count = n_o \ ; \ \ Current\ cell\ count\ at\ time\ t = n(t)$$

$$Percent\ cell\ mortality = 100\%\left(\frac{n_o - n(t)}{n_o}\right)$$

$$Average\ tissue\ mtROS\ concentration = \left(\frac{\sum_0^i [Peroxide + Superoxide]}{i(t)}\right)$$

$$Average\ tissue\ ATP\ concentration = \left(\frac{\sum_0^i [ATP]}{i(t)} + \frac{\sum_0^n [ATP_{Glycolysis}]}{n(t)}\right)$$

$$Percent\ mtDNA\ copies\ damaged = \left(\frac{\sum_0^i [\Delta mtDNA]}{\sum_0^i [mtDNA] + \sum_0^i [\Delta mtDNA]}\right) * 100\%$$

$Average\ tissue\ NAD^+\ concentration = \left(\frac{\sum_0^i [NAD^+]}{i(t)}\right)$ → Normalized to earliest time point (relative)

$$Average\ tissue\ oxygen\ consumption\ rate = \left(\frac{\sum_0^i [J_O]}{i(t)}\right)$$

Modeling alterations for virtual pharmacological and genetic perturbations

Use of Rapamycin and Bafilomycin. One virtual pharmacological perturbation mode within the model addresses mitophagy flux. One perturbation deals with the established role of the mechanistic target of rapamycin (mTOR), which normally acts to inhibit selective mitophagy and reduce the rate of mitochondrial degradation. It has been identified that this protein is well conserved among eukaryotes, and such a homolog of this protein has been identified in *C. elegans* [227] which is indeed, as it is in mammals, inhibited upon rapamycin administration [215]. It has been well established that rapamycin acts through this mechanism to decrease heteroplasmic mtDNA accumulation in immortalized neurons [228] and to alleviate general mitochondrial dysfunction in whole rat brains (as assessed by oxidative damage biomarkers and ATP levels) [229]. Assuming this therapeutic effect is mechanistically conserved among eukaryotes, rapamycin is used here as a virtual xenobiotic to increase the rate of mitophagy. It is administered virtually within different dosing schemes at a concentration of 15 nM (which equates to 18.3 μg/L, within the therapeutic range for serum levels of 5-20 μg/L [228]). Once administered instantaneously, it virtually affects the cells by a maximal fraction (X_R) of 1.5 in relation to its EC_{50} (estimated at ~10 nM [228]), and it begins to decrease in concentration with an aqueous half-life of about 10 h [230]. Bafilomycin A1, in contrast, facilitates an inhibition of autophagy in *C. elegans* by preventing the maturation and accumulation of autophagic vesicles [231]. Bafilomycin A1 is virtually administered here within different dosing schemes in a similar fashion at 10 nM, with a maximal fraction (X_B) of 0.5, an EC_{50} of ~7 nM [231], and a low-end estimate of the culture half-life at 40 h (adapted from *in vivo* pharmacokinetic data for

the structurally similar azithromycin [232]). The pharmacodynamic equations outlined below (Box 4.7) for rapamycin or bafilomycin administration are multiplied by the stochastic mitophagy transitions 7, 8 and 9 within the mitochondrial agent-based paradigm (Box 4.3), and subsequently integrated over time for different dosing schemes (*note: there is no direct effect when concentrations of either chemical are zero*).

Use of Paraquat. As an additional and different type of mechanistic perturbation, paraquat is virtually used here for its aging-related pro-oxidant properties within the mitochondria [233–235] and for its ability to induce the UPR^{mt} [187]. Paraquat is virtually administered here in a similar fashion to rapamycin and bafilomycin, at a concentration of 100 μM (high) or 5 μM (low), with an environmental half-life that far exceeds the normal nematode lifespan [236], and so paraquat concentrations will simply be clamped within different dosing schemes. Paraquat perturbs the system using the same types of equations, however, since paraquat perturbs the system in two different areas (superoxide production rate *and* mitochondrial import of ATFS-1) in two distinctly different and opposing ways, the functions for each are separately categorized, as outlined below (Box 4.7). For the function pertaining to its pro-oxidant properties: the constant for maximal rate increase, X_{PQR}, is set at 0.4, and the EC_{50} for this effect is set at 25 μM [estimations; 237, 238]. For the function pertaining to its UPR^{mt} activation (presumably due to lack of ATFS-1 mitochondrial import efficiency): the constant for maximal impedance effect, X_{PQU}, is set at 0.75, and the EC_{50} for this effect is set at 50 μM [estimations; 187]. These functions PQ_{ROS} and PQ_{UPRmt} (Box 4.7) are integrated over time for various dosing schemes and are then multiplied to the rates of mitochondrial superoxide production (Box 4.2) and mitochondrial ATFS-1 import (Box

4.4), respectively (*note: there is no direct effect when exposure concentration of paraquat is zero*).

Use of Pterostilbene. Plant-derived stilbenes have been extensively studied as anti-aging therapies, with special emphasis on resveratrol and pterostilbene (prominent constituents of blueberries, red grapes and red wine products). Pterostilbene has been recorded as a more potent neuromodulator than resveratrol in aging, even when administered at low doses [239], and therefore is used as the stilbene in this simulation study. Pterostilbene has direct radical scavenging properties and mitigates ROS through highly conserved oxidative stress response pathways as well, via sirtuin activity that acts upon transcription factors such as SKN-1 and DAF-16 in worms [240, 211]. These effects ultimately manifest as reduced ROS content and increased bioenergetic efficiency in aging organisms, and specifically has reduced the levels of ROS in *C. elegans* by about 26% when constantly administered at a concentration of 100 μM [240]. Because of these observations, the pterostilbene function used in this model (same format as rapamycin) utilizes an EC_{50} of 20–60 μM (conservative estimate) and a maximal ROS-mitigating ($X_{PTR)}$ and sirtuin-activating effect (X_{PTS}) of 0.26 and 0.5, respectively, which are applied to the non-peroxide-forming superoxide elimination rate and the Sirtuin_activity dynamic variable. Pterostilbene is administered here at a dose of 100 μM and assumes a culture half-life of 12 h due to its poor aqueous stability [241] and rapid pharmacokinetic clearance [242]. All of these factors are incorporated into the function *PT* (Box 4.7), which is applied to the rates (seen in Box 4.2) of mitochondrial superoxide elimination and peroxide elimination (*note: there is no direct effect when exposure concentration of pterostilbene is zero*).

Varied Dosing Schemes. Dosing schemes for rapamycin, bafilomycin, pterostilbene and paraquat were altered and/or combined to produce an array of exposure scenarios. For rapamycin, bafilomycin and pterostilbene, doses were administered at 0 min and every 2500 min thereafter; the resulting cellular exposure at any given time point was determined by their culture half-life kinetics. For paraquat, high or low doses were clamped to maintain a constant exposure value. For all of these xenobiotics, their administration was performed constantly, early (0–10000 min), mid-life (10000–15000 min), or late (15000–30000 min).

Genetic Perturbations. To identify the role of key genes as they relate to this system, several were virtually knocked down and the endpoints of interest were observed and compared to the control group. Such genes were those encoding for MnSOD, SKN-1, and DAF-16. To make these virtual perturbations, the rate of productive expression for these functional proteins were fractionalized for the duration of the simulation, to simulate such reduced genetic activity for the corresponding genes.

Accessibility of simulation files

The complete simulation along with the corresponding file packages can be accessed online through the RunTheModel platform and AnyLogic Cloud platform (https://cloud.anylogic.com/#/model/c5ab331e-20aa-42ce-9ce6-39e80fe44983). Full file packages are openly accessible (.alp format) via both platforms as well as upon direct request to the corresponding author. A free version of the AnyLogic software for all operating systems is available from the distributer as a Personal Learning Edition (PLE), and a trial package of the University Researcher license is available.

EQUATION BOX 4.7

Box 4.7: Functions used to define virtual pharmacological perturbations within the model.

Function of pharmacological perturbation by rapamycin: $\boldsymbol{R} = 1 + X_R\left(\frac{[Rapamycin]}{[Rapamycin] + EC_{50}}\right)$

Function of pharmacological perturbation by bafilomycin: $\boldsymbol{B} = 1 - X_B\left(\frac{[Bafilomycin]}{[Bafilomycin] + EC_{50}}\right)$

Function of increased ROS production by paraquat: $\boldsymbol{PQ_{ROS}} = 1 + X_{PQR}\left(\frac{[Paraquat]}{[Paraquat] + EC_{50}}\right)$

Function of ATFS-1-mito-import inhibition by paraquat: $\boldsymbol{PQ_{UPRmt}} = 1 - X_{PQU}\left(\frac{[Paraquat]}{[Paraquat] + EC_{50}}\right)$

Function of mito-sirtuin activation by pterostilbene: $\boldsymbol{PT} = 1 + X_{PTS}\left(\frac{[Pterostilbene]}{[Pterostilbene] + EC_{50}}\right)$

Function of radical-scavenging capacity by pterostilbene: $\boldsymbol{PT} = 1 + X_{PTR}\left(\frac{[Pterostilbene]}{[Pterostilbene] + EC_{50}}\right)$

4.1.3 Simulation results for mitochondrial aging

Multimethod simulation development

The pathways of interest for the model were selected based on their broadly protective or damaging mitochondrial effects and their conserved significance toward the aging process observed over recent years. Such pathways were then compiled into a fully integrated system of mitochondrial health (Fig. 4.1A). This network was constructed within our simulation interface predominately by using deterministic frameworks to model both intramitochondrial reactions (Fig. 4.2, panel A) and cytosolic and nuclear activities (Fig. 4.3, panel A). To extend our investigation beyond traditional single-method deterministic modeling, we overlaid an agent-based framework for

multiple events that have classically been difficult to model with differential equations and flow rates. This framework was primarily added to observe the aging kinetics of mitochondrial stress-state phenotyping (Fig. 4.2, panel B) and mito-compromised cell states that eventually result in apoptotic cell death (Fig. 4.3, panel B). Such agent-based events occur discretely within the model and are bound by conditions or stochastic damage-dependent frequencies.

It is important to note that this multimethod framework was built expansively and hierarchically (Fig. 4.1B), where the model simulated a population of cells each with its own functioning reaction network and with its own population of mitochondria that were constantly undergoing biogenesis, stress-dependent mitophagy, and mitochondrial recycling. Each mitochondrion within a cell's population also contained its own stochastic reaction network that controlled not only its own phenotypic stress state, but the state of the cell and thus the states of other mitochondria.

To fill this network with realistic parameters and relevant reaction schemes for the aging nematode, we gathered a vast set of information from the literature to determine: mitochondria counts and mtDNA counts (Table 4.1 and Equation Box 4.1); mitochondrion-level system-dynamics and discrete-event computational methods for oxidative metabolism, proteostasis, and heteroplasmic mtDNA analysis (Table 4.2 and Equation Box 4.2); damage-dependent agent-based progression and recovery through mitochondrial stress states that lead to mitophagy (Equation Box 4.3); cell-level system-dynamics computational methods surrounding the UPR^{mt} and mitochondrial protein import (Table 4.3 and Equation Box 4.4); and agent-based principles that govern stress-dependent cellular degeneration (Equation Box 4.5). These modeled reaction schemes

consist of logically-derived ordinary differential equations (ODEs) or discrete-event statements, which simulate reactions such as ATP production, superoxide production, peroxide formation, mtROS elimination, baseline protein production and transcriptionally-activated protein synthesis, protein import, and damage to and clonal expansion of mtDNA copies. The parameters used to fill these reaction schemes were (1) directly obtained and/or converted from previous models, (2) assumed based on qualitative evidence, or (3) individually optimized over 5,000 parameter iterations to reach appropriate curves for the separate model components. All values and corresponding sources are reported as such in the methods.

We have drawn upon previous deterministic computational models of aging, including a deterministic mathematical analysis of superoxide production and disposition to complement *C. elegans* data [182] and a compartmentalized dynamic model of oxidative metabolism carried out to predict endpoints seen in PD development [243]. We have also gained insights from a sophisticated stochastic modeling analysis of damaged mtDNA in aging mitochondria [174], where an OXPHOS defect threshold between 60–90% determined a deleterious senescence state with poor mitochondrial quality control. We built upon these original constructs and greatly expanded the focus to create a more complete view of the conserved cellular mechanisms implicated in biological aging. In doing so, we made a variety of assumptions and simplifications in our theoretical model to preserve the significance of the pathways involved and to arrive at a network that is mathematically logical. Importantly, the simulation assumes an isothermal environment (20°C) for the duration of each virtual experiment, as *C. elegans* are poikilotherms and thus cannot properly adapt to drastic changes in temperature.

Additional simplifications involve the condensed inclusion of conserved transcription factors DAF-16 (FOXO family *C. elegans* ortholog) and SKN-1 (orthologous to mammalian NRF family proteins), both of which have had profound implications in regulating longevity. When activated, DAF-16 and SKN-1 are largely responsible for mediating metabolic signals and antioxidant activities, and they have also been closely linked to the UPR^{mt} and mitophagy regulation [188, 193, 215, 234]. Since the focus of this study is on mitochondrial function, these two transcription factors were explicitly embedded into the biological network to account mainly for the responses they elicit that significantly affect mitochondrial populations.

To make functional use of our cellular simulation, we have designed equations to capture key endpoints that have been observed quantitatively or qualitatively in aging *C. elegans*. Said endpoints include relative NAD^+ levels, oxygen consumption rates, ATP content, tissue-level and single-cell mtROS content, tissue-level and single-cell mtDNA/ΔmtDNA copy numbers, mitochondrial stress states and mitophagy flux, mitochondria count, and age-dependent cellular senescence states and cell death (Equation Box 4.6). The time frame simulated was between 0 and 30,000 min, to assess a window of time surrounding the average nematode lifespan of 2–3 weeks.

Model performance and predictions for spontaneous functional declines

Cellular characteristics of aging are all directly associated with a general decrease in cellular performance and are predominately regulated by OXPHOS functionality and overall mitochondrial health—especially in tissues with high energy demands. These functional declines ultimately manifest as decreases in ATP

production, which have been ascribed to a variety of factors but the most significant of which include faulty matrix proteins and decreased metabolic substrate availabilities [211]. As a key substrate needed for respiration and other metabolic functions, NAD^+ has been closely studied as an important molecule in healthy aging, and has shown to decline in whole organisms over time [188, 244]. As such, nucleotide dynamics have been incorporated into our simulation constructs as a critical mediator of bioenergetic function, and we have with reasonable uncertainty predicted the relative declines that have been observed in C. elegans experimentally (Fig. 4.4A). As an additional measurable parameter of mitochondrial health and bioenergetic efficiency, oxygen consumption rates were calculated by the simulation over the course of a nematode lifespan and were compared to experimental datasets of the same decline generated by Gruber *et al.* [182], Moroz *et al.* [245] and Mouchiroud *et al.* [188] (Fig. 4.4B). Some experimental oxygen consumption values were converted to units of pmol min^{-1} $worm^{-1}$ assuming an average protein mass per worm of 0.681 $\pm$ 0.002 µg (Table 4.1). As an ultimate output of the bioenergetic simulation component, cellular ATP levels were assessed and compared to values quantified in whole worms by Gruber *et al.* [182] (Fig. 4.4C). The concentration values generated by Gruber *et al.* [182] have been converted to units of mM assuming an average worm body volume of 3.5×10^{-9} L (Table 4.1). In the model, a sharp decline in tissue ATP presents itself after NAD^+ levels have begun to decline (around 7500 min). ATP reduction then saturates around 20,000 min and becomes erratic toward the end of life due to the battery of activated stress responses in age-compromised cells.

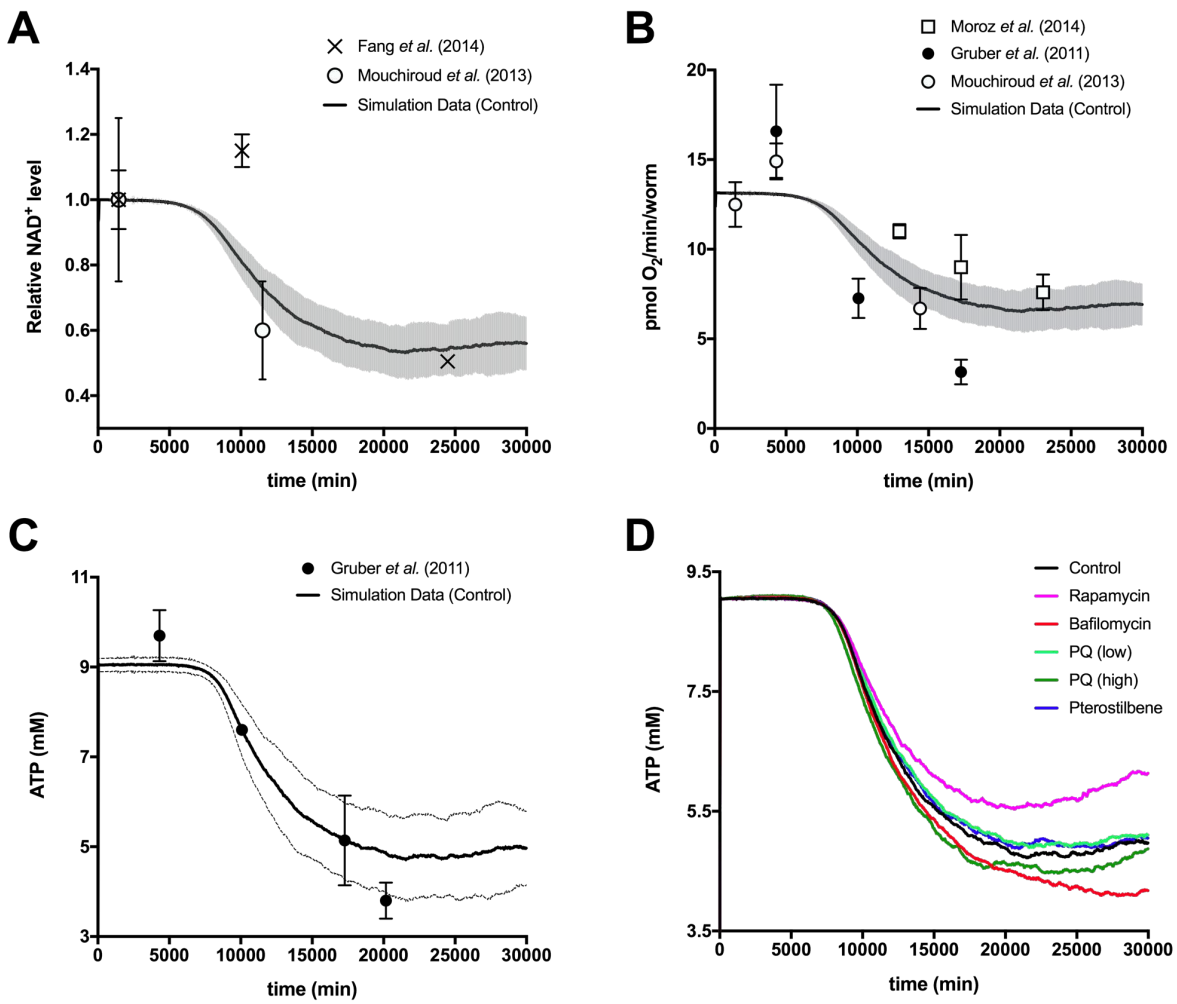

FIGURE 4.4

Experimental and predictive biomarkers of bioenergetic function for normal and pharmacologically-altered aging in *C. elegans*. **(A)** Predicted NAD^+ values over time relative to initial time point values, compared to *C. elegans* experimental data from Fang *et al*. [244] and Mouchiroud *et al*. [188]. **(B)** Simulated oxygen consumption decline with age, compared to *C. elegans* experimental data from Mouchiroud *et al.* [188], Gruber *et al.* [182] and Moroz *et al.* [245]. Some experimental oxygen consumption values were converted assuming an average protein mass per worm of 0.681 ± 0.002 µg. **(C)** Simulation ATP data for normal aging, compared to ATP levels shown experimentally in aging *C. elegans* by Gruber *et al*. [182]. Experimental ATP values were converted assuming an average worm body volume of 3.5×10^{-9} L. **(D)** Simulation ATP data was collected for the duration of natural aging as well as a variety of dosing schemes, including those that increased ATP production (rapamycin, pterostilbene, low-dose paraquat) and those that decreased ATP production (bafilomycin, high-dose paraquat).

Because of the hierarchical modeling scheme employed here, we were able to analyze markers of aging at both the tissue-level and in single cells. Specifically, we produced quantitative predictions of single-cell mtROS and heteroplasmic mtDNA content. The model was also designed to phenotypically categorize each individual mitochondrion based on its intramitochondrial OXPHOS defects. Displayed here are three representative cells from the simulated population (Fig. 4.5), each displaying unique characteristics—due to the stochastic modeling techniques used to emulate a real-world degree of expected randomness. Mitochondrial phenotyping (Fig. 4.5, row A), referred to hereafter as mito-phenotyping, allowed us to visualize the totality of the cells' mitochondrial stress states over time: healthy, fully-functioning (green); slightly stressed, unable to greatly activate stress response mechanisms (yellow); significantly stressed, fully capable of stress response activation (orange); and severely damaged, little to no proper respiratory function (red). Some cells saw a steady functional decline with respect to this mito-phenotyping (Fig. 4.5, Cell 1), whereas others saw modest recovery toward late stages in life (Fig. 4.5, Cells 2 & 3). These stress states correspond well with the levels of mtROS seen in each modeled cell (Fig. 4.5, row B). Of these representative cells, the third (Cell 3) experienced the highest level of oxidative stressors early on, but also experienced the highest level of recovery. This corresponds with the hypothesis that superoxide or other free radical species may not be inherently damaging and may actually provide a signal that promotes longevity [183]. Single-cell mtDNA and significantly-damaged mtDNA (ΔmtDNA) copy numbers were also assessed in the simulation (Fig. 4.5, row C), displaying the age-dependent accumulation of heteroplasmic mtDNA. As expected, the cells that accumulated higher

copy numbers of ΔmtDNA faster—especially when far exceeding unperturbed mtDNA copy numbers—experienced the greatest deal of mitochondrial stress.

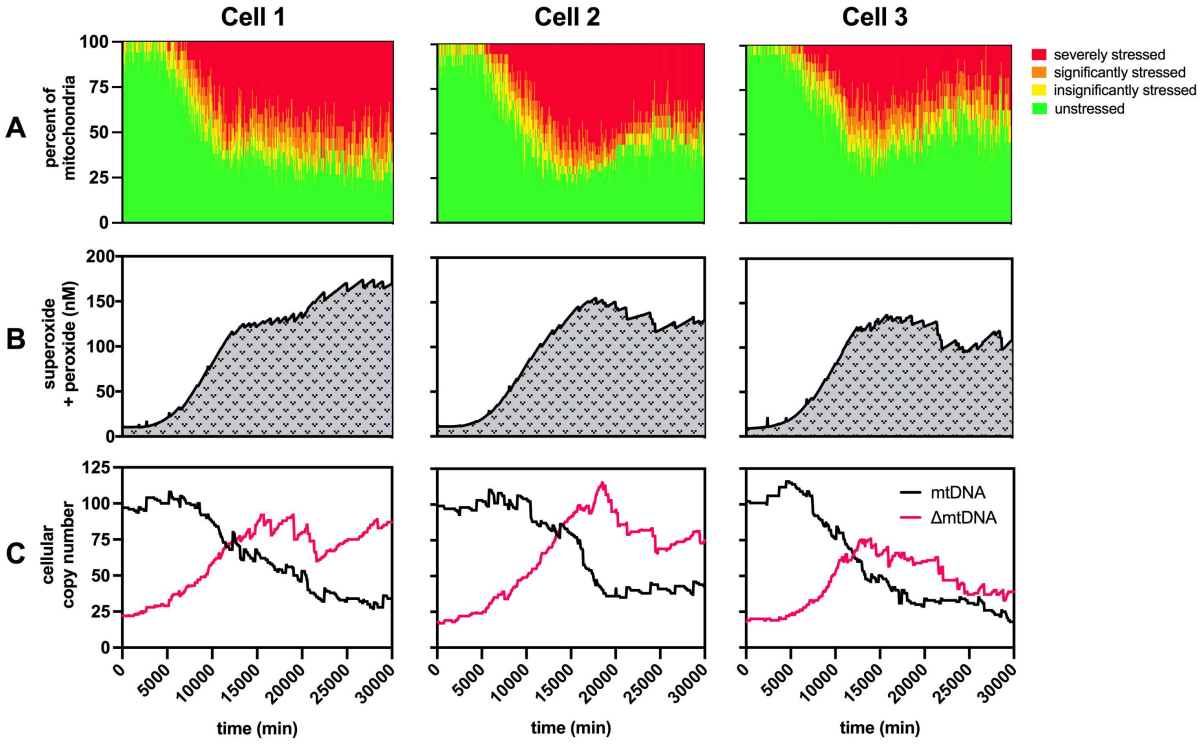

FIGURE 4.5

Stochastic single-cell mitochondrial health data from three representative cells in the model. **(Row A)** Mitochondrial stress-state phenotyping was performed to view the accumulation of stressed or damaged mitochondria over time. Different states of stress are based on metrics of mitochondrial dysfunction, including low respiratory capacity, oxidative burden and poor proteostasis. Some cells saw a steady decline in mitochondrial function (represented by Cell 1), whereas others were able to successfully recover significant portions of their mitochondrial populations (represented by Cells 2 & 3). **(Row B)** Single-cell mtROS content was captured, which inversely correlated with the corresponding phenotypic trends in mitochondrial health. **(Row C)** Single-cell mtDNA and damaged mtDNA (ΔmtDNA) copies were analyzed, where high mutation and damage accumulation corresponded with highly dysfunctional phenotypes.

Mitochondrial dynamics, including biogenesis and selective mitophagy, were simulated, and organelle counts were tracked for an entire population of cells (Fig. 4.6A). Natural aging (control) allowed for a modest increase in mitochondrial content until a midlife stage, and counts significantly declined until the end of life. This is consistent with previously published trends seen in *C. elegans* [193], concerning both general cellular activity as well as neuron-specific mitochondrial tracking. In the simulated cell population, mtDNA and ΔmtDNA content were tracked and presented as a deleterious heteroplasmic mtDNA percentage (Fig. 4.6B). As with other makers of age-related damage, mtDNA copies experienced steady and significant damage with normal aging (control), and the damage percentage saw a slight, yet erratic, decline in late stages of life due to natural defense mechanisms. Oxidative stress levels were measured *in silico* as well (Fig. 4.7A), and closely matched spontaneous increases seen previously in C. elegans [188]. Experimental and simulation values were both normalized to the respective oxidative stress levels immediately preceding the simulated age-compromised state (day 7).

While the network motifs employed in our simulation allow us to reproduce the levels of certain age-dependent respiratory function markers, a sensitivity analysis was also conducted to determine which model functions and constants provide the strongest control over the system. The results of this analysis are tabulated in Table 4.4, where ROS outputs and macromolecule damage levels were sensitively controlled by many different parameters at various ages. Perhaps most notably, mitophagy activity and mitochondrial content at a late age time point were deemed to be the most sensitively controlled by many parameters of the model.

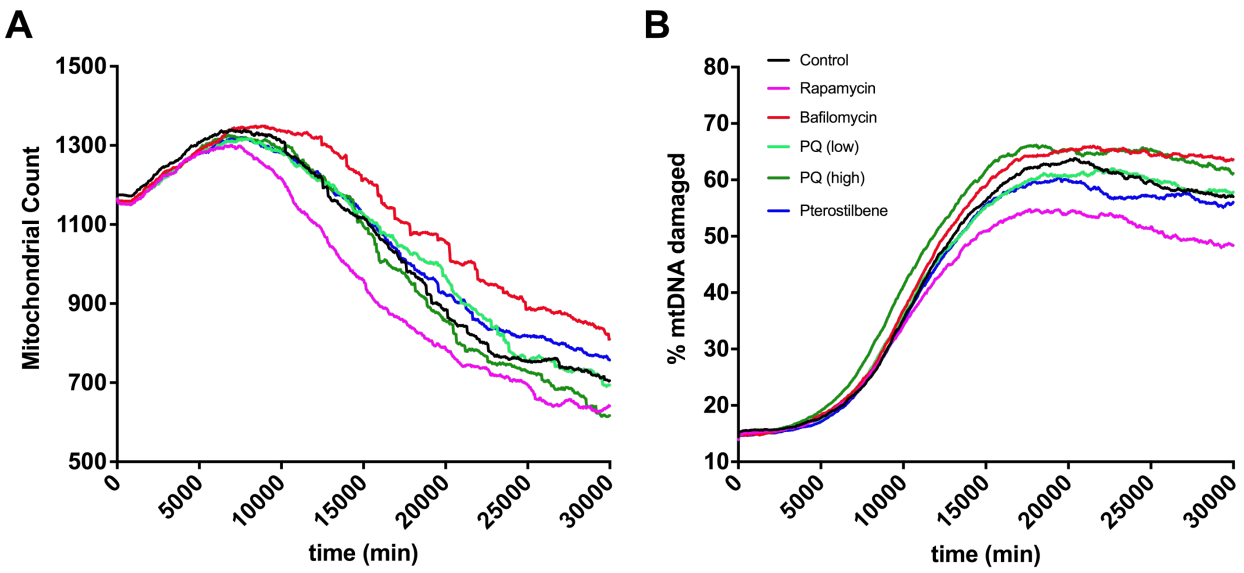

FIGURE 4.6

Model-generated mitochondrial counts and heteroplasmic mtDNA content in normal and pharmacologically-altered aging. **(A)** Mitochondrial counts were assessed in our control simulation and also in the same treatment groups as Fig. 4.4D, displaying results that give rise to changes in aging mitochondrial dynamics, i.e., mitophagy and mitochondrial recycling. **(B)** Percent of mtDNA damage was calculated in each simulation experiment as an important metric of age-related mitochondrial dysfunction. Different perturbation schemes modulated the accumulation of mtDNA modifications, which when reduced has been implicated as a relevant intervention in combatting age-related disease.

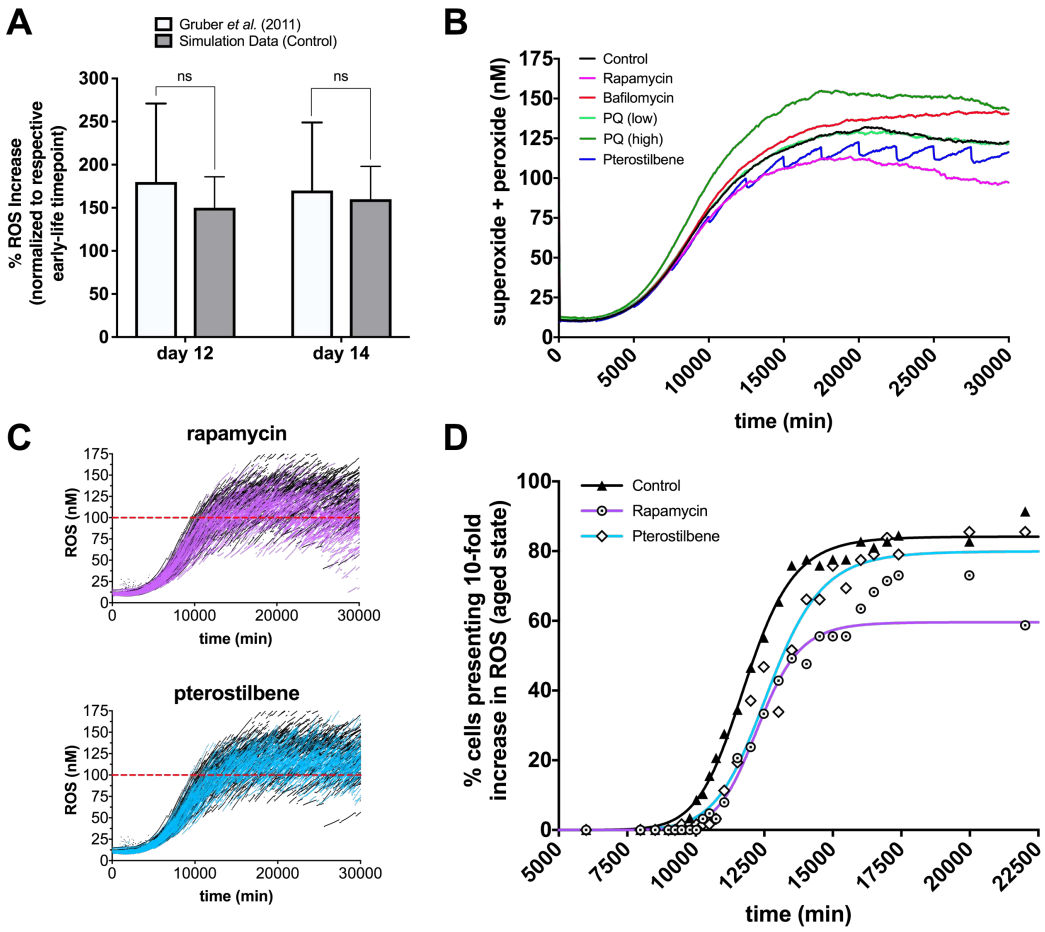

FIGURE 4.7

Simulation analysis of normal and pharmacologically-modified oxidative burden in aging cells. **(A)** The simulation was able to reproduce age-related increases in oxidative species as compared to *C. elegans* data from Gruber and colleagues [188] (ns: $p>0.05$). Increases within simulation or experimental data were normalized to their respective levels seen at the time point immediately preceding a fully aged state determined by the model (~day 7). **(B)** Average oxidative stressor levels, superoxide and peroxide, were determined in a variety of experiments (same treatments as Fig. 4.4D) for the population of cells simulated over the timeframe of interest. **(C)** Single-cell reactive oxygen species (ROS) data were model-generated for each individual cell in natural aging, in rapamycin-exposed cells (top panel, overlaid with control), and in pterostilbene-exposed cells (bottom panel, overlaid with control). These data signify probabilistic, rather than deterministic, mitochondrial activities within each cell giving rise to the natural stochasticity that determines composite ROS values for aging tissues. **(D)** Simulation time required for cells to switch to the age-compromised state, characterized by a 10-fold increase in ROS.

TABLE 4.4

Table 4.4. Normalized sensitivity coefficients (SC) reported for age-dependent mitochondrial population numbers, ROS accumulation, and percent mtDNA heteroplasmy at early (3000 min), midlife (10,000 min) and late (22,000 min) time points throughout the simulation (parameter deemed to have sensitive control when |SC| ≥ 1). Parameters that elicited significant changes to specific response variables are bolded. The normalized sensitivity coefficients also represent positive or negative changes to response variables, as indicated by the sign that precedes each value.

Parameter	**Response variable**								
	Mitochondrial population count			Steady-state ROS concentration			mtDNA heteroplasmy percentage		
	Early	Midlife	Late	Early	Midlife	Late	Early	Midlife	Late
k1	+0.0326	+0.3922	**+1.7021**	-0.1884	-0.0622	+0.0749	-0.6544	-0.5552	-0.1316
k2	+0.0978	+0.4392	+0.7092	-0.4384	**-1.0074**	**-1.0789**	-0.3135	**-1.0288**	-0.1741
k3	+0.0815	+0.2824	**+1.0402**	+0.7218	+0.3029	+0.3872	-0.2911	+0.0716	+0.0752
v4	+0.0978	+0.1412	**+1.4894**	-0.3051	-0.6650	**-1.0557**	-0.5524	-0.7417	-0.4431
k5	+0.0326	+0.1725	-0.2364	**+1.4054**	+0.9251	-0.1180	-0.2090	+0.8689	-0.2198
v6	+0.0489	-0.0157	-0.8511	+0.0167	-0.6347	-0.5773	+0.2252	-0.9644	-0.6175
k7	-0.2445	+0.0000	**+1.3239**	+0.0867	-0.3880	-0.6227	-0.3421	-0.3237	-0.1929
K_{NADH}	-0.0326	+0.1098	**+1.1584**	-0.0483	-0.2734	-0.9642	-0.1879	+0.0211	-0.3222
K_{Ψ}	+0.0326	-0.0627	**+1.0875**	+0.1417	-0.0431	**-1.0619**	-0.5574	+0.0694	-0.4438
K_{NAD+}	+0.0489	+0.4863	**+1.7730**	+0.0167	-0.1214	+0.2700	**-1.1173**	-0.7256	+0.8263
v8	-0.0326	+0.4549	+0.0236	-0.0633	+0.0264	-0.4707	-0.6271	-0.0416	-0.3666
k9	+0.0815	+0.1412	**+2.2695**	-0.0167	-0.4031	-0.5208	-0.3546	-0.2848	-0.4914
k10	-0.1630	+0.1412	**-1.5603**	+0.1250	-0.3349	-0.8619	-0.3036	-0.6079	-0.9190
Kros	-0.1630	+0.1412	+0.1182	+0.1250	-0.3349	-0.7398	-0.3036	-0.6079	-0.3637
k11	-0.0326	+0.4549	+0.0236	-0.0633	+0.0264	-0.4707	-0.6271	-0.0416	-0.3666
k12	-0.0326	+0.4549	+0.0236	-0.0633	+0.0264	-0.4707	-0.6271	-0.0416	-0.3666
Kc	-0.0489	+0.2353	+0.7565	+0.0750	-0.1488	-0.9302	**-1.1285**	+0.4009	-0.8623
Kp	+0.0000	+0.2667	**+2.2695**	-0.4468	**-1.8395**	-0.8127	-0.0697	**-1.3180**	+0.1621
v13	-0.0326	+0.4549	+0.0236	-0.0633	+0.0264	-0.4707	-0.6271	-0.0416	-0.3666
k14	-0.2282	-0.2980	+0.1891	+0.3501	-0.5980	-0.5832	-0.4852	-0.5774	-0.2580
damageRate	-0.0163	+0.1569	+0.1418	+0.2217	-0.4593	-0.4791	**-1.3910**	**-1.0532**	-0.4794
destroyRate	+0.0652	+0.2667	+0.1891	+0.0583	+0.0370	-0.6627	+0.0361	+0.6651	-0.4668
stressConstant	-0.0326	+0.1098	-0.0946	+0.0550	-0.6159	**-1.0147**	-0.5375	**-1.0504**	-0.5832
recovConstant	+0.0000	+0.1412	**+1.3712**	-0.0367	-0.1571	-0.6270	+0.0012	+0.0233	-0.2532
Kb	+0.0163	+0.0784	+0.3310	-0.2884	-0.1350	-0.8480	+0.1294	-0.0816	-0.2509
Kmt	+0.0815	-0.0941	+0.7092	+0.0117	-0.2027	-0.5101	+0.2774	+0.0539	+0.0451
Ka	-0.0489	+0.0000	+0.8747	+0.1634	+0.1755	-0.7183	-0.5860	-0.2854	-0.2989
Kni	+0.0163	+0.1098	+0.2364	+0.1617	-0.2800	-0.5324	-0.0921	-0.1588	-0.0104
Kt	-0.0163	-0.0627	**+1.5603**	-0.0767	-0.4973	-0.2604	-0.1008	-0.7479	-0.1942
$K_{dROSact}$	+0.0652	+0.0157	-0.3546	+0.4168	-0.1309	**-1.5124**	-0.1605	-0.1643	**-1.1647**
$K_{dSIRact}$	+0.0652	+0.2667	+0.8511	+0.2534	-0.3006	-0.1683	+0.0946	-0.7751	-0.4593
$K_{sROSact}$	-0.1304	-0.2353	**+1.0402**	+0.0967	-0.7151	-0.5198	+0.0547	+0.1560	-0.3485
$K_{sSIRact}$	+0.0652	-0.3608	-0.1891	+0.2767	-0.2410	-0.1924	+0.0299	-0.3476	+0.2198

Endpoint changes after control of selective mitophagy

To perturb the computational model, we determined mathematical methods for introducing rapamycin or bafilomycin as regulators of mitophagy (Equation Box 4.7). Such methods included the estimated dose-response curve for autophagy activation/inhibition as well as the culture pharmacokinetics for determining the presence of each agent. Rapamycin is a well-known inhibitor of the mechanistic target of rapamycin (mTOR) complex [215], which ultimately allows for increased autophagic activity (Fig. 4.1A, see Rapa). Bafilomycin, on the other hand, inhibits the formation of autophagosomes, and therefore inhibits general autophagy and selective mitophagy [246] (Fig. 4.1A, see Baf). In our simulation, constant low-level dosing of each of these compounds (15 nM rapamycin or 10 nM bafilomycin, refreshed every 2,500 min) was used in these comparative perturbations. As expected, rapamycin (pink line) curbed the decline of ATP production in aging cells within the simulation experiments, whereas bafilomycin (red line) exacerbated this specific decline in energy production (Fig. 4.4D). Demonstrating that our mathematical perturbations were successful in emulating the function of pharmacological mitophagy-modulators, rapamycin and bafilomycin elicited drastic decreases and increases in mitochondrial count compared to the control, respectively (Fig. 4.6A). In addition, accumulation of deleterious heteroplasmic mtDNA was initiated sooner by bafilomycin exposure and was stunted by exposure to rapamycin (Fig. 4.6B). Rapamycin was used previously to investigate this exact effect, where it was shown to attenuate the accumulation of mtDNA harboring a specific pathogenic mutation [228]. As a result of harboring defective mitochondria, simulated mtROS levels were perturbed by these mitophagy modulators as well, where

rapamycin-exposed cells saw less oxidative stress with age and bafilomycin-exposed cells saw much more (Fig. 4.7B).

Direct and indirect modulation of age-dependent oxidative stress levels

To target alternative pathways involved in our *in silico* cellular mechanism, we chose two particular agents known to modulate mitochondrial processes associated with age-dependent oxidative damage: paraquat and pterostilbene (Equation Box 4.7). Paraquat is a well-established potent ETC uncoupling agent [234] that causes profound increases in oxidative stress (Fig. 4.1A, see PQ). Pterostilbene is best known as a constituent of certain berries and red wine and as a relative of resveratrol, a more commonly known stilbenoid compound. In contrast to paraquat, exposure to pterostilbene or synthetic relatives has shown to indirectly decrease oxidative stress in *C. elegans*, in part by contributing to the activation of DAF-16 and SKN-1 [240] (Fig. 4.1A, see PT). In our simulation, constant dosing of 100 μM pterostilbene and 5 or 100 μM paraquat was used in these comparative perturbations. Interestingly, ATP content was considerably reduced by high-dose paraquat but slightly improved by low-dose paraquat and pterostilbene treatments (Fig. 4.4D). Compared to the control, low-dose (light green line) and high-dose (dark green line) paraquat caused increases and decreases in mitochondrial counts, respectively (Fig. 4.6A), and only high dose paraquat enabled a greater accumulation of ∆mtDNA (Fig. 4.6B). A similar mtROS-dependent effect has been shown experimentally for mtDNA double strand breaks causing accelerated aging in mice [247]. Virtual pterostilbene exposure (blue line) elicited marginally less mitochondrial turnover toward late age (Fig. 4.6A). This finding is

surprising as stilbene compounds have been suggested as agents that promote autophagy [248], but perhaps not with selective and non-selective mitophagy. Pterostilbene was the only compound that prolonged the accumulation of ΔmtDNA even though it eventually reached the same percentage as the control (Fig. 4.6B). This highlights the interesting aging response phenomena associated with stilbene compounds, especially with those that potently affect intramitochondrial reaction networks.

Indicating our mathematics were successful in emulating the toxicological uncoupling effect at the ETC, low-dose paraquat resulted in very slight increases in oxidative stress, whereas the higher dosing scheme prompted a drastic surge in both superoxide and peroxide production (Fig. 4.7B). It is important to note that although low-dose paraquat initially causes increases in mtROS, it also at times caused reductions compared to control at late time points. A similar reduction in mtROS was also observed in our simulation after ablating *sod-2* (MnSOD) at increasing levels (Fig. 4.8A & 4.8B). Consistent with previously published nematode data [240], pterostilbene administration in our analysis allowed for around a 20–25% reduction (slowly reversible) in oxidative stress at the maximal response time points in the model after reaching fully aged states (Fig. 4.7B). Since pterostilbene and rapamycin showed the most promising results for slowing the damaging effects of aging mitochondria, we analyzed their oxidative stress modulation at the single-cell level. Our computational model allowed us to visualize mtROS levels over time overlaid with control data for a population of cells (n = 65; 500 time points), demonstrating both the highly stochastic nature of the model and the protective effects of rapamycin (Fig. 4.7C, top panel) and pterostilbene (Fig. 4.7C,

bottom panel). To distill this information, we determined that 100 nM combined superoxide and peroxide allowed for a deleteriously-aged cellular phenotype and assessed how many cells crossed this threshold at various time points for natural aging (control), rapamycin, and pterostilbene (Fig. 4.7D). Pterostilbene and rapamycin greatly extended the time required for the majority of cells to cross this threshold; however, rapamycin further reduced the number of total cells that experienced this aged phenotype.

Cell death predictions and implications for age-related neurodegeneration

Given that aging and senescence are implicated in various cognitive deficits and neurodegenerative diseases, we used our computational methods to ultimately simulate an age-compromised cell state and subsequent probabilistic death for post-mitotic energetically-demanding cells (Fig. 4.9A). The rate of spontaneous degeneration simulated here corresponds well with wide speculations made about the slow loss of neuronal mass that accompanies old age in mammals [223]. This degenerative response has been more complex to quantitate in nematodes, as the neuronal network appears to be conserved with age [225] yet vacuolization and cellular damage certainly occur [226]. Cells within the model began to enter the compromised state around 10,000 min, shortly after cells began crossing the model-determined mtROS threshold (10-fold increase) as mentioned in the previous section and shown in Fig. 4.7D. Viable cell and cell survival curves, associated with age-compromised cell states and degenerative aging, were generated for a battery of *in silico* mechanistic perturbations,

including the pharmacological treatments of interest as well as reductions in *sod-2*, *daf-16* and *skn-1* expressions (Fig. 4.9B & 4.9C).

Pterostilbene exposure (blue lines) rapamycin exposure (pink lines), low-dose paraquat exposure (light greens) and 90% *sod-2* ablation (yellow lines) all delayed immersion into compromised states and extended cellular longevity, with rapamycin and pterostilbene eliciting the strongest effects. The remaining treatment groups, bafilomycin (red lines) high-dose paraquat (dark green lines), 90% *daf-16* ablation (orange lines) and *skn-1* ablation (purple lines), all resulted in rapid aging and severely decreased survival rates. While *sod-2* ablation resulted in a marginally beneficial response, our simulation results indicate that its expression must be fully reduced to see any increases in longevity-promoting effects (Fig. 4.8C & 4.8D), due to the stress responses that the increased endogenous mtROS activate. This aging delay brought on by the mathematical model substantiates previous studies that have linked increases in oxidative species to extended lifespans [183, 188], however, the timing and duration of genetically- or pharmacologically-induced mtROS must play a critical role in regulating these mechanisms as well.

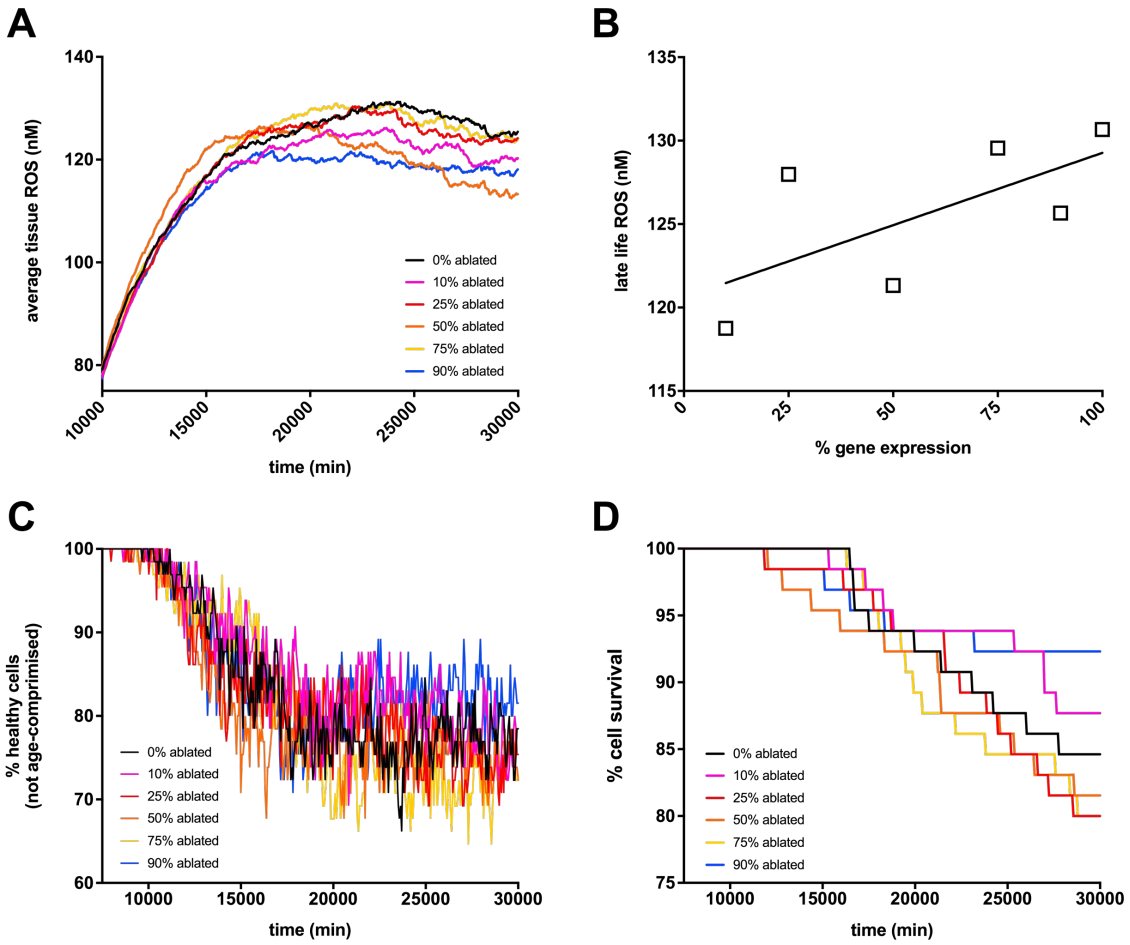

FIGURE 4.8

Varied expressional magnitude of mitochondrial manganese-dependent superoxide dismutase (MnSOD). **(A)** Complete survey of ROS accumulation over time after varying levels of MnSOD ablation. **(B)** Analysis of late life ROS output (24,000 min time point) against varying levels of MnSOD expression. **(C)** Viable cell survey over time after varying levels of simulated knockout. **(D)** Cell survival survey over time after varying levels of simulated knockout.

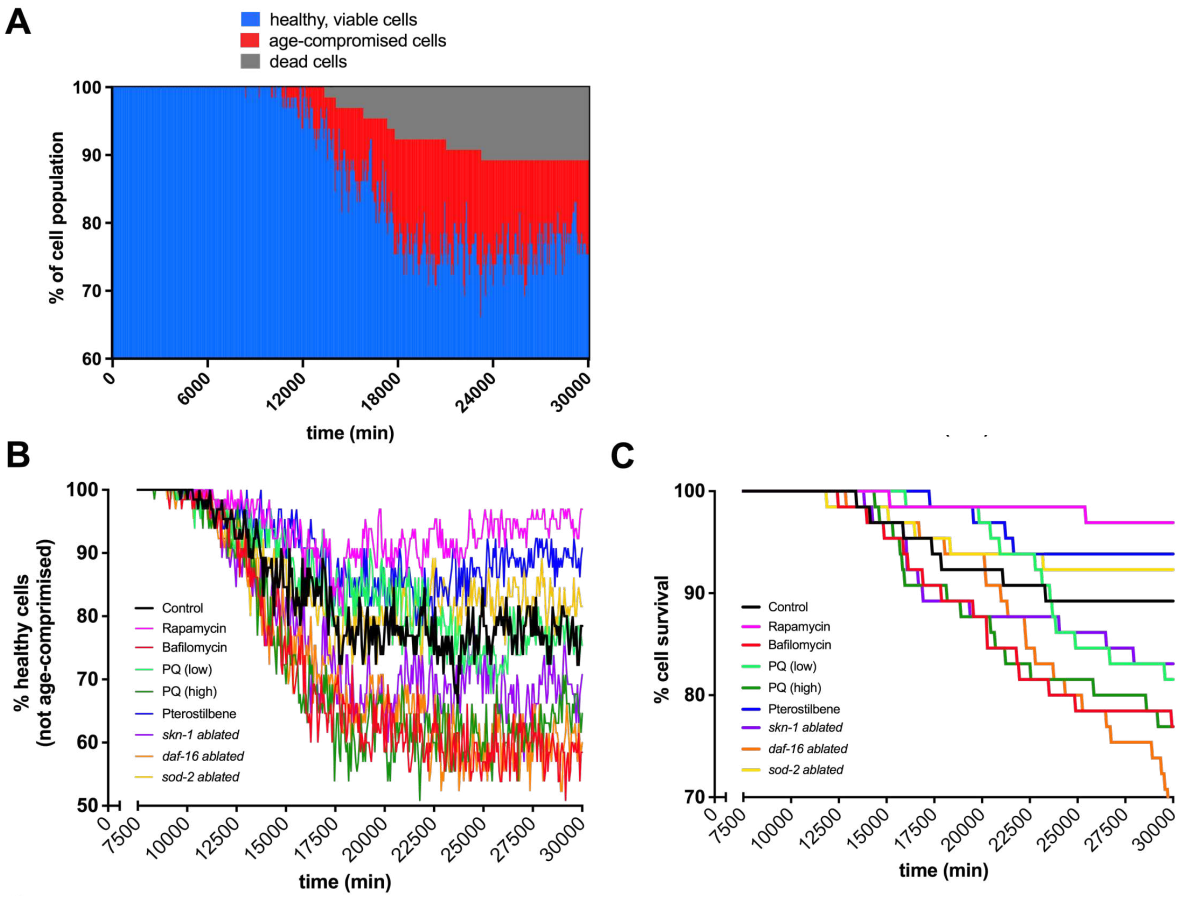

FIGURE 4.9

Age-dependent total cellular damage and degeneration analysis. **(A)** Natural aging, presumably as a result of faulty mitochondrial dynamics, forced healthy cells (blue) into a compromised state (red) in our simulation, where they were required to overcome mitochondrial defects in order to recover. If recovery was insufficient, they died off (gray). **(B)** The dynamics of natural age-compromised cell accumulation (control) was compared to those virtually altered by pharmacological (rapamycin, bafilomycin, paraquat, or pterostilbene exposure) and genetic (*daf-16*, *skn-1*, or *sod-1* ablation) simulation schemes. **(C)** Natural cell survival rates were compared to the same perturbation schemes of interest. Many schemes caused cells to age faster in the simulation, resulting in more death early on. Some simulation perturbations, however, were able to slow the rate of aging and natural degeneration, either slightly or robustly.

4.1.4 Discussions and conclusions

Biological aging is the primary phenomenon governing organismal fitness and has often been deemed the most important risk factor in debilitating and fatal diseases. Age-dependent diseases that are degenerative or senescence-controlled in nature are generally confined to tissues with high energy demands, such as skeletal and cardiac muscle and nervous tissue [249]. These incidences suggest that severe mitochondrial dysfunction and aging are not mutually exclusive processes. The fundamental causalities between the two, however, are considerably complex and challenging to investigate, denoting the ongoing need for innovative and powerful methods in aging research. To provide an additional and systematic means of investigation, we have designed a computational network that integrates many of the sophisticated experiments completed in recent years. By balancing spontaneous free radical damage as well as corresponding mitochondrial stress responses, we have been able to make apt predictions about the aging process in a well-studied model organism. Several of our large-dataset predictions have been validated quantitatively (Fig. 4.4A, 4.4B & 4.4C, Fig. 4.7A) or qualitatively, while several have yet to be experimentally examined, leaving well-designed hypotheses for future work.

As part of our modeling study, we sought to understand how crucial the UPR^{mt} and mitophagy are in balancing the oxidative stress and macromolecule damage that accompany normal, healthy aging. It was revealed in our experiments and global sensitivity analysis that mitochondrial turnover and quality control levels were the most important processes in either softening or exacerbating the deleterious effects of mitochondrial dysfunction in aging. This is substantiated by previous experiments done

in *C. elegans*, which suggest the UPR^{mt} is not a potent regulator of longevity pathways [224], whereas mitophagy likely is [192]. The UPR^{mt}, although not apparently important in regulating the lifespan of a full organism, may play a critical role in the cellular aging mechanisms that regulate tissue-specific healthspans. This is especially true for sensitive tissues with high mitochondrial counts, as they have a direr need to quickly regulate their antioxidant defenses and mitochondrial protein environments. Adding to this complexity, activation of this response must be done carefully, and likely on a low-frequency basis, as the UPR^{mt} has been implicated as a mechanism that can protect aberrant mitochondrial contents [190]. In particular, over-activation of this response has been linked to a higher persistence of mtDNA heteroplasmy. The mechanisms by which this occurs are poorly understood, although they are not entirely dependent upon mitophagy. However, mitophagy may certainly play a small role in the UPR^{mt}'s ability to maintain defective mitochondria, as TIMM-23 expression is upregulated by the UPR^{mt} and is responsible for the import and degradation of pro-mitophagy proteins such as PINK-1 [191]. Therefore, an overexpression of TIMM-23 may limit, for a short duration of time, the amount of mitophagy activity. In contrast to this theory, it has been shown that the complete absence of TIMM-23 isoforms constitutively induces the UPR^{mt} and leads to decreases in lifespan [224]. These observations exemplify the physiological need for an incredibly tight regulation of TIMM-23-dependent transport processes and mitophagic activities that may be programmed to vary with age in an attempt to maximize mitochondrial healthspans.

In addition to gaining mechanistic insights, we used our multimethod simulation to predict the cellular effects brought on by different pharmacological agents that have

been widely studied as modulators of aging, especially in neuronal tissue. Most agents that have been discovered as longevity-promoters have also been known to promote mitochondrial health. Rapamycin exposure has led to stark increases in stress resistance to age-dependent damage in a wide variety of organisms [215, 250, 251], presumably due to its regulatory role in metabolic processes and non-selective autophagy. In our simulation experiments, we applied it as a mitophagy inducer and observed remarkable decreases in heteroplasmic mtDNA content and increases in antioxidant capacity. Both of these rapamycin-induced effects have been observed experimentally [215, 228]. Previous experiments and our simulation work draw attention to rapamycin as not only an agent that can extend the lifespan of an organism, but as a compound that does so by preserving the quality of mitochondria. Plant-derived polyphenols, such as resveratrol and pterostilbene, have also been studied for their potential ability to stunt the aging process through antioxidant activities and mitochondrial pathways. In *C. elegans*, resveratrol has been shown to alleviate oxidative stress and resulting mitochondrial damage associated with respiratory chain deficiencies, resulting in extended lifespan [252]. Although a significant portion of the literature has documented the longevity-promoting effects of resveratrol, much of the recent focus has fallen on pterostilbene and synthetic derivatives, as they have been observed as more potent compounds capable of modulating cellular processes in aging and age-related neurodegeneration [239, 240], in part through the DAF-16 and SKN-1 axes. For this reason, we chose pterostilbene as the virtual stilbene compound to be used in our simulation work. Based on dose-response data that allowed us to calculate its mtROS remediation [240], pterostilbene prolonged mitochondrial damage

accumulation and age-dependent cellular degeneration in our simulations, albeit to a lesser extent than rapamycin. Notably, pterostilbene acts by increasing the activity of NAD^+-dependent deacylases known as sirtuins [211], which promote well-balanced oxidative metabolism within mitochondria, and particular isoforms are involved in activating the UPR^{mt} [188, 253]. If the UPR^{mt} and mild antioxidant defenses are not as powerful anti-aging contributors as mitophagy and mitochondrial biogenesis, this explains the more favorable simulation results returned for rapamycin. Pterostilbene, however, has been known to induce autophagy on some level [248], and NAD^+-dependent sirtuin activities are important in regulating not only bioenergetic functions and antioxidant capacity but mitochondrial dynamics as well [244]; therefore, it must be investigated whether this compound can effectively stimulate the process of selective mitophagy in relevant cell types to promote significant increases in mitochondrial quality.

Computational modeling has recently become a more commonplace technique in gerontological research, with many different types of developed models surfacing over the past decade [173]. Such models include purely deterministic analyses of oxidative metabolism [243], well-developed Boolean approaches for understanding molecular aging networks [254], discrete-event modeling of mtDNA dynamics [174], and high-precision statistical modeling of lifespan determinants [255].

Here we have contributed a new multimethod computational modeling technique for studying the cellular mechanisms of aging as they relate to mitochondrial function and dysfunction. We have built the groundwork for a comprehensive computational model that can reproduce levels of mitochondrial and cellular biomarkers implicated in

aging, with respect to *C. elegans*. In particular, our model has highlighted the potent effects of (1) mitophagy induction or inhibition and (2) the critical stress response genes, such as *daf-16* and *skn-1*, required to maintain healthy aging and to further promote longevity through oxidative mechanisms. After further mechanism integration and experimental interrogation, this computationally intensive tool may be able to accurately predict aging phenotypes and neurodegenerative disease markers—first in nematodes and eventually in larger, more complex organisms. In addition, future *in silico* interrogations will provide a powerful, quick, high-throughput, and cost-effective means by which to test experimental drugs and dietary supplements that may very well slow the deleterious effects of aging and the pathogenesis of age-related diseases.

CHAPTER 5: MODELING MOLECULAR SIGNATURES IN AGING AND DISEASE

5.1 Integrating the established simulation approach in disease contexts

After designing a foundational model that can effectively ascribe triggering events to the general cellular aging process, which we have determined to be primarily mitochondrial in origin, we then found it valuable to apply this experimental approach to a specific disease state. As deleterious aging primarily impacts energetically-demanding cells, it is no surprise that a majority of age-dependent diseases are neurodegenerative ones. Of the highest occurrence in this category of diseases is Alzheimer's disease (AD), and the general events that cause this pathology are yet to be fully understood. In this chapter we attempt to unpack the cellular conditions that render neurons vulnerable to stressors of aging and result in tau-mediated dysfunction, as it is observed in the progression of AD. This is done by utilizing the foundational computational simulation of mitochondrial and oxidative aging from the previous chapter. The resulting computational design was intended to improve on the shortcomings of the previous work, as discussed in detail. The results of this chapter convey important computational improvements in translatability, robustness, and the inclusion of critical molecular details. Part of the information in this chapter has been submitted for peer review to the scientific journal *Frontiers in Molecular Biosciences* as: *Hoffman et al. (2019) Network simulations reveal molecular signatures of vulnerability to age-dependent stress and tau accumulation.*

5.1.1 Aging, Alzheimer's disease, and the need for simulation studies

Alzheimer's disease (AD) has become the most prevalent age-dependent neurodegenerative disorder, with over 46.8 million reported cases of AD worldwide [256]. If disease diagnostics and treatments remain in their current ineffective state, this metric is expected to at least triple by 2050, meaning 1 in 85 individuals worldwide will be living with the disease [257]. The United States alone is expected to see >60% increases in AD cases by 2025 [258]. AD and similar age-dependent neurodegenerative diseases are characterized by severe memory impairment and widespread loss of brain function, with AD predominantly affecting neurons of the hippocampus [259, 260]. At the cellular level, neurodegeneration is the cumulative result of oxidative stress, tau accumulation and misfolded protein stress, inflammation, loss of mitochondrial function, impaired autophagy processes, and more [2, 178, 191, 261]. While many cellular pathways and processes contribute to this neuronal damage, age is the strongest and most ubiquitous risk factor [249, 262], warranting AD researchers to continually revisit the fundamentals of biological aging.

It is well understood that mitochondria play a critical role in the aging process [2, 178, 263]. Because of this, energetically-demanding cells (e.g., myocytes, neurons) that rely heavily on the integrity of their abundant mitochondrial populations are most affected by age. Age-dependent declines in mitochondrial function are heavily implicated in the pathogenesis of AD [264], leading researchers to target mitochondrial health through a variety of strategies in combatting AD onset and progression [265]. The exacerbated mitochondrial dysfunction that ensues in symptomatic AD outcomes in humans can theoretically be ameliorated through (i) direct tau binding and reduced tau

oligomerization, (ii) direct radical scavenging to curb mitochondrial ROS production, and (iii) targeting bioenergetic efficiency directly in an attempt to rescue failing neurons [262, 265, 266]. While these approaches are rooted in sound theory and have promising pre-clinical results, human studies have seen negligible efficacy [265]. One particular pathway that has been gaining considerable attention for diseases of aging is the mitochondrial unfolded protein response (UPR^{mt}), a response that is intended to protect mitochondria and is activated by a wide spectrum of stressors [187]. Analysis of the frontal cortex of human AD brains has shown significant increases in UPR^{mt} genes, demonstrating that this stress response is spontaneously activated in an attempt to improve mitochondrial content and combat the disease [267]. Further pharmacological activation of the UPR^{mt} has been shown to enhance mitochondrial proteostasis and alleviate neurological dysfunction in nematode and mouse AD models [268, 269].

Spontaneous mitochondrial dysfunction remains a target of investigation for neurodegeneration, but it is far from the only significant condition that render neurons vulnerable to stress. Factors that impair neuronal proteostasis over time play an equally important role [270]. It is well understood that AD rapidly affects the brain through the aggregation of aberrant β-amyloid (Aβ) peptides and tau proteins [271–273], and properly balanced proteostasis pathways are essential to hinder the activity of these aggregates. Specifically, targeting and controlling the ER-based unfolded protein response (UPR^{ER}) has resulted in substantial neurological protection and recovery in mammalian models of tauopathy [274, 275] and similar neurodegenerative models of aberrant prion protein propagation [276–278]. The UPR^{ER}, when dysregulated by Aβ and tau overexpressions, is also linked to deleterious mitochondrial deficits [279]; in the

same regard, therapeutic pharmacological targeting of the UPR^{ER} has shown concomitant activation of the UPR^{mt} and overall improvement in AD phenotypes [268]. These observations highlight the complex interconnectivity between cellular proteostasis mechanisms and mitochondrial dynamics.

The adjacent pathways by which cells adapt to these mitochondrial, oxidative and proteotoxic insults are also paramount to their survival. Particular stress responses that appear to curb AD pathogenesis under the appropriate circumstances are macroautophagy, mitophagy [191], and the Nrf2/SKN-1- and FoxO/DAF-16-mediated oxidative stress responses [280, 281]. Autophagy processes, especially those concerning the mitochondria, have shown to have a critical impact on the way organisms age, with significant neurological deficits resulting from autophagic dysregulation [192, 193]. Alzheimer's brains often display this level of dysregulation naturally, and many molecular and cognitive improvements have been achieved in mammalian AD models upon both autophagy and mitophagy hyperactivation [282, 283]. With regard to the Nrf2/SKN-1 and FoxO/DAF-16 oxidative stress responses, probing the elements of these pathways have shown remarkable decreases in age-dependent stress in a number of experimental models [215, 284]. Furthermore, tau-challenged neuronal models have naturally elicited these oxidative stress responses [285], and further pharmacological upregulation of either Nrf2/SKN-1 or FoxO/DAF-16 has ameliorated neurodegenerative disease phenotypes [280, 286].

While all of these cellular events and responses are involved in the aging process and in neurodegenerative results, elucidating the finite relationships within this complex network is imperative. Examples of these relationships are the definitive links between autophagy and ER stress [287] and the links between mitochondrial integrity and proteostasis [263, 269]. In addition to understanding the pathways involved and their connected relationships, it is also important to consider the temporal nuances of such cellular activities. Neuronal integrity at various life stages is rooted in specific quality control processes. Early-life maintenance requires functional oxidative stress responses to sustain an appropriate redox balance [178]. Early-life maintenance also requires reliable mitochondrial stress responses to perpetually weed out faulty mitochondrial materials before they have the ability to propagate [2]. Later in life, neurons have already accumulated the oxidative stressors and protein aggregates that cause damage; this is when the cell relies heavily on robust autophagy processes [191] and potent stress responses [261, 275] intended to remove damaging materials and absorb the impacts of damaging biomolecules. These temporally-nuanced cellular mechanisms highlight the complex nature of pharmacologically altering all of these processes to optimize neuronal function at all stages of life. These time- and magnitude-based systems biology obstacles underscore the critical need for more comprehensive experimental and therapeutic approaches for AD research.

The idea that neuron subpopulations have selective vulnerability has been postulated to explain degeneration patterns within the brain [288–290]. More generally, types of response-based vulnerabilities have been theorized for any neuronal subpopulation, with emphasized examples involving UPR^{ER} functionality [291]. The vast

network of general molecular conditions (e.g., conserved stress responses, redox environments) that precipitate and define vulnerability phenotypes within cellular populations are difficult to characterize with the limitations of conventional experimental approaches. An increasing number of researchers posit that integrative computational methods will provide more complete information for such queries [173]. Techniques that integrate *in silico* methods with *in vitro* and *in vivo* experiments are now frequently emerging for neurodegenerative research [292]. Previous *in silico* approaches of this nature have been successful in theorizing oxidative characteristics of aging and disease [243], lipid raft characteristics in AD development [55], and metabolic shifts in normal aging [293].

We have previously established a multimethod computational simulation approach that has demonstrated the ability to characterize relationships between aging and mitochondrial pathways. We have integrated new computational networks into the preexisting work. The resulting computational design of this chapter was intended to improve on the shortcomings of the previous simulation, as discussed in detail in the subsequent subsections. The results of this chapter convey important computational improvements in disease-specific translatability, experimental translatability, robustness, and the inclusion of critical molecular details. In this study, we have built upon our foundational studies to construct a computational simulation tool that integrates all of the aforementioned molecular mechanisms characterizing neuronal conditions of neuronal vulnerability, as they relate to experimental observations in the model organism *Caenorhabditis elegans*.

Such conditions are recognized here as the measured set of pathways and responses that drive and accompany the aging process. This set of measurements produced by the simulation can be considered a time- and magnitude-based ***molecular signature***, similar to signatures previously developed and used for toxicological screening assays [16] and cancer cell prognostic studies [294]. The signature outputs presented here vary within the cellular population and defines phenotypic outcomes of resilience or vulnerability, based on the experimentally-determined pathway relationships. Analyzing this molecular signature over the lifespan of an organism is the hallmark of this approach. To prevent neuronal vulnerability to aging and protein misfolding, our previous work suggests that appropriate cellular activities of the UPR^{mt} and UPR^{ER} stress responses are critical, which is also in accordance with literature [275]. Here the simulation outputs fall in line with these hypotheses and predict temporal trajectories that result in neuronal populations most vulnerable to oxidative and proteotoxic stressors. Overall, this approach provides the community with a means to more accurately grasp (i) the timing of multiple stress events in AD development, and (ii) the neuroprotective effects of stress response mechanisms in AD prevention and treatment.

5.1.2 Experimental procedures in the adapted simulation

Hierarchical cell simulation design and agent-based modeling

In order to simulate the mitochondrial and cellular relationships of interest, we formulated our model using AnyLogic® multimethod simulation software (version 8.3; The AnyLogic Company; Chicago, IL), which allowed us to develop a hierarchical agent-based simulation scheme, as we have described in the previous chapter. Access to the simulation is described in the subsequent section regarding data availability. To briefly describe the methodology, this simulation was constructed with a population of cell agents, with each individual cell agent containing its own population of mitochondrion agents. Each agent contained discrete event statements and system-dynamics reaction networks, both of which were programmed to deal with natural biological stochasticity. Cellular agents contained their own continuous genetic and biochemical networks, which produced an array of intracellular conditions, referred to here as the molecular signature. These conditions were analyzed for sensitivity and determining control over the system to reveal phenotypes of response deficiencies and ultimately vulnerability, which are highlighted in the results section. These bifurcating transitions that allow agents to move through different states are written as java-based expressions, and are all unpacked in the corresponding subsequent sections.

Deterministic modeling components

As Boolean approaches have been successful in representing mathematical relationships between biomolecules and genes, especially for systems of aging [173, 254, 295], this discrete binary concept was converted to Hill-based deterministic (ODE-

based) relationships of gene expressions and response activities to produce a continuous computational simulation that could be easily managed temporally alongside biochemical equation frameworks and the aforementioned agent-based phenotyping methods. The manually-selected and organized network is hinged primarily upon age-dependent oxidative signaling and many adjacent stress responses, as depicted in the results section. These curated molecular relationships are detailed in the results, and all of the equations and corresponding parameters used are organized and tabulated in the corresponding subsequent sections.

Sensitivity analysis

To determine the quantitative significance of certain parameters and functions within the system, a similar global sensitivity strategy was used that has been described previously [174]. Briefly, each parameter was individually reduced by 5%, and the resulting model output of cellular ROS levels was assessed. This was done for all static parameters within the model, and the response variable changes were measured at particular time points determined for young age (day 5), midlife (day 10), and old age (day 19). Sensitivity coefficients were calculated as:

$$SC = \left(\frac{\partial O_i}{\partial P_j}\right) \times \left(\frac{P_j}{O_i}\right) = \left(\frac{\partial O_i}{O_i}\right) \times 20$$

where *SC* represents the normalized sensitivity coefficient, O_i is the model output value, P_j is the value of the parameter of interest, and ∂ represents the partial derivative of either the parameter value or model output. When |SC| ≥ 1.0000, i.e. when the

proportional change in the response variable is greater than the proportional change in the parameter, the parameter is deemed to have significant sensitive control over the respective output at the specified age. SC absolute values falling between 0.1000 and 0.9999 were also considered for further analyses of system control.

Mathematical analyses and graphical visualizations

Statistical analyses of Gaussian distributions, sigmoidal curve-fitting, and survival analyses were performed using GraphPad Prism software (version 8). Illustrations and vector drawings were created using ChemDraw Professional (version 15.1).

General model setup and time units for lifespan analyses

Upon model setup, the *C. elegans* lifespan amount was assumed to be 20 days (higher end of *C. elegans* age probability at 20 °C as per [255], and for temporal extrapolation calculations, human lifespan amount was assumed at 100 years or 29,200 days for simulation compatibility (approaching the maximum human lifespan, per [296]. Mitochondrial counts within each cell were taken from the Poisson distributions determined in our previous simulation. In each of the simulation experiments, 200 neurons were simulated to achieve robustness in the distributions of node output and resulting phenotype analyses. This agent number was determined by Monte-Carlo analyses that resulted in the lowest possible variance between runs. While variance was tested in populations of up to 10,000 cell agents, any number of cell agents above 200 caused stochastic changes to saturate, leading us to reach 200 as the proper level of robustness without creating a design that was too computationally intense.

Mitochondrial system-dynamics and discrete computational methods for normal aging

The framework for mitochondrial ROS generation, a pivotal player in the degenerative aging process, was simplified from our previous simulation design to focus more on the cellular genetic network of interest and more nuanced states of neuronal vulnerability for cellular phenotyping. A simplification down to this level did not significantly alter the behavior of the cellular environment, as the hierarchical modeling structure from the previous simulation remains intact here, but instead this reduced the ability to simulate the same nuances in mitochondrial stress states as before. Since mitochondrial characterizations were outside the scope of this study, this simplification was appropriate for producing a more applicable and easily understood tool that was less computationally intense for the community. The stochastic equations, agent transitions, and event statements pertaining to mitochondrion-level biochemical kinetics are displayed in Equation Box 5.1, with corresponding descriptions and references of the logical derivations. The AnyLogic simulation schematics of the mitochondrial framework are also displayed for both the agent-based methods (Figure 5.1A) and deterministic ODE methods (Figure 5.1B).

EQUATION BOX 5.1

Box 5.1: Equations, agent transitions, and event statements pertaining to mitochondrion-level biochemical kinetics.

Differential equations governing time-dependent mitochondrial ROS accumulation and elimination, comprised of general production and elimination constant distributions that resulted from our previous work as well as logically-derived expressions for tau-mediated ROS accumulation and UPR^{mt}-mediated elimination [297–301]. Expressions shown in purple are dictated from the cell-level environment:

$$\frac{d[ROS_{mt}]}{dt} = \frac{nM\ ROS_{mt}}{day} = K2 * \frac{Tau_{Agg}}{Tau_{Agg} + TM} - kMRE[ROS_{mt}] * UPRmt\_activity$$

Discrete events governing (i) movement through mitochondrial health and stress states and (ii) mitochondrial biogenesis and mitophagy events dictated by cellular activities of mitochondria-altering proteins:

Stochastic condition defining gain of mitochondrial ROS triggering a defective organelle phenotype:

$$[ROS_{mt}] > (triangular(30\ nM, 40\ nM, 50\ nM))$$

Static condition defining remediation of mitochondrial ROS restoring a healthy organelle phenotype:

$$[ROS_{mt}] < cell'sspecific\ threshold\ distribution\ value\ from\ previous\ expression$$

PINK-1-dependent rate of mitochondrial loss via mitophagy (agent removal):

$$\frac{Compromised\_mito\ destroyed}{day} = \frac{1}{pink1\_activity}$$

Basal and SKN-1-dependent rate of mitochondrial biogenesis (new agent addition):

$$days\ until\ agent\ addition = uniform(1,2) - \frac{1}{4} skn1\_activity$$

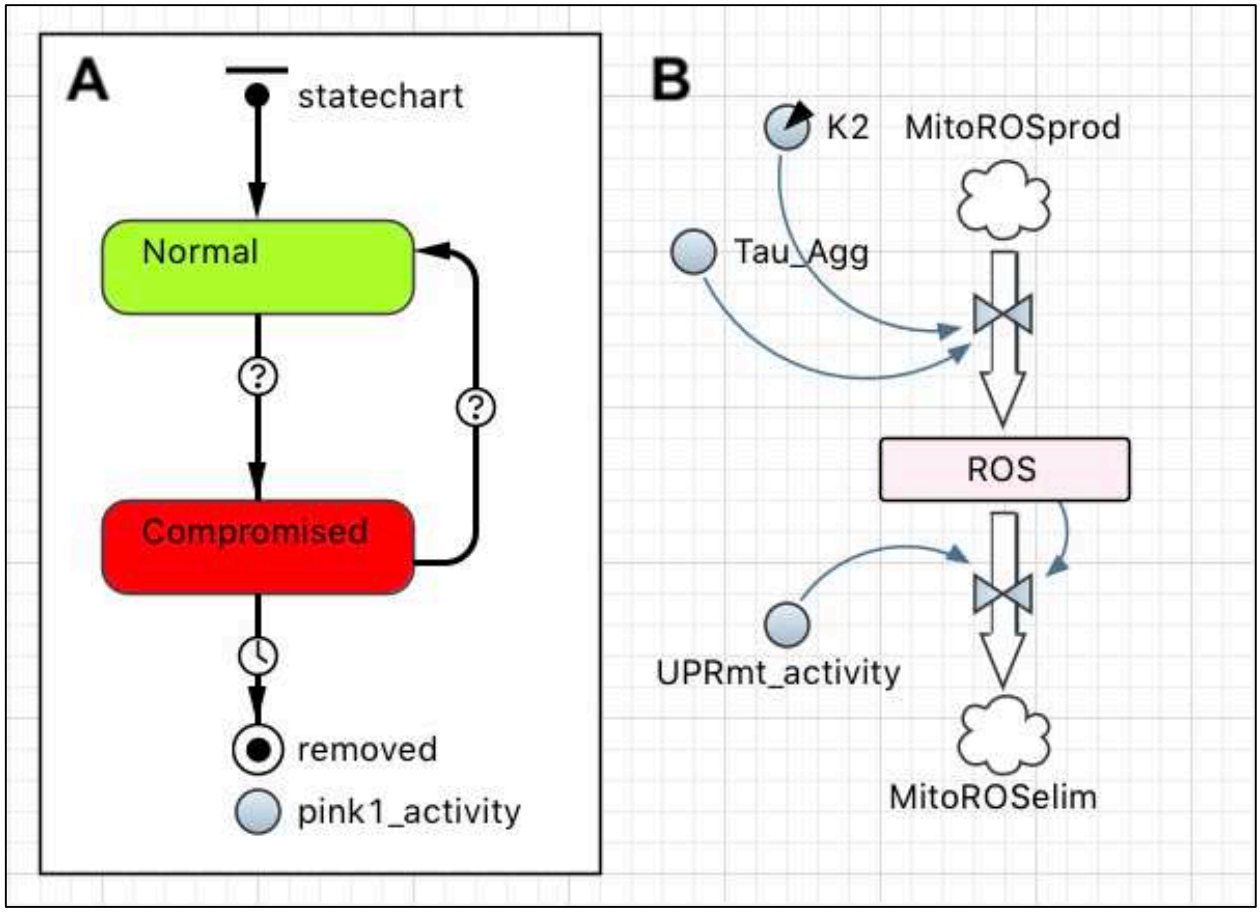

FIGURE 5.1

Simulation schematic displaying mitochondrial framework in the simulation software. **(A)** Agent state chart delineating stress-response-based conditional mitochondrial integrity. Final state denotes mitochondrial removal via mitophagy. **(B)** Simplified mitochondrial equation-based dynamics based primarily off of mitochondrial ROS production and content.

Cell-level system-dynamics and discrete-event computational methods for normal aging

Since the primary focus of this simulation study was to garner more nuanced information about neuronal vulnerability that arises in the aging process, the cellular dynamics were more intricate than those that make up the mitochondrial framework. The gene network of interest that is driven in part by age-dependent oxidative signalling is connected by deterministic nodes of activity as well as some biochemical reaction schemes describing protein accumulation and phosphorylation events. The nodes of activity for the genes and responses of the network were given deterministic ODE-based expressions of primarily Hill functions, in order to draw some similarities to the binary nature of Boolean gene networks that have been successful in previous studies [254, 295]. This conversion allowed for (i) more graded activity to be seen within individual nodes for more detailed analyses, (ii) better implication of stochasticity within the cell agent population, and (iii) easier integration with other ODE-based frameworks and agent-based frameworks within the complete hierarchical model. The parameters and corresponding equations delineating this curated network are displayed in Table 5.1 and Box 5.2, respectively; the corresponding schematic of this equation network is shown in Figure 5.2A. The agent-based transitional events that allow cell agents in the simulation to possess different conditionally-bound phenotypes are expressed in Box 5.3; the corresponding schematic of this agent state chart is shown in Figure 5.2B.

TABLE 5.1

Table 5.1. Parameters of interest for the proposed intramitochondrial-intracellular functional genomic system.

Parameter function	Symbol	Value Range	Source
Cellular ROS generation constant	*K1*	25–50 (nM day^{-1})	100%[SS]
Mitochondrial ROS generation	*K2*	120–240 (nM day^{-1})	[182][C]
ROS remediation constant	*K3*	0.1–0.5 (day^{-1})	[200][SS]
skn-1 ROS-dependent activity coefficient	*K4*	60 (nM)	[Chapter 4][C]
daf-16 ROS-dependent activity coefficient	*K5*	75 (nM)	[Chapter 4][C]
sod-2 production constant	*K6*	1	[182][O]
UPR^{mt} activity coefficient (ROS_{mt}-based)	*K7*	40–60 nM	[208][C]
UPR^{ER} activity coefficient (BiP-based total)	*K8*	triangular(0.5,0.75,1)	100%[SS]
PERK phosphorylation coefficient	*K9*	0.015 (day^{-1})	[275][A]
skn-1-controlled mTOR activity coefficient	*K10*	2.0	[215][A]
bec-1 production constant	*K11*	0.25 (% day^{-1})	100%[SS]
pink-1 activity constant	*K12*	1.0	[307][A]
PERK protein production constant	*PP*	1 (% day^{-1})	100%[SS]
Total PERK degradation constant	*PE*	0.1 (day^{-1})	100%[SS]
Mitochondrial ROS elimination constant	*kMRE*	0.2–2.0 (day^{-1})	[182][C]
Mitochondrial tau activity coefficient	*TM*	200 (%)	[297][O]
Cellular tau activity coefficient	*TC*	300–400 (%)	[302][A]
Mutation fraction related to tau production	*mF*	0.5–1.5	[266][A]
ROS-dependent tau conversion constant	*RT*	50 (nM)	[199][A,C]
mTOR-driven bec-1 inhibition constant	*MB*	1.5	[303][A]
UPR^{ER}-mediated bec-1 increase constant	*UB*	1.5	[304][A]
Max. ROS-based increase in UPR^{mt} activity	*KMT*	1.0	[301][A]

[SS] Optimized in the simulation to achieve the reported unstressed physiological steady-state percentage or range.
[O] Individually optimized value, generated using AnyLogic calibration to best emulate reported kinetic curves.
[A] Quantitated assumption based on qualitative evidence.
[C] Units converted to adhere to model standards.

EQUATION BOX 5.2

Box 5.2: Equations pertaining to cell-level biochemical kinetics and activity nodes.

Differential equations governing (i) time-dependent cellular ROS accumulation and elimination [182], (ii) PERK phosphorylation events [275], (iii) tau protein production, aggregation and elimination, (iv) bec-1 protein content, and (v) UPR^{mt}-controlled hsp-60 content [187]:

$$\frac{d[ROS_{cell}]}{dt} = ROS_{mt} + K1\left(1 - \left(\frac{skn1^3}{skn1^3 + 1.5^3}\right)\right)\left(\frac{Tau_{Agg}^5}{Tau_{Agg}^5 + TC^5}\right) - K3 * ROS_{cell}\left(\frac{sod2}{sod2 + 1.5}\right)$$

$$\frac{PERK}{dt} = PP - PERK * K9\left(\frac{Tau_{Agg}^3}{Tau_{Agg}^3 + 1/2 * TC^3}\right)$$

$$\frac{pPERK}{dt} = PERK * K9\left(\frac{Tau_{Agg}^3}{Tau_{Agg}^3 + 1/2 * TC^3}\right) - PE * pPERK$$

$$\frac{Tau}{dt} = 100\% * mF * \left(2 - \frac{pPERK}{pPERK + 1.5}\right) - \left(Tau\left[\frac{UPR}{UPR + 1.5}\right] * hsp60 * \frac{1}{\%_{hsp60}\ day}\right) - uniform(15{,}30) * Tau\left(\frac{ROS_{cell}^3}{ROS_{cell}^3 + RT^3}\right)$$

$$\frac{Tau_{Agg}}{dt} = uniform(15{,}30) * Tau\left(\frac{ROS_{cell}^3}{ROS_{cell}^3 + RT^3}\right) - \left(\frac{bec1}{bec1 + 50}\right) * Tau\_Agg$$

$$\frac{bec1}{dt} = 0.5 + k11 * \left(\frac{UPR^5}{UPR^5 + UB^5}\right) - bec1\left(\frac{mTOR^{1.5}}{mTOR^{1.5} + MB}\right)$$

$$\frac{hsp60}{dt} = 1 + \frac{UPRmt}{UPRmt + 1} * triangular(1, 1.5, 2) - \frac{1}{day} * hsp60$$

Dynamics and normalized activity of reporter genes and responses involved in the molecular signature, dictated by Hill dynamics as opposed to Boolean functions. Hill dynamics theorized here and elsewhere have been mathematically optimized (as previously described in this dissertation) based on each node's corresponding literature information seen in Table S1. All corresponding assumptions are stated as well. KD and KS are fractional parameters that can be altered for genetic ablation experiments (basal = 1):

$$\frac{d[UPR^{mt}]}{dt} = 1 + KMT * \left(\frac{ROS_{mt}^4}{ROS_{mt}^4 + K7^4}\right) - \left(\frac{Tau_{Agg}^2}{Tau_{Agg}^2 + TC^2}\right)$$

$$\frac{d[BiP]}{dt} = \frac{d[UPR]}{dt} = 1 - K8\left(\frac{Tau_{Agg}^4}{Tau_{Agg}^4 + 2 * TC^4}\right)$$

$$\frac{d[sod2]}{dt} = K6 * UPRmt * daf16$$

$$\frac{d[daf16]}{dt} = KD\left[1 + \left(\frac{ROS_{cell}^8}{ROS_{cell}^8 + K5^8}\right)\right]$$

$$\frac{d[skn1]}{dt} = KS\left[1 + \left(\frac{ROS_{cell}^2}{ROS_{cell}^2 + K4^2}\right)\right]$$

$$\frac{d[pink1]}{dt} = 2 - mTOR * K12$$

$$\frac{d[mTOR]}{dt} = 1.5 - \left(\frac{skn1^2}{skn1^2 + K10^2}\right)$$

EQUATION BOX 5.3

Box 5.3: Agent-based methods applied for cellular vulnerability phenotyping.

As the ultimate outputs of the model, age-dependent cellular phenotype percentages are captured based on each cell's conditions of the dynamic response network. These conditionally-bound phenotypes are created using agent-based "state chart" functions, and are based on characteristically bifurcated conditions that arose from the bistability analyses performed. Transitions indicate the movement through several phenotypes, as depicted in Figure 5.2B. Cells first move through either possessing UPR^{ER} or UPR^{mt} deficiencies, and then both; once both deficiencies have been achieved from the aging process, neurons can then be rendered vulnerable to the effects of high ROS levels and tau protein aggregates. Once this final conditionally-bound vulnerability state is achieved, they then have a stochastic time requirement to activate stress responses and rescue from these deleterious conditions or they will be removed from the simulation to emulate cell death. These model developments are substantiated by the findings that UPR^{mt} activation promotes longevity and phenotypic resilience to ROS- and aggregation-mediated neurodegenerative outcomes [305, 306]. These model developments are also substantiated by the fact that total UPR^{ER} activation is beneficial in preserving resilient cell phenotypes due to autophagic control and proteostatic measures, while the PERK translational branch upon aggregate-dependent overactivation leads to vulnerability [275].

Transitions of increasing stress states within the agent-based framework (T1-T5), including the final optimized rate-dependent irreversible transition of full vulnerability to cell death (T6):

$$\boldsymbol{T1}: UPT^{mt}\_activity < 50\%$$

$$\boldsymbol{T2}: UPR\_activity < 50\%$$

$$\boldsymbol{T3}: UPR\_activity < 50\%, UPT^{mt}\_activity < 50\%$$

$$\boldsymbol{T4}: UPT^{mt}\_activity < 50\%, UPR\_activity < 50\%,$$

$$\boldsymbol{T5}: UPT^{mt}_{activity} < 50\%, UPR_{activity} < 50\%, pPERK > 150\%, ROS_{cell} > 100$$

$$\boldsymbol{T6}: exponential\ rate = cell\ death\ events\ per\ day = uniform(1, 2)$$

Transitions of reversible recovery from stress states within the agent-based framework (R1-R5):

$$\boldsymbol{R1}: UPT^{mt}_{activity} < 50\%, UPR_{activity} < 50\%, pPERK \leq 150\%, ROS_{cell} \leq 100$$

$$\boldsymbol{R2}: UPT^{mt}\_activity < 50\%, UPR\_activity \geq 50\%$$

$$\boldsymbol{R3}: UPT^{mt}\_activity \geq 50\%, UPR\_activity < 50\%$$

$$\boldsymbol{R4}: UPT^{mt}\_activity \geq 50\%, UPR\_activity \geq 50\%$$

$$\boldsymbol{R5}: UPT^{mt}\_activity \geq 50\%, UPR\_activity \geq 50\%$$

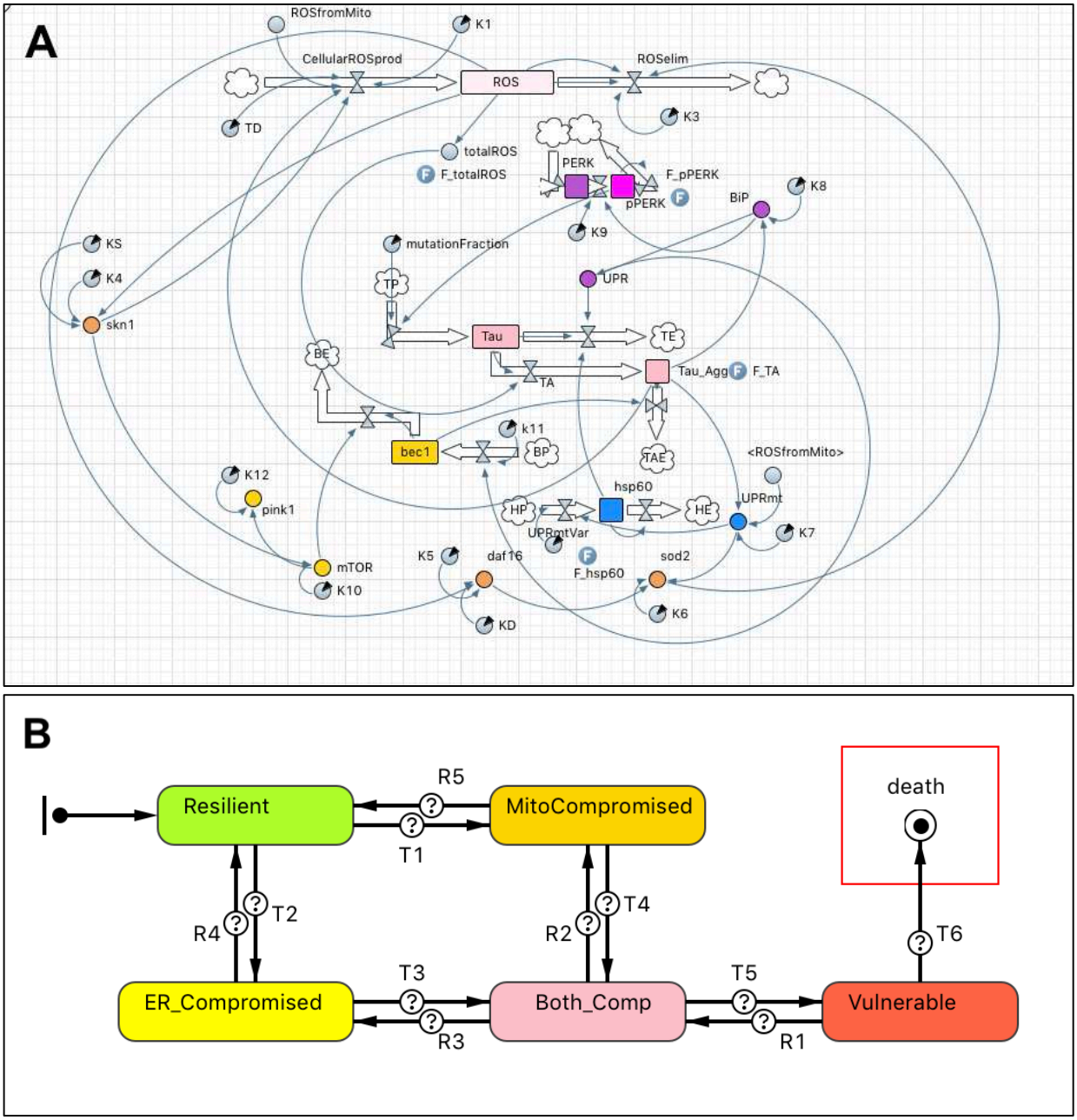

FIGURE 5.2

Simulation schematic displaying cell-level framework in the simulation software. **(A)** Deterministic equation-based network of defining cluster reporters and activators. **(B)** Agent state chart with condition-based transitions leading to phenotypic agent states of vulnerability. Final state denotes cell death.

Global sensitivity analysis

Parameters were tested for sensitivity within the network using a 5% value perturbation, as we have previously performed and as it is described in the method section of the main article. The results are shown in Table 5.2.

TABLE 5.2

Table 5.2. Sensitivity analysis of cellular process parameters and stress response parameters within the molecular simulation network. Sensitivity coefficients (SC) with an absolute value greater than or equal to 1.0000 were deemed to have sensitive control over the system. SC values with an absolute value between 0.1000 and 0.9999 were considered for further analyses of system control. The response variable assessed for change in the analysis was cellular ROS, as this drives many aging processes.

Parameter function	***Symbol***	***Early-life SC***	***Mid-life SC***	***Late-life SC***
Cellular ROS generation constant	*K1*	0.0422	0.2236	-0.1032
Mitochondrial ROS generation	*K2*	1.2348	0.4279	0.3418
ROS remediation constant	*K3*	-1.8216	-1.7145	-1.4484
skn-1 ROS-dependent activity coefficient	*K4*	0.0310	-0.1275	-0.2192
daf-16 ROS-dependent activity coefficient	*K5*	0.0000	0.0000	0.0000
sod-2 production constant	*K6*	0.0000	0.0000	0.0000
UPR^{mt} activity coefficient (ROS_{mt}-based)	*K7*	0.1112	-0.0740	-0.3841
UPR^{ER} activity coefficient (BiP-based total)	*K8*	0.0077	-0.0435	-0.4232
PERK phosphorylation coefficient	*K9*	0.0141	-0.0638	-0.6431
skn-1-controlled mTOR activity coefficient	*K10*	0.0021	-0.0638	-0.1759
bec-1 production constant	*K11*	0.0113	-0.3318	-0.2969
pink-1 activity constant	*K12*	0.0443	-0.0314	0.4873
PERK protein production constant	*PP*	0.0310	-0.1106	-0.6459
Total PERK degradation constant	*PE*	0.0471	-0.1151	-0.0226
Mitochondrial ROS elimination constant	*kMRE*	-0.6424	-0.4813	-0.5626
Mitochondrial tau activity coefficient	*TM*	-0.9069	-0.5100	-0.5084
Cellular tau activity coefficient	*TC*	-0.1949	-0.3889	-0.1930
ROS-dependent tau conversion constant	*RT*	-1.9560	-1.3090	-0.4021
mTOR-driven bec-1 inhibition constant	*MB*	-0.0134	-0.0595	-0.4529
UPR^{ER}-mediated bec-1 increase constant	*UB*	0.0303	-0.0595	-0.1095
Max. ROS-based increase in UPR^{mt} activity	*KMT*	0.0091	-0.3336	-0.0322

Inclusions of aberrant tau accumulation

To emulate tau-expressing anti-aggregating and pro-aggregating models within *C. elegans* [266] so that this simulation can be easily translatable in future nematode-based tau experiments, expressions governing tau production, accumulation and degradation have been made computationally malleable. For the simulation experiments of this study, the mutation fraction within the anti-aggregating cell populations (tau control) was set at 0.4, whereas the value for the pro-aggregating group was given a 100% increase at 1.4. The processes within the simulation controlled by tau content are primarily rooted in cellular and mitochondrial oxidative stress signaling and also notably involve the UPR^{ER} activities of the BiP and p-PERK branches (expressions included in Equation Box 5.1 and Equation Box 5.2).

Data availability

The simulation tool is available as both a java applet and downloadable file (.alp) via the AnyLogic Cloud (https://cloud.anylogic.com/model/ec37d0d4-fcbf-4158-9f31-d0a2e213dcb0). For use of the original file, users may download a free version (Personal Learning Edition) of the AnyLogic software from the company's website. Other datasets upon which the results presented in the paper are based can be requested by sending an email to the corresponding author.

5.1.3 Results and discussions of normal and tau-altered neuronal aging

Simulation design and the molecular signature

The simulation constructs used in this study centered around age-dependent cellular and mitochondrial oxidative signaling, similar to our previous work, however the model presented here was designed with a wider array of stress responses experimentally determined to be significant to neuronal vulnerability phenotypes. The nodes producing the normalized expressions of critical markers and stress response activities are shown as functional clusters in Figure 5.1A. This network was constructed within our simulation interface in part by integrating the on-off behavior of Boolean network modeling, however, the nodes were designed using system-dynamics techniques (ODE-based) of primarily saturable Hill functions, which we have previously modeled for nuclear receptors. This allowed us to produce normalized response fractions for each of the molecular markers involved in the full signature of interest. This conversion to an equation-based network also allowed us to integrate the response nodes with an agent-based system of (i) varying cellular behavior within a cell population (ii) varying mitochondrial populations within each cell, (iii) crosstalk between the molecular network and cellular and mitochondrial behaviors, and (iv) nuanced relationships between the molecular network and cellular agent phenotypic outcomes. Expressions concerning mitochondrial conditions and behavior are delineated in Box 5.1 and Figure 5.1, whereas the expressions concerning the cellular biomolecular network and agent population behaviors are delineated in Box 5.2, Box 5.3 and Figure 5.2; all corresponding model parameters are tabulated in Table 5.1.

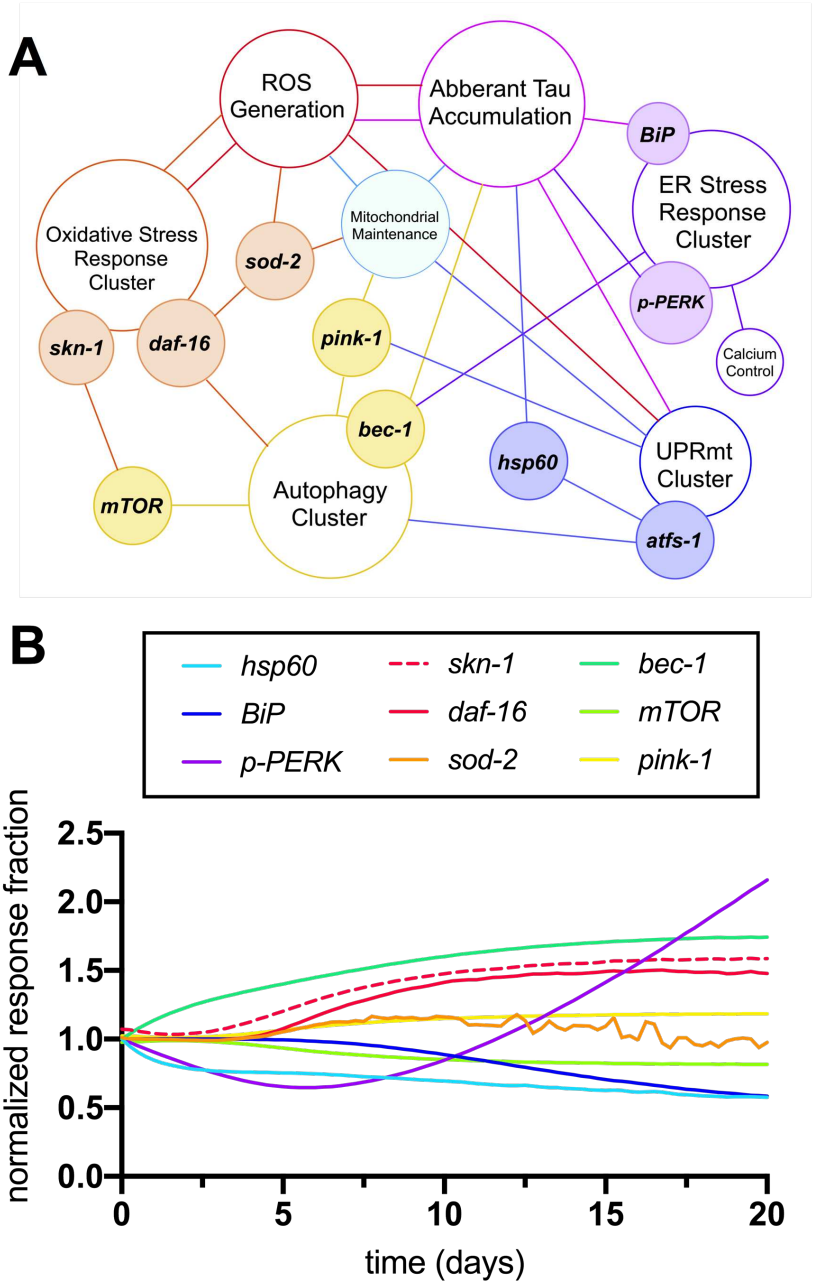

FIGURE 5.3

Simulation design and initial outputs. **(A)** Molecular network analyzed in the multimethod simulation paradigm. **(B)** Temporal trajectory of the molecular signature in normal aging neurons

The initial simulation output was determined to be the molecular signature of 9 nodes of interest as they correspond to markers within *C. elegans*: *hsp-60* (UPR^{mt} activity), *BiP* (total UPR^{ER} activity), *p-PERK* (translational branch of the UPR^{ER}), *skn-1* activity, *daf-16* activity, *sod-2* (mitochondrial superoxide dismutase activity), *bec-1* (general macroautophagy machinery), *mTOR* (anti-autophagic activity), and *pink-1* (pro-mitophagy activity). The patterns of response fractions for each of these functional pathways were measured in the simulation over a 20-day period (the higher end of lifespan probability for a wild-type nematode; [255]). This temporal trajectory is shown in Figure 5.3B, with distinct patterns of stress response dysregulation upon normal aging. Of note, the simulation predicts an age-dependent dysregulation of autophagic processes, which has manifested experimentally in aging nematodes as an accumulation of autophagosome content in neuronal tissue with variable changes in autophagic flux [308, 309]. Also in accordance with preliminary simulation results, the spontaneous nuclear localization of *daf-16* along with *skn-1* expression have been shown to increase in normal aging nematodes [310]. It is important to note that skn-1/Nrf2 activity across nematode and mammalian lifespans has been measured in variable expression patterns [311], and even when increased, skn-1/Nrf2 activation alone has not demonstrated enough compensatory effects to combat the oxidative stressors of aging. The simulation results also mirror observed impairments in UPR^{ER}, UPR^{mt} and mitochondrial maintenance with neuronal age, allowing permissive oxidative damage and vulnerability to proteotoxic insults [312–316].

Nodes triggering the genesis of vulnerability phenotypes

To determine sensitive controllers of the simulated network, a standard global sensitivity analysis was performed for all static parameters. The resulting sensitivity coefficients are displayed in Table 5.2, with expected significant sensitivity found at all stages of life for the parameters defining age-dependent ROS production and elimination. While falling slightly below strongly sensitive values, the coefficients returned for UPR^{mt}- UPR^{ER}- and skn-1-based activities suggested that they also play a critical role in determining changes within the molecular system at both mid- and late-life stages. Due to these formal observations, both UPR^{mt} and UPR^{ER} activities were analyzed with respect to the model's natural age-dependent increase in ROS levels. The temporal movement through these dose-response plots are displayed in Figure 5.4A and Figure 5.4B (left panels) for normalized UPR^{mt} and UPR^{ER} activities, respectively. The temporal movement displayed impairments in both these responses, and removal of ROS content at late-life stages did not recover these impairments; instead, the model predicted that these cells would continue a trajectory within the dose-response that approaches 50% activity levels for both responses. Because of these data, these activity values were chosen as triggering conditions for cellular vulnerability within the simulated cell population. The population distribution of UPR^{mt} and UPR^{ER} activities at the end of life (day 20) are displayed in Figure 5.4A and Figure 5.4B (right panels), with over a quarter of the cells satisfying these impaired conditions. These data are consistent with findings about defective proteostasis mechanisms triggering cellular vulnerability phenotypes in neurodegenerative disorders [291].

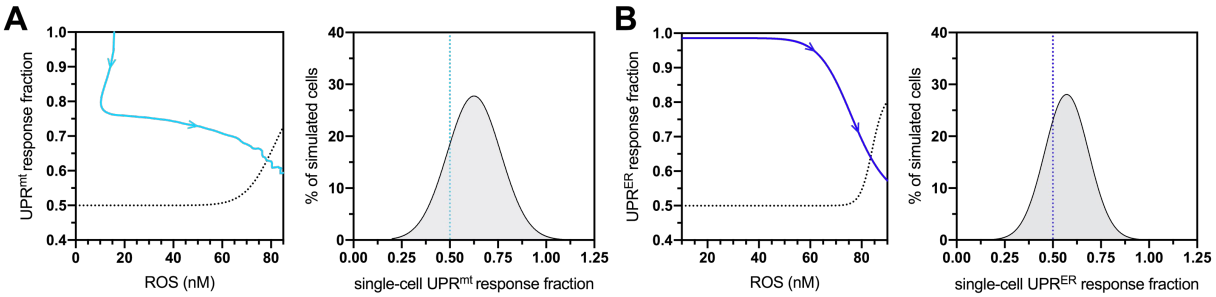

FIGURE 5.4

Cellular vulnerability characterizations of UPR^{mt} and UPR^{ER} activities with respect to increasing age-dependent oxidative insults. **(A)** Dose-response curve denoting bistable UPR^{mt} activity in response to age-dependent ROS increases, with the UPR^{mt} activity of late-life cell aggregates approaching 0.5 (left panel). Also shown is the UPR^{mt} activity distribution of simulated cells at the 20-day mark, with the lower end (26%) satisfying the < 0.50 condition. **(B)** Dose-response curve denoting bistable UPR^{ER} activity in response to age-dependent ROS increases, with the UPR^{ER} activity of late-life cell aggregates approaching 0.5 (left panel). Also shown is the UPR^{ER} activity distribution of simulated cells at the 20-day mark, with the lower end (32%) satisfying the < 0.50 condition.

The age-dependent cellular conditions defined in the computational network were then used to produce bifurcations through phenotypic states of vulnerability that were quantified for the simulated cell population (Figure 5.5A). At simulation startup, all cell agents exist with the fully resilient phenotype and no deviations from the normalized response activities. Cells then conditionally transition to states of UPR^{mt} and/or UPR^{ER} compromised activities, and when both mitochondrial and ER deficiencies are satisfied, the cells are then rendered vulnerable to age-dependent increases in oxidative and proteotoxic stressors. Once cells enter into the final vulnerability state, they then move through a rate-dependent transition into cell death, where they are finally removed from the simulation. After designing this bifurcation landscape, the phenotype percentages for normal aging were quantified (Figure 5.5B). As we have predicted and discussed in our previous work, compromised mitochondrial processes set in early on in aging, with an ER-compromised setting in later in life. Ultimately, a steady increase in full vulnerability was observed shortly after day 12, with a gradual decline in cell survival seen after day 14. In a direct extrapolation of these values to a human lifespan of 100 years, vulnerable neurons would surface around 60 years with the onset of neurodegeneration occurring at 70 years.

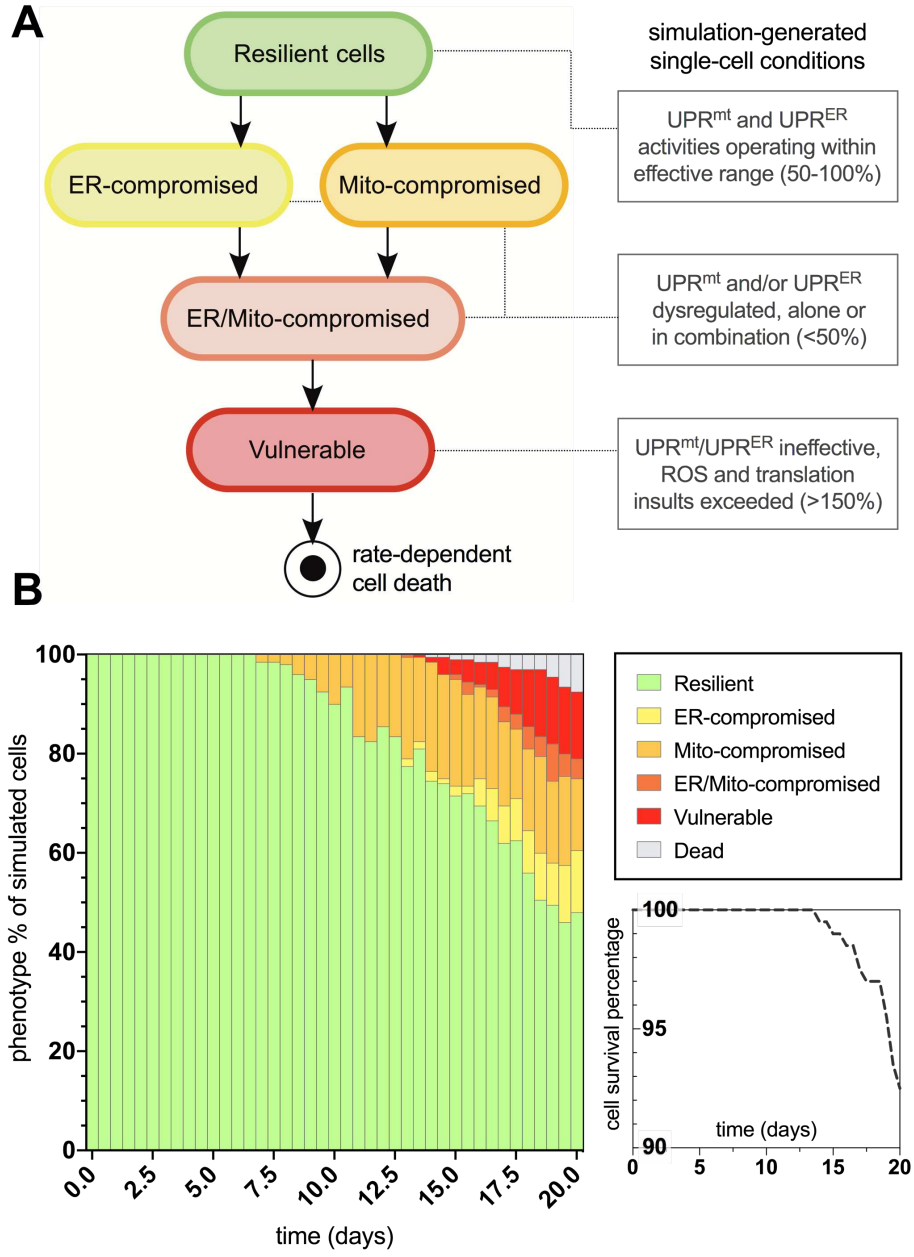

FIGURE 5.5

Bifurcated phenotypic characterizations and simulation results for normal aging neurons. **(A)** States of increasing cellular vulnerability with respect to the UPR^{mt} and UPR^{ER} analyses, which result in an ultimate vulnerability state conditionally bound by age-dependent oxidative and proteotoxic insults. **(B)** Simulation results of cellular phenotype percentages over time for normal aging neurons, including theorized rate-dependent cell survival with respect to vulnerability increases.

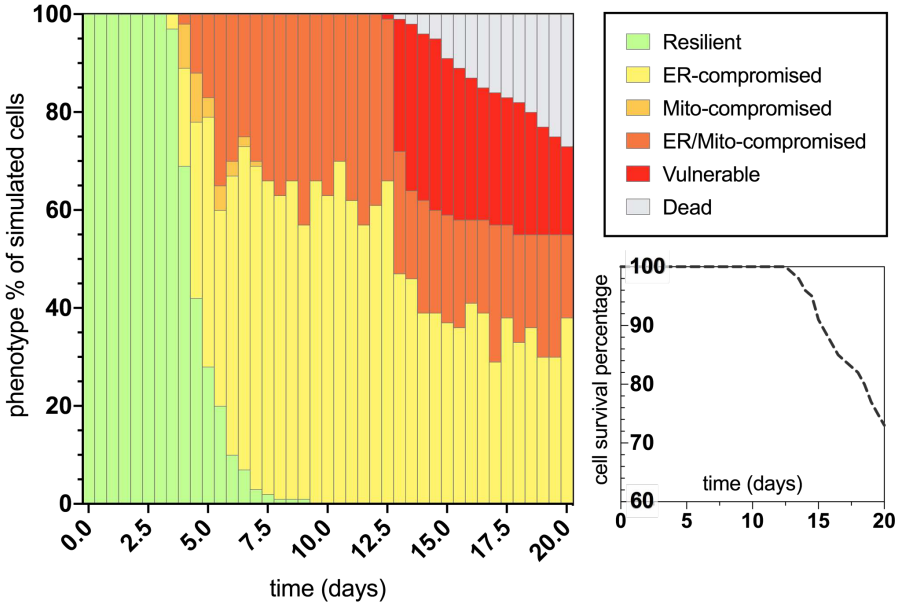

FIGURE 5.6

Bifurcated phenotypic characterizations and simulation results for tau-exacerbated aging neurons. Simulation results of cellular phenotype percentages over time for tau-insulted (100% increase) aging neurons, including theorized rate-dependent cell survival with respect to vulnerability increases.

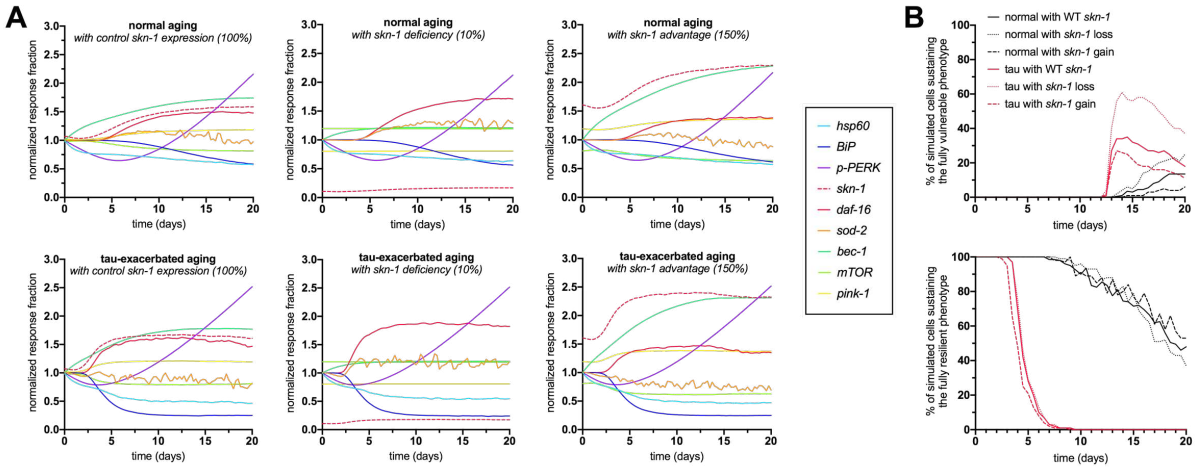

FIGURE 5.7

Molecular signatures in normal and tau-exacerbated aging neurons sustaining variable activities of the *skn-1*-mediated oxidative stress response. **(A)** Changes in the temporal trajectory of the simulation-generated molecular signature are shown for normal aging neurons (top panels) and for tau-exacerbated neurons (bottom panels) after skn-1 ablation and skn-1 overexpression. **(B)** Varying time-course phenotype measurements for each of the six genetically-altered groups. The age-dependent genesis of the vulnerability phenotype with corresponding cell percentages are shown (top panel) as well as the maintenance of the resilient phenotype and its corresponding cell percentages (bottom panel).

Vulnerability is enhanced with increased tau aggregation and oxidative signaling

After characterizing the molecular signature in the trajectory of normal aging, we then applied a 100% increase in tau aggregation within the simulation interface to quantitate its effects on the predicted outputs. The bifurcated phenotypic characterizations that resulted after integrating this tau insult are displayed in Figure 5.6. The maintenance of the resilient neuronal phenotype is markedly decreased, with absolutely no cell agents remaining in this state after 9 days of age (directly extrapolated to a human lifespan to theorize the loss of neuronal resilience at age 45 for outstanding tau-insulted individuals). As expected, ER stress is substantially heightened in the tau-exacerbated simulation and UPR^{ER} dysregulation precedes or coincides with mitochondrial deficits, in contrast to the normal aging results. Cell survival was markedly decreased in the tau-exacerbated network, emulating the neuronal dysfunction and neurodegenerative outcomes seen in tau-expressing pro-aggregating nematodes [266].

Following the neuronal phenotyping analyses for normal and tau-exacerbated aging, the molecular signatures for both scenarios were generated by the simulation to observe differences in the response trajectories of both models (Figure 5.7A, left panels). In addition, because of *skn-1* sensitive system control revealed during the development of the computational network, the expression of this node was altered for additional experiments to gain insight about loss (Figure 5.7A, middle panels) or gain (Figure 5.7A, right panels) of function in *skn-1*-mediated activities for both normal and tau-exacerbated aging. This genetic alteration was also chosen as many therapeutic approaches have been successful in targeting and modulating the *skn-1/Nrf2* antioxidant response pathway [280]. Simulation results indicate that *skn-1* alterations

resulted in slight alterations in maintaining ER and mitochondrial functionality within the molecular signature, particularly in autophagy and mitophagy activities. The changes in skn-1 led to more substantial benefits or consequences in mitigating oxidative damage, especially in the tau-exacerbated worms. These *skn-1*-dependent changes in the molecular signature trajectories corresponded with changes in age-dependent vulnerability phenotyping, displayed in Figure 5.7B. Simulation results indicate that *skn-1* was not required for the maintenance of the most resilient phenotype in either natural or tau-exacerbated aging (bottom panel), however, it was exceptionally important in mitigating chronic oxidative stress required for simulated cell agents to enter into the final vulnerability phenotype (top panel) that is proportional with poor cell survival. These simulation data are consistent with experimentally-observed relationships regarding skn-1/Nrf2-mediated cytoprotection in the context of antioxidant functions. autophagic maintenance and tauopathy amelioration in worms, mice and humans [285, 317, 318].

Neuronal survival during aging depends on multiple stress response pathways

As a final output of the simulation, neuronal survival was assessed over the full 20-day lifespan analysis for normal and tau-exacerbated cell populations and for response deficiencies. The results displayed here compare cell survival rates between the fully functional response network and groups lacking *skn-1*, *daf-16*, UPR^{mt} or UPR^{ER} activities (Figure 5.8). For normal aging (left panel), all simulated deficiencies except for the UPR^{mt} caused a decrease in cell survival. This is consistent with finding that UPR^{mt} modifications in normal aging nematodes without stress led to no stark changes in

longevity [187, 224]. For tau-exacerbated aging (right panel), all simulated deficiencies including the UPR^{mt} caused a decrease in cell survival, suggesting all of these pathways are critical in mitigating tau-dependent damage in aging nervous systems. This is especially consistent with findings that display the profound ameliorative effects of daf-16/FOXO activation, specific UPR^{ER} activation and regulation, UPR^{mt} activation and mitophagy on proteotoxic AD models of neurodegeneration [269, 286, 319, 320]. It is speculated here that all of these responses must act in concert to maintain resilient neuronal phenotypes, but the age-dependent deterioration of these quality control processes is yet to be fully understood.

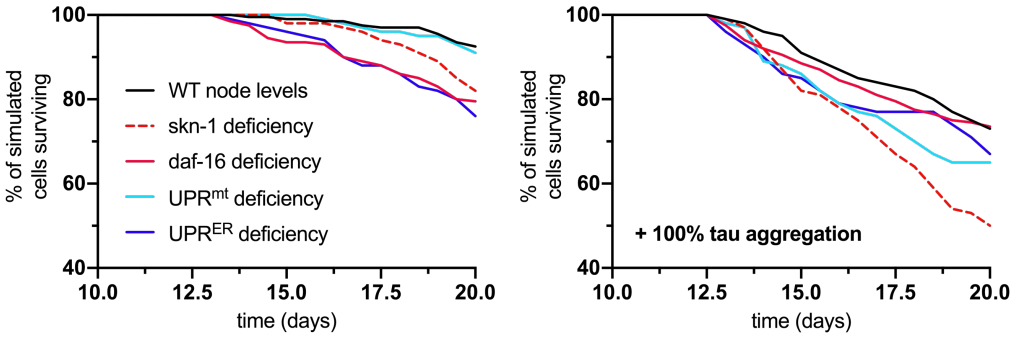

FIGURE 5.8

Analysis of cell survival in normal aging (left panel) and tau-exacerbated aging (right panel) neurons with respect to different node deficiencies. Time-course plots display no change in genetic nodes (denoted WT), and reduced levels of several nodes and response activities. Nodes of interest that were altered include skn-1, daf-16, UPR^{mt}, and UPR^{ER} activities, as these were selected as having strong determining potential against the phenotypic outputs and ultimate neuronal vulnerability.

Insights into investigating comprehensive pathway maintenance during aging

Because developing AD appears to be an inevitable event in the aging process and due to the refractory nature of the associated pathophysiology, actions taken toward preventing the triggers of AD are currently the most suitable options [262, 321]. Such actions are typically environmental interventions intended to reduce AD risk factors. Environmental enhancements include cognitive training, stress management, social engagement, physical activity, lipoprotein control for vascular health, nutritional approaches and phytochemical supplementation [322]. Certain stilbenoid phytochemicals such as resveratrol and pterostilbene have gained growing interest for their ability to prime cells to mount beneficial responses and combat age-dependent damage [2, 265]. All of these preventative measures appear to have selective cellular benefits against neuronal dysfunction that appears to silently progress for many years before pathological AD onset [323]. Any neurodegenerative disease, as we have quantitatively unpacked in this simulation study for AD pathogenesis, is born out of a multitude of intrinsic and environmental factors [323–325], and thus it is likely it will take multiple environmentally-based interventions to have a fully protective or even restorative effect on all neuronal populations.

Investigating all of these critical conditions that render neuron populations vulnerable to the triggers of AD and similar neurodegenerative diseases is difficult to perform *in vivo*. Computational models of aging have provided many insights into the systems biology obstacles of researching AD [173], and our previous simulation approach has offered value to the field of age-related diseases. However, this previous model was not without its limitations. Primarily, the previous simulation (i) lacked

nuanced details in the phenotypes describing age-dependent vulnerability, (ii) could have benefitted from more translational power in experimental biomarkers specific to genetic declines in disease states, (iii) and warranted more robustness and usability in computationally-intensive models. In the current study, we aimed to remedy these shortcomings of the previous model. The simulation presented here relies on a defined network capable of revealing heavily nuanced vulnerability phenotypes in aging organisms. The simulation was also constructed in a manner that allows AD researchers to follow up on defined reporter genes and biomolecules of stress responses highly relevant to aging and to the disease progression; such genes have been well-defined for a simple model organism. Finally, the simulation was mathematically simplified in areas that did not change critical network motifs for this study, and it was also expanded upon in areas that required more detail for aging and AD specifics; this ultimately allowed for a less computationally-intense model to increase agent-based population robustness and user friendliness. These improvements will bring us to better investigative tools for integrative experimental and computational neurodegenerative research.

In conclusion, the simulation results generated here highlight the importance of response pathway maintenance in degenerative aging and AD development, as evidenced by the temporal molecular signatures predicted. Of importance, this study quantitatively corroborates the growing understanding that mitochondrial and ER maintenance through specific UPR^{mt} and UPR^{ER} programming play a critical role in mitigating age-dependent vulnerability to proteotoxic and oxidative stressors. Additionally, this work confirms the importance oxidative stress responses mediated by

skn-1 and *daf-16* in prolonging age-dependent triggers of cell damage. As comprehensive studies integrating these responses continue to surface, we will continue to approach more detailed prognostic tools for age-related diseases and for AD prevention and treatment.

CHAPTER 6: FUTURE WORK

The simulation experiments have established new quantitative values for responses that are theoretically critical to toxicological, pharmacological and pathological research. The datasets generated for intraspecies food additive uncertainty can be applied to more compounds used as ingredients and may require future validation in toxicological research for regulatory purposes. The datasets generated for AhR-mediated effects through the use of several dietary ligands require additional single-cell validations and more high resolution time-course information about the ligand-dependent response for both toxicological and therapeutic purposes related to the AhR. Finally, the final datasets generated are critical to understanding the progression of degenerative aging and the tau-mediated progression of AD, however, some more descriptive experimental validations are now required to continue forward. As the computational simulations have been developed as translational tools for *C. elegans* research, the next progression of experiments involve testing the aforementioned scenarios of interest in nematode strains that have been established for wild-type and tau-mediated results. Such experiments will involve the inclusion of behavioral assays to test neurological function as well as molecular assays for stress response maintenance over individual lifespans as it corresponds to the molecular signatures predicted. This work is already underway, and will assist in validating the computational tools while presenting novel experimental information about the pathogenesis of age-dependent degenerative outcomes. The collective and iterative results will aid in producing more accurate and precise strategies for preventing and treating AD and similar diseases of aging.

CHAPTER 7: CONCLUSIONS

In conclusion, the experimental information elucidated here has shown the success of a new multimethod computational simulation paradigm for toxicological, pharmacological and pathological research. This experimental platform has especially been valuable in quickly theorizing critical cellular changes over organism lifespans, and the temporal datasets that have been produced are both expansive and sizably complex in their ability to measure many events simultaneously. In addition, simulation studies have been able to predictively tease out molecular determinants triggering cellular states of vulnerability in aging and disease. In all, the data presented in this dissertation define new modes of experimentation that have been useful in adding value to experimental data and in developing theories involving cellular responses. This work as a whole will aid in paving the path to a more quantitative future in scientific research.

CHAPTER 8: ORIGINAL CONTRIBUTIONS

8.1 Peer-reviewed publications

Hoffman TE, Hanneman WH (2017) Physiologically-based pharmacokinetic analysis of benzoic acid in rats, guinea pigs and humans: Implications for dietary exposures and interspecies uncertainty. *Computational Toxicology.* **3**, 19–32.

Hoffman TE, Barnett KJ, Wallis L, Hanneman WH (2017) A Multimethod Computational Simulation Approach for Investigating Mitochondrial Dynamics and Dysfunction in Degenerative Aging. *Aging Cell.* **16**(6), 1244–1255.

Hoffman TE, Hanneman WH (2018) Mitochondrial Avatars for Quantitative Aging Research. *Aging (Albany NY).* **10**(3), 301–302.

Hoffman TE, Acerbo ER, Carranza KF, Gilberto VS, Wallis LE, Hanneman WH (2018) Ultrasensitivity Dynamics of Diverse Aryl Hydrocarbon Receptor Modulators in a Hepatoma Cell Line. *Archives of Toxicology.* [Epub ahead of print]

8.2 Publications in progress

Hoffman TE, Moreno JA, Hanneman WH (2019) Network Simulations Reveal Molecular Signatures of Vulnerability to Age-dependent Stress and Tau Accumulation. Submitted to *Frontiers in Molecular Biosciences* for peer review.

Acerbo ER, Li Puma LC, Hoffman TE, Gilberto VS, Carranza KF, Hanneman WH (2019) Sulforaphane Protects Against Nitric Oxide-induced Mitochondrial Dysfunction. Submitted to *Journal of Food Science* for peer review.

Hoffman TE, Legare ME, Hanneman WH (2019) Uncertainty Analysis of an MCF-7-based Estrogen Response Assay. Submitted to *Dose-Response* for peer review.

8.3 Conference publications

Hoffman TE, Wallis LE, Hanneman WH (2016) A Predictive Simulation of Subacute PCB-induced Oxidative Stress in the Liver Using a Combination of Techniques. *The Toxicologist (Society of Toxicology Annual Meeting)*.

8.4 Oral platform presentations

Center for Environmental Medicine 2017 Symposium (45-minute Platform Presentation):
The Role of Mitochondrial Dysfunction in Cellular Aging: Insights from Computational Modeling and Simulation.

8.5 Conference poster and simulation presentations

Hoffman TE, Wallis LE, Hanneman WH (2016) A Predictive Simulation of Subacute PCB-induced Oxidative Stress in the Liver Using a Combination of Techniques. Society of Toxicology 2016 Annual Meeting (New Orleans, LA).

Hoffman TE, Hanneman WH (2016) Multimethod Computational Modeling Analysis of Mitochondrial Dysfunction Underlying Degenerative Senescence. Colorado State University 2016 Graduate Student Showcase (Fort Collins, CO).

Hoffman TE, Hanneman WH. (2016) Multimethod Computational Modeling Analysis of Spontaneous and Xenobiotic-Modulated Mitochondrial Dysfunction Underlying Degenerative Senescence. International Society of Computational Biology 2016 Rocky Meeting (Aspen/Snowmass, CO).

Hoffman TE, Hanneman WH. (2017) Physiologically-Based Pharmacokinetic Analysis of Benzoic Acid in Rats, Guinea Pigs and Humans: Implications for Dietary Exposures and Interspecies Uncertainty. Center for Environmental Medicine 2017 Symposium (Fort Collins, CO).

Hoffman TE, Hanneman WH. (2017) Multimethod Computational Modeling Analysis of Spontaneous and Xenobiotic-Modulated Mitochondrial Dysfunction Underlying Degenerative Senescence. Center for Environmental Medicine 2017 Symposium (Fort Collins, CO).

Hoffman TE, Hanneman WH (2018) Emerging Multimethod Computational Simulation Approaches for Investigating Cellular Network Dynamics and Cellular Damage. Winter Q-BIO 2018 (Maui, HI).

Hanneman WH, Secor TR, Hoffman TE (2018) Understanding Ultrasensitivity in Liver Hepatocytes Exposed to Exogenous Environmental Compounds. Winter Q-BIO 2018 (Maui, HI).

Vick ZD, Hoffman TE, Hanneman WH (2018) Computational Simulation Analysis of Metronidazole Pharmacokinetics and Potential Neurotoxicity Correlations. Colorado State University 2018 Graduate Student Showcase (Fort Collins, CO). ***CVMBS Top Scholar Winner.***

Kamal F, Hoffman TE, Hanneman WH (2018) Benzalkonium Chloride Induces Ocular Inflammation: Understanding the Response Through Computational Modeling. Colorado State University 2018 Graduate Student Showcase (Fort Collins, CO).

Hoffman TE, Acerbo ER, Carranza KF, Gilberto VS, Wallis LE, Hanneman WH (2019) Ultrasensitivity Dynamics of Diverse Aryl Hydrocarbon Receptor Modulators in a Hepatoma Cell Line. Winter Q-BIO 2019 (Kapolei, HI).

Hoffman TE, Moreno JA, Legare ME, Hanneman WH (2019) Network Simulations Reveal Molecular Signatures of Resilience to Age-Dependent Stress and Tau Accumulation. Winter Q-BIO 2019 (Kapolei, HI).

REFERENCES

1. Underwood E (2015) The final countdown. *Science*, 350(6265): 1188-1190.

2. Wang Y, Hekimi S (2015) Mitochondrial dysfunction and longevity in animals: Untangling the knot. *Science*, 350(6265): 1204-1207.

3. Luzzatto L, Pandolfi PP (2015) Causality and Chance in the Development of Cancer. *The New England Journal of Medicine*, 373(1): 84-88.

4. Geman D, Ochs M, Price ND, Tomasetti C, Younes L (2015) An argument for mechanism-based statistical inference in cancer. *Human Genetics*, 134(5): 479–495.

5. Hanneman WH, Legare ME, Tiffany-Castiglioni E, Safe SH (1996) The need for cellular, biochemical, and mechanistic studies. *Neurotoxicology and teratology*, 18(3): 247-50; discussion 271.

6. Judson R, Richard A, Dix DJ, Houck K, Martin M, Kavlock R et al. (2009) The toxicity data landscape for environmental chemicals. *Environmental Health Perspectives*, 117(5): 685-695.

7. Bhattacharya S, Zhang Q, Carmichael PL, Boekelheide K, Andersen ME (2011) Toxicity testing in the 21 century: defining new risk assessment approaches based on perturbation of intracellular toxicity pathways. *PLoS One*, 6(6): e20887.

8. Agoram BM, Martin SW, van der Graaf PH (2007) The role of mechanism-based pharmacokinetic-pharmacodynamic (PK-PD) modelling in translational research of biologics. *Drug discovery today*, 12(23-24): 1018-1024.

9. Ioannidis JP (2005) Why most published research findings are false. *PLoS Medicine*, 2(8): e124.

10. Begley CG, Ioannidis JP (2015) Reproducibility in science: improving the standard for basic and preclinical research. *Circulation research*, 116(1): 116-126.

11. Prinz F, Schlange T, Asadullah K (2011) Believe it or not: how much can we rely on published data on potential drug targets? *Nature reviews. Drug discovery*, 10(9): 712-712.

12. Begley CG, Ellis LM (2012) Drug development: Raise standards for preclinical cancer research. *Nature*, 483(7391): 531-533.

13. Lazebnik Y (2002) Can a biologist fix a radio? — Or, what I learned while studying apoptosis. *Cancer cell*, 2(3): 179-182.

14. Palsson B (2000) The challenges of in silico biology. *Nature Biotechnology*, 18(11), 1147-1150.

15. Beard DA, Kushmerick MJ (2009) Strong inference for systems biology. *PLoS Computational Biology*, 5(8), e1000459.

16. Simmons SO, Fan C, Ramabhadran R (2009) Cellular stress response pathway system as a sentinel ensemble in toxicological screening. *Toxicological sciences*, 111(2), 202-225.

17. National Research Council (2007) Toxicity testing in the 21st century: A vision and a strategy. Washington, DC: *The National Academies Press.*

18. Sturla SJ, Boobis AR, FitzGerald RE, Hoeng J, Kavlock RJ, Schirmer K, ... Peitsch MC (2014) Systems toxicology: from basic research to risk assessment. *Chemical research in toxicology*, 27(3), 314-329.

19. Adeleye Y, Andersen M, Clewell R, Davies M, Dent M, Edwards S, … Carmichael PL (2015) Implementing Toxicity Testing in the 21st Century (TT21C): Making safety decisions using toxicity pathways, and progress in a prototype risk assessment, *Toxicology*, 332, 102-111.

20. Settivari RS, Ball N, Murphy L, Rasoulpour R, Boverhof DR, Carney EW (2015) Predicting the future: opportunities and challenges for the chemical industry to apply 21st-century toxicity testing. *Journal of the American Association for Laboratory Animal Science*, 54(2), 214-223.

21. Boekelheide K, Campion SN (2010) Toxicity testing in the 21st century: using the new toxicity testing paradigm to create a taxonomy of adverse effects. *Toxicological sciences*, 114(1), 20-24.

22. Yuan H, Zhang Q, Guo J, Zhang T, Zhao J, Li J, ... Peng S (2016) A PGC-1α-Mediated Transcriptional Network Maintains Mitochondrial Redox and Bioenergetic Homeostasis against Doxorubicin-Induced Toxicity in Human Cardiomyocytes: Implementation of TT21C. *Toxicological sciences*, 150(2), 400-417.

23. Hoeng J, Talikka M, Martin F, Sewer A, Yang X, Iskandar A, ... Peitsch MC (2014) Case study: the role of mechanistic network models in systems toxicology. *Drug discovery today*, 19(2): 183-192.

24. Williams DP, Shipley R, Ellis MJ, Webb S, Ward J, Gardner I, Creton S (2013) Novel in vitro and mathematical models for the prediction of chemical toxicity. *Toxicology Research*, 2(1), 40-59.

25. Noble D (2002) The rise of computational biology. *Nature Reviews. Molecular Cell Biology*, 3(6), 459-463.

26. Pérez-Nueno VI (2015) Using quantitative systems pharmacology for novel drug discovery. *Expert opinion on drug discovery*, 10(12), 1315-1331.

27. Breithaupt H (2006) The engineer's approach to biology. *EMBO Reports*, *7*(1), 21–23.

28. Zhang Q, Bhattacharya S, Andersen ME, Conolly RB (2010) Computational systems biology and dose-response modeling in relation to new directions in toxicity testing. *Journal of toxicology and environmental health. Part B*, 13(2-4), 253-276.

29. Ebhardt HA, Root A, Sander C, Aebersold R (2015) Applications of targeted proteomics in systems biology and translational medicine. *Proteomics*, 15(18), 3193-3208.

30. Cai Y (2013) Editorial: The application of systems biology and bioinformatics methods in proteomics, transcriptomics and metabolomics (PART II). *Protein & peptide letters*, 20(3), 241-242.

31. Stegle O, Teichmann SA, Marioni JC (2015) Computational and analytical challenges in single-cell transcriptomics. *Nature Reviews. Genetics*, 16(3), 133-145.

32. Kadioglu O, Efferth T (2014) Contributions from emerging transcriptomics technologies and computational strategies for drug discovery. *Investigational New Drugs*, 32(6), 1316-1319.

33. Gurwitz D (2014) From transcriptomics to biological networks. *Drug development research*, 75(5), 267-270.

34. Faustino RS, Wyles SP, Groenendyk J, Michalak M, Terzic A, Perez-Terzic C (2015) Systems biology surveillance decrypts pathological transcriptome remodeling. *BMC Systems Biology*, *9*, 36.

35. Parikshak N, Gandal MJ, Geschwind DH (2015) Systems biology and gene networks in neurodevelopmental and neurodegenerative disorders. *Nature Reviews. Genetics*, 16(8), 441-458.

36. Kutmon M, Evelo CT, Coort SL (2014) A network biology workflow to study transcriptomics data of the diabetic liver. *BMC Genomics*, *15*(1), 971.

37. Voutetakis K, Chatziioannou A, Gonos ES, Trougakos IP (2015) Comparative Meta-Analysis of Transcriptomics Data during Cellular Senescence and *In Vivo* Tissue Ageing. *Oxidative Medicine and Cellular Longevity*, *2015*, 732914.

38. Pérez Millán M, Dickenstein A (2015) Implicit dose-response curves. *Journal of Mathematical Biology*, 70(7), 1669-1684.

39. Thomas R, Thieffry D, Kaufman M (1995) Dynamical behaviour of biological regulatory networks--I. Biological role of feedback loops and practical use of the concept of the loop-characteristic state. *Bulletin of Mathematical Biology*, 57(2), 247-276.

40. Ferrell JE, Xiong W (2001) Bistability in cell signaling: How to make continuous processes discontinuous, and reversible processes irreversible. *Chaos*, 11(1), 227-236.

41. Ferrell JE, Ha SH (2014) Ultrasensitivity part I: Michaelian responses and zero-order ultrasensitivity. *Trends in biochemical sciences*, 39(10), 496-503.

42. Ferrell JE, Ha SH (2014) Ultrasensitivity part III: cascades, bistable switches, and oscillators. *Trends in biochemical sciences*, 39(12), 612-618.

43. Ferrell JE, Ha SH (2014) Ultrasensitivity part II: multisite phosphorylation, stoichiometric inhibitors, and positive feedback. *Trends in biochemical sciences*, 39(11), 556-569.

44. Ha SH, Ferrell JE (2016) Thresholds and ultrasensitivity from negative cooperativity. *Science*, 352(6288), 990-993.

45. Ferrell JE, Machleder EM (1998) The biochemical basis of an all-or-none cell fate switch in Xenopus oocytes. *Science*, 280(5365), 895-898.

46. French CT, Hanneman WH, Chubb LS, Billings RE, Andersen ME (2004) Induction of CYP1A1 in primary rat hepatocytes by 3,3',4,4',5-pentachlorobiphenyl: evidence for a switch circuit element. *Toxicological sciences*, 78(2): 276-286.

47. Broccardo CJ, Billings RE, Chubb LS, Andersen ME, Hanneman WH (2004) Single cell analysis of switch-like induction of CYP1A1 in liver cell lines. *Toxicological sciences*, 78(2): 287-294.

48. Ingalls BP (2013) Mathematical modeling in systems biology: an introduction. *MIT press.*

49. Gentner D, Stevens AL (1983) Mental models. Hillsdale, NJ: *L. Erlbaum Associates*. 7-8.

50. Johansson F (2006) The Medici effect: What elephants and epidemics can teach us about innovation. Boston, MA: *Harvard Business School Press*. 26.

51. An G, Mi Q, Dutta-Moscato J, Vodovotz Y (2009) Agent-based models in translational systems biology. *Wiley interdisciplinary reviews. Systems biology and medicine*, 1(2), 159-171.

52. Cosgrove J, Butler J, Alden K, Read M, Kumar V, Cucurull-Sanchez L, ... Coles M (2015) Agent-Based Modeling in Systems Pharmacology. *CPT: pharmacometrics and systems pharmacology*, 4(11), 615-629.

53. Macal CM, North MJ (2010) Tutorial on Agent-Based Modeling and Simulation. *Journal of Simulation* 4(3), 151-162.

54. Székely T, Burrage K (2014) Stochastic simulation in systems biology. *Computational and Structural Biotechnology Journal*, 12(20-21), 14-25.

55. Santos G, Díaz M, Torres NV (2016) Lipid Raft Size and Lipid Mobility in Non-raft Domains Increase during Aging and Are Exacerbated in APP/PS1 Mice Model of Alzheimer's Disease. Predictions from an Agent-Based Mathematical Model. *Frontiers in Physiology*, *7*, 90.

56. Sterman JD (2001) System Dynamics Modeling: Tools for Learning in a Complex World. *California Management Review*, *43*(4), 8-25.

57. Sager JE, Yu J, Ragueneau Majlessi I, Isoherranen N (2015) Physiologically Based Pharmacokinetic (PBPK) Modeling and Simulation Approaches: A Systematic Review of Published Models, Applications, and Model Verification. *Drug metabolism and disposition*, 43(11), 1823-1837.

58. Chiang AW, Liu WC, Charusanti P, Hwang MJ (2014) Understanding system dynamics of an adaptive enzyme network from globally profiled kinetic parameters. *BMC Systems Biology*, *8*, 4.

59. Cilfone NA, Kirschner DE, Linderman J (2015) Strategies for efficient numerical implementation of hybrid multi-scale agent-based models to describe biological systems. *Cellular and Molecular Bioengineering*, 8(1), 119-136.

60. HJ Scholl (2001) Agent-based and system dynamics modeling: a call for cross study and joint research. *Proceedings of the 34th Annual Hawaii International Conference on System Sciences*, Maui, HI, USA, 2001, 8.

61. Kaul H, Ventikos Y (2015) Investigating biocomplexity through the agent-based paradigm. *Briefings in bioinformatics*, 16(1), 137-152.

62. Bartocci E, Lió P (2016) Computational Modeling, Formal Analysis, and Tools for Systems Biology. *PLoS Computational Biology*, 12(1), e1004591.

63. Krinner A, Roeder I, Loeffler M, Scholz M (2013) Merging concepts - coupling an agent-based model of hematopoietic stem cells with an ODE model of granulopoiesis. *BMC Systems Biology*, *7*, 117.

64. Pollmächer J, Figge MT (2015) Deciphering chemokine properties by a hybrid agent-based model of *Aspergillus fumigatus* infection in human alveoli. *Frontiers in Microbiology*, *6*, 503.

65. Balkacem K, Foudil C (2012) An AnyLogic Agent Based Model for the Lymph Node Lymphocytes First Humoral Immune Response. *International Proceedings of Computer Science & Information Tech*, 34, 163-169.

66. Warth AD (1991) Mechanism of action of benzoic acid on Zygosaccharomyces bailii: effects on glycolytic metabolite levels, energy production, and intracellular pH. *Appl. Environ. Microbiol.* **57**(12), 3410–3414.

67. Nair B (2001) Final report on the safety assessment of Benzyl Alcohol, Benzoic Acid, and Sodium Benzoate. *Int. J. Toxicol*. **20** (Suppl. 3), 23–50.

68. White A (1941) Growth inhibition produced in rats by the oral administration of sodium benzoate. Effects of various dietary supplements. *Yale. J. Biol. Med.* **13**, 759−768.

69. Kreis H, Frese K, Wilmes G (1967) Physiological and histological changes in rats fed benzoic acid. *Food Cosmet. Toxicol.* **5**, 505−511. [German article, English abstract.]

70. Kieckebusch W, Lang K (1960) The tolerability of benzoic acid in chronic feeding experiments. *Arzneimittelforschung* **10**, 1001−1003. [Translated from German.]

71. JECFA (2015) Evaluation of certain food additives and contaminants. (Eightieth report of the Joint FAO/WHO Expert Committee on Food Additives). *WHO Technical Report Series*, No. **995**, Benzoates: dietary exposure assessment, 13–16.

72. Ling MP, Lien KW, Wu CH, Ni SP, Huang HY, Hsieh DP (2015) Dietary exposure estimates for the food preservatives benzoic acid and sorbic acid in the total diet in Taiwan. *J. Agric. Food Chem.* **63**(7), 2074–2082.

73. Ma KM, Chan CM, Chung SW, Ho YY, Xiao Y (2009) Dietary exposure of secondary school students in Hong Kong to benzoic acid in prepackaged non-alcoholic beverages. *Food Addit. Contam. Part A* **26**(1), 12–16.

74. European Food Safety Authority Panel on Food Additives and Nutrient Sources Added to Food (2016) Scientific Opinion on the re-evaluation of benzoic acid (E 210), sodium benzoate (E 211), potassium benzoate (E 212) and calcium benzoate (E 213) as food additives. *EFSA J. 2016* **14**(3), 4433.

75. Mancini FR, Paul D, Gauvreau J, Volatier JL, Vin K, Hulin M (2015) Dietary exposure to benzoates (E210-E213), parabens (E214-E219), nitrites (E249-E250), nitrates (E251-E252), BHA (E320), BHT (E321) and aspartame (E951) in children less than 3 years old in France. *Food Addit. Contam. Part A* **32**(3), 293–306.

76. Bilau M, Matthys C, Vinkx C, De Henauw S (2008) Intake assessment for benzoates in different subgroups of the Flemish population. *Food Chem Toxicol.* **46**(2), 717–723.

77. Leth T, Christensen T, Larsen IK (2010) Estimated intake of benzoic and sorbic acids in Denmark. *Food Addit. Contam. Part A* **27**(6), 783–792.

78. Bridges JW, French MR, Smith RL, Williams RT (1970) The fate of benzoic acid in various species. *Biochem. J*. **118**(1), 47–51.

79. Schwab AJ, Tao L, Yoshimura T, Simard A, Barker F, Pang KS (2001) Hepatic uptake and metabolism of benzoate: a multiple indicator dilution, perfused rat liver study. *Am. J. Physiol. Gastrointest. Liver Physiol.* **280**(6) G1124–G1136.

80. Gatley SJ, Sherratt HS (1977) The synthesis of hippurate from benzoate and glycine by rat liver mitochondria, submitochondrial localization and kinetics. *Biochem. J*. **166**(1), 39–47.

81. Campbell JL, Andersen ME, Hinderliter PM, Yi KD, Pastoor TP, Breckenridge CB, Clewell, HJ (2016) PBPK Model for Atrazine and Its Chlorotriazine Metabolites in Rat and Human. *Toxicol. Sci.* **150**(2), 441–453.

82. Chen K, Seng K-Y (2012) Calibration and validation of a physiologically based model for soman intoxication in the rat, marmoset, guinea pig and pig. *J. Appl. Toxicol.* **32**, 673–686.

83. Brown RP, Delp MD, Lindstedt SL, Rhomberg LR, Beliles RP (1997) Physiological parameter values for physiologically based pharmacokinetic models. *Toxicol. Ind. Health* **13**(4), 407–484.

84. International Commission on Radiological Protection (2002) Basic anatomical and physiological data for use in radiological protection: reference values. A report of age- and gender-related differences in the anatomical and physiological

characteristics of reference individuals. *ICRP Publication 89. Ann ICRP* **32**(3-4), 5–265.

85. Sweeney RE, Langenberg JP, Maxwell DM (2006) A physiologically based pharmacokinetic (PB/PK) model for multiple exposure routes of soman in multiple species. *Archiv für Toxikologie* [Archives of Toxicology] **80**(11), 719–731.

86. Langenberg JP, Van Dijk C, Sweeney RE, Maxwell DM, De Jong LPA, Benschop HP (1997) Development of a physiologically based model for the toxicokinetics of C(±)P(±) soman in the atropinized guinea pig. *Arch. Toxicol.* **71**, 320–331.

87. Haddad S, Poulin P, Krishnan K (2000) Relative lipid content as the sole mechanistic determinant of the adipose tissue:blood partition coefficients of highly lipophilic organic chemicals. *Chemosphere* **40**(8), 839–843.

88. Schmitt W (2008) General approach for the calculation of tissue to plasma partition coefficients. *Toxicol. In Vitro* **22**(2), 457–467.

89. Kubota K, Ishizaki T (1991) Dose-dependent pharmacokinetics of benzoic acid following oral administration of sodium benzoate to humans. *Eur. J. Clin. Pharmacol.* **41**(4), 363–368.

90. Akira K, Farrant RD, Lindon JC, Caddick ST, Nicholls AW, Nicholson JK (1994) High-field deuterium nuclear magnetic resonance spectroscopic monitoring of the pharmacokinetics of selectively deuterated benzoic acid in man. *Anal. Biochem.* **221**(2), 297–302.

91. Macpherson SE, Barton CN, Bronaugh RL (1996) Use of in vitro skin penetration data and a physiologically based model to predict in vivo blood levels of benzoic acid. *Toxicol. Appl. Pharmacol.* **140**(2), 436–443.

92. Gregus Z, Halászi E, Klaassen CD (1999) Effect of chlorophenoxyacetic acid herbicides on glycine conjugation of benzoic acid. *Xenobiotica* **29**(6), 547–559.

93. Akira K, Takagi N, Takeo S, Shindo H, Baba S (1993) Application of 13C-labeling and nuclear magnetic resonance spectroscopy to pharmacokinetic research: measurement of metabolic rate of benzoic acid to hippuric acid in the rat. *Anal. Biochem.* **210**(1), 86–90.

94. Yuan JH, Goehl TJ, Abdo K, Clark J, Espinosa O, Bugge C, Garcia D (1995) Effects of gavage versus dosed feed administration on the toxicokinetics of benzyl acetate in rats and mice. *Food Chem. Toxicol.* **33**(2), 151–158.

95. Abdo KM, Huff JE, Haseman JK, Boorman GA, Eustis SL, Matthews HB, Burka LT, Prejean JD, Thompson RB (1985) Benzyl acetate carcinogenicity, metabolism, and disposition in Fischer 344 rats and B6C3F1 mice. *Toxicology* **37**(1-2), 159–170.

96. Licata AC, Dekant W, Smith CE, Borghoff SJ (2001) A physiologically based pharmacokinetic model for methyl tert-butyl ether in humans: implementing sensitivity and variability analyses. *Toxicol. Sci.* **62**(2), 191–204.

97. Peters SA (2012) *Physiologically based pharmacokinetic (PBPK) modeling and simulations: principles, methods, and applications in the pharmaceutical industry* (8.5 Sensitivity Analysis). Jon Wiley & Sons, Inc. Hoboken, New Jersey. Print. 172 p.

98. Del Olmo A, Calzada J, Nuñez M (2015) Benzoic Acid and Its Derivatives as Naturally Occurring Compounds in Foods and as Additives: Uses, Exposure and Controversy. *Crit. Rev. Food Sci. Nutr*. (E-publication, accessed 18 October 2016).

99. National Toxicology Program (1986) Toxicology and Carcinogenesis Studies of Benzyl Acetate in F344/N Rats and B6C3F1 Mice (Gavage Studies). *Technical Report Series (NTP)* **250**, 1–204.

100. Sheftel VO (2000) *Indirect food additives and polymers: Migration and toxicology*. Lewis Publishers. Boca Raton, FL. 835 p.

101. Kluwe WM, Montgomery CA, Giles HD, Prejean JD (1983) Encephalopathy in rats and nephropathy in rats and mice after subchronic oral exposure to benzaldehyde. *Food Chem. Toxicol.* **21**(3), 245–250.

102. Andersen A (2006) Final report on the safety assessment of benzaldehyde*. Int. J. Toxicol.* **25**(Suppl. 1), 11–27.

103. World Health Organization, International Programme on Chemical Safety (2010) Characterization and Application of Physiologically Based Pharmacokinetic Models in Risk Assessment. *IPCS Harmonization Project Document No. 9*.

104. van der Sluis R, Badenhorst CP, Erasmus E, van Dyk E, van der Westhuizen FH, van Dijk AA (2015) Conservation of the coding regions of the glycine N-acyltransferase gene further suggests that glycine conjugation is an essential detoxification pathway. *Gene* **571**(1), 126–134.

105. Gregus Z, Fekete T, Halászi E, Gyurasics A, Klaassen CD (1998) Effects of fibrates on the glycine conjugation of benzoic acid in rats. *Drug Metab. Dispos.* **26**(11), 1082–1088.

106. Pelekis M, Emond C (2009) Physiological modeling and derivation of the rat to human toxicokinetic uncertainty factor for the carbamate pesticide aldicarb. *Environ. Toxicol. Pharmacol.* **28**(2), 179–191.

107. Troutman JA, Rick DL, Stuard SB, Fisher J, Bartels MJ (2015) Development of a physiologically-based pharmacokinetic model of 2-phenoxyethanol and its metabolite phenoxyacetic acid in rats and humans to address toxicokinetic uncertainty in risk assessment. *Regul. Toxicol. Pharmacol.* **73**(2), 530–543.

108. Hasegawa R, Hirata-Koizumi M, Dourson ML, Parker A, Sweeney LM, Nishikawa A, Yoshida M, Ono A, Hirose A (2010) Proposal of new uncertainty factor application to derive tolerable daily intake. *Regul. Toxicol. Pharmacol.* **58**(2), 237–242.

109. Landers JP, Bunce NJ (1991) The Ah receptor and the mechanism of dioxin toxicity. *Biochemical Journal*. 276(2): 273–287.

110. Abel J, Haarmann-Stemmann T (2010) An introduction to the molecular basics of aryl hydrocarbon receptor biology. *Biological Chemistry*. 391(11): 1235–1248.

111. Chubb LS, Andersen ME, Broccardo CJ, Legare ME, Billings RE, Dean CE, Hanneman WH (2004) Regional induction of CYP1A1 in rat liver following

treatment with mixtures of PCB 126 and PCB 153. *Toxicologic Pathology*. 32(4): 467–473.

112. Whitlock J (1999) Induction of cytochrome P4501A1. *Annual Review of Pharmacology and Toxicology*. 39: 103–125.

113. Denison MS, Soshilov AA, He G, DeGroot DE, Zhao B (2011) Exactly the Same but Different: Promiscuity and Diversity in the Molecular Mechanisms of Action of the Aryl Hydrocarbon (Dioxin) Receptor. *Toxicological Sciences*. 124(1): 1–22.

114. Wei Y, Zhao L, He W, Yang J, Geng C, Chen Y, Liu T, Chen H, Li Y (2016) Benzo[a]pyrene promotes gastric cancer cell proliferation and metastasis likely through the Aryl hydrocarbon receptor and ERK-dependent induction of MMP9 and c-myc. *International Journal of Oncology*. 49(5): 2055–2063.

115. Beischlag TV, Morales JL, Hollingshead BD, Perdew GH (2008) The Aryl Hydrocarbon Receptor Complex and the Control of Gene Expression. *Critical Reviews in Eukaryotic Gene Expression*. 18(3): 207–250.

116. Kiss EA, Diefenbach A (2012) Role of the Aryl Hydrocarbon Receptor in Controlling Maintenance and Functional Programs of RORγt^{+} Innate Lymphoid Cells and Intraepithelial Lymphocytes. *Frontiers in Immunology*. 3: 124.

117. Kolluri S, Jin U, Safe S (2017) Role of the aryl hydrocarbon receptor in carcinogenesis and potential as an anti-cancer drug target. *Archives of Toxicology*. 91(7): 2497–2513.

118. Safe S, Cheng Y, Jin UH (2017) The Aryl Hydrocarbon Receptor (AhR) as a Drug Target for Cancer Chemotherapy. *Current Opinion in Toxicology*. 2: 24–29.

119. Bowers OJ, Sommersted KB, Sowell RT, Boling GE, Hanneman WH, Titus RG, Dekrey GK (2006) 2,3,7,8-tetrachlorodibenzo-p-dioxin (TCDD) reduces Leishmania major burdens in C57BL/6 mice. The *American Journal* of *Tropical Medicine* and *Hygiene*. 75(4): 749–752.

120. Rogan E (2006) The natural chemopreventive compound indole-3-carbinol: State of the science. *In Vivo*. 20(2): 221–228.

121. Bradlow H, Zeligs M (2010) Diindolylmethane (DIM) spontaneously forms from indole-3-carbinol (I3C) during cell culture experiments. *In Vivo*. 24(4): 387–391.

122. Patel AR, Spencer SD, Chougule MB, Safe S, Singh M (2012) Pharmacokinetic evaluation and In Vitro–In Vivo Correlation (IVIVC) of novel methylene-substituted 3,3′ diindolylmethane (DIM). *European Journal of Pharmaceutical Sciences*. 46(1-2): 8–16.

123. Stepankova M, Bartonkova I, Jiskrova E, Vrzal R, Mani S, Kortagere S, Dvorak Z (2018) Methylindoles and methoxyindoles are agonists and antagonists of human aryl hydrocarbon receptor AhR. *Molecular Pharmacology*. [Epub ahead of print].

124. Fan S, Meng Q, Saha T, Sarkar FH, Rosen EM (2009) Low concentrations of diindolylmethane, a metabolite of indole-3-carbinol, protects against oxidative stress in a BRCA1-dependent manner. *Cancer Research*. 69(15): 6083–6091.

125. Poornima J, Mirunalini S (2014) Regulation of carbohydrate metabolism by indole-3-carbinol and its metabolite 3,3'-diindolylmethane in high-fat diet-induced C57BL/6J mice. *Molecular and Cellular Biochemistry*. 385(1-2): 7–15.

126. Natividad JM, Agus A, Planchais J, Lamas B, Jarry AC, Martin R, Michel M-L, Chong-Nguyen C, Roussel R, Straube M, Jegou S, McQuitty C, Gall ML, da Costa G, Lecornet E, Michaudel C, Modoux M, Glodt J, Bridonneau C, Sovran B, Dupraz L, Bado A, Richard ML, Langella P, Hansel B, Launay J-M, Xavier RJ, Duboc H, Sokol H (2018) Impaired Aryl Hydrocarbon Receptor Ligand Production by the Gut Microbiota Is a Key Factor in Metabolic Syndrome. *Cell Metabolism.* S1550-4131(18): 30444–30443.

127. Murray IA, Perdew GH (2017) Ligand activation of the Ah receptor contributes to gastrointestinal homeostasis. *Current Opinion in Toxicology*. 2: 15–23.

128. Li Y, Innocentin S, Withers D, Roberts N, Gallagher A, Grigorieva E, Wilhelm C, Veldhoen M (2011) Exogenous stimuli maintain intraepithelial lymphocytes via aryl hydrocarbon receptor activation. *Cell*. 147(3): 629–640.

129. Kawajiri K, Kobayashi Y, Ohtake F, Ikuta T, Matsushima Y, Mimura J, Pettersson S, Pollenz RS, Sakaki T, Hirokawa T, Akiyama T, Kurosumi M, Poellinger L, Kato S, Fujii-Kuriyama Y (2009) Aryl hydrocarbon receptor suppresses intestinal carcinogenesis in $Apc^{Min/+}$ mice with natural ligands. *Proceedings of the National Academy of Sciences of the United States of America*. 106(32): 13481–13486.

130. Su M, Qian C, Hu Y, Lu W, Huang R, Chen M, Chen J (2017) Inhibitory effect of the low-toxic exogenous aryl hydrocarbon receptor modulator 3′3-diindolylmethane on gastric cancer in mice. *Oncology Letters.* 14(6): 8100–8105.

131. Hooper L (2011) You AhR what you eat: Linking diet and immunity. *Cell*. 147(3): 489–491.

132. Hubbard T, Murray I, Nichols R, Cassel K, Podolsky M, Kuzu G, Tian Y, Smith P, Kennett MJ, Patterson AD, Perdew G (2017) Dietary Broccoli Impacts Microbial Community Structure and Attenuates Chemically Induced Colitis in Mice in an Ah receptor dependent manner. *Journal of Functional Foods*. 37: 685–698.

133. Song J, Clagett-Dame M, Peterson RE, Hahn ME, Westler WM, Sicinski RR, DeLuca HF (2002) A ligand for the aryl hydrocarbon receptor isolated from lung. *Proceedings of the National Academy of Sciences of the United States of America*. 99(23): 14694–14699.

134. Henry EC, Bemis JC, Henry O, Kende AS, Gasiewicz TA (2006) A potential endogenous ligand for the aryl hydrocarbon receptor has potent agonist activity in vitro and in vivo. *Archives of Biochemistry and Biophysics*. 450(1): 67–77.

135. Goettel JA, Gandhi R, Kenison JE, Yeste A, Murugaiyan G, Sambanthamoorthy S, Griffith AE, Patel B, Shouval DS, Weiner HL, Snapper SB, Quintana FJ (2016) AHR activation is protective against colitis driven by T cells in humanized mice. *Cell Reports*. 17(5): 1318–1329.

136. Abron JD, Singh NP, Mishra MK, Price RL, Nagarkatti M, Nagarkatti PS, Singh UP (2018) An endogenous aryl hydrocarbon receptor (AhR) ligand, ITE induces regulatory T cells (Tregs) and ameliorates experimental colitis. *American Journal of Physiology: Gastrointestinal and Liver Physiology.* [Epub ahead of print].

137. Denison MS, Nagy SR (2003) Activation of the aryl hydrocarbon receptor by structurally diverse exogenous and endogenous chemicals. *Annu Rev Pharmacol Toxicol.* 43: 309–334.

138. Yamaori S, Kinugasa Y, Jiang R, Takeda S, Yamamoto I, Watanabe K (2015) Cannabidiol induces expression of human cytochrome P450 1A1 that is possibly mediated through aryl hydrocarbon receptor signaling in HepG2 cells. *Life Sciences.* 136: 87–93.

139. Ciolino HP, Daschner PJ, Wang TTY, Yeh GC (1998) Effect of curcumin on the aryl hydrocarbon receptor and cytochrome P450 1A1 in MCF-7 human breast carcinoma cells. *Biochem. Pharmacol.* 56:197–206.

140. Gradelet S, Leclerc J, Siess M-H, Astorg PO (1996) B-Apo-8′-carotenal, but not β-carotene, is a strong inducer of liver cytochromes P4501A1 and 1A2 in rat. *Xenobiotica*. 26: 909–919.

141. Gradelet S, Astorg P, Leclerc J, Cheva- lier J, Vernevaut M-F, Siess M-H (1996) Effects of canthaxanthin, astaxanthin, lycopene and lutein on liver xenobiotic-metabolizing enzymes in the rat. *Xenobiotica*. 6: 49–63.

142. Bock K (2016) Human and rodent aryl hydrocarbon receptor (AHR): From mediator of dioxin toxicity to physiologic AHR functions and therapeutic options. *Biological Chemistry*. 398(4): 455–464.

143. Murray IA, Patterson AD, Perdew GH (2014) Ah Receptor Ligands in Cancer: Friend and Foe. *Nature Reviews. Cancer*. 14(12): 801–814.

144. Wisler JW, Xiao K, Thomsen ARB, Lefkowitz RJ (2014) Recent developments in biased agonism. *Current Opinion in Cell Biology*. 0: 18–24.

145. Pradhan AA, Smith ML, Kieffer BL, Evans CJ (2012) Ligand-directed signalling within the opioid receptor family. *British Journal of Pharmacology*. 167(5): 960–969.

146. Shan J, Khelashvili G, Mondal S, Mehler EL, Weinstein H (2012) Ligand-Dependent Conformations and Dynamics of the Serotonin 5-HT_{2A}Receptor Determine Its Activation and Membrane-Driven Oligomerization Properties. *PLoS Computational Biology*. 8(4): e1002473.

147. Wootten D, Savage E, Willard F, Bueno A, Sloop K, Christopoulos A, Sexton P (2013) Differential activation and modulation of the glucagon-like peptide-1 receptor by small molecule ligands. *Molecular Pharmacology*. 83(4): 822–834.

148. Hadley K, Louw A, Hapgood J (2011) Differential nuclear localisation and promoter occupancy play a role in glucocorticoid receptor ligand-specific transcriptional responses. *Steroids*. 76(10-11): 1176–1184.

149. Maier MS, Legare ME, Hanneman WH (2007) The aryl hydrocarbon receptor agonist 3,3',4,4',5-pentachlorobiphenyl induces distinct patterns of gene expression between hepatoma and glioma cells: chromatin remodeling as a mechanism for selective effects. *Neurotoxicology*. 28(3): 594–612.

150. Henry EC, Welle SL, Gasiewicz TA (2010) TCDD and a Putative Endogenous AhR Ligand, ITE, Elicit the Same Immediate Changes in Gene Expression in Mouse Lung Fibroblasts. *Toxicological Sciences*. 114(1): 90–100.

151. Wu Y, Chen X, Zhou Q, He Q, Kang J, Zheng J, Wang K, Duan T (2014) ITE and TCDD Differentially Regulate the Vascular Remodeling of Rat Placenta via the Activation of AhR. *PLoS ONE*. 9(1): e86549.

152. Ehrlich A, Pennington J, Bisson W, Kolluri S, Kerkvliet N (2018) TCDD, FICZ, and Other High Affinity AhR Ligands Dose-Dependently Determine the Fate of $CD4^+$ T Cell Differentiation. *Toxicological Sciences*. 161(2): 310–320.

153. Broccardo CJ, Billings RE, Andersen ME, Hanneman WH (2005) Probing the control elements of the CYP1A1 switching module in H4IIE hepatoma cells. *Toxicological Sciences.* 88(1): 82–94.

154. Zhang Q, Bhattacharya S, Andersen ME (2013) Ultrasensitive response motifs: basic amplifiers in molecular signalling networks. *Open Biology*. 3(4), 130031.

155. Nagy SR, Sanborn JR, Hammock BD, Denison MS (2002) Development of a green fluorescent protein-based cell bioassay for the rapid and inexpensive detection and characterization of Ah receptor agonists*. Toxicological Sciences.* 65(2): 200–210.

156. Corrada D, Soshilov AA, Denison MS, Bonati L (2016) Deciphering Dimerization Modes of PAS Domains: Computational and Experimental Analyses of the AhR:ARNT Complex Reveal New Insights Into the Mechanisms of AhR Transformation. *PLoS Comput. Biol*. 12(6): e1004981.

157. Wu D, Potluri N, Kim Y, Rastinejad F (2013) Structure and Dimerization Properties of the Aryl Hydrocarbon Receptor PAS-A Domain. *Molecular and Cellular Biology*. 33(21): 4346–4356.

158. Powis M, Celius T, Matthews J (2011) Differential ligand-dependent activation and a role for Y322 in aryl hydrocarbon receptor-mediated regulation of gene expression. *Biochemical and Biophysical Research Communications*. 410(4): 859–865.

159. Dolciami D, Gargaro M, Cerra B, Scalisi G, Bagnoli L, Servillo G, Fazia MAD, Puccetti P, Quintana FJ, Fallarino F, Macchiarulo, A (2018) Binding Mode and Structure-Activity Relationships of ITE as an Aryl Hydrocarbon Receptor (AhR) Agonist. *ChemMedChem*. 13(3): 270–279.

160. Li Y, Wang K, Zou QY, Magness RR, Zheng J (2015) 2,3,7,8-Tetrachlorodibenzo-*p*-Dioxin Differentially Suppresses Angiogenic Responses in Human Placental Vein and Artery Endothelial Cells. *Toxicology*. 336: 70–78.

161. Li Y, Wang K, Zou QY, Jiang YZ, Zhou C, Zheng J (2017) ITE Suppresses Angiogenic Responses in Human Artery and Vein Endothelial Cells: Differential Roles of AhR. *Reproductive Toxicology*. 74: 181–188.

162. Saito R, Miki Y, Hata S, Takagi K, Iida S, Oba Y, Ishida T, Suzuki T, Ohuchi N, Sasano H (2014) Aryl hydrocarbon receptor in breast cancer—a newly defined prognostic marker. *Hormones & Cancer*. 5(1): 11–21.

163. Marques M, Laflamme L, Benassou I, Cissokho C, Guillemette B, Gaudreau L (2014) Low levels of 3,3′-diindolylmethane activate estrogen receptor α and induce proliferation of breast cancer cells in the absence of estradiol. *BMC Cancer*. 14: 524.

164. Pavuk M, Patterson DG Jr, Turner WE (2014) Serum concentrations of TCDD and other dioxin-like compounds in US Air Force veterans of Operation Ranch Hand. *Chemosphere*. 102: 18–23.

165. Warner M, Mocarelli P, Brambilla P, Wesselink A, Patterson DG, Turner WE, Eskenazi B (2014) Serum TCDD and TEQ Concentrations among Seveso Women, Twenty Years after the Explosion. *Journal of Exposure Science & Environmental Epidemiology*. 24(6): 588–594.

166. Magoni M, Donato F, Speziani F, Leonardi L, Orizio G, Scarcella C, Gaia A, Apostoli P (2016) Substantial decline of polychlorinated biphenyls serum levels 10years after public health interventions in a population living near a contaminated site in Northern Italy. *Environ. Int.* 95: 69–78.

167. Campbell J, Franzen A, Van Landingham C, Lumpkin M, Crowell S, Meredith C, Loccisano A, Gentry R, Clewell H (2016) Predicting lung dosimetry of inhaled

particleborne benzo[a]pyrene using physiologically based pharmacokinetic modeling. *Inhalation Toxicology*. 28(11): 520–535.

168. Moussata J, Wang Z, Wang J (2014) Development and validation of an HPLC method for the simultaneous quantification of indole-3-carbinol acetate, indole-3-carbinol, and 3,3'-diindolylmethane in mouse plasma, liver, and kidney tissues. *Journal of Chromatography.* 958: 1–9.

169. Anderton MJ, Manson MM, Verschoyle R, Gescher A, Steward WP, Williams ML, Mager DE (2004) Physiological modeling of formulated and crystalline 3,3'-diindolylmethane pharmacokinetics following oral administration in mice. *Drug. Metab. Dispos*. 32(6): 632–638.

170. Hložek T, Uttl L, Kadeřábek L, Balíková M, Lhotková E, Horsley RR, Nováková P, Šíchová K, Štefková K, Tylš F, Kuchař M, Páleníček T (2017) Pharmacokinetic and behavioural profile of THC, CBD, and THC+CBD combination after pulmonary, oral, and subcutaneous administration in rats and confirmation of conversion in vivo of CBD to THC. *Eur. Neuropsychopharmacol.* 27(12): 1223–1237.

171. Harman D (1956) Aging: a theory based on free radical and radiation chemistry. *J. Gerontol.* **11**(3), 298–300.

172. Merksamer PI, Liu Y, He W, Hirschey MD, Chen D, Verdin E (2013) The sirtuins, oxidative stress and aging: an emerging link. *Aging (Albany NY)*, ***5***(3), 144–150.

173. Mooney KM, Morgan AE, Mc Auley MT (2016) Aging and computational systems biology. *Wiley Interdiscip. Rev. Syst. Biol. Med.* **8**, 123–139.

174. Tam ZY, Gruber J, Halliwell B, Gunawan R (2015) Context-Dependent Role of Mitochondrial Fusion-Fission in Clonal Expansion of mtDNA Mutations. *PLoS Comput. Biol.* **11**, e1004183.

175. Ferrell JE (2009) Q&A: systems biology. *Journal of biology*, *8*(1), 2.

176. Van Raamsdonk JM, Hekimi S (2010) Reactive Oxygen Species and Aging in Caenorhabditis elegans: Causal or Casual Relationship?. *Antioxid. Redox Signal.* **13**, 1911–1953.

177. Balaban RS, Nemoto S, Finkel T (2005) Mitochondria, oxidants, and aging. *Cell* **120**, 483–495.

178. Hekimi S, Lapointe J, Wen Y (2011) Taking a "good" look at free radicals in the aging process. *Trends Cell Biol.* **21**, 569–576.

179. Ziegler DV, Wiley CD, Velarde MC (2015) Mitochondrial effectors of cellular senescence: beyond the free radical theory of aging. *Aging Cell* **14**, 1–7.

180. Kennedy SR, Salk J, Schmitt MW, Loeb LA (2013) Ultra-sensitive sequencing reveals an age-related increase in somatic mitochondrial mutations that are inconsistent with oxidative damage. *PLoS Genet.* **9**, e1003794.

181. Kujoth GC, Hiona A, Pugh TD, Someya S, Panzer K, Wohlgemuth SE, Hofer T, Seo AY, Sullivan R, Jobling WA, Morrow JD, Van Remmen H, Sedivy JM, Yamasoba T, Weindruch R, Leeuwenburgh C, Prolla TA (2005) Mitochondrial DNA mutations, oxidative stress, and apoptosis in mammalian aging. *Science* **309**, 481–484.

182. Gruber J, Ng LF, Fong S, Wong YT, Koh SA, Chen C, Shui G, Cheong WF, Schaffer S, Wenk MR, Halliwell B (2011) Mitochondrial changes in ageing Caenorhabditis elegans—what do we learn from superoxide dismutase knockouts?. *PLoS One* **6**, e19444.

183. Yang W, Hekimi S (2010) A mitochondrial superoxide signal triggers increased longevity in Caenorhabditis elegans. *PLoS Biol.* **8**, e1000556.

184. Schulz AM, Haynes CM (2015) UPR(mt)-mediated cytoprotection and organismal aging. *Biochim. Biophys. Acta* **1847**, 1448–1456.

185. Pulliam DA, Deepa S, Liu Y, Hill S, Lin A, Bhattacharya A, Shi Y, Sloane L, Viscomi C, Zeviani M, Van Remmen H (2014) Complex IV-deficient Surf1(-/-) mice initiate mitochondrial stress responses. *Biochem. J.* **462**, 359–371.

186. Yoneda T, Benedetti C, Urano F, Clark SG, Harding HP, Ron D (2004) Compartment-specific perturbation of protein handling activates genes encoding mitochondrial chaperones. *J. Cell Sci.* **117**, 4055–4066.

187. Nargund AM, Pellegrino MW, Fiorese CJ, Baker BM, Haynes CM (2012) Mitochondrial import efficiency of ATFS-1 regulates mitochondrial UPR activation. *Science* **337**, 587–590.

188. Mouchiroud L, Houtkooper RH, Moullan N, Katsyuba E, Ryu D, Cantó C, Mottis A, Jo YS, Viswanathan M, Schoonjans K, Guarente L, Auwerx J (2013) The

NAD+/sirtuin pathway modulates longevity through activation of mitochondrial UPR and FOXO signaling. *Cell* **154**, 430–441.

189. Nargund AM, Fiorese CJ, Pellegrino MW, Deng P, Haynes CM (2015) Mitochondrial and nuclear accumulation of the transcription factor ATFS-1 promotes OXPHOS recovery during the UPR(mt). *Mol. Cell* **58**, 123–133.

190. Lin Y, Schulz AM, Pellegrino MW, Lu Y, Shaham S, Haynes CM (2016) Maintenance and propagation of a deleterious mitochondrial genome by the mitochondrial unfolded protein response. *Nature* **533**, 416–419.

191. Menzies FM, Fleming A, Rubinsztein DC (2015) Compromised autophagy and neurodegenerative diseases. *Nature Rev. Neurosci.* **16**, 345–357.

192. Palikaras K, Tavernarakis N (2012) Mitophagy in neurodegeneration and aging. *Front. Genet.* **3**, 297.

193. Palikaras K, Lionaki E, Tavernarakis N (2015) Coordination of mitophagy and mitochondrial biogenesis during ageing in C. elegans. *Nature* **521**, 525–528.

194. McCulloch D, Gems D (2003) Body size, insulin/IGF signaling and aging in the nematode Caenorhabditis elegans. *Exp. Geront.* **38**, 129–136.

195. Reina A, Subramaniam AB, Laromaine A, Samuel AD, Whitesides GM (2013) Shifts in the distribution of mass densities is a signature of caloric restriction in Caenorhabditis elegans. *PLoS ONE* **8**(7), e69651.

196. Wiesner RJ, Rüegg JC, Morano I (1992) Counting target molecules by exponential polymerase chain reaction: copy number of mitochondrial DNA in rat tissues. *Biochem. Biophys. Res. Commun.* **183**, 553–559.

197. Tsang WY, Lemire BD (2002) Mitochondrial genome content is regulated during nematode development. *Biochem. Biophys. Res. Commun.* **291**, 8–16.

198. Cadenas E, Davies KJ (2000) Mitochondrial free radical generation, oxidative stress, and aging. *Free Radic. Biol. Med.* **29**, 222–230.

199. Dukan S, Farewell A, Ballesteros M, Taddei F, Radman M, Nyström T (2000) Protein oxidation in response to increased transcriptional or translational errors. *Proc. Natl. Acad. Sci. U. S. A.* **97**, 5746–5749.

200. Giorgio M, Trinei M, Migliaccio E, Pelicci PG (2007) Hydrogen peroxide: a metabolic by-product or a common mediator of ageing signals?. *Nature Rev. Mol Cell Biol.* **8**, 722–728.

201. Stewart MA, Franks-Skiba K, Chen S, Cooke R (2010) Myosin ATP turnover rate is a mechanism involved in thermogenesis in resting skeletal muscle fibers. *Proc. Natl. Acad. Sci. U. S. A.* **107**, 430–435.

202. Burd NA, Tardif N, Rooyackers O, van Loon LJ (2015) Optimizing the measurement of mitochondrial protein synthesis in human skeletal muscle. *Appl. Physiol. Nutr. Metab.* **40**, 1–9.

203. Cabiscol E, Bellí G, Tamarit J, Echave P, Herrero E, Ros J (2002) Mitochondrial Hsp60, resistance to oxidative stress, and the labile iron pool are closely connected in Saccharomyces cerevisiae. *J. Biol. Chem.* **277**, 44531–44538.

204. Chondrogianni N, Petropoulos I, Grimm S, Georgila K, Catalgol B, Friguet B, Grune T, Gonos ES (2014) Protein damage, repair and proteolysis. *Mol. Aspects Med.* **35**, 1–71.

205. Stadtman ER (2006) Protein oxidation and aging. *Free Radic. Res.* **40**, 1250–1258.

206. Sohal RS (2002) Role of oxidative stress and protein oxidation in the aging process. *Free Radic. Biol. Med.* **33**, 37–44.

207. Goto S, Radak Z (2013) Implications of oxidative damage to proteins and DNA in aging and its intervention by caloric restriction and exercise. *J. Sport Health Sci.* **2**, 75–80.

208. Nelson CJ, Li L, Jacoby RP, Millar AH (2013) Degradation rate of mitochondrial proteins in Arabidopsis thaliana cells. *J. Proteome Res.* **12**, 3449–3459.

209. Bertram R, Gram Pedersen M, Luciani DS, Sherman A (2006) A simplified model for mitochondrial ATP production. *J. Theo. Biol.* **243**(4), 575–586.

210. Saa A, Siqueira KM (2013) Modeling the ATP production in mitochondria. *Bull. Math. Biol.* **75**(9), 1636–1651.

211. Imai S, Guarente L (2014) NAD+ and sirtuins in aging and disease. *Trends Cell Biol.* **24**(8), 464–471.

212. Verdin E (2015) NAD^+ in aging, metabolism, and neurodegeneration. *Science* **350**(6265), 1208–1213.

213. Jasper H (2013) Sirtuins: Longevity focuses on NAD+. *Nat. Chem. Biol.* **9**(11), 666–667.

214. Raimundo N (2014) Mitochondrial pathology: stress signals from the energy factory. *Trends Mol. Med.* **20**, 282–292.

215. Robida-Stubbs S, Glover-Cutter K, Lamming DW, Mizunuma M, Narasimhan SD, Neumann-Haefelin E, Sabatini DM, Blackwell TK (2012) TOR signaling and rapamycin influence longevity by regulating SKN-1/Nrf and DAF-16/FoxO. *Cell Metab.* **15**, 713–724.

216. Blackwell TK, Steinbaugh MJ, Hourihan JM, Ewald CY, Isik M (2015) SKN-1/Nrf, stress responses, and aging in Caenorhabditis elegans. *Free Radic. Biol. Med.* **88**(B), 290–301.

217. Hesp K, Smant G, Kammenga JE (2015) Caenorhabditis elegans DAF-16/FOXO transcription factor and its mammalian homologs associate with age-related disease. *Exp. Gerontol.* **72**, 1–7.

218. Ahting U, Floss T, Uez N, Schneider-Lohmar I, Becker L, Kling E, Iuso A, Bender A, de Angelis MH, Gailus-Durner V, Fuchs H, Meitinger T, Wurst W, Prokisch H, Klopstock T (2009) Neurological phenotype and reduced lifespan in heterozygous Tim23 knockout mice, the first mouse model of defective mitochondrial import. *Biochim. Biophys. Acta.* **1787**, 371–376.

219. Karlsson K, Sandström J, Edlund A, Marklund SL (1994) Turnover of extracellular-superoxide dismutase in tissues. *Lab. Invest.* **70**, 705–710.

220. Bittner CX, Loaiza A, Ruminot I, Larenas V, Sotelo-Hitschfeld T, Gutiérrez R, Córdova A, Valdebenito R, Frommer WB, Barros LF (2010) High Resolution Measurement of the Glycolytic Rate. *Front. Neuroenergetics* **2**, 26.

221. Rossignol R, Faustin B, Rocher C, Malgat M, Mazat J, Letellier T (2003) Mitochondrial threshold effects. *Biochem. J.* **370**, 751–762.

222. Tower J (2015) Programmed cell death in aging. *Ageing Res. Rev.* **23**, 90–100.

223. Peters R (2006) Ageing and the brain. *Postgrad. Med. J.* **82**, 84–88.

224. Bennett CF, Wende HV, Simko M, Klum S, Barfield S, Choi H, Pineda VV, Kaeberlein M (2014) Activation of the mitochondrial unfolded protein response does not predict longevity in Caenorhabditis elegans. *Nature Commun.* **5**, 3483.

225. Herndon LA, Schmeissner PJ, Dudaronek JM, Brown PA, Listner KM, Sakano Y, Paupard MC, Driscoll M (2002) Stochastic and genetic factors influence tissue-specific decline in ageing C. elegans. *Nature* **419**(6909), 808–814.

226. Hall DH, Gu G, García-Añoveros J, Gong L, Chalfie M, Driscoll M (1997) Neuropathology of degenerative cell death in Caenorhabditis elegans. *J. Neurosci.* **17**(3), 1033–1045.

227. Long X, Spycher C, Han ZS, Rose AM, Müller F, Avruch J (2002) TOR deficiency in C. elegans causes developmental arrest and intestinal atrophy by inhibition of mRNA translation. *Curr. Biol.* **12**, 1448–1461.

228. Dai Y, Zheng K, Clark J, Swerdlow RH, Pulst SM, Sutton JP, Shinobu LA, Simon DK (2014) Rapamycin drives selection against a pathogenic heteroplasmic mitochondrial DNA mutation. *Hum. Mol. Gen.* **23**, 637–647.

229. Li Q, Zhang T, Wang J, Zhang Z, Zhai Yu, Yang G, Sun X (2014) Rapamycin attenuates mitochondrial dysfunction via activation of mitophagy in experimental ischemic stroke. *Biochem. Biophys. Res. Commun.* **444**, 182–188.

230. Edinger AL, Linardic CM, Chiang G, Thompson CB, Abraham RT (2003) Differential effects of rapamycin on mammalian target of rapamycin signaling functions in mammalian cells. *Cancer Res.* **63**, 8451–8460.

231. Pivtoraiko VN, Harrington AJ, Mader BJ, Luker AM, Caldwell GA, Caldwell KA, Roth KA, Shacka J (2010) Low-dose bafilomycin attenuates neuronal cell death associated with autophagy-lysosome pathway dysfunction. *J. Neurochem.* **114**, 1193–1204.

232. Lode H (1991) The pharmacokinetics of azithromycin and their clinical significance. *Eur. J. Clin. Microbiol. Infect. Dis.* **10**, 807–812.

233. Cochemé HM, Murphy MP (2008) Complex I is the major site of mitochondrial superoxide production by paraquat. *J. Biol. Chem.* **283**, 1786–1798.

234. Park SK, Tedesco PM, Johnson TE (2009) Oxidative Stress and Longevity in *C. elegans* as Mediated by SKN-1. *Aging Cell*. **8**, 258–269.

235. Ray A, Martinez BA, Berkowitz LA, Caldwell GA, Caldwell KA (2014) Mitochondrial dysfunction, oxidative stress, and neurodegeneration elicited by a bacterial metabolite in a *C. elegans* Parkinson's model. *Cell Death Dis.* ***5***, e984.

236. Roberts TR, Dyson JS, Lane MCG (2002) Deactivation of the Biological Activity of Paraquat in the Soil Environment: a Review of Long-Term Environmental Fate. *J Agricult. Food Chem.* **50**, 3623–3631.

237. Lee SJ, Hwang AB, Kenyon C (2010) Inhibition of respiration extends *C. elegans*' lifespan via reactive oxygen species that increase HIF-1 activity. *Curr. Biol.* **20**, 2131–2136.

238. Yang W, Hekimi S (2010) A Mitochondrial Superoxide Signal Triggers Increased Longevity in Caenorhabditis elegans. *PLoS Biol.* **8**, e1000556.

239. Chang J, Rimando A, Pallas M, Camins A, Porquet D, Reeves J, Shukitt-Hale B, Smith MA, Joseph JA, Casadesus G (2012) Low-dose pterostilbene, but not resveratrol, is a potent neuromodulator in aging and Alzheimer's disease. *Neurobiol. Aging* **33**, 2062–2071.

240. Fischer N, Büchter C, Koch K, Albert S, Csuk R, Wätjen W (2017) The resveratrol derivatives trans-3,5-dimethoxy-4-fluoro-4′-hydroxystilbene and trans-2,4′,5-trihydroxystilbene decrease oxidative stress and prolong lifespan in Caenorhabditis elegans. *J. Pharm. Pharmacol.* **69**, 73–81.

241. Francioso A, Mastromarino P, Restignoli R, Boffi A, d'Erme M, Mosca L (2014) Improved stability of trans-resveratrol in aqueous solutions by carboxymethylated (1,3/1,6)-β-D-glucan. *J. Agricult. Food Chem.* **62**, 1520–1525.

242. Remsberg CM, Yáñez JA, Ohgami Y, Vega-Villa KR, Rimando AM, Davies NM (2008) Pharmacometrics of pterostilbene: preclinical pharmacokinetics and metabolism, anticancer, antiinflammatory, antioxidant and analgesic activity. *Phytother. Res.* **22**, 169–179.

243. Cloutier M, Wellstead P (2012) Dynamic modelling of protein and oxidative metabolisms simulates the pathogenesis of Parkinson's disease. *IET Syst. Biol.* **6**, 65–72.

244. Fang EF, Scheibye-Knudsen M, Brace LE, Kassahun H, SenGupta T, Nilsen H, Mitchell JR, Croteau DL, Bohr VA (2014) Defective mitophagy in XPA via PARP-1 hyperactivation and NAD(+)/SIRT1 reduction. *Cell* **157**, 882–896.

245. Moroz N, Carmona J, Anderson E, Hart AC, Sinclair DA, Blackwell TK (2014) Dietary restriction involves NAD^+-dependent mechanisms and a shift toward oxidative metabolism. *Aging Cell* **13**, 1075–1085.

246. Mauro-Lizcano M, Esteban-Martínez L, Seco E, Serrano-Puebla A, Garcia-Ledo L, Figueiredo-Pereira C, Vieira HL, Boya P (2015) New method to assess mitophagy flux by flow cytometry. *Autophagy* **11**, 833–843.

247. Pinto M, Pickrell AM, Wang X, Bacman SR, Yu A, Hida A, Dillon LM, Morton PD, Malek TR, Williams SL, Moraes CT (2017) Transient mitochondrial DNA double strand breaks in mice cause accelerated aging phenotypes in a ROS-dependent but p53/p21-independent manner. *Cell Death Differ.* **24**(2), 288–299.

248. Poulose SM (2015) Effects of pterostilbene and resveratrol on brain and behavior. *Neurochem. Int.* **89**, 227–233.

249. Niccoli T, Partridge L (2012) Ageing as a risk factor for disease. *Curr. Biol.* **22**, R741–R752.

250. Martínez-Cizuelo V, Gómez J, García-Junceda I, Naudí A, Cabré R, Mota-Martorell N, López-Torres M, González-Sánchez M, Pamplona R, Barja G (2016) Rapamycin reverses age-related increases in mitochondrial ROS production at complex I, oxidative stress, accumulation of mtDNA fragments inside nuclear DNA, and lipofuscin level, and increases autophagy, in the liver of middle-aged mice. *Exp. Gerontol.* **83**, 130–138.

251. Kolosova NG, Vitovtov AO, Muraleva NA, Akulov AE, Stefanova NA, Blagosklonny MV (2013) Rapamycin suppresses brain aging in senescence-accelerated OXYS rats. *Aging* **5**, 474–484.

252. McCormack S, Polyak E, Ostrovsky J, Dingley SD, Rao M, Kwon YJ, Xiao R, Zhang Z, Nakamaru-Ogiso E, Falk MJ (2015) Pharmacologic targeting of sirtuin and PPAR signaling improves longevity and mitochondrial physiology in respiratory chain complex I mutant Caenorhabditis elegans. *Mitochondrion* **22**, 45–59.

253. Papa L, Germain D (2014) SirT3 regulates the mitochondrial unfolded protein response. *Mol. Cell. Biol.* **34**, 699–710.

254. Verlingue L, Dugourd A, Stoll G, Barillot E, Calzone L, Londoño-Vallejo A (2016) A comprehensive approach to the molecular determinants of lifespan using a Boolean model of geroconversion. *Aging Cell* **15**, 1018–1026.

255. Stroustrup N, Anthony WE, Nash ZM, Gowda V, Gomez A, López-Moyado IF, Apfeld J, Fontana W (2016) The temporal scaling of Caenorhabditis elegans ageing. *Nature* **530**, 103–107.

256. Cummings J, Aisen PS, DuBois B, Frölich L, Jack CR, Jones RW, Morris JC, Raskin J, Dowsett SA, Scheltens P (2016) Drug development in Alzheimer's disease: the path to 2025. *Alzheimer's research & therapy*. **8**, 39.

257. Brookmeyer R, Johnson E, Ziegler-Graham K, Arrighi HM (2007) Forecasting the global burden of Alzheimer's disease. *Alzheimers & Dementia.* **3**(3), 186–191.

258. Weuve J, Hebert LE, Scherr PA, Evans DA (2015) Prevalence of Alzheimer disease in US states. *Epidemiology.* **26** (1): e4–e6.

259. Moodley KK, Chan D (2014) The hippocampus in neurodegenerative disease. *Front Neurol Neurosci.* **24**, 95–108.

260. Milenkovic I, Petrov T, Kovacs GG (2014) Patterns of hippocampal tau pathology differentiate neurodegenerative dementias. *Dement Geriatr Cogn Disord.* **38**(5-6), 375–388.

261. Kraemer BC, Burgess JK, Chen JH, Thomas JH, Schellenberg GD (2006) Molecular pathways that influence human tau-induced pathology in Caenorhabditis elegans. *Human Molecular Genetics***. 15**(9), 1483–1496.

262. Guerreiro R, Bras J (2015) The age factor in Alzheimer's disease. *Genome Medicine*. **7**, 106.

263. Labbadia J, Brielmann RM, Neto MF, Lin Y-F, Haynes CM, Morimoto RI (2017) Mitochondrial stress restores the heat shock response and prevents proteostasis collapse during aging. *Cell Reports.* **21**(6), 1481–1494.

264. Piaceri I, Rinnoci V, Bagnoli S, Failli Y, Sorbi S (2012) Mitochondria and Alzheimer's disease. *J Neurol Sci.* **322**(1-2), 31–34.

265. Anand R, Gill KD, Mahdi AA (2014) Therapeutics of Alzheimer's disease: Past, present and future. *Neuropharmacology*. **76**(Pt. A), 27–50.

266. Fatouros C, Pir GJ, Biernat J, Koushika SP, Mandelkow E, Mandelkow EM, Schmidt E, Baumeister R (2012) Inhibition of tau aggregation in a novel Caenorhabditis elegans model of tauopathy mitigates proteotoxicity. *Human Molecular Genetics.* **21**(16), 3587–3603.

267. Beck JS, Mufson EJ, Counts SE (2016) Evidence for Mitochondrial UPR Gene Activation in Familial and Sporadic Alzheimer's Disease. *Current Alzheimer research*. **13**(6), 610–614.

268. Regitz C, Fitzenberger E, Mahn F, Dußling L, Wenzel U (2016) Resveratrol reduces amyloid-beta ($A\beta_{1-42}$)-induced paralysis through targeting proteostasis in an Alzheimer model of Caenorhabditis elegans. *European Journal of Nutrition.* **55**(2), 741–747.

269. Sorrentino V, Romani M, Mouchiroud L, Beck JS, Zhang H, D'Amico D, Moullan N, Potenza F, Schmid AW, Rietsch S, Counts SE Auwerx J (2017) Enhancing mitochondrial proteostasis reduces amyloid-β proteotoxicity. *Nature.* **552**(7684), 187–193.

270. Anisimova AS, Alexandrov AI, Makarova NE, Gladyshev VN, Dmitriev SE (2018) Protein synthesis and quality control in aging. *Aging*. **10**(12), 4269–4288.

271. Murphy MP, LeVine H (2010) Alzheimer's disease and the amyloid-beta peptide. *Journal of Alzheimer's disease*. **19**(1), 311–323.

272. Lopes S, Vaz-Silva J, Pinto V, Dalla C, Kokras N, Bedenk B, Mack N, Czisch M, Almeida OF, Sousa N, Sotiropoulos I (2016) Tau protein is essential for stress-induced brain pathology. *Proceedings of the National Academy of Sciences of the United States of America* **113**(26), E3755–E3763.

273. Butterfield DA, Boyd-Kimball D (2018) Oxidative Stress, Amyloid-β Peptide, and Altered Key Molecular Pathways in the Pathogenesis and Progression of Alzheimer's Disease. *Journal of Alzheimer's Disease*. **62**(3), 1345–1367.

274. Radford H, Moreno JA, Verity N, Halliday M, Mallucci GR (2015) PERK inhibition prevents tau-mediated neurodegeneration in a mouse model of frontotemporal dementia. *Acta Neuropathologica.* **130**(5), 633–642.

275. Halliday M, Radford H, Zents KAM, Molloy C, Moreno JA, Verity NC, Smith E, Ortori CA, Barnett DA, Bushell M, Mallucci GR (2017) Repurposed drugs targeting eIF2α-P-mediated translational repression prevent neurodegeneration in mice. *Brain.* **140**(6), 1768–1783.

276. Moreno JA, Mallucci GR (2010) Dysfunction and recovery of synapses in prion disease: implications for neurodegeneration. *Biochemical Society Transactions.* **38**(2), 482–487.

277. Moreno JA, Radford H, Peretti D, Steinert JR, Verity N, Martin MG, Halliday M, Morgan J, Dinsdale D, Ortori CA, Barrett DA, Tsaytler P, Bertolotti A, Willis AE, Bushell M, Mallucci GR (2012) Sustained translational repression by eIF2α–P mediates prion neurodegeneration. *Nature.* **485**(7399), 507–511.

278. Moreno JA, Halliday M, Molloy C, Radford H, Verity N, Axten JM, Ortori CA, Willis AE, Fischer PM, Barrett DA, Mallucci GR (2013) Oral treatment targeting the unfolded protein response prevents neurodegeneration and clinical disease in prion-infected mice. *Science Translational Medicine.* **5**(206), 206ra138.

279. Poirier Y, Grimm A, Schmitt K, Eckert A (2019) Link between the unfolded protein response and dysregulation of mitochondrial bioenergetics in Alzheimer's disease. *Cell Mol. Life Sci.* [Epub] Accessed February 3, 2019.

280. Johnson DA, Johnson JA (2015) Nrf2—a therapeutic target for the treatment of neurodegenerative diseases. *Free Radical Biology & Medicine*. **88**(Pt B), 253–267.

281. Hesp K, Smant G, Kammenga JE (2015) Caenorhabditis elegans DAF-16/FOXO transcription factor and its mammalian homologs associate with age-related disease. *Exp Gerontol.* **72**, 1–7.

282. Rocchi A, Yamamoto S, Ting T, Fan Y, Sadleir K, Wang Y, Zhang W, Huang S, Levine B, Vassar R, He C (2017) A Becn1 mutation mediates hyperactive autophagic sequestration of amyloid oligomers and improved cognition in Alzheimer's disease. *PLoS genetics*, *13*(8), e1006962.

283. Du F, Yu Q, Yan S, Hu G, Lue LF, Walker DG, Wu L, Yan SF, Tieu K, Yan SS (2017) PINK1 signalling rescues amyloid pathology and mitochondrial dysfunction in Alzheimer's disease. *Brain.* **140**(12), 3233–3251.

284. Sun X, Chen W-D, Wang Y-D (2017) DAF-16/FOXO Transcription Factor in Aging and Longevity. *Frontiers in Pharmacology*. **8**, 548.

285. Chew YL, Götz J, Nicholas HR (2015) Neuronal protein with tau-like repeats (PTL-1) regulates intestinal SKN-1 nuclear accumulation in response to oxidative stress. *Aging Cell.* **14**(1), 148–151.

286. Chen X, McCue HV, Wong SQ, Kashyap SS, Kraemer BC, Barclay JW, Burgoyne RD, Morgan A (2015) Ethosuximide ameliorates neurodegenerative disease phenotypes by modulating DAF-16/FOXO target gene expression. *Mol. Neurodegener.* **10**, 51.

287. Jo C, Gundemir S, Pritchard S, Jin YN, Rahman I, Johnson GVW (2014) Nrf2 reduces levels of phosphorylated tau protein by inducing autophagy adaptor protein NDP52. *Nature Communications.* **5**, 3496.

288. Mattsson N, Schott JM, Hardy J, Turner MR, Zetterberg H (2016) Selective vulnerability in neurodegeneration: insights from clinical variants of Alzheimer's disease. *J Neurol Neurosurg Psychiatry.* **87**(9), 1000–1004.

289. Bartsch T, Wulff P (2015) The hippocampus in aging and disease: From plasticity to vulnerability. *Neuroscience.* **309**,1–16.

290. Roselli F, Caroni P (2015) From Intrinsic Firing Properties to Selective Neuronal Vulnerability in Neurodegenerative Diseases. *Neuron.* **85**, 901–910.

291. Filézac de L'Etang A, Maharjan N, Cordeiro Braña M, Ruegsegger C, Rehmann R, Goswami A, Roos A, Troost D, Schneider BL, Weis J, Saxena S (2015)

Marinesco-Sjögren syndrome protein SIL1 regulates motor neuron subtype-selective ER stress in ALS. *Nat Neurosci.* **18**(2), 227–238.

292. Wood LB, Winslow AR, Strasser SD (2015) Systems Biology of Neurodegenerative Diseases. *Integrative Biology: Quantitative Biosciences from Nano to Macro*. **7**(7), 758–775.

293. Hastings J, Mains A, Virk B, Rodriguez N, Murdoch S, Pearce J, […] Casanueva O (2019) Multi-Omics and Genome-Scale Modeling Reveal a Metabolic Shift During *C. elegans* Aging. *Frontiers in molecular biosciences*, *6*, 2.

294. Lal S, McCart Reed AE, de Luca XM, Simpson PT (2017) Molecular signatures in breast cancer. *Methods.* **1**, 131–135.

295. Schwab JD, Siegle L, Kühlwein SD, Kühl M, Kestler HA (2017) Stability of Signaling Pathways during Aging-A Boolean Network Approach. *Biology*, *6*(4), 46.

296. Dong X, Milholland B, Vijg J (2016) Evidence for a limit to human lifespan. Nature. 538(7624): 257–259.

297. Cenini G, Voos W (2016) Role of Mitochondrial Protein Quality Control in Oxidative Stress-induced Neurodegenerative Diseases. Curr Alzheimer Res. 13(2): 164–173.

298. Fiorese CJ, Haynes CM (2017) Integrating the UPR^{mt} into the mitochondrial maintenance network. *Critical reviews in biochemistry and molecular biology*, *52*(3), 304–313.

299. Kaufman DM, Wu X, Scott BA, Itani OA, Van Gilst MR, Bruce JE, Crowder CM (2017) Ageing and hypoxia cause protein aggregation in mitochondria. *Cell death and differentiation*, *24*(10), 1730–1738.

300. Pharaoh G, Pulliam D, Hill S, Sataranatarajan K, Van Remmen H (2016) Ablation of the mitochondrial complex IV assembly protein Surf1 leads to increased expression of the UPR(MT) and increased resistance to oxidative stress in primary cultures of fibroblasts. *Redox biology*, *8*, 430–438.

301. Shpilka T, Haynes CM (2018) The mitochondrial UPR: mechanisms, physiological functions and implications in ageing. Nat Rev Mol Cell Biol. 19(2): 109–120.

302. Alavi Naini SM, Soussi-Yanicostas N (2015) Tau Hyperphosphorylation and Oxidative Stress, a Critical Vicious Circle in Neurodegenerative Tauopathies? *Oxidative medicine and cellular longevity*, *2015*, 151979.

303. Antikainen H, Driscoll M, Haspel G, Dobrowolski R (2017) TOR-mediated regulation of metabolism in aging. *Aging cell*, *16*(6), 1219–1233.

304. Koh JH, Wang L, Beaudoin-Chabot C, Thibault G (2018) Lipid bilayer stress-activated IRE-1 modulates autophagy during endoplasmic reticulum stress. *J Cell Sci.* 131(22). pii: jcs217992.

305. Cooper JF, Machiela E, Dues DJ, Spielbauer KK, Senchuk MM, Van Raamsdonk JM (2017) Activation of the mitochondrial unfolded protein response promotes longevity and dopamine neuron survival in Parkinson's disease models. *Scientific reports*, *7*(1), 16441.

306. Wu Z, Senchuk MM, Dues DJ, Johnson BK, Cooper JF, Lew L, […] Van Raamsdonk JM (2018) Mitochondrial unfolded protein response transcription factor ATFS-1 promotes longevity in a long-lived mitochondrial mutant through activation of stress response pathways. *BMC biology*, *16*(1), 147.

307. Zhang Y, Nguyen DT, Olzomer EM, Poon GP, Cole NJ, Puvanendran A, Phillips BR, Hesselson D (2017) Rescue of Pink1 Deficiency by Stress-Dependent Activation of Autophagy. *Cell Chem Biol.* 24(4):471–480.e1–e4.

308. Chang JT, Kumsta C, Hellman AB, Adams LM, Hansen M (2017) Spatiotemporal regulation of autophagy during Caenorhabditis elegans aging. *eLife,* 6, e18459.

309. Chapin HC, Okada M, Merz AJ, Miller DL (2015) Tissue-specific autophagy responses to aging and stress in C. elegans. *Aging,* 7(6), 419–434.

310. Li ST, Zhao HQ, Zhang P, Liang CY, Zhang YP, Hsu AL, Dong MQ (2019) DAF-16 stabilizes the aging transcriptome and is activated in mid-aged Caenorhabditis elegans to cope with internal stress. *Aging Cell.* e12896.

311. Zhang H, Davies K, Forman, H. J. (2015) Oxidative stress response and Nrf2 signaling in aging. *Free radical biology & medicine,* 88(Pt B), 314–336.

312. Frakes AE, Dillin A (2017) The UPR(ER): Sensor and Coordinator of Organismal Homeostasis. *Mol Cell.* 66(6):761–771.

313. Labbadia J, Morimoto RI (2015) Repression of the Heat Shock Response Is a Programmed Event at the Onset of Reproduction. *Molecular cell,* 59(4), 639–650.

314. Morsci NS, Hall DH, Driscoll M, Sheng ZH (2016) Age-Related Phasic Patterns of Mitochondrial Maintenance in Adult Caenorhabditis elegans Neurons. *The Journal of neuroscience: the official journal of the Society for Neuroscience,* 36(4), 1373–1385.

315. Taylor RC, Dillin A (2013) XBP-1 is a cell-nonautonomous regulator of stress resistance and longevity. *Cell*, *153*(7), 1435–1447.

316. Yasuda K, Ishii T, Suda H, Akatsuka A, Hartman PS, Goto S, Miyazawa M, Ishii N (2006) Age-related changes of mitochondrial structure and function in Caenorhabditis elegans. *Mech Ageing Dev*. 127(10):763–770.

317. Rojo A I, Pajares M, Rada P, Nuñez A, Nevado-Holgado AJ, Killik R, […] Cuadrado A (2017) NRF2 deficiency replicates transcriptomic changes in Alzheimer's patients and worsens APP and TAU pathology. *Redox biology*, *13*, 444–451.

318. Tang M, Ji C, Pallo S, Rahman I, Johnson G (2017) Nrf2 mediates the expression of BAG3 and autophagy cargo adaptor proteins and tau clearance in an age-dependent manner. *Neurobiology of aging*, *63*, 128–139.

319. Fang E, Hou Y, Palikaras K, Adriaanse B, Kerr J, Yang B, [...] Bohr V (2019) Mitophagy inhibits amyloid-β and tau pathology and reverses cognitive deficits in models of Alzheimer's disease. *Nature Neuroscience. 22*(3), 401–412.

320. Marcora M, Belfiori-Carrasco L, Bocai N, Morelli L, Castaño E (2017) Amyloid-β42 clearance and neuroprotection mediated by X-box binding protein 1 signaling decline with aging in the Drosophila brain. *Neurobiology of Aging. 60*, 57–70.

321. Moffitt TE, Belsky DW, Danese A, Poulton R, Caspi A (2016) The Longitudinal Study of Aging in Human Young Adults: Knowledge Gaps and Research Agenda. *The journals of gerontology. Series A, Biological sciences and medical sciences*, *72*(2), 210–215.

322. Han J-Y, Han S-H (2014) Primary Prevention of Alzheimer's Disease: Is It an Attainable Goal? *Journal of Korean Medical Science*. **29**(7), 886–892.

323. Huang Y, Mucke L (2012) Alzheimer Mechanisms and Therapeutic Strategies. *Cell*. **148**(6), 1204–1222.

324. Xie A, Gao J, Xu L, Meng D (2014) Shared Mechanisms of Neurodegeneration in Alzheimer's Disease and Parkinson's Disease. *BioMed Research International*. **2014**, 648740.

325. Serý O, Povová J, Míšek I, Pešák L, Janout V. (2013) Molecular mechanisms of neuropathological changes in Alzheimer's disease: a review. *Folia Neuropathol.* **51**(1), 1–9.